Electrochromic properties and coloration mechanisms of sol-gel NiO-TiO_2 layers and devices built with them

Dissertation

Zur Erlangung des Grades

Doktor der Wissenschaften

An der Naturwissenschaftlich-Technischen Fakultät III

Der Universität des Saarlandes

Vorgelegt von

Amal Alkahlout

Saarbrücken

2006

Tage des Kolloquims:

Dekan: Professor Dr. Kaspar Hegetschweiler

Berichterstatter: Professor Dr.Michel A. Aegerter

Berichterstatter: Professor Dr. Wulff Possart

Vorsitzender: Professor Dr. Michael Veith

Beisitzer: Dr. Andreas Rammo

Dedicated to

my own soul out of my soul ....Mustafa

Acknowledgment

GOD...without your help and support, I could not survive or achieve any thing.

First, I thank Professor Dr. M.A. Aegerter for giving me the chance to be one of his students and for his generous advices, valuable discussions which helped me greatly, and the good proof reading of this thesis. He did not only guide this work and find time to discuss with me but also gave me the confidence to express my ideas freely. I will always remember how his ideas and suggestions always work and how he could simply pick the small mistakes. I am also most grateful to him for giving me the chance to have realized some scientific work at the university of São Paulo in São Carlos (Brazil). I have to say that your presence at INM is the best thing could happen to my thesis.

I am also thankful to the members of the institute for their support; especially to Dr. S. Heusing for the lab safety instructions, and her readiness to discuss some of my results, Dr. J. Pütz for his valuable notes whenever he was asked for, and Dr. S. Gerbes for his careful and detailed explanations. Thanks to all technicians, Dr. Grobelsek, Mrs. Haettich and Dr. Koch. Special thanks to my former colleague Dr. Sun who guided gently my first steps at INM. The former and the present secretaries Mrs. Bonard and Gogelgans for carrying out efficiently the secretarial services I needed.

I would also acknowledge the financial support from Al-Azhar University (Gaza), the State of Saarland, the Federal Ministry for Research and Education (Germany) and the Brazilian-German exchange program PROBRAL (DAAD).

Special thanks to Prof. Dr.S. Zourab for his effort to get leave of absence from Al-Azhar to work for this thesis and his endless support, to Dr. N. Al-Dahoudi for introducing me to my supervisor, Mrs A. Romina from ZIS office at Saarland University for her kind help in all administrative work.

I stand by these few lines to express my deepest gratitude and appreciation for the constant support, understanding and love that I received from my husband Mustafa, who helped me to focus on my work. He always gave me the chance and support to travel abroad to enrich my professional and educational career. I have to say it clearly that without him in my life, I would never be able to achieve my goals. You are my candle.

I also need to address my sweet children who have been wonderful independent children and showed a lot of understanding when I spent the time working for this thesis. Dana who started her school and could not support as a full time mother usually does, Haya who hides in my cloth as a cat smelling me, and little Mohammed who was born at the beginning of this work. You have been one of my motivations to work harder to finish this work faster. I love you all.

My parents, your unconditioned love and trust modelled me in the shape I am. I know how much you suffer while I was away working for this project. Forgive me.

I would also thank my friends Mohammed, Zaher, Samah, Adriana, Maria and Muserra. You always found a way to support and help me during the hard times.

Still need to add thanks to the hard times and people who put me in hard times, as they gave me the chance to learn how to be stronger.

List of abbreviations:

ADD	Alternative dipping deposition
ATO	Antimony tin oxide
CA	Chronoamperometry
CBD	Chemical bath deposition
C.E	Counter electrode
CC	chronocoulometry
CE	Coloration efficiency
CR	Contrast ratio
CP	Chronopotentiometry
CV	Cyclic voltammetry
dc	Direct current
DTA	Differential thermal analysis
E	Electrolyte
EC	Electrochromic
ECD	Electrochromic device
EQCM	Electrochemical quartz crystal microbalance
FTIR	Fourier Transform Infrared
FTO	Fluorine doped tin oxide
GS	Gram-Schmidt
HWFM	Half width at full maximum
INM	Leibniz-Institute for New Material
i	Current density
IS	Ion storage
ITO	Indium tin oxide
M	Mole/Litre
MS	Mass spectroscopy
LBD	Liquid bath deposition
PC	Propylene carbonate
OER	Oxygen evolution reaction
PLD	Pulsed laser deposition
PVD	Physical vapour deposition
Q, q	Electric charge

QCM	Quartz Crystal Microbalance
SEM	Scanning electron microscopy
RE	Reference electrode
t	time
T_b	Transmission in the bleached state
T_c	Transmission in the colored state
TCE	Transparent conductive electrode
TCO	Transparent conducting oxide
TG	Thermal gravimetry
TMO	Transparent metal oxide
UV	Ultra violet
UV-VIS-NIR	Ultra violet-visible-near infrared
WE	Working electrode
XPS	X-Ray Photoelectron Spectroscopy
XRD	X-Ray Diffraction
wt. %	Weight percent
Δm	Mass change
ΔQ	Charge change
ΔOD	Change in optical density

Abstract

Electrochromic films of $NiO\text{-}TiO_2$ with Ni concentration of 100, 90, 87, 83, 75, 66, 50 and 33 mol % have been obtained via the sol-gel route by dip coating technique using ethanolic sols of nickel acetate tetrahydrate ($Ni(CH_3COO)_2{\cdot}4H_2O$) and titanium n–propoxide ($Ti(O\text{-}CH(CH_3)_2)_4$) precursors and sintered in air between 250 and 500 °C. Xerogels obtained by drying the sols have been studied up to 900 °C by thermal analysis (DTA/TG) coupled to mass and IR spectroscopy. The crystalline structure and morphology of the layers in the as deposited, bleached and colored states was determined by X-ray diffractometry, scanning electron microscopy and transmission electron microscopy. Their electrochromic properties have been studied in 1 M KOH aqueous electrolyte as a function of the layer composition, thickness and sintering temperature. Deep brown color with reversible transmittance changes have been obtained using cycling voltammetry and chronoamperometry processes. The best composition to get stable sols, a high reversible transmittance change and fast switching times (10 s) was obtained with double $NiO\text{-}TiO_2$ layers 160 nm thick having 75 % Ni molar concentration, and sintered between 300 and 350 °C. The electrochromism of the layer was also studied in $LiClO_4$-PC electrolyte.

The mechanisms of coloration and morphology transformation of the layer during cycling in 1 M KOH electrolyte are discussed in terms of an activation and degradation period. The nature of the ions involved in the coloration process has been studied using Electrochemical Quartz Crystal Microbalance (EQCM). It was found that the degradation period is associated with an unusual large increase of the mass of the layer after each cycle due to the irreversible incorporation of OH^- groups and/or the irreversible formation of water ($OH^- + H^+ \rightarrow H_2O$).

Finally, devices have been mounted and tested using the $NiO\text{-}TiO_2$ layer as a working electrode together with $CeO_2\text{-}TiO_2$ layer or with a WO_3 or a Nb_2O_5 cathodic layer acting as an active counter electrode. Also a new type of electrolyte based on KOH mixed with starch has been also developed and tested with complete windows.

Kurzfassung

Elektrochrome Schichten bestehend aus NiO und TiO_2 mit Ni-Gehalten von 33 bis 100 mol % wurden mit Hilfe des Sol-Gel-Prozesses durch Tauchbeschichtung aus alkoholischen Lösungen von Nickelacetat-Tetrahydrat ($Ni(CH_3COO)_2 \cdot 4H_2O$) und Titan-n-propoxid ($Ti(O\text{-}CH(CH_3)_2)_4$) hergestellt und bei Temperaturen zwischen 250 und 500°C an Luft gesintert. Xerogele, die durch die Trocknung der Sole erhalten wurden, wurden bis zu einer Temperatur von 900 °C mittels thermischer Analysen (DTA/TG) in Verbindung mit Massen- und IR-Spektroskopie untersucht. Die kristalline Struktur und Morphologie der Schichten im abgeschiedenen, entfärbten und gefärbten Zustand wurde durch Röntgendiffraktrometrie, Elektronenmikroskopie und Transmissionselektronenmikroskpie untersucht. Die Analyse ihrer elektrochromen Eigenschaften erfolgte unter Verwendung eines wässrigen Elektrolyten (1 mol/l KOH) in Bezug auf die Schichtzusammensetzung, Dicke und Sintertemperatur. Eine dunkelbraune Farbe mit einer reversiblen Transmissionsänderung wurde durch Cyclovoltammetrie- und Chronoamperometrie-Prozesse erzielt. Die beste Zusammensetzung zur Erzielung stabiler Sole, einer hohen, reversiblen Transmissionsänderung und schneller Schaltzeiten (10 S.) wurde mit $NiO\text{-}TiO_2$ Doppelschichten (Dicke ca. 160 nm) mit einem Nickelgehalt von 75 mol % und für Sintertemperaturen zwischen 300 und 350°C erreicht. Die Elektrochromie der Schichten wurde darüber hinaus in einem $LiClO_4$-Polycarbonat-Elektrolyten untersucht.
Ein Mechanismus für Farb- und Morphologieumwandlung der Schicht während des Schaltzyklus in KOH-Elektrolyt wird im Sinne eines Aktivierungs- und Degradierungsprozesses diskutiert. Die Art der Ionen, die am Färbungsprozess beteiligt sind, wurde mit Hilfe der elektrochemischen Quartzmikrowaage (EQCM) untersucht. Es wurde beobachtet, dass der Aktivierungsprozess mit einer Zunahme der Schichtmasse nach jedem Zyklus aufgrund einer sukzessiven Aufnahme von OH-Gruppen und der Umwandlung von $Ni(OH)_2$ in hydratisiertes NiOOH einhergeht, was schliesslich eine braune Färbung und den Einbau von Wasser ($OH^- + H^+ \rightarrow H_2O$) in das Kristallgitter zur Folge hat. Die allmähliche Veränderung der Schichtzusammensetzung führte zu einer porösen und zerbrechlichen Morphologie, die letztendlich eine Aufnahme von K^+-Ionen und weiterer Wassermoleküle ermöglichte und für den einsetzenden Degradierungsprozess in Verbindung mit einem ungewöhnlich starken Anstieg der Schichtmasse nach jedem Zyklus verantwortlich ist.
Schließlich konnten elektrochrome Fenster konstruiert werden, welche zum einen reine $NiO\text{-}TiO_2$-Schichten, zum anderen mit einer dünnen dielektrischen Antikorrosionsschicht versehene $NiO\text{-}TiO_2$-Schichten als Arbeitselektrode enthielten. Als kathodische Gegenelektrode fungierten Schichten von $CeO_2\text{-}TiO_2$ bzw. WO_3 oder Nb_2O_5. Des Weiteren erfolgte die Entwicklung eines neuen Elektrolyt-Typs basierend auf KOH in Verbindung mit Stärke, der an kompletten Fenstern getestet wurde.

Zusammenfassung

Nickeloxid-Titanoxid ($NiO-TiO_2$) Xerogele und Schichten unterschiedlicher Nickel-Gehalte wurden im Sol-Gel Verfahren hergestellt. Durch Tauchverfahren und Sinterung bis zu 500° C Transparente Einzel- und Mehrfachschichten mit der Gesamtdichte bis zu 240 nm konnten auf FTO - beschichteten Glasssubstraten abgeschieden werden.
Die Bildung von Xerogelen wurde durch zeitgleiche Differentialthermoanalyse und. Differential-Thermogravimetrie (DTA-TG), gekoppelt an Massen- und Infrarotspektrometrie, untersucht. Das Hauptmerkmal der DTA-Kurve stellte ein starker exothermischer Doppelpeak zwischen 300 und 360° C mit Maximum bei 344 und 357°C. Diese korrespondieren mit ebensolcher für die Massenverlust von ca. 35 wt %. Eine sorgfältige Analyse der Infrarotspektren der bei dieser Temperatur entstehenden Gase zeigt, dass die Bildung von anorganischen Nickelverbindungen, die vor allem NiO_x und möglicherweise $NiCO_3$ beinhalten, nur bei der Temperatur bis zu 350° C erfolgt, wobei dem zweiten Maximum bei 357° C, die Transformation von $NiCO_3$ in NiO entspricht.
SEM- Bilder von Beschichtungen mit verschiedenen Nickel-Gehalten zeigen, dass alle Schichten homogen ohne Narben und Rissen waren. Alle Beschichtungen wiesen eine leicht grünliche Farbe auf.
Bei Temperaturen bis zu 500° C gesinterte Sol-Gel $NiO-TiO_2$ Schichten hatten eine kubische NiO-Struktur (Bunsenit) unabhängig von der Nickelkonzentration. Die Kristallinität der Schichten stiegt mit der Sintertemperatur an und die mit dem (200) Peak kalkulierte Kristallit- Größe betrug 2,5; 4,7 und 8 nm nach der Sintern bei 300, 400 bzw. 500° C.
Die elektrochromen Eigenschaften der Schichten sind mithilfe von zyklischer Voltametrie (CV) und Chronoamperometrie in 1 M wässriger Lösung von KOH in Abhängigkeit von Potential-Bereich, Nickelgehalt, Wärmebehandlung und Schichtdichte untersucht worden. Reine NiO Schichten zeigten eine schlechte Haftung auf dem Substrat, eine permanent braune Färbung schon nach 50 CV Zyklen und wurden schnell von Elektrolyten angegriffen. Die Haftung konnte eindeutig durch die Erhöhung von Titangehalt verbessert werden. Jedoch ließen optische Dichte und Ladungskapazität mit steigendem Titangehalt kontinuierlich nach. Die besten Eigenschaften wiesen zwischen 300° und 350 °C gesinterte 160 nm dicke Doppelschichten mit einem Nickelgehalt von 75 mol % auf. Bei Zyklendurchlauf zwischen -0,6 und +1 V vs. SCE zeigten sie eine tiefe reversible braune Färbung mit Transmissionsänderung zwischen 90 und 25 % bei 550 nm, eine dauerhafte Stabilität von ca. 2000 Zyklen und eine kurze Schaltzeit <10 S. Die Färbung von $NiO-TiO_2$ beginnt in der dünnen Zwischenschicht (etwa 40-50nm), die mit steigenden Zyklenzahl solange an Dichte zunimmt, bis am Ende der so genannten Aktivierungsperiode, die bis ca. 1000 Zyklen dauert, die volle Tiefe der Schicht erreicht ist, abhängig von den Schaltspannungen, Schichtdichte und Sintertemperatur. Gleichzeitig findet ein langsamer Abbau statt, in dessen Verlauf eine passive, irreversibel gefärbte und sehr fragile Schicht entsteht. Dieser Vorgang ist klar nach ca. 1000 Zyklen zu beobachten, in dessen Verlauf die ausgebaute Ladung als auch die Transmission im gebleichten Zustand und die Änderung der optische Dichte abnehmen.
Der Färbungsmechanismus von $NiO-TiO_2$ Schichten in der KOH Elektrolyte wurde mithilfe von Quarzkristallmikrobalance (QCM). Es wurden einige Modelle vorgeschlagen und erörtert. Ohne genauer Kenntnis der kompletten Umgebung der NiO Nanopartikel gab es eine mögliche Gleichung, die Ergebnisse für $E > 0{,}37$ V zu beschreiben:

$$Ni(OH)_2 + OH^- \leftrightarrow (NiOOH)\cdot(y/x)H_2O + (1-(y/x))\ H_2O + e^-$$

Wobei gilt $0 \leq y \leq x+1$.

Diese Formel beschreibt die chemische Bindung von Hydroxylionen an $Ni(OH)_2$ unter Bildung von wasserhaltigem NiOOH, das die Färbung in der Schicht verursacht. Darüber hinaus sieht die vorgeschlagene Gleichung auch die Bildung von Kristallwasser.
Die irreversible Zunahme von Masse und ausgetauschter Ladung wurde als Folge der Zunahme an $Ni(OH)_2$ nach

$$NiO + z\ H_2O \rightarrow Ni(OH)_2 + (1\text{-}z)NiO$$

interpretiert.
Dies ermöglicht ein besseres Verständnis der Erhöhung von Färbungsverhalten der Schicht und die Änderung ihrer Morphologie, wie bei der TEM-Messung beobachtet wurde.
Die sukzessive Änderung der Morphologie führte auch zu einer offenen und mechanisch zerbrechlicheren Struktur, so dass außergewöhnlich große Erhöhungen der Schichtmasse mit jedem Zyklus und nach ca. 330 Zyklen zu beobachten war. Dies wurde als eine Folge der Aufnahme von K^+ Ionen und Wasser, was zur Abbauperiode führte, interpretieret.
Die elektrochrome Eigenschaften der Schichten wurden auch in einen mit $LiClO_2$-PC gefüllten drei Elektroden, mit $Ag/AgC1O_4$-PC als Bezugselektrode, getestet. Es wurde vorgeschlagen, dass ein EC Verfahren, das mit kathodischer Ladung von bis zu $9mC/cm^2$ (für eine 80 nm dicke Schicht) einhergeht, an irreversible Änderung in Zusammensetzung von $Ni(OH)_2$ mit der Zersetzung geringer Menge von in der Schicht verbleibenden Wasser angeknüpft ist. Bei einem negativerem Potential kann Li^+ zusammen mit e^- kathodisch in die Schicht eingebaut werden und die Zusammensetzung gehet über in $Li_zNiO\text{-}TiO_2$. Das Elektron könnte dabei durch Wechselwirkung mit $Ni2^+$ oder eher mit Li^+ lokalisiert oder delokalisiert sein, was zur Bildung von Polarons führt. In diesem Fall wird ein Mechanismus, der dem von kathodisch elektrochromen Materialien wie WO_3 und Nb_2O_5 gleicht, beobachtet, sich die Schichten färben.
Braun färbende electrochrome Folien sind mit $NiO\text{-}TiO_2$ Schichten in der Konfiguration Glas/ FTO/ $NiO\text{-}TiO_2$ (160nm)/ 1M flüssige KOH/ $CeO_2\text{-}TiO_2$/ FTO/ Glas hergestellt worden. Die Änderung in optischer Dichte der Schicht lag im Bereich von 0,3 mit Färbeffiktivität von ca. 41 cm^2/C. Das Fenster bekam mit steigenden Zyklenzahleine permanent braune Farbe in Folge der permanenten Färbung der $NiO\text{-}TiO_2$ Schicht. Die lang anhaltende Stabilität der Schichten konnte durch doppelte $NiO\text{-}TiO_2$ Schichten an Stelle von Einzelschichten von 4000 Zyklen auf 7000 Zyklen verbessert werden.
Durch Ablagerung dünner Schicht von dielektrischen Oxiden wie z. B. ZrO_2, TiO_2, Al_2O_3 und $CeO_2\text{-}TiO_2$ (alle 20 bis 25 nm dick) auf der $NiO\text{-}TiO_2$ Schicht, wurde die Korrosionsresistenz in KOH Elektrolyte verbessert, so dass eine Langzeitstabilität bis zu 17000 Zyklen erreicht werden.
Elektrochrome Systeme mit Nb_2O_5:Mo als katodischer Gegenelektrode anstatt der passiven $CeO_2\text{-}TiO_2$ in der Konfiguration Glas/ FTO/ $NiO\text{-}TiO_2$ (160nm)/ 1M wässriger KOH /Nb_2O_5:Mo (200nm)/ FTO/ Glas sind auch im Potentialbereich -1 bis 1,9 V. getestet worden. Im gefärbten Zustand waren diese Folien grau-braun. Die Verwendung der Nb_2O_5:MoSchicht verbesserte die Änderung in der optischen Dichte der Folien (0,36), jedoch verschlechterte sich ihre Stabilität (nur 5000 Zyklen).
Ein neuer KOH erhaltende Gel Elektrolyt wurde ebenfalls entwickelt, einsetzbar für fast alle Festkörper-Systeme. Fenster in der Konfiguration K-Glas/ $NiO\text{-}TiO_2$/ Stärke (KOH)/ $CeO_2\text{-}TiO_2$/ K-Glas sind im Spannungsbereich von -0,7 V bis zu + 1,9 V montiert und getestet worden. Während der ersten Zyklen wies das Fenster eine hohe Transmissionsänderung (von 70 % auf zu 26 %) ohne jeglicher Aktivierungsperiode auf. Die Änderung der optischen Dichte war dabei ziemlich hoch (0,42). In den nächsten wenigen Zyklen aber verringerte sich ΔOD von 0,42 auf 0,1 fiel. Die Leistung des Fensters wurde wieder durch Schalten verbessert und der ΔOD Werte von bis zu 0,27 wurden nach 2000 Zyklen beobachtet.

Table of Contents

Chapter 1
Introduction and Overview

Smart materials are materials that have one or more property that can be significantly altered in a controlled fashion by external stimuli, such as stress, temperature, moisture, pH and electric or magnetic fields. Smart materials cover a wide and developing range of technologies. A particular class of smart materials, known as chromogenic material is receiving special interest [1] as they are optically active with controllable transmittance, absorption and reflectance when an external field is applied. Chromogenic includes electrochromism, suspended particle electrophoresis, polymer dispersed liquid crystals, electrically heated thermotropics, and gasochromics [1]. There are numerous proposed applications based on these materials as they can be used for large area glazing in buildings, automobiles, planes, and for certain types of electronic display, sunglasses and electrochromic mirrors [2]. Glazing is the application which is receiving a special interest driven by the need to produce more energy efficient systems which can lead to a reduction in fossil fuel consumption where the world lives currently a double energy problem. First is the lack of energy sources and the other is the bad environmental effects of fossil and nuclear fuel. Another attractive motivation behind the special interest in glazing technology is the possibility of living in an entirely automated home. For application in the external glazing of buildings only transparent and non-reflecting electrochromic devices are particularly useful. Electrochromism is a property of some materials that are able to change their optical properties by the double injection of electrons and protons or light alkali atoms in their crystalline lattice [3]. Electrochromic smart windows are able to change their transmittance of light and solar energy by electrical charging/discharging, thereby being able to provide a comfortable indoor climate together with large energy efficiency [4]. The advantage of electrochromic materials over the other chromogenics materials are [1]

- Electric energy consumption is only needed during the switching process
- low switching voltage (1 to 5 V),
- different colours (blue, grey, brown, etc)
- always transparent-typical ECDs have an optical spectral transmittances of 70-50 % in the bleached state and 25-10 % in the fully coloured state in the region of visible light.

Electrochromic devices (ECDs) are composed of several elements assembled in a layered configuration. Obviously, one of the layers is an electrochromic (EC) film. This is accompanied by an ion storage (IS) film which can also show an electrochromic behavior, the two layers being placed on each sides of a solid (or liquid) electrolyte layer (E) [5]. The EC and IS layers, are generally thin films of amorphous or crystalline oxides deposited on transparent conducting oxide (TCO) coated glass or plastic sheets, and can be prepared by a variety of standard deposition techniques. Because of the inexpensive deposition equipment and a wide choice of precursors, the sol–gel method has become a popular means among researchers for producing EC and IS films.

A Nickel oxide thin film is an anodic electrochromic material used as an optical active counter electrode in electrochromic devices. This is due to the natural grey colour which results from combining the brown colour of NiO in the oxidized state together with the blue colour of the reduced tungsten trioxide. Electrochromism of NiO thin films is rather complicated and in spite of the rich literature reports, there is still a lack in the understanding of the coloration mechanism although it is generally accepted that the transition from a bleached to a colored state is related to a charge-transfer process between Ni(III) and Ni(II).

Following ideas which led to the development of CeO_2-TiO_2 electrochromic sol-gel layers, for which it was found that very small CeO_2 crystallite nanoparticles can be grown in an amorphous TiO_2 matrix improving considerably the amount of charge that can be inserted reversibly into the electrode, the aim of this research is the development and characterization of NiO-TiO_2 films produced by the sol-gel dip coating process.
This work presents therefore a detailed study of the thermal behavior of xerogels, of the structure of the layers before and after coloration and of the electrochemical and optical behavior of layers tested in KOH and $LiClO_4$-PC electrolytes. Detailed quartz crystal microbalance measurements have been performed to understand the electrochromism of the layer. A model based on these results to explain the mechanism of coloration and the film morphology transformation during cycling is proposed and discussed. The important result of this work is the experimental confirmation that the coloration of the layers during the initial cycles occurs in a very thin layer of about 50 nm at the interface electrolyte/coating (activation period) that grows with cycling till reaching the full thickness of the layer (steady state). Then a degradation period is observed in which the

optical and electrochemical properties are gradually degradated, the layers becoming very soft and fragile to be even slowly detached from their support until the complete removal of the coating.

Devices have been mounted and tested using the NiO-TiO_2 layer as a working electrode together with CeO_2-TiO_2 layer or with a WO_3 or a Nb_2O_5 cathodic layer acting as an active counter electrode.

Also a new type of electrolyte based on KOH mixed with starch has been also developed and tested with complete windows.

Chapter 2
Fundamentals

2.1 The Sol-Gel process

The surface of solid bodies such as glasses or plastics represents a simple target for the application of functional coatings. This is much easier to accomplish than to design new bulk materials for specific application [6].

The Sol-Gel process has been touted as an exciting and potentially useful technique for the preparation of high performance materials. The advantage of this process include the purity of reagents, the control of the degree of homogeneity of mixing of the precursors, the potential control of the phase evolution and microstructure, and the opportunity for fabrication of materials into useful non-traditional shapes (fibers, thin films, spheres, optical elements, patterned surfaces, etc.)

The sol-gel process is a method for synthesizing inorganic, mainly oxide networks by soft chemistry routes [7]. As the name implies, it involves the evolution of inorganic networks through the formation of a colloidal suspension (sol) and gelation of the sol to form a network in a continuous liquid phase (gel) [8].

Sols are dispersions of colloidal particles in a liquid. *Colloids* are solid particles with diameters of 1-100 nm. *A gel* is an interconnected, rigid network with pores of sub micrometer dimensions and either polymeric chains whose average length is greater than micrometer [9] or aggregation of particles.

The sol-gel process of thin films includes the following steps

- preparation of a sol
- gelling the sol on a substrate
- drying and densification by sintering.

2.1.1. Preparation of sols

A sol is formed by mechanical mixing of the desired material precursor in water or alcohol i.e. solvents where hydrolysis and condensation reactions occur at the numerous sites within the sol. The precursors used for a sol synthesis consists usually of a metal or metalloid element surrounded by various active ligands. They can be salts, soluble oxides or hydroxides, complexed alkoxides or other complexes [10]. Metal alkoxides are the most popular because they react readily with water.

Hydrolysis

When a metal precursor is dissolved in water, metal cations are solvated by water molecules and hydrated metals are formed [7] according to equation (2.1)

$$\equiv Me\text{-}X + H_2O \Rightarrow \equiv Me\text{-}OH + HX \quad (2.1)$$

where Me is a metal, X a reactive ligand like halogen, NO_3, OR (R is alkyl group).

The reaction starts with the nucleophilic addition of negatively charged $OH^{\delta-}$ groups into the positively charged $Me^{\delta+}$ leading to an increase of the coordination number of the metal atom. For transition metal cations, the charge transfers from the filled 3a1 bonding orbital of the water molecule to the empty *d* orbital of the transition metal [11]. So generally speaking the hydrolysis reaction replaces the grouping ligand (X) with hydroxyl groups (OH).

Condensation:

The hydrated metals react in a condensation reaction forming M-O-M bonds [7].

$$\equiv Me\text{-}OH + X\text{-}Me\equiv \Rightarrow \equiv Me\text{-}O\text{-}Me\equiv + XH \quad (2.2)$$

$$\equiv M\text{-}OH + OH\text{-}M\equiv \Rightarrow \Rightarrow \equiv Me\text{-}O\text{-}Me\equiv + HOH \quad (2.3)$$

Linkage of additional M-OH occurs and finally a Me-O-Me network is formed. The H_2O and by-products resulting from the reactions remain in the pores of the network. When enough interconnected M-O-M bonds is formed they respond cooperatively as colloidal particles and a sol is formed. If the diameter of these colloidal particle is less than 20 nm, a high optical quality of these sols is obtained [7]. The sol is stable as long as the particle- to-particle interaction is low. The condensation products could be monomer, dimmer , linear or circular trimmer, cyclic tetramer and higher order rings.

Many factors influence the kinetics of hydrolysis and condensation and the ratio of their rates determines the properties and characteristic of the formed network. Many species are present in the solution and furthermore the hydrolysis and condensation reactions occur simultaneously. The most important factors that affect the rate of hydrolysis and condensation are pH, temperature, catalyst nature and concentration and water to metal ratio (R) [12]. A general rule, one can say the hydrolysis rate increases with [10]

- increasing polarity of the Me-X bond (increasing the charge density on the metal)

- decreasing stabilization of solvation or complex forming effect of solvents or complex formers (increasing the number of metal bridged by hydroxo)
- increasing concentration of catalysts, acid or bases.
- temperature

and decreases with

- increasing chain length of alkyl chain
- use of complex formers (e.g. β-diketonate complex of Ti alkoxide)

2.1.2 Gelation

The colloidal particles and condensed metal species grow and link together to form macroparticles within a three dimensional network which can elastically support a stress (gel). The transition from the sol state to the gel state can be achieved by three different ways:[10]

- growth of polymeric molecules (which cross link randomly to a three dimensional network)
- growth of individual particles (which grow together as they become larger)
- stabilization of colloids by surface charges (change of zeta potential and following interparticular condensation process leads to gelation).

The gelation point of any sol-gel system is easy to observe qualitatively but extremely difficult to measure analytically. The process occurs gradually and there is no activation energy that can be measured [9]. The gel properties depend on the particle size and cross-linking prior to gelation and all the subsequent properties depend on the gel structure formed during gelation.

2.1.3 Drying and Sintering

After the deposition of the liquid film, a drying or curing and in most cases also a further heat treatment is necessary to obtain the desired coating material. While the drying usually performed at room temperature or at moderate temperature up to 250 °C, the heat treatment often requires more drastic conditions with temperatures of 400 to 600 °C or higher and some times even special gas atmospheres [13]. The highest temperature level is limited by the substrate material where the borosilicate glass with their higher thermal shock resistance are favoured to soda lime glass.

Alternatively , thermal irradiation techniques like CO_2 laser firing have been investigated but the result still not satisfactory. Thermal induced polymerisation using UV have already proven their efficiency and stability [14].

2.2 The Sol-gel dip coating process

According to figure 2.1 the dip coating procedure starts by immersing a clean substrate into a coating solution where it stays for a defined period of time which should be long enough to guarantee a heat equilibrium and settle down the turbulence caused by the immersion of the substrate in solution [13]. The substrate is withdrawn then from the solution at moderate speed and stopped adequate distance above the solution bath to unhindered the drying, this is called the steady state of the process. After drying the deposited film, a curing is needed in order to obtain the desired film material. This is usually done by heating the system in an oven.

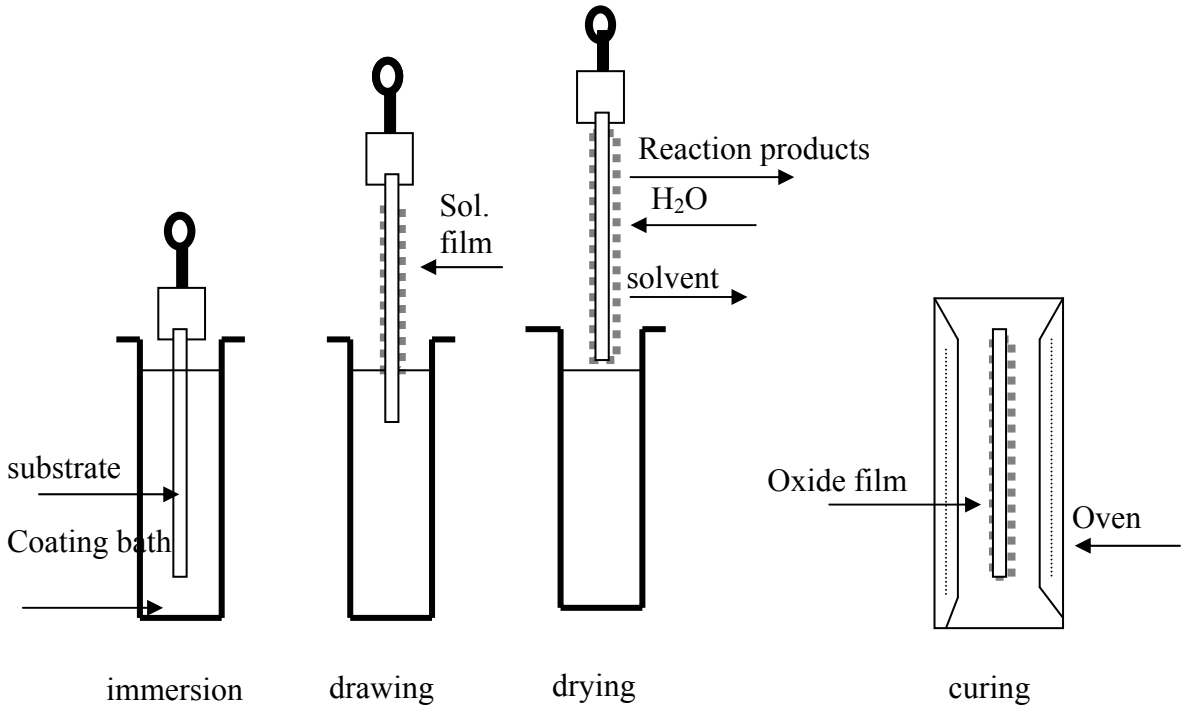

Fig.2.1: Steps of sol-gel oxide film deposition by dip coating process [6, 13]

Principals

According to [11] the whole dip coating process can be divided to five stages: Immersion, start-up, deposition, draining and evaporation.

The process starts with the immersion of the substrate in the coating liquid, on the withdrawal of the substrate, it entrains liquid in a fluid mechanical boundary layer carrying some of the liquid toward the deposition region. A streamline splits the boundary layer in two layers: the inner layer which moves upward with the substrate and the outer layer which moves downward to return to solution container. The thickness of the obtained layer depends on the position of the streamline which is controlled by six forces [11]

1. viscous drag upward on the liquid by the moving substrate
2. force of gravity
3. resultant force of surface tension in the concavely curved meniscus
4. inertial force of the boundary layer liquid arriving at the deposition region
5. surface tension gradient
6. the disjoining or conjoining pressure.

The final film thickness (h), for a pure liquid with viscosity η and density ρ drawn with a speed U, which balance the viscous drag (αηU/h) and gravity force (ρgh) is given by the Landau- Levich equation [11]

$$H = 0.94 \frac{(\eta U)^{\frac{2}{3}}}{\gamma^{\frac{1}{6}} (\rho g)^{\frac{1}{2}}} \qquad (2.4)$$

The exponent of U is dependent on the chemical composition of the coating solution.

The chemical formation of the coating starts when the solvents evaporate, increasing the concentration of the solution on the substrate, the water diffuses from the atmospheres into the layer where hydrolysis and polycondensation keep going on. Correspondingly the viscosity of the solution in the film increases. The polymer growth during the deposition stage may happen in a way similar to a cluster-cluster aggregation [11] with a trajectory ranging from Brownian (in the beginning) to ballistic (at the later part of this stage). Gelation occurs when the layer withstands the flow due to gravity but is still filled with solvents.

The fluid flow during evaporation process accompanied by the attachment of the precursor species to the substrate results in shear stress in the layer, while continuing shrinkage during the drying process causes a tensile stress. The stress in the film is approximately equal to the tension in liquid. Therefore as the film becomes rigid the tension in the film

becomes equal to the capillary stress which would shatter a macroscopic gel. However it is found experimentally that this does not necessarily crack the films but films thicker than 1 μm usually crack.

To get a compact smooth morphology, the sol-gel coatings need heat treatment, which could be at low temperature < 200 °C (for drying), at high temperature > 500 °C (for sintering), or using IR or UV treatment. The heat treatment decreases the film thickness due to the evaporation of the solvents (80 - 250 °C) followed by a consumption of the organics (250 - 300 °C) and a reduction in the porosity of the layers [15].

2.3 Electrochromic concepts

Chromism is a reversible change in a substance's colour resulting from a process caused by some form of stimulus [16]. In most cases, chromism is based on a change in the electron states [17] of molecules, especially the π- or d-electron state, so this phenomenon can be induced by various external stimuli which can alter the electron density of substances.

Electrochromism is the reversible and visible change in transmittance and/or reflectance that is associated with an electrochemically induced oxidation–reduction reaction. It results from the generation of electronic absorption bands in the visible region, by switching between redox states [18].

An electrochromic material is a material that changes color in a persistent but reversible manner by an electrochemical reaction. These materials can exhibit different oxidation states, the color resulting from the electron delocalization between these states [3].

A generalised form of the electrochromic reaction may be written as

$$\underset{oxidized}{O} + ne^- \longrightarrow \underset{reduced}{R} \qquad (2.5)$$

where an electrode acts as the source or sink of electron(s), e^- [17, 19].

Electrochromism is known in a number of organic and inorganic substances. Almost all of the interesting inorganic materials are oxides and found to belong to the transition series of the periodic table [20]. This indicates that the electrochromism has a strong relation with the electronic structure of the materials [20].

Electrochromic materials fall in two main categories depending on the electron transfer process which results in the coloration, namely they are anodic and cathodic materials. Cathodic materials colour when they are reduced at a negative electrode while anodic

materials are colored at an anode [19]. Ti, Nb, Mo, Ta and W (typically group VI-B) oxides exhibit cathodic electrochromism while Ce, Mn, Fe, Co Ir, Rb and Ni (group VIII) oxides exhibit an anodic electrochromism. Vanadium is found to exhibit both anodic and cathodic electrochromism depending on its oxidation state [21].

It is important to notice that for any electrochromic material to be able to exhibit electrochromism, it should be integrated in a system where potential application is possible [20].

The Coloration Efficiency is an important property to compare the efficiency of electrochromic layers. It is also called electrochromic efficiency and has the units cm^2C^{-1}. It is defined as

$$CE(\lambda) = \eta = \frac{\Delta OD(\lambda)}{q} \tag{2.6}$$

where $\Delta OD(\lambda)$ represents the change in optical density at the wavelength λ, resulting from (q) charge transferred per cm^2. **The Optical density (OD)** is an expression of the optical transmittance of an element at a given wavelength and is expressed as $\log_{10}$ (1/T) where *T* is the transmittance.

2.4 Electrochemical cells

All electrochromic systems can be represented in principle as electrochemical cells [19] so it is worthwhile to explain the principals of electrochemical cells. Electrochemical methods are divided into two main methods:

Static electrochemical method: no current passes between the electrodes, concentration of species in electrochemical cell remains unchanged

Dynamic electrochemical method: a current flows and concentrations change as a result of a redox reaction

An electrochemical cell is composed of two compartments or half-cells, each composed of an electrode dipped in an electrolyte solution. These half-cells are designed to contain the oxidation and reduction halves-reactions separately where in each a certain chemical exists in two charge states namely a reduced (R) and an oxidized (O) states which are called a redox couple. If the potential of this redox couple is different from the equilibrium potential then either the oxidation will occur as follows.

$$R \rightarrow O + ne^- \tag{2.7}$$

or the reduction reaction in the reverse direction.

The simplest example of an electrochemical cell is shown in fig.2.2

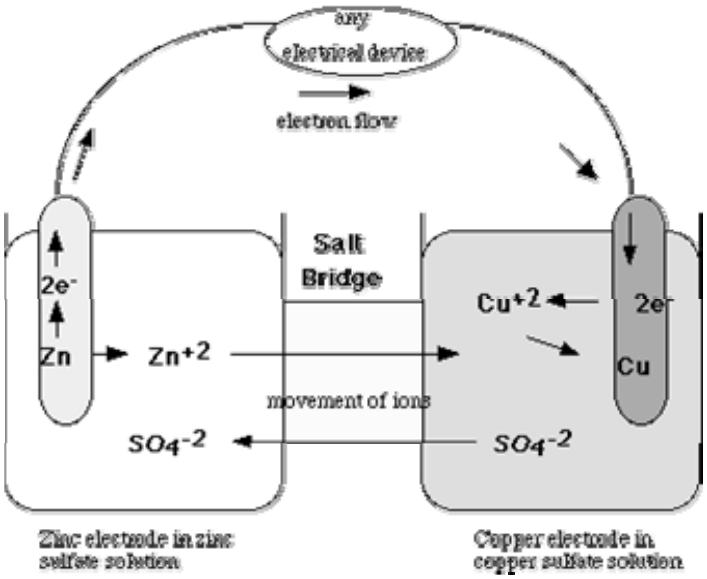

Fig. 2.2: Schematic representation of a simple electrochemical cell [22]

The half-cell called the anode is the site at which the oxidation of zinc occurs as shown below.

$$Zn\ (s) \rightarrow Zn^{+2}\ (aq) + 2e^{-} \qquad (2.8)$$

During the oxidation of zinc, the zinc electrode will slowly dissolve to produce zinc ions (Zn^{+2}), which enter into the solution containing Zn^{+2} (aq) and SO_4^{-2} (aq) ions.

The half-cell called the cathode is the site at which the reduction of copper occurs as shown below.

$$Cu^{+2}\ (aq) + 2e^{-} \text{ -------> } Cu\ (s) \qquad (2.9)$$

When the reduction of copper ions (Cu^{+2}) occurs, copper atoms accumulate on the surface of the solid copper electrode. As a result an immbalance of electrical charge would occur, the anode would become more positive as zinc cations are produced, and the cathode would become more negative as copper cations are removed from solution. This problem can be solved by using a "*salt bridge*" connecting the two cells as shown in the fig 2.2. A *salt bridge* is a porous barrier which prevents the spontaneous mixing of the aqueous solutions in each compartment, but allows the migration of ions in both directions to maintain electrical neutrality.

The electrode potential of any half cell is related to the concentration of the redox couple according to **Nernst equation**:

$$E = E^0 + \frac{RT}{nF}\ln(\frac{[O]}{[R]}) \quad (2.10)$$

where the square brackets denote concentrations, R is the ideal gas constant, F the Faraday constant, T the thermodynamic temperature and n the number of electrons involved in the reaction. E^0 is the standard electrode potential.

It is important to recall that it is impossible to measure the electrode potential independently, but the difference in electric potential is only measurable. The E_{cell} is defined as the potential difference to be applied to the cell to prevent any reaction (zero current).

$$E_{cell} = E_{cathode} - E_{anode} \quad (2.11)$$

Electrochemists concentrate on the reactions at one electrode only which is called the *working electrode*. In order to establish a scale for measuring the working electrode potential, notation of *reference electrode* is introduced. The purpose of the reference electrode is to complete the measuring circuit and provide a stable and reproducible potential against which the working electrode is compared. The contact is made through a liquid junction that allows the electrolyte to contact the sample. The reference electrode is designed to produce the same potential no matter in what solution it is placed. The most famous reference electrode is the standard hydrogen electrode (SHE) also called normal hydrogen electrode (NHE), $Pt|H_2(g)(1atm), H^+$ (unit concentration)

It is assigned an electrode potential $E = 0$ at all temperatures.

One of the most common reference electrodes is the KCl saturated calomel half cell (SCE). A simple form of this electrode can be assembled by adding in a tube, mercury metal, a small amount of solid mercury (II) chloride, several grams of solid KCl and some distilled water. Connection to the external measuring circuit can be made by using a fine platinum wire dipping into the mercury pool. The potential of the SCE is 0.244 V with respect to NHE. The principal disadvantage of the SCE as a reference is that the solubility of KCl changes substantially with temperature and therefore the cell potential has a relatively large temperature coefficient.

2.5 Three electrode cell

Electrochromic materials are generally first studied as a single electrode under potentiostatic or galvanostatic control. Generally, a cell used for electrochromic measurements has three functional electrodes (see fig. 2.3). The first of the three electrodes

is the ***working electrode (WE)***. This is the electrode at which the electrochemical phenomena being investigated takes place.

The second functional electrode is the ***reference electrode (RE)***. This is the electrode whose potential is constant enough that it can be taken as the reference standard against which the potentials of the other electrodes present in the cell can be measured.

The final functional electrode is the ***counter electrode (C.E)*** which serves as a source or sink for electrons so that current can be passed from the external circuit through the cell. In general, neither its true potential nor current is ever measured or known.

To characterize the layer a current is passed through the layer electrode in a controllable way by applying a potential to the electrode that is different from the equilibrium potential. This is in contrary to the static state which allows zero current. The potential of the working electrode (WE) is measured against the reference electrode (RE). The current is allowed to pass through counter electrode (C.E) to complete the current flow circuit. The potential difference between working electrode and reference electrode is controlled by means of a potentiostat.

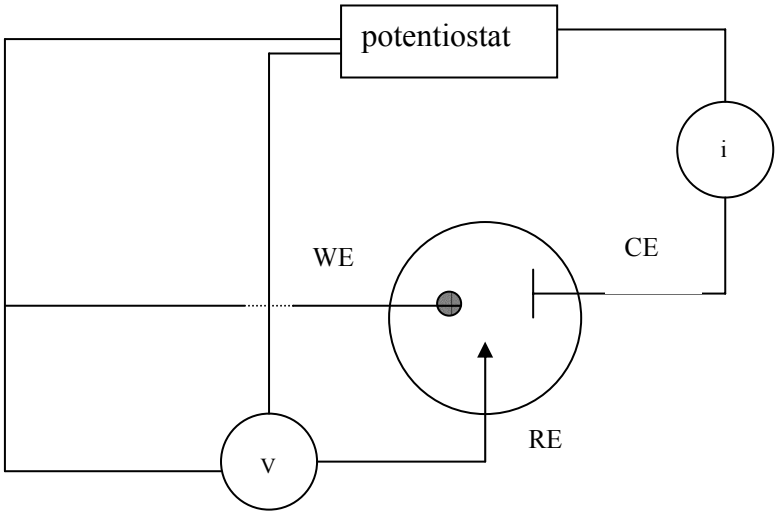

Fig.2.3: Schematic representation of three electrode cell used in electrochemical characterization [19].

2.6 Electrochromic devices

An electrochromic window (EC)W) is an electrochromic device (ECD) which allows electrochemically driven modulations of transmitted and/or reflected light. Such electrochromic optical switching device is also called a "*smart window*" [23]. There are

many possible device constructions depending on the application. Fig.2.4 illustrates a standard construction that allows basic features and operating principles to be introduced conveniently. It is a 5-layers design covered on two sides by glass substrates. The operating mode is explained with an EC window of the configuration glass/ TCE/ WO_3/ electrolyte/ CeO_2-TiO_2/ TCE/ glass. Initially the system is transparent. After applying a voltage with negative polarization at the WO_3 side, WO_3 is reduced and simultaneously the M^+ ions (M^+: H^+, Li^+) stored in the ion-storage layer diffuse through the electrolyte into the WO_3 layer to form a deep blue colored intercalation compound M_xWO_3. The following reversible coloration and bleaching reactions occur:

$$WO_3 + x\ M^+ + x\ e^- \leftrightarrow M_xWO_3. \qquad (2.12)$$

WO_3 colors in the reduced form and is called a cathodic electrochromic material. After reversing the polarization, M_xWO_3 is oxidized and simultaneously the M^+-ions diffuse back to the counter electrode. The counter electrode, which was oxidized during the coloration step, will be reduced and the EC-device is bleached.

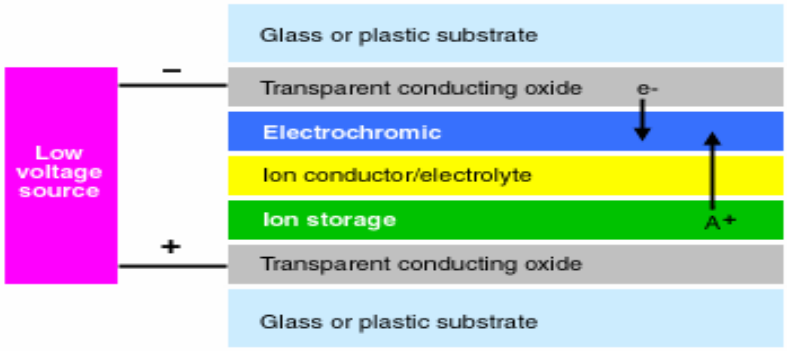

Fig. 2.4: Typical 5-layers electrochromic device

Examples of the 5 layers typically used in ECDs are:

2.6.1 Transparent Conductive electrode (TCE):

It is made of a transparent material with low resistivity deposited on a top of glass or plastic substrate. The main role of TCE is to conduct electrons to and out of the adjacent electrochromic layer and to offer a mechanical support and protection of the device. For all practical sizes, the sheet resistance should be less than 20 Ω/sq. The materials are typically tin-doped indium oxide (ITO), antimony-doped tin oxide or fluorine-doped tin oxide (FTO) [24]. ITO and FTO are prepared for commercial applications by physical and chemical vapour deposition respectively while ATO is prepared by sputtering. The

electrical properties of sol-gel deposited ITO are not good enough for practical uses [24]. FTO is the least expensive TCE. The FTO layers are essentially fabricated by spray pyrolysis on float glass at 550 °C, so that their sheet resistance remains stable up to 550 °C giving a superiority on ITO for applications which need a temperature treatment higher than 300 °C. It is reported also that it is electrochemically more stable than ITO [25]. It should be mentioned here that other TCEs are mentioned in the literature, such as aluminium-doped zinc oxide and fluorine-doped zinc oxide [26].

2.6.2 The electrochromic (EC) layer.

This is typically a transition metal oxide that can exhibit several valence states upon reduction. There are many requirements for the electrochromic layer.

- The optical modulation should be high enough to be recognized by a normal vision observer,
- The response time should be fast,
- The ionic and electronic conductivity should be high,
- The structure should be permeable to allow an easy ion (H^+, Li^-) insertion

Several materials are reported for being used as electrochromic cathodically colouring layers:

1) Tungsten oxide, WO_3 is the most widely studied electrochromic layer. This is because of its superior EC properties and relative ease of deposition by sputtering, evaporation, chemical vapour deposition and sol-gel. The optical properties of WO_3 change upon reduction and depend strongly on the structure of the layer. Polycrystalline tungsten oxide modulates the optical transmittance by reflection (especially in the near infrared region) whereas amorphous tungsten oxide does that by absorption [27, 28]. Its colour changes from transparent or yellow to deep blue due to the formation of a tungsten bronze. For energy-efficient EC materials tungsten oxide with reflection modulation are preferred. The proposed reaction for electrochromism in W oxide is represented in a simple form as in equation (2.12) above.

This is an oversimplified reaction where all the details are ignored. For instance thin films of practical interest are normally hydrated i.e., contain hydroxyl groups and water molecules and may deviate to some extent from the stated WO_3 stoichiometry in the last equation [29].

As the size of the intercalated ions increases, the rate of diffusion decreases, thereby decreasing the rate of optical modulation [30]. The diffusion coefficient is affected

strongly by the structure of the layers. Nagai et al. [31] reported that the diffusion coefficient of Li^+ increased from $3x10^{-12}$ to $1.5x10^{-9}$ cm^2S^{-1} by decreasing the layer density from 5.84 to 3.38 g/cm^3.

Electrochromic films of W oxide can be prepared by a variety of techniques [32, 33], such as evaporation [34], sputtering [35], chemical vapor deposition [36], spray deposition [37] and sol-gel [38]. The properties of the layer depends strongly on the preparation condition [20]. Granqvist reported in detail the techniques used in electrochromic W oxide preparation [29].

i. Evaporation has been used successfully to produce WO_3 layer for commercial EC products such as automotive mirrors. The as-deposited films are heavily disordered with a porosity dependent on the presence of gas. In particular, evaporation in the presence of 5×10^{-4} Torr of H_2O yields a relative density of 0.6, whereas the deposition in a good vacuum produces films with a relative density of 0.8 [39]. As seen by infrared spectroscopy [40, 41] evaporated electrochromic W oxide films tend to be hydrated even if they are produced without intentionally adding water to the deposition unit. The porous W oxide films can be crystallized by heating. A monoclinic WO_3 films were obtained by deposition onto a substrate at 200 °C followed by a post-deposition anneal at 430°C in O_2 [42]. A triclinic crystalline structure was obtained by annealing at 400°C, 500°C, and 600°C [43].

ii. DC and RF sputtering are suitable techniques for preparing electrochromic W oxide layers with good properties. The parameters of the sputtering process have a significant effect on the obtained layer properties [29]. Films of relative density of 0.75 and O/W ratio of 3.1± 0.1 have been reported [44]. The substrate temperature has a strong effect on the degree of crystallinity of the layer and it is reported that the crystallization of the films takes place at temperatures between 300 °C and 350 °C [45-47]. There is a strong relation between the thickness of the layer and its crystal structure [48]. Detailed study of the structure of layers prepared by RF sputtering is given by Nabba [49]. The addition of Ti to the W oxide improved the electrochromic properties such as the bleached state transmittance, the colour stability and the aging durability [50].

iii. Chemical vapour deposition on the glass float line for large area electrochromic applications might have a cost advantage in that they do not require large expensive vacuum controlled deposition chambers. Amorphous electrochromic layers with O/W ratio in the 2.7–3.2 range were prepared by low-temperature atmospheric-pressure chemical

vapor deposition route. The films were deposited at 100–350 °C from tungsten alkoxide complexes [51].

iv. Sol-gel technique offers an opportunity to control the particle size and microstructure of the layer, beside the low cost. Several precursor solutions have been used to obtain electrochromic tungsten oxide films of the desired stoichiometry, thickness and cosmetic quality. The precursors were based on tungsten alkoxides [52], chloralkoxides [53, 54], colloidal solutions of tungstic acid obtained by an ion exchange method [32], and peroxopolytungstic acid [53, 55].

For large area application the alkoxide route is not a popular choice due to high cost of materials. The thickness of the layers obtained using a hexaethoxide precursor was in the range of 50 nm which is not enough to get a high contrast for electrochromic application. To get thicker layer, multi coatings are used which results in cracked layers [36]. Hydrolysis of tungsten alkoxide of the two components $WO(OEt)_4$ and $WO_2(OEt)_2$ has been studied. The hydrolysis products and the partially hydrolyzed solutions have been characterized by means of X-ray diffraction, IR, electron spectroscopy and small-angle X-ray scattering. The obtained tungsten solutions have been described as typical polymeric sols. Sols were used for the preparation of electrochromic and photochromic films by spin-coating techniques [56]. An alternative low cost method is to use chloroalkoxide precursor which resulted from reacting tungsten chloride with alcohol The resulting material is diluted with more alcohol to obtain the solution [57-59]. Films with nanocrystals of tungsten oxide are embedded in an amorphous matrix and Hydrous phases WO_3 ($WO_3 \cdot nH_2O$) are also present. These features improve the electrochromic properties allowing high charge transfer during the electrochromic process, fast optical switching and stability of the optical state. Layers heated at temperature higher than 300 °C are less efficient with respect to those annealed at lower temperatures [59].

The peroxo route starts with tungsten metal and reacting it with excess hydrogen peroxide (or its mixture with an organic acid) under controlled conditions of temperature, resulting in a precursor with enhanced stability [60-63]. It offers the advantage of the formation of pristine metal oxide films at a relatively low temperature owing to the clean burn out properties of organic additives (with low carbon content) and other volatiles from the as-deposited film Further improvements in the properties are possible by chemical modification of the precursor material and by controlling the post deposition thermal treatment [64]. Modifying the precursor solution chemistry by adding 0 to 5 wt.% of oxalic

acid dihydrate modifies the microstructure of the films. The film obtained from a sol with 3 wt.% oxalic acid dihydrate, showed a coloration efficiency of 102 C cm^{-2} (at 800 nm), fast color–bleach kinetics (t_c of about 192 s and t_b of about 28 s) and an ion storage capacity of 18.6 mC cm^{-2} [62]

One of the advantages of the sol gel method is the control of the microstructure of the layer by introducing chemical dopants to the reactant sols. Different amounts of *Titanium* precursor was mixed with tungsten precursor (1, 5, 10 and 15 mol %). Although, the coloration efficiency decreases when the titania content is increased, the electrochromic properties of the WO_3–TiO_2 films heat treated at a relatively high temperature were improved due to the amorphous structure preserved by the Ti-addition. Even small additions of titania can produce significant structural changes of tungsten oxide films [58].

The electrochemical responses of amorphous thin films of *lithium doped* tungsten trioxide (Li_xWO_3) prepared by the sol gel method (by reacting metallic tungsten with hydrogen peroxide (30%) and acetic acid) were studied by quartz crystal microbalance technique. It was observed that the coloration mechanism is the same for the pure and the doped films. However, the kinetics of the processes are different for the undoped and doped films. These differences are in agreement with the electrochemical properties presented by these films. In the pure WO_3 films, in which the deintercalation processes are more difficult, the kinetics of the coloration process is slower. In other words, the undoped films visibly return to the original color more slowly than the doped films does [65].

Electrochromic W-Mo oxide films were fabricated by adding different percentages of molybdenum to tungsten oxide ranging from 0.5 wt % to 7 wt% of deposition solution. Normal optical transmittance was also measured and it was found that coloration occurs in a shorter time than the bleaching. The time constant of the process tends to increase with the molybdenum oxide doping concentration [66].

Although a hexagonal-like structure is obtained by different deposition techniques, a tetragonal structure has been reported for layers obtained by adding ethylene glycol to tungsten precursor [67] and annealed at a temperature of 500 °C.

The color of tungsten trioxide changes from transparent to deep blue upon reduction. This blue color can be changed through the addition of other oxides or metals. In the case of V_2O_5 addition, the reduced film is green, and when gold particles are added to a cermet of tungsten oxide, the reduced material was red.

.

2) Niobium oxide, Nb_2O_5, is reported to have EC properties comparable to those of WO_3, although the use of this material has been limited as a cathodic EC film in a patented device. The suggested reaction is

$$Nb_2O_5 + 2H^+ + 2e^- \leftrightarrow Nb_2O_3(OH)_2 \text{ or } 2Nb_2O_2.H_2O \quad (2.13)$$

It can be deposited by many methods including sputtering [68, 69], chemical vapor deposition [70] and wet chemical routes [71]. $Nb(OR)_5$ alkoxides are quite expensive and highly sensitive to moisture so that sol-gel routes are based mainly on chloroalkoxides [71, 72]. The color of the reduced layer depend on the crystallization degree: the amorphous layer turns to a gray brown color upon reduction, the crystallized turns to dark blue [24]. Lithiation of Nb_2O_5 through the addition of a lithium salt to the precursor solution enhances the EC kinetics in particular the bleach rate and the reversibility for lithium intercalation. This was shown for both the amorphous and crystalline material [73]. In comparison to WO_3, niobium oxide requires higher potentials for color and bleach and has slower EC kinetics. Coatings of pure and Zr, Sn, Li, Ti and Mo doped niobium pentoxide have been prepared by the sol–gel process and deposited on ITO-coated glass using the dip coating technique. The coatings were transparent and, depending on the nature and amount of the doping and the sintering temperature, they presented a brown, gray or blue color after Li^+ insertion [74]. Nb_2O_5 films containing TiO_2 between 0.05 and 0.5 mol% showed an increase in ΔT and CE compared to undoped layers and presented ΔT= 84% and CE=26.9 $cm^2\ C^{-1}$. Above this concentration, the ΔT and CE values decreased [75].

Many other TMOs thin film are electrochromic, e.g. the oxide of **Molybdenum** MoO_3, [76, 77] where both amorphous and polycrystalline MoO_3 show an electrochromic effect similar to WO_3 and **vanadium** V_2O_5 which is reported to have cathodic and anodic electrochromic properties. Electrochromic layers of mixed oxides have been also reported.

2.6.3 Counter electrodes or Ion Storage layer

The counter-electrode should offer a high transmittance in the visible range, with fast kinetics for the electrochemical reaction, and should have a sufficiently high charge capacity for the insertion/extraction of ions. There are two choices for the counter-electrodes: they can be optically passive, i.e. their transmittance remains unchanged during the ion intercalation /de-intercalation process to avoid interference with the electrochromic layer coloration and they are called ion storage layer (IS), or they may exhibit

colouration/bleaching properties in complementary way with the electrochromic layer. In the later case the device has a cathodic EC layer and an anodic EC counter electrode so that both coatings colour and bleach at the same time.

a) Anodically coloring counter electrodes

1) Nickel oxide, NiO, is one of the most widely studied materials. NiO has been used in an all-solid state thin film devices involving the insertion of both protons and hydroxyl groups [78]. The NiO films are colorless in the reduced state and become dark brown when oxidized. Beside being used as counter electrode with cathodically coloring layer it could be used also as working EC layer with passive counter electrode as it will be explained in this work.

Many techniques are available for preparing electrochromic NiO thin films. The major methods are categorized into physical, chemical and electrochemical ones. For the different deposition techniques the layers have molecular species primary built with NiO_6 blocks and it is regarded as a cluster-assembled material [20].

i. Chemical methods

Vacuum techniques, typically evaporation and sputtering need vacuum which makes them expensive methods. Wet chemical deposition is an alternative method for producing amorphous thin films with high surface area [79]. The problem faces this method is the lack of soluble nickel alkoxide.

Sol-gel: NiO films have been prepared using sols of different precursors. In the beginning sol-gel routes went into two main ways, using either sulphate or nitrate precursor but later other precursors like nickel chloride and nickel acetate have been used. Aqueous sols of $Ni(OH)_2$ have been obtained by precipitating $NiSO_4$ in presence of LiOH and acetic acid. NiO with grain size of about 2-3 nm was detected by TEM. Change in transmittance in the range of 40-60 % and 35-40 mC/cm^2 charge capacity are reported [80-83]. The same sol was prepared by alternate immersion in $NiSO_4$ and KOH solutions [84]. Sols of nickel diacetate tetrahydrate ($Ni(CH_3COO)_2.4H_2O$) dissolved in pure methanol [85] or in dry dimethylaminoethanol (dmaeth) [86, 87] or of nickel diacetate dmaeth (Ni(acetate)2(dmaeth)) in dry dimethyaminoethanol have been used. The layers have an amorphous structure. The coloration efficiency varied between 6.2 and 16.4 cm^2/C according to the concentration of the sol and the thickness of the layer [86]. Layers prepared with sols of nickel chloride ($NiCl_2$) in different solvents are found to consist of

$Ni(OH)_2$ together with NiO crystal structure after sintering at 300 °C while the NiO structure is found alone at higher temperatures. The electrochromism of the layers increased by increasing sintering temperature up to 300 °C then decreased [88]. Sharma et al. believed that the water content has an important role in the hydrolysis reaction of films prepared by the sol gel technique. Predetermined amount of water were added to $NiCl_2$ in 1-butanol solution. The layers were found to have an increase NiO structure with increasing the water content in the sol. The crystallite size and thickness increase with water content from 10 to 16 nm and 350 to 500 nm respectively [88]. Sols of nickel nitrate hexahydrate ($Ni(NO_3)_2.6H_2O$) dissolved in lower carbon alcohol with additives have been also reported [89, 90]. One work reported the use of $Ni(OH)_2$ nanoparticles synthesized by precipitation of $NiCl_2.H_2O$. The obtained layers have NiO structure when sintered at high temperature and have CE of about 33.5 cm^2C^{-1} [91]. Nickel chloride hexa hydrated $NiCl_2.6H_2O$ in butanol is used also with additives of citric acid and water. NiO structure of the layers appear only at temperature higher than 350 °C [92]. It is also worthwhile to mention the preparation of Ni(Si)-oxide films where small NiO nanoparticles (size of 2,5 nm) have been grown at 300 °C. The precursor was $Ni(OH)_2$ prepared from nickel sulphate in presence of LiOH. The CE of the layers were in the range of 26 cm^2C^{-1} [93]. Electrochromic lithiated nickel oxide (Li_xNiO_2, $0 \leq x \leq 1$) sintered at high temperature has also been reported. The layers have $LiNiO_2$ layer structure with crystallite size of 12 nm and CE of 9 cm^2C^{-1} [94]. Cobalt (Co) was added to Ni oxides in order to improves their performance. Nickel oxide was prepared from Nickel nitrate hexahydrate precursor as in [95]. The obtained layers had amorphous structure with cathodic charge capacity of 30 $mCcm^{-2}$ [79].

$Cu_xNi_{1-x}O$ electrochromic thin films still have the cubic NiO structure. UV–VIS absorption spectra show that the absorption edges of the $Cu_xNi_{1-x}O$ films can be tuned from 335 nm ($x = 0$) to 550 nm ($x = 0.3$), but the transmittance of the colored films decrease as the content of Cu increases. Both the coloring and bleaching time for a $Cu_{0.2}Ni_{0.8}O$ film were less than 1 s, with a variation of transmittance up to 75% at the wavelength of 632.8 nm [96].

Other chemical methods have been used for preparing $Ni(OH)_2$ layers for electrochromic use:

Electrochemically deposited layers from solution of nickel sulphate and sodium acetate and potassium hydroxide with pH of 7.2 [97] showed a transmittance change from 72 to

33 % and response time from 20 to 40 s. The ones which deposited from 0.01 M $Ni(NO_3)_2$ solution with different proportions of $Mn(NO_3)_2$ varied from 0 to 100 % showed a shift in Ni(II)/Ni(III) redox reaction to less positive potentials. The solution which showed a good result related to the stability was that with 95 % $Ni(OH)_2$ and 5 % $Mn(OH)_2$.[98]. NiO_x thin films were deposited on sol-gel ITO coated glass using triangular waveform between -0.5 to 1.5 V from solution of 0.1 $NiSO_4$ and 0.1 M NH_4OH [99]. The layers were tested in both $LiClO_4$ and KOH solutions. $Ni(OH)_2$ layers were cathodically deposited from solution of $Ni(NO_3)_2$ [100] or anodically in order to improve the stability of the obtained layer.

Layer deposited by ***Alternative dipping deposition (ADD)*** using solutions of $NiSO_4$ and KOH exhibited CE of 35 cm^2C^{-1} [84] and those using solution of $NiSO_4$ with NaOH had CE of about 70 cm^2C^{-1} [101],

Chemical Bath Deposition (CBD) and ***Liquid Bath Deposition (LBD)*** techniques have been also used to prepare NiO layers using cold ammonia complex solution of $NiSO_4$ and Na_2S solutions [98] and mixed solution of saturated NiF_2 and H_3BO_3 [101]respectively.

ii. Physical Techniques

Sputtering is considered as the most common physical techniques used for thin films depositions. Preparing electrochromic Nickel oxide thin films by rf reactive magnetron sputtering started in 1986 [102]. Later DC reactive magnetron sputtering techniques have been also used [103-109]. In general the reported layers have a polycrystalline NiO structure with (111) preferred orientation [110], while the grain size varies widely with the deposition conditions from 3 to 150 nm [111].

One of the consistent problems of sputtered NiO layers is the residual coloration of the bleached state. Different additives have been tried to improve the transmittance of the layer in the as-deposited and bleached states such as (Cr, Al, V and Mg oxides) [105-108]. Cr oxide is found to decrease the transmittance change while the charge capacity is not affected. The structure is found to consists of NiO crystals impeded in amorphous structure of CrO with a grain size of 10 nm [105]. In general Al and Mg oxides additives increase significantly the luminance transmittance of the layers in the bleached states while the charge capacity is maintained [112].

In general, the life time of electrochromic sputtered NiO films ($2x10^4$ cycles) [102] is higher than that of the layers prepared by the other techniques.

The effect of oxygen flow in sputtering chamber was tested by changing the gas mixture of Ar and O_2 from 5% to 30% maintaining the other parameters constant [103]. It was found to have a strong effect on the charge capacity of NiO layers sputtered from NiO target that decreases from $4.9x10^{-2}$ mC/cm^2 nm^1 with a 5 % O_2 flow to $1.9x10^{-2}$ mC/cm^2nm^1 at 30%. The lowest detected Ni/O ratio by RBS was 0.5. The O_2 flow did not have the same strong effect with samples sputtered from a Ni target while the Ni/O ratio increased from .9 to 1.5 by increasing O_2 flow [103].

Another study by Avendano et al. [107] performed on mixed NiV oxide layers showed that by increasing the O_2 content in the sputtering gas from 0.4 to 6.4%, the layer evolved from a metallic to a transparent to brown. The O/Ni ratio as determined by RBS increased from 0.63 (.8% O_2) to 1.85 at 2 % O_2. The electrochromic characteristics of the layers were also found strongly dependent on the O_2 content of the sputtering gas, an intermediate content only giving rise to significant transmittance change and charge capacity. The optimum performance was found at an oxygen concentration smaller than 1.5 %. Layers deposited at low oxygen level did not exhibit any electrochromic effect while high O_2 level leads to a deterioration of the optical modulation.

While an excess of O_2 in the gas mixture lowers the transmittance of the as-deposited films, H gas addition produces transparent layers with better crystallinity [113] and improves the electrochromic effect [113-115]. On the other hand Azen et al. [116] found no differences between devices using nickel oxide layers deposited in the presence or absence of H.

Electrochromic lithium nickel oxide thin films are made by rf sputtering from $LiNiO_2$ target [117]. They had a coloration efficiency between 40 and 50 $cm^2C^{-1}$and a transmittance change of about 70 %.

The effect of rf power on the structure of non stoichiometric NiOx films sputtered from metallic nickel target was investigated [110] and it was found that the lattice parameter decreases by increasing the rf. power. Oxygen to nickel ratio higher than one was detected with huge ratio of hydrogen to nickel. The maximum transmittance change (52 %) was detected for rf power of 150 W.

The role of defects on the electrochromic response time of sputtered Ni oxide films was tested by Ahn et al. [118] where it was found that the excess interstitial oxygen and voids disturb the proton intercalation/deintercalation process. Wu et al. [119] found that the ion transport behavior during the electrochromic process is so complex and dependent on the

layer deposition and testing conditions where the change of oxygen and nickel vacancies is suggested to be responsible for such behavior.

Electron beam evaporation: Layers were prepared by electron beam evaporation showed a NiO structure [120-123] with (111) preferable orientation [121].

The effect of *substrate temperature* on the electrochromic properties of NiO layers deposited by electron beam evaporation from pellet of NiO powder was investigated by changing the substrate temperature between 80 and 250 °C. The transmittance of the as-deposited state remains within the same range (70 %) for temperature between 80- 200 °C while layers deposited on substrate maintained at 250 °C have a slight blue color and lower transmittance value. This was explained as due to a change in the composition of the layer due to the lack of oxygen or due to the decomposition of the NiO at high temperature. The absorption edge also is shifted with increasing substrate temperature which means a decrease in the band gap. The poor electrochromic effect of layers deposited at high temperatures was attributed to the compact granular structure of the with large grain size and small grain boundaries. Durability tests were also performed with layers deposited on substrates at different temperatures and the results showed that 150 °C was the optimum temperature with a change in optical density of 0.88 and a cathodic charge capacity of about 18.1 cm^2C^{-1} [120].

The effect of the *deposition pressure* on the microstructures and electrochromic properties of NiO layers deposited by electron beam evaporation was tested by Agawal et al.[122]. The layers were found to have a NiO microcrystalline cubic structure regardless of the deposition pressure, but by increasing the pressure in the chamber from $6.7x10^{-2}$ to $2.7x10^{-4}$ Pa. The porosity of the films increases due to the decrease of the grain size from 6.7 to 4 nm. The calculated O/Ni ratio increased from 1.17 to 1.25. The coloration efficiency decreased by increasing the pressure from 40 to 32.5 cm^2C^{-1}.

The interesting conclusion of this report is that the authors believe that the active site in NiO films are in the bulk and not at the surface of the film where they found that large surface leads to poor electrochromic effect. The hydration of the surface and the intercrystalline OH^- are important for high ionic (hdroxyl ion) conductivity.

The Pulsed laser deposition technique was used also to produce electrochromic NiO layers [124-126] and lithiated Nickel oxide [127]. The layers were polycrystalline with the cubic NiO structure. Cobalt and tantalum have been added to enhance the electrochromic

performances of nickel-based oxide thin films. Among the two series of metal additions ($M \leq 20\%$), the Ni–Co–O (5% Co) and Ni–Ta–O (10 % Ta) thin films showed the highest electrochemical performances and especially an improved durability [128]. W addition was tried also by Penin et al. [129] and led to a progressive film amorphization. An increase in cyclability for Ni–W–O (5 % WO_3) electrode, cycled in 1 M KOH electrolyte, was associated with a limited dissolution of the oxidized phases was achieved with tungsten addition. HRTEM investigations of cycled films revealed that the stabilization is correlated to the existence of an α(II)-nickelhydroxide phase.

2) Iridium oxide, IrO_2, is another anodic material [130, 131]. It colours from transparent to light brown at positive potential in Li^+ based electrolytes. IrO_2 was prepared by different methods, reactive sputtering [130, 131], vacuum deposition of iridium metal [132], thermal oxidation of vacuum-deposited iridium-carbon composite films [133] and sol gel [134]. The sol gel route is rather difficult because the synthesis of iridium alkoxide is difficult and therefore the precursors solutions were based mainly on $IrCl_3.3H_2O$ [135, 136]. The colouration efficiency and the response time of IrO_2 are comparable to WO_3 [137]. An electrochromic devices based on WO_3 as electrochromic layer and IrO_2 as counter electrode was realized [138]. In spite of its good electrochromic efficiency and stability, IrO_2 is not used for practical applications because it is an extremely expensive material.

3) Vanadium pentoxide V_2O_5 colours anodically from nearly colourless to a bright yellow state when oxidized. This film works best with a non-aqueous lithium ion electrolyte but the change in coloration in the visible range is not strong enough to be used as an electrochromic layer so it is used as an ion storage layer rather than as an electrochromic layer. As V_2O_5 has a weak cathodic coloration in the red and infrared, it is not a good electrochromic counter electrode with tungsten oxide, due to its modulation of the solar spectrum [139]. However, mixed oxides of vanadium and chromium or niobium oxides [140] have been reported to significantly decrease or eliminate the modulation in the near infrared while maintaining a high charge capacity.

b) Passive counter electrodes

1) Cerium–Titanium oxide layer (CeO_2-TiO_2)

Between the different used counter electrodes, CeO_2 which has two stable valences states (III) and (IV), was proposed for transparent and colourless electrodes but its response time is too low compared to those of WO_3. To overcome the slow reaction kinetics in CeO_2 films, Baudry et al. [141] suggested the replacement of part of the Ce atoms by an element of lower ionic radius such as Ti. For the preparation of this new oxide thin film, they used $Ce(NH_4)_2$ $(NO_3)_6$ and $Ti(OPr^i)_4$ in ethanol as starting materials and found that the current densities obtained for a thin film with Ce/Ti molar ratio of 1:1 are 3 times higher than that obtained for pure CeO_2 films and the diffusion coefficient of Li ions is 10 times higher. As the electronic resistivity of TiO_2 has the same order of magnitude as that of CeO_2 [142, 143], the increase in current densities when Ti is added is due to the increase of Li mobility. The work of Baudry et al. [141] was followed by series of other papers [144] using the same precursor in ethanol, isopropanol or methoxy-ethanol.

100 nm thick CeO_2-TiO_2 layers with a molar ratio of Ce/Ti = 0.5 were prepared by Avellaneda et al. [145] by the sonocatalytic sol–gel method using the same precursor in isopropanol. The layers were calcined at 450 °C in an oxygen atmosphere. Xerogels were characterized by thermal analysis (DTA–TG) and X-ray diffraction. The cathodic and anodic charges during cyclic voltammetry measurements at a scan rate of 50 mV/s were about 16 mC/cm^2 and the process was fully reversible up to 4500 cycles.

Equimolar CeO_2-TiO_2 films were fabricated with the same precursors in a mixture of ethanol and water and with addition of a small amount of acetic acid by Ghodsi et al. [146]. The surface composition of the films were studied by X-ray photoelectron spectroscopy (XPS). A scanning electron microscope was used for the analysis of the surface structure. The optical band gaps were E_g^d=3.59±0.12 eV and E_g^{ind}=3.19±0.08 eV for the direct and the indirect transitions, respectively independent of the dipping rate and the number of layers.

Optical indices of CeO_2-TiO_2 films have been determined by Rubin et al. [147] for stoichiometric composition prepared by both PLD and sol–gel. Measurements were made using a combination of variable-angle spectroscopic ellipsometry and spectroradiometry. The optical constants were then extracted using physical and spectral models. The sol–gel films were much rougher than the PLD films and poor agreement between the surface roughness predicted by the optical model and that derived from the AFM measurements

was found. The index of both films is however similar and they follow the classical normal dispersion forms decreasing asymptotically towards higher wavelengths. For the PLD film, n= 1.76 at 550 nm and for the sol–gel film a little bit higher n=1.83. The films were slightly yellow with the fundamental absorption falling off to negligible levels around 450 nm.

Cerium chloride ($CeCl_3$) and titanium isopropoxide $Ti(i\text{-}PrO)_4$ were the starting materials in the method proposed by Makishima et al. [148, 149] and used later by Stangar et al. [150]. Ce/Ti mole ratio of one to one was used. The use of these precursors improved the electrochemical properties of the obtained layers but not the optical ones.

Nothing was reported about the structure of the CeO_2–TiO_2 structure until Tonazzi et al. [151] studied by X-ray scattering the same films prepared by Baudry et al. [141] and proposed that small crystallites of CeO_2 are included in an amorphous matrix of TiO_2. No defined compound was observed.

Later Keomany et al. [152, 153] studied the structure of CeO_2-TiO_2 films prepared using other precursors e.g. by mixing two alkoxides, $Ce(OBu^s)_4$ and $Ti(OBu^n)_4$ and varying the composition range between pure TiO_2 and pure CeO_2. The coatings were found amorphous for concentrations of CeO_2 below 50 % and the size of the CeO_2 nano crystallites included in the TiO_2 amorphous matrix increases from ~1 nm for 5 % CeO_2 to 5 nm for pure CeO_2.

Recently Verma et al. [154] studied the structure of CeO_2–TiO_2 layers deposited by dip coating from an ethanolic solution of $CeCl_3 \cdot 7H_2O$ (0.22 M) and $Ti(OPr)_4$ with different Ce/Ti compositions. The XRD investigations showed the prevalence of amorphicity in the films constituted with 50 % or lower mole percentage of CeO_2. The compositions with higher CeO_2 contents exhibited nanocrystallinity and were distinguished by the existence of diffraction peaks assigned to cerianite and the mixed compound $CeO_{1.6} \cdot 2TiO_2$. In all the compositions the presence of TiO_2 in the amorphous phase was clearly evident.

The improvement obtained by adding TiO_2 to the pure CeO_2 layers depends on the material preparation mode and on the nature of the electrolyte, as shown e.g. by Stangar et al. [150]. who performed cyclic voltammetric measurements in LiOH electrolyte for both pure CeO_2 and mixed CeO_2-TiO_2 layers. The CeO_2 system exhibits higher overall electrochemical reversibility when compared to the CeO_2-TiO_2 system. Coulometric measurements as a function of the coating thickness showed that CeO_2 exhibits a larger storage capability. The CeO_2/LiOH system is also less sensitive with regard to the coating thickness. These

differences could be due to the presence of protons, differently adsorbed at the surface of CeO_2 and TiO_2, or to a different film structure, because the films of CeO_2 and CeO_2-TiO_2 were prepared using different cerium precursors; inorganic ($(NH_4)_2Ce(NO_3)_6$) precursor which was used for the preparation of the CeO_2 thin solid films while the CeO_2-TiO_2 coatings have been made by using mixed organic-inorganic ($Ti(OiPr)_4$ and $CeCl_3 \cdot 7H_2O$) precursors.

There are also instances where laboratory sol–gel devices have been fabricated without an IS film but using a suitable electrolyte [155].

2.6.4 Electrolyte

A suitable electrolyte with low electronic and high ionic conductivity is placed between the electrochromic (EC) and ion storage layers (IS). Besides acting as an ionic conductor, the electrolyte has also a mechanical role in supporting the device. Usually, the electrolyte must fulfil several requirements: it must be an electronic insulator ($\sigma_e < 10^{-12}$ S/cm) and be a good ionic conductor (usually $10^{-7} < \sigma_i < 10^{-4}$ S/cm). If the application requires that the device can be switched to the transparent state, then the ionic conductor must be also transparent and neutral colouring. The electrolyte should also not react with the two insertion electrodes in between it is sandwiched. This chemical stability must be ensured both during the deposition and during the cycling. Finally, for certain applications (e.g. windows), the electrolyte must be also stable in certain temperature range and under solar radiation [156]. In general the electrolytes used in electrochromic devices can be classified into two main categories: liquid and solid electrolyte

A Liquid electrolyte has the advantage of having high diffusion rates for the ions. Its use is limited to small size ECD due to the risk of leakage and dissolution of the EC and IS layer which leads to a fast degradation of the device [24]. Inspite of that, liquids are still being used for laboratory studies and are prepared using easily ionised salt dissolved in appropriate solvents. The most common salts are $LiClO_4$ and $LiBF_4$ salts for Li ions conduction where propylene carbonate (PC) and dimethyle florine (DMF) are used as solvents.

A Solid electrolyte can be classified into organic and inorganic electrolyte. *Organic electrolytes* fall into two main types: polymer electrolyte and polyelectrolytes. Polymers electrolyte are macromolecules containing dissolved Li salt or acid [19] depending on the needed ion transport. Cross-linked polyether (CPE), polyethylene oxide (PEO) and

polyvinyl alcohol (PVA) are the most common polymer matrix used in solid electrolyte synthesis. $LiClO_4$ and H_3PO_4 have been used as ion sources.

Polyelectrolytes are polymers containing ion-labile groups. Most common examples are polyperflourosulphonic acid (Nafion) poly methyl methacrylate (polyMMA) and polyethylene sulphonic acid (polyESA) [19].

The inorganic electrolytes are mainly oxides which serve as media for cation conduction, such as Ta_2O_5 and ZrO_2. It has the advantage over organic electrolytes in their enhanced stability to photolytic degradation.

The main problem of solid electrolytes are the significant interfacial contact resistances and their fragility. Many researchers have attempted to address these problems by using various thickened electrolytes consisting of a major solvent system, an ionic salt, and an intermediate molecular-weight polymer. This type of electrolyte is attractive for device applications due to the ease of preparation and the ability to reduce many of the unwanted effects shown by a strictly liquid electrolyte. Ideally, however, a more rigid electrolyte is desirable. While a rigid electrolyte can be achieved with high molecular-weight polymer additions, it can lead to great difficulty during filling and assembly of the devices by requiring high pressure and or temperature to achieve a proper flow for rapid and uniform assembly.

Some hybrid organic–inorganic sol–gel materials have been suggested as electrolytes in EC devices. "Aminosils" are obtained from $H_2NSi(OR)_3$ precursors hydrolyzed in the presence of strong mineral acids such as $HClO_4$ or HCF_3SO_3 [153]. The silica backbone provides mechanical strength while the amino groups and the acid provide the proton conduction [157].

Sol–gel-derived and polymeric solid or semi-solid electrolytes of different kinds are now used in experimental electrochromic devices

All gel electrochromic devices have been made using hybrid gels made from $Ti(OBu^n)_4$, acetic acid and glycerol as a proton conducting electrolyte [33].

2.7 Area of applications

The motivation for all efforts to develop electrochromic materials is their potential technical application. Few of them have already found their way to the markets such as rear-view mirrors for cars and vehicle. Next will come the electrochromic glazing where the main areas are automotive and architectural, with automotive being the most likely entry point because of its smaller size although it is necessary to have a high transmittance

of the bleached state (more than 70 %), a requirement is not so critical for architectural applications. Finally come the display devices. Some other applications are to be in use in the future such as EC ophthalmic eyewear [3]. In general ECDs are not so common in the markets due to lack of suitable manufacturing techniques and durability of the available devices [158].

2.7.1 Smart window

It is one of the most important applications, which works as light and heat filters for the external glazing of buildings leading to a reduction in fossil fuel consumption. It has the typical structure of five layers EC device structure shown above (fig. 2.4). The primary advantage of an EC glazing is the capability for a dynamic control of the transmittance of the glass. In summer it is used to reject the maximum possible IR radiation to lower the air conditioning cost while in winter it is set to pass as much as possible the IR to warm the interior place. This has great economical benefits. One main advantage of EC glazing is the dynamic control of the color state so it can provide nighttimes insulation and privacy and can be also adjusted to reduce glare. A number of criteria are necessary for electrochromic smart window applications. They are summarized as follows [159, 160]:

- continuous range in solar and optical transmittance, reflectance and absorptions between bleached and colored states,
- contrast ratio (CR) of at least 5 : 1,
- coloring and bleaching times (switching speed) of a few minutes,
- operating glass surface temperatures of –20 °C to +80 °C,
- switching with applied voltages of 1 to 5 V,
- open circuit memory of a few hours (maintains a fixed state of transmittance without corrective voltage pulses),
- acceptable neutral color,
- large area with excellent optical clarity,
- sustained performance over 20–30 yr,
- acceptable cost

The automotive glazing like sunroof and side windows have an advantage over the architectural windows because of their smaller size and shorter required life time, although the upper temperature limits are higher (90–100 °C) [158]. Table. Summarize the important requirements for glazing used in automobile glazing (sunroof and side windows) [24].

Table 2.1: Important requirement for glazing used in automobile (sunroof and side windows) [24].

Visible transmittance	Bleached 41-70%, colored 20-10%
IR reflection	Colored > 70%
Response time	<15 min, but preferably <2 min
Cycling life time	At least >$2x10^4$ but preferably >10^5 cycles
Shelf life time	>5 years, preferably 10 years
Operating temperature	Preferably -40 to +100

2.7.2 Non-emissive information displays

The electrochromic information display device keeps the same standard 5 layers structure of electrochromic devices, with the difference that the electrochromic layer is embodied in front of a diffusely scattering surface. The electrochromic layer could be patterned [20]. Such application was proposed at the discovery of the electrochromic phenomenon, but durability issues as well as progress in liquid-crystal-based devices have led to a total dominance of the latter. The contrast ratio, defined as the ratio of the intensity of light diffusely reflected through the bleached state of the display to the intensity of light diffusely reflected from the colored state, is an important parameter for evaluating the performance of display devices. Requirements for electrochromic materials to be used in commercial devices [123].

- a high contrast ratio,
- high coloration efficiency,
- long cycle life,
- high write–erase efficiency,
- fast response time.

Electronic paper is just a special case of electrochromic display where digitised images could be formed by directing voltage pulses to pixel electrodes, in contact with a paper incorporating an electrochromic species and electrolyte, the non-image side being simply a conducting surface comprising the counter electrode [161]. Printing systems based on this phenomenon have been proposed [19, 162].

In the first rigorous study of an electrochromic paper [161], methyl viologen (MV) has been incorporated into a paper as an aqueous solution and in the viscous polyAMPS electrolyte. The availability of the MV for electron-transfer has been investigated by cyclic

voltammetry at a stationary platinum disc electrode. The brief study of the electrochemistry of prussian blue (PB) and methyl viologen in paper was published by Rosseinsky and Monk in 1989 [162], in which the electrochromes methyl viologen, 1-methyl-1′-hyphoxyethylphenyl viologen and PB were separately immobilised in the paper, the working electrode being a glassy carbon. Their conclusion was that the voltammetric response of all three electrochromes was essentially the same in paper as that in solution, albeit with complexities caused by *iR* drop and fluctuating humidity.

2.7.3 Electrochromic Mirror

This is the most mature electrochromic application and it is already available in market as rear and side view mirrors for cars and vehicles. One modification has to be done to the standard electrochromic device construction, and a reflecting electrically conductive back electrode is used instead of a rear transparent conductive electrode.

During daytime viewing, the rear view mirror is set so that the electrochromic component is in the bleached state with a reflection from the back reflecting part of the mirror. At night, the mirror is switched on when the headlights behind the car only hit a photosensitive sensor on the front glass surface of the mirror. Since the light has to pass twice through an absorbing medium, the reflectivity of the system is low and the glare is significantly reduced. The function of electrochromic mirrors was discussed intensively by Baucke [163, 164].

2.8 State of art of electrochromic devices based on NiO_x electrode

Electrochromic devices behaves as rechargeable thin film batteries whose energy content or state of oxidation is optically indicated [165].

Special attention has been devoted to designs incorporating electrochromic hydrated nickel oxide films operating in conjunction with electrochromic tungsten oxide. This combination of materials is favorable with regard to electrochemical potentials and also for the possibility to attain a neutral gray color in the dark state [4]. Many glass-based devices have been investigated.

Fundamental properties of all-solid-state electrochromic windows to control the solar energy have been investigated using devices with configuration Glass/ITO/NiO/Inorganic Electrolyte (Ta_2O_5, etc.)/ WO_3/ITO/ Adhesive Film/ Glass. They modified the visible transmittance between 72.6 % and 17.6 % and had a cyclic life over 100000 cycles at 60 °C. Based on the accelerated weathering tests, the stability of the system is estimated to

be over five years for outdoor applications. In general, the most important features of such systems are their environmental stability and the possibility of large area applications technology [166].

The *IR* r*emittance* modulation was tested for prototypical small area electrochromic device of crystalline tungsten oxide and nickel oxide charge storage films. Using crystalline tungsten oxide instead of highly disordered amorphous tungsten oxide it is possible to modulate the IR transmittance/reflection instead of the normal visible light. Such systems show change in emissivity from about 0.60 to about 0.68, that is a total modulation of 13%. The remittance performance was calculated, based on the reflectivity modulation [167].
The possibility of a NIR-reflectance control was exemplified for electrochromic glazing with the configuration WO_3/PEO-based Li^+ electrolyte/NiOx which showed promising solar control properties [168].
When an acidic electrolyte is used, a protective layer for nickel oxide is needed due to its instability in acidic media. Six-layer electrochromic devices with the configuration indium tin oxide (ITO)/NiO_xH_y/WO_3/ZrP-electrolyte/WO_3/ITO were made by reactive dc magnetron sputtering and lamination. The WO_3 layer between the acidic ZrP-based electrolyte and the NiO_xH_y layer served as optically passive protective layer [169].
To demonstrate the advantage of using $Li_xNi_{1-y}O$ as a counter electrode over V_2O_5, WO_3/V_2O_5 and $WO_3/Li_xNi_{1-y}O$ cells were assembled. The WO_3/V_2O_5 cell switched between 65 and 17% T_{Ph}, with a coloration efficiency CE_{Ph} of 42 $cm^2\ C^{-1}$, essentially that of the tungsten oxide film. The $WO_3/Li_xNi_{1-y}O$ device switched between 65 and 8% T_{Ph} with excellent cycle-to-cycle stability and a high coloration efficiency (CE_{Ph}=56 $cm^2\ C^{-1}$) [117].

The angular dependence of the direct solar transmittance, T_{sol}, and the visual transmittance, T_{vis} was examined by using a 5×5 cm^2 electrochromic prototype with WO_3 and NiO sputtered electrochromic layers and a proton electrolyte. The spectral transmittance was measured in the bleached and colored state over the solar wavelength range at angles of incidence $\Phi = 0$, 40, 60 and 70° [170].
A large optical electrochromic shutter, arranged as a matrix (8×8 devices) was used to quantify the advantages for energy saving during the summer and winter season by darkening windows and to evaluate the visual comfort obtainable by transmittance variation. Each device was 144 cm^2 in situ, made from rf sputtered tungsten trioxide

working electrode and electrochemically deposited nickel oxide counter electrode and (ethylene glycol methacrylate) (PEGMA) based electrolyte [171]. Residual coloration due to the presence of residual charges has been reported [172].

Electrochromic devices on polyester foils are more difficult to realize than those on glass, because a polyester foil is deformed at temperatures >100°C. This is a serious problem, since thin films evaporated on substrates with temperatures <100°C are less stable. This could be a reason for the fact that so far most devices are produced on glass and only a few reports exist about electrochromic films on polymeric substrates [165, 173].

In 1998, tungsten oxide (WO_3), vanadium and nickel-hydroxide (VO_xH_y and NiO_xH_y)-films were evaporated on glass and polymeric substrates covered with indium-tin oxide (ITO). Films of nickel-oxide (NiO_x) were reactively sputtered from a nickel target. In order to obtain electrochromic devices the WO_3 film was used as one electrode and with a polymeric solid state electrolyte (PSSE) glued to each of the other films which served as different counter electrodes. The films and the complete devices were investigated by optoelectrochemical and other methods. The most stable device was the WO_3–VO_xH_y system which even improved their electrochromic properties after 3×10^4 cycles. The conversion of the system with NiO_x as the counter electrode on polyester foil was not possible, because a post deposition heat treatment at a temperature higher than 150°C is disadvantageous for the NiO_x film and the polyester foil does not resist this temperature [165].

Recently a new flexible electrochromic foil device with sufficient optical modulation range, dynamic, and durability for practical uses was reported [174]. The device incorporates a film of W oxide made by sputtering in the presence of hydrogen, another film of Ni–V oxide made by sputtering and post deposition treatment in ozone, and a polymer laminate. Application as variable-transmittance visors for motorcycle helmets is discussed. Devices of the type described above were cycled between colored and bleached states using trapezoidal voltage pulses between −1.6 and +1.5 V, respectively. The foils switches between a high level of about 70 % and a low level of 35–40% at a wavelength of 550 nm.

Chapter 3
Theoretical background

3.1 Nickel oxide compounds

It is obvious that a detailed theoretical understanding of the electrochromism hinges on reliable theoretical modelling of the electronic structure of the layer material.

Nickel is a transition metal belonging to the group VIII of the Periodic. The 38 elements in groups III through XII of the periodic table are called "*transition metals*". As for all metals, the transition elements are both ductile and malleable, and conduct electricity and heat. Their interesting feature is that their valence electrons, that are the electrons they use to combine with other elements, are present in more than one shell. This is the reason why they often exhibit several common oxidation states. Nickel is one of three noteworthy elements in the transition metals family (iron, cobalt, and nickel) that are known to produce a magnetic field. The electronic structure of Ni is $1s^2 2s^2 2p^6 3s^2 3p^6 \mathbf{3d^8} 4s^2$. Its outer electrons shell has a $4s_2 3d_8$ configuration. While nickel can exist in oxidation states 0, +1, +2, +3, and +4, its only important oxidation state is 2 under normal environmental conditions. Nickel forms useful alloys with many metals. It is added to metals to increase their hardness, strength, and corrosion resistance. The most familiar nickel-ferrous alloys are stainless steel and coinage metal.

There are many nickel compounds such as nickel ammonium sulphate, nickel sulphate, nickel chloride, and nickel nitrate that usually exist as hexahydrates, while nickel acetate, nickel cyanide, and nickel sulfamate are in a tetrahydrate form.

3.1.1 Nickel Monoxide

Nickel monoxide belongs to the 3d transition metal oxides with a NaCl structure and a density of 6700 kg m^{-3}. Stoichiometric NiO is an anti-ferromagnetic insulator. However, like the other transition metal oxides, NiO has defect structure with excess oxygen and nickel vacancies [175]. This causes the oxidation of Ni^{2+} to Ni^{3+} around the nickel vacancies which pushes the Fermi level to the top of the valence band (oxygen 2p band) [176] and the monoxide behaves like a p-type semiconductor. The conduction is explained to be a result of the migration of these vacancies. These vacancies also give a catalytic activity to nickel monoxide [175]. The valence band consists of localized nickel 3d-bands with a width of 4.3-4.4 eV [175, 176] at about 2eV above the Fermi level at –8.74 eV. The band gap between the valence and the conduction band is about 0.2 eV. The presence of

nickel vacancies besides some other impurities like OH^{-1}, CO_3^{-2} in defect nickel monoxide affects the electronic structure of the oxygen atom where extra O 1s peaks with higher binding energy are observed by XPS in addition to the typical O 1s peaks of oxygen in stoichiometric NiO. [175]. NiO is transparent in the thin film form.

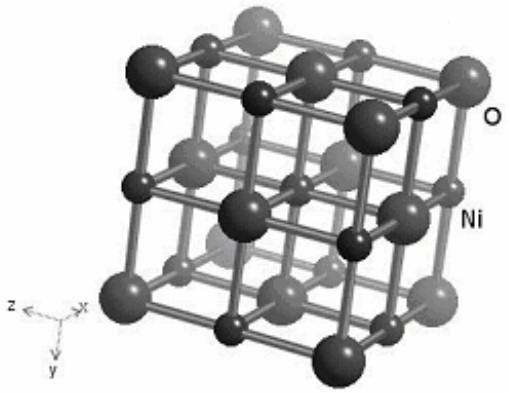

Fig. 3.1: Crystal structure of cubic NiO [177]

There are two main theories for explaining the optical absorption gap in NiO: it is due to either a p→d transition in one Ni atom [178] or a d→ d transition between two adjacent Ni atoms in the lattice [179].

3.1.2 Nickel hydroxide $Ni(OH)_2$

Poorly crystalline or XRD amorphous solids containing nickel, oxygen, are usually called simply oxides [20]. As shown in fig. 3.2 there are two known phases of $Ni(OH)_2$ namely the α-$Ni(OH)_2$ and the β-$Ni(OH)_2$ phases.

β-$Ni(OH)_2$ has a layered structure, each layer consisting of an hexagonal plane arrangement of Ni(II) ions with an octahedral coordination of oxygen, three oxygen atoms lying above the Ni plane and three lying below. Protons are located in tetrahedral sites above and below the oxygen sites. The layers are stacked along the c-axis [20, 180]. The O-H bond is thought to be parallel to c-axis with no interaction between the OH^- bond of the different planes [181]. The unit cell of this structure has a= 3.1Å (Ni-Ni distance in the layer) and c= 4.6 Å (inter slab distance) [182].

α-$(NiOH)_2$ is the hydrated form of the β-$Ni(OH)_2$ where water molecules are intercalated between $Ni(OH)_2$ layers. The interlamellar distance is higher (7 Å) [180, 182]. Bode et al. [183] proposed that the intercalar water molecules have definite positions between the

layers where there is a quasi-compact stacking of OH-H_2O-OH. The number of water molecules is defined according to the formula $3Ni(OH)_2 \cdot 2H_2O$ [183].

This model was rejected by Le Bihan [184] and McEwan [185] who proposed a turbostratic structure consisting of equidistant randomly oriented $Ni(OH)_2$ layers separated by intercalary water molecules bonded to hydroxyl group by hydrogen bond.

An α-$Ni(OH)_2$ to β-$Ni(OH)_2$ phase transformation is possible by aging in their mother solution or by hydrolysis. In the first case the crystal growth proceeds by joining the primary particles in the solution. In water the turbostratic α-$Ni(OH)_2$ seems to be dissolved slowly in water and β-$Ni(OH)_2$ is formed by nucleation and growth from the solution [181]. Both $Ni(OH)_2$ compounds are transparent in thin film form.

3.1.3 Nickel oxihydroxide NiOOH

Nickeloxihydroxide, NiOOH, having Ni with a higher oxidation state (+3) also exists in two main phases β-NiOOH and γ-NiOOH [181]. Both are colored compounds.

The β-$Ni(OH)_2$ phase can be oxidized to β-NiOOH phase by removing one proton and one electron without significant structural deformation (see fig. 3.2) [182]. This is associated with a volume expansion (c = 4.85 Å) [20, 180, 182] due to the electrostatic repulsion between the oxygen atoms in the adjacent layers after removing the protons[20, 182].

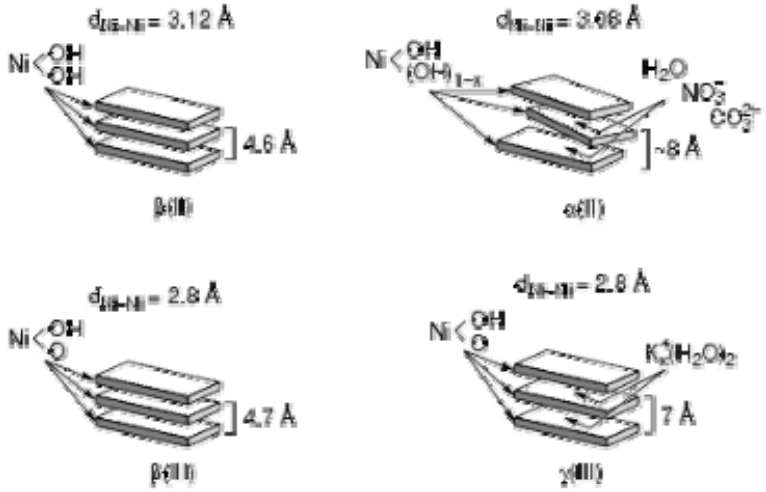

Fig. 3.2: Schematic diagram of the structure of the difference $Ni(OH)_2$ and NiOOH phases [186].

There is also a complete family of γ-NiOOH compounds. In general it is represented by the formula $A_xH_y(H_2O)_z.NiO_2$ where A represents an alkali ion (most probable K^+or Na^+).

γ-NiOOH has different oxidation states ranging from 3 to 3.75 depending on the preparation route. It has also a layered structure with water, protons and alkali ions inserted between the slabs of NiO_2.

3.1.4 Mechanism of Coloration

Nickel oxide was studied intensively for being used as an active material for nickel positive electrodes in Ni-based rechargeable batteries, electrochromic devices, and as promising catalysts for oxygen evolution reaction (OER). Electrochromism of NiO based electrodes implies in its most simple form the reversible oxidation of Ni(II) to Ni(III), i.e. a one-electron transfer. Regardless the long investigation of electrochemistry of Ni-oxides and hydroxides, the oxidation/reduction mechanism is far not well known. To throw some light on electrochromic mechanism it may good to start with the proposed mechanisms for bulk nickel oxide materials used in battery. Most of the studies are based on the old reaction scheme proposed by Bode et al. for NiO electrodes cycles in KOH [183].

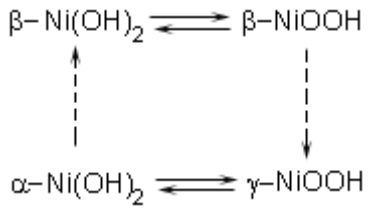

Fig. 3.3: Bode scheme for NiO electrode oxidation reduction reaction

The main feature of the Bode scheme is the transition between Ni(II) and Ni(III) by dehydration. There are two possible routes for the transition, (1) or (2). Route (1) implies a β-$Ni(OH)_2$ to β-NiOOH transition, with only one electron is transferred. The electrode can be cycled between these two phases by avoiding overcharge. In the α-$Ni(OH)_2$ to γ-NiOOH transition (route 2) at least 1.3 electrons are transferred due to the higher valence of the nickel in the γ -phase. Regarding the kinetics of the two reactions, it is reported that α/γ is faster than β^{II}/β^{III} while the oxidation potential of the later is about 50 mV higher than that of the former [181].

Irreversible β-NiOOH transformation to γ-NiOOH is possible through overcharge of the electrode or aging in KOH [181]. The formation of γ -NiOOH is associated with a volume expansion or swelling of the nickel hydroxide electrode due to the greater intersheet distances in γ-NiOOH compared to β-NiOOH (7 Å versus 4.85 Å). The phase change from β-NiOOH to γ -NiOOH can be correlated to a 44 % increase in volume.

Sac-Epee et al [180] proposed another mechanism (see fig. 3.4) where the main difference with the Bode scheme is the possibility of a direct transformation of γ–NiOOH to β-$Ni(OH)_2$.

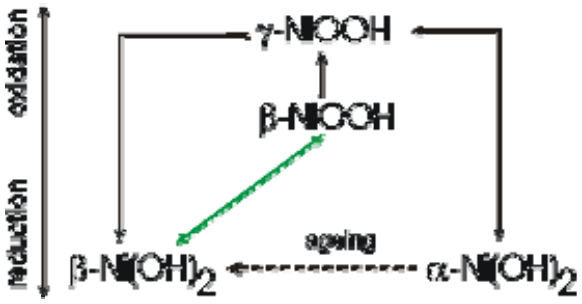

Fig. 3.4: Sac-Epee scheme for NiO electrode oxidation reduction reaction [180]

There are many problems risen on applying these schemes, the most important being that the stoichiometry of the compounds included in the schemes is not as simple as seems in the model e.g., the formula of α -$Ni(OH)_2$ and γ -NiOOH also include cations and anions intercalated and the oxidized form also contained Ni^{IV} [187].

The electrochromic mechanisms of the nickel oxides thin films based on the above schemes are still unclear although numerous textbook examples of the intercalation kinetics have been published. There are three main reactions based on studies of NiO thin films in aqueous media. The reactions differ according to the composition of the layer (NiO or $Ni(OH)_2$) and on the intercalated ions (H^+ or OH^-). They are:

$$Ni(OH)_2 \leftrightarrow NiOOH + H^+ + e^- \quad (3.1)$$

$$Ni(OH)_2 + OH^- \leftrightarrow NiOOH + H_2O + e^- \quad (3.2)$$

$$NiO + OH^- \leftrightarrow NiOOH + e^- \quad (3.3)$$

NiO and $Ni(OH)_2$ are transparent while NiOOH is colored in thin film form.

Most of the reports accept the general mechanism of equation (3.1) without any detalied investigations [84, 91, 93, 100, 188, 189], while others accept equation (3.2) [79, 103, 121] and (3.3) [103]. Fantini at al. [97] beleived that the reaction starts according to equation (3.2) then NiOOH is reduced to $Ni(OH)_2$ and the reaction proceeds according to equation (3.1).

Some others performed details measurements to find out the meachnism for the redox reaction. Surca et al. [83] performed detailed IR measurements of bleached and colored sol-gel NiO layers. They found that part of the structure of as-deposited layers has a

turbostratic α-$Ni(OH)_2$ structure which contains foreign ions (SO_4, CO_2, OH and H_2O). Small amount of a bad crystalline β-$Ni(OH)_2$ phase has been detected. The colored layers have an oxohydroxy Ni^{+3} phase which was confirmed by the presence of hydrogen bonded OH-O stretching mode. Their final conclusion was that the coloration/bleaching mechanism of the films takes place by intercalation of OH^- with a progressive development of the β-$Ni(OH)_2$ and β-NiOOH phases accompanying the bleaching/coloring cycles.

A different reaction was proposed by Azen et al. for sputtered layers [116].

$$NiO + H_2O \leftrightarrow NiOOH + H^+ + e^- \quad (3.4)$$

In such reaction neither $Ni(OH)_2$ nor OH^- are important for the electrochromism of NiO layers, but only water which may present initially in the pores of the oxide film is needed. OH^- groups do not enter the grains upon coloration, and NiOOH is formed on the grain surface. This does not contradict the condense structure of NiO. This proposal is in agreement with the absence of any structural changes observed during the coloration and with the importance of the grain boundary for the efficiency of electrochromic layers [116].

Decker´s group [190] went in a different way to prove that the water in the aqueous electrolyte has no role in the coloration/bleaching reactions. A layer was covered with a Pd film to work as a barrier for water insertion in the layer when cycled in aqueous electrolyte. A similar layer was tested in dry H^+ gaseous environment. The two layers could be bleached equally fast and efficiently. An increase in the compressive stress was noticed during the bleaching cycle of layers deposited on flexible substrate. The sputtered layers were considered to be a mixture of two phases, NiO and Ni_3O_4 and the proposed reaction was [190]

$$NiO + Ni_3O_4 + 2\,H^+ + e^- \leftrightarrow Ni(OH)_2 + 3NiO \quad (3.5)$$

where NiO and $Ni(OH)_2$ are transparent while Ni_3O_4 is coloured.

Rougier et al. [124] put a well organized proposal to explain the electrochromic redox reactions for PLD NiO layer. In the beginning $Ni(OH)_2$ is formed chemically on the surface of NiO by immersion in KOH according to $NiO + H_2O \rightarrow Ni(OH)_2$. Then the reaction goes in the direction $Ni(OH)_2$/NiOOH. The oxidized phase (NiOOH) is not stable

and is dissolved in KOH and a new layer of NiO has to transform into $Ni(OH)_2$ to continue the process.

Considering the electrochromism of NiO_x layers in aprotic electrolytes containing Li^+ salt, Passerini [191] was the first to show that nickel oxide samples can undergo a reversal lithium intercalation-deintercalation process accompanied by relevant electrochromic effect.

Later [192, 193] Li^+ intercalation in the NiO_x layer has been divided into two processes, activation period which involves irreversible uptake of Li^+ in the host structure of NiO_x layer. This followed by a reversible intercalation/deintercalation accompanied electrochromic bleaching/coloration process. The following two reaction describes the whole process

$$NiO_x + yLi^+ + ye^- \rightarrow Li_yNiO_x \quad (3.6)$$

$$Li_yNiO_x + zLi^+ + ze^- \leftrightarrow Li_{y+z}NiO_x \quad (3.7)$$

To further substantiate this model, Passerini et al. [193] measured the expansion of the host oxide matrix during the activation period by determining the mechanical stress induced by ion intercalation. The initial increase in stress at the negative potential indicates a slow ion diffusion in the layer. By reversing the sign of the current the induced mechanical stress remained unchanged. This process involved 20 $mC/cm^2\mu m$. When higher charges is used the extra stress became reversible.

Investigations based on cyclic voltammetric, impedance analysis stress measurement scanning electron microscopy showed that the intercalation of lithium induces phase changes in the nickel oxide structure [194]. A diffusion coefficient of about $1.0x10^{-11}$ cm^2S^{-1} at room temperature was estimated.

Cathodic electrochromic behavior was noticed upon overcharge of nickel oxide electrode. A small polaron model was proposed to explain the modification of the nickel oxide layer upon lithium intercalation [195]. The model assumed that on charging, the nickel oxide changes progressively from a degenerated metal like p-type semiconductor in the pristine state to a p-type semiconductor in the low intercalation state (Q_{Li}<140 $mC/cm^2\mu m$), then to a n-type semiconductor in the high intercalated state (Q_{Li}> 140 mC/cm^2. μm) and again to a degenerated, metal like material in the full intercalated state.

Chapter 4

Experimental methodology

4.1 Preparation of the sols and deposition of layers

4.1.1 $NiO-TiO_2$ sols and layers

$NiO-TiO_2$ sol was prepared according to an recipe developed at INM [89]. 0.5 M solution was prepared by dissolving 23.38 g of $Ni(CH_3COO)_2 \cdot 4H_2O$ in 200 ml ethanol at room temperature with continuous stirring for 7 hours. Then 7.8 g of titanium n-propoxide $Ti(C_3H_7O)_4$ were dissolved in 50 ml ethanol and added to the Ni solution in a glove box filled with nitrogen (humidity ≤ 5%) in order to obtain Ni molar concentration of 33 mol %. The sol was then stirred at room temperature for 30 min. and, upon completion filtered using a 0.2 μm filter. Apart from this composition, series of solution with total concentration of 0.5 M but with different Ni molar concentrations ranging from 100 to 10 % were also studied.

$NiO-TiO_2$ were deposited by the dip coating process (withdrawal speed of 3 mm/s, 20 °C, RH = 38 %) onto 10 x10 cm^2 float glass and commercial conducting SnO_2:F coated glass having a sheet resistance of 17 Ω/ (K-glass). The layers then heat treated in air at a rate of 2 K/min up to the desired temperature and then the system was left at this temperature for about 30 min.

Up to 3 layers have been deposited. For this purpose the same heat treatment was performed after each deposition. Also single layers having different thickness values have been deposited by changing the withdrawing speed from 0.5 to 4 mm/s.

4.1.2 $(CeO_2)-(TiO_2)$ sols and layers

The $(CeO_2)_x(TiO_2)_{1-x}$ sol was prepared according to a recipe developed at INM [196]. First 24.4254 g $Ce(NO_3)_3 \cdot 6H_2O$ were dissolved in 125 ml absolute ethanol (0.45 mol/l Ce), then 19.5429 g $Ti(i\text{-}OPr)_4$ were dissolved in 125 ml absolute ethanol (0.55 mol/l Ti) and added to the cerium nitrate ethanol solution in a glove box with nitrogen atmosphere. These solutions were aged at 30°C during several days under mechanical stirring in closed glass vessels to prevent rapid a precipitation of the Ti alkoxide due to hydrolysis.

The CeO_2-TiO_2 layers were deposited on pre-treated K-glass by the dip-coating technique with a withdrawal rate of 4 mm/s at 20 °C with 38 % air humidity. The layers were then

heated from room temperature up to 550 °C with a heating rate of 2.5 K/min, maintained at 550 °C for 1 hour and then cooled down to room temperature.

4.1.3 Nb_2O_5:Mo sols and layers

The Nb_2O_5:Mo sol was prepared according to a INM recipe [197]. First 0.12 M of $H_3[P(Mo_3O_{10})_4]\cdot H_2O$ were weighted in glove box under nitrogen atmosphere and dissolved in 125 ml ethanol. Second 125 ml anhydrous ethanol was dropped to 0.4 M $NbCl_5$ using pressure equalizer in order to obtain niobium chloroethoxide sol [144]. 30 ml acetic acid (99-100 %) and the molybdenum sol were added then to this during stirring in about 5 min. The mixture was put into an ice bath and subject to an ultrasonic treatment for 4 hours. Aging at temperature of 20 °C in a closed glass recipient for two days is needed before using the sol for coating.

Double Nb_2O_5:Mo layers were deposited onto pre-treated K-glass by dip coating process at a withdrawal speed of 4 mm/s. The first deposited layer was dried for 30 min at 100 °C in an oven under synthesis air. Another layer was then deposited and dried in the same way and the double layers were sintered directly at 500 °C for 30 min, then cooled down to room temperature.

4.1.4. Anti corrosion layers

A 0.5 M of Al_2O_3 sol was prepared by dissolving 12.3 g of Aluminium tri-sec butylate ($C_{12}H_{27}AlO_3$) in 100 ml of butanol under stirring in glove box..

A 0.5M of ZrO_2 was prepared by dissolving 16.35 g of zirconium n-propoxide ($Zr(OC_3H_7)_4$) in 100 ml of isopropanol under stirring in glove box..

A 0.5 M of TiO_2 sol was obtained by dissolving 14.2 g of Titanium n-propoxide ($Ti(C_3H_7O)_4$) in 100 ml of ethanol.

The layers was deposited on the top of NiO-TiO_2 coating by dip coating technique at withdrawal speed of 0.5 mm/s and sintered at 300 °C.

4.2. Synthesis of electrolyte

4.2.1 liquid KOH electrolyte

5.6 g of KOH crystal was dissolved in 100 ml of bidistalled water under stirring for a few minutes to get aqueous KOH electrolyte of 1 molar concentration.

4.2.2 Gel KOH electrolyte

1.8 g of starch $(C_6H_{10}O_5)n$ was dissolved in 30 ml of bidistilled water at room temperature. The sol temperature was raised gradually to 85 °C with continuous stirring for 3 hours. The

sol then left to cool down to 50 °C with stirring. Small amount of KOH was then dissolved in 5 ml bidistilled water and added to the starch sol. 1.5 g of glycerol ($C_3H_8O_3$) was added and stirred for one min. 0.5 g formaldehyde (CH_2O) could be added to increase the cross linking of the electrolyte. The electrolyte should be filled in the devices as soon as it is prepared.

4.2.3 Nanocomposite electrolyte

A solid ionic conductor has been prepared according to a method used at INM [198, 199]. The composition is based on glycidoxypropyltrimethoxysilane (GPTS), $LiClO_4$, $Zr(OnPr)_4$ and tetraethylene glycol (TEG). GPTS serves as network formers, whereas TEG acts as a plasticizer. Lithium perchlorate is the conducting salt and $Zr(OnPr)_4$ is added as a starter for thermal curing. Dried $LiClO_4$ was first dissolved in a mixture of TEG and prehydrolysed GPTS. TEOS and $Zr(OnPr)_4$ were then added. The volatiles were removed by rotary evaporation immediately prior to the filling it in the EC windows.

4.3 Mounting of EC-devices

The preparation of the EC devices was performed first by gluing 1 mm thick, 3 mm wide a adhesive tape at the edges of one of the functional coatings (e.g. k-glass/EC layer) then the other coated substrate was put on the first substrate in a way that the two coatings face each other inside the assembled window. A 1 cm width adhesive copper tape was pressed to the free edge of each substrate for electrical connection. The electrolyte was injected in the mounted cells using a syringe. In the case of ormolyte the devices were then heated up to 105 °C for 12 hours. For EC devices made with wet electrolyte, the amount of water (1 to 3 wt%) was first dissolved into the electrolyte before filling the EC device

4.4 Thermal analysis (DTA/TG/IR/MS)

Simultaneous DTA and TG have been performed on NiO-TiO_2 xerogels dried overnight (Ni concentration 75 mol %) using a Netzsch STA 449C/3G Jupiter equipment coupled to a Mass spectroscopy (MS) (QMS 403C Aeolos) and an Infrared spectrometer (FTIR) (Tensor 27-FTIR, Brucker). The xerogels were grounded in a mortar to get a fine powder. 33.3 mg of the powder was heated in synthetic air in an Al_2O_3 crucible up to 600°C at a heating rate of 2K/min.

The *Differential Thermal analysis (DTA)* is a technique that provides information on the chemical reactions, phase transformations, and structural changes that occur in a sample

during a heat-up or a cool-down process. DTA measures the differences in energy released or absorbed, and the changes in heat capacity of materials as a function of temperature.

Thermogravimetry (TG) is a technique by which the mass changes of a sample is monitored while the sample is subjected to a temperature-time program in a well defined atmosphere.

The combination of Thermal Analysis and Spectroscopic Analysis delivers extremely valuable information for material characterization and phase changes during thermal decomposition. The spectroscopic techniques depend on Evolved Gas Analysis (EGA). The most common ones are:

Mass spectroscopy (MS) is a technique of determining the nature and amount of volatile product formed during thermal analyses. During real-time DTA/TG, the mass spectrometer ionises the evolved gases, which are identified by their characteristic fragments. The spectrometer can either scan over a range of 0-300 amu or monitor individual ions of interest. The last method was followed in our measurements.

aa*Infrared spectroscopy (FT-IR)* is a technique for identification of gases released directly from the sample or during thermal treatment. IR spectroscopy is a classical technique, which depends upon the interaction of infrared radiation with the vibrating dipole moments of molecules. It gives, with the exception of homonuclear diatomic and noble gases, a characteristic spectrum for each substance.

Gram-Schmidt orthogonalization (GS) is a powerful data analysis tool [200], used to detect the presence of infrared radiation absorbing species evolved in the real time between 400 and 4000 cm^{-1}.

4.5 Thickness measurement

The thickness of the layers was determined by a TENCOR P-10 surface profilometer. Samples were scratched deeply with a sharp item at three different positions (for more accuracy) few minutes after dip coating during the drying stage. After heat treatment, the surface of the sample was scanned by a diamond stylus through the scratches from one edge to the other. The step height between the layer surface and FTO at the scratch represents the layer thickness.

4.6 Morphology and structure analysis

4.6.1 Surface morphology studied by Scanning Electron Microscopy (SEM)

Scanning Electron Microscopy (SEM) of the surface has been obtained using a JEOL JSM-6400F equipment using the secondary electron signal excited at 10 k eV primary beam. A very thin conducting gold was sputtered on the surface of the sample before testing it to get charge free surface.

4.6.2 Layer morphology studied by Transmittance Electron Microscopy (TEM)

Transmittance Electron Microscopy (TEM) measurements have been made with fresh, bleached and colored thin rasped layers using a JEOL.JEM-2010 Gatan MSC equipment.

4.6.3 X-ray diffraction

X-ray diffraction is an investigation method which can identify an unknown mineral, or characterize the atomic-scale structure of an already identified mineral The structural investigation of fresh triple NiO-TiO_2 layers deposited on float glass and heat treated from 250 to 500 °C was achieved using X-ray diffraction (XRD) (X'Pert Philips- MPD, $CuK\alpha_{1,2}$) in the range 26 ° < 2θ < 80 ° at 0.3° grazing incidence and scan steps of 0.02°. The crystallite size were determined from the half width of the full maxima (HWFM) of specific XRD peaks using the Scherrer equation. To check the effect of Ni molar ratio, XRD of layers with different Ni molar concentration ranging from 33 to 90 % deposited on float glass and sintered at 400 °C were also measured.

To test a possible change of the structure during the EC process, triple layers have been also deposited onto 4x10 cm^2 ITO coated glass substrate (Asahi Glass). The NiO-TiO_2 layers have been cycled in 1 M KOH electrolyte up to 270 (CV) cycles (see section 4.7), then disconnected at the positive potential (colored state +1 V vs SCE), or at the negative potential (bleached state –0.6 V vs. SCE) and dried in air before performing the XRD (range 10 < 2θ< 90 °, 0.02 ° steps). The colored layers remained deeply coloured within the X-ray scan time of 12 hour. For comparison, fresh layers have been also measured in the same way.

4.7 Electrochemical characterization

Electrochemical measurements have been carried on using a three electrode cell shown in fig. 4.1. The working electrode was the layer to be characterized deposited on K-glass, the counter electrode was a Platinum foil of 2.1 cm^2 area, the reference electrode was

Saturated Calomel electrode (SCE) when 1 M KOH was used as an electrolyte and $Ag/AgClO_4$.PC with the $LiClO_4$-PC electrolyte. The effective area of the layer which is in contact with the electrolyte was 7 cm^2. The characterization was done using an EG&G 237A Potentiostat. Cyclic voltammetry (CV), chronoamperometry (CA) and Chronopotentiometry (CP) measurements have been carried out.

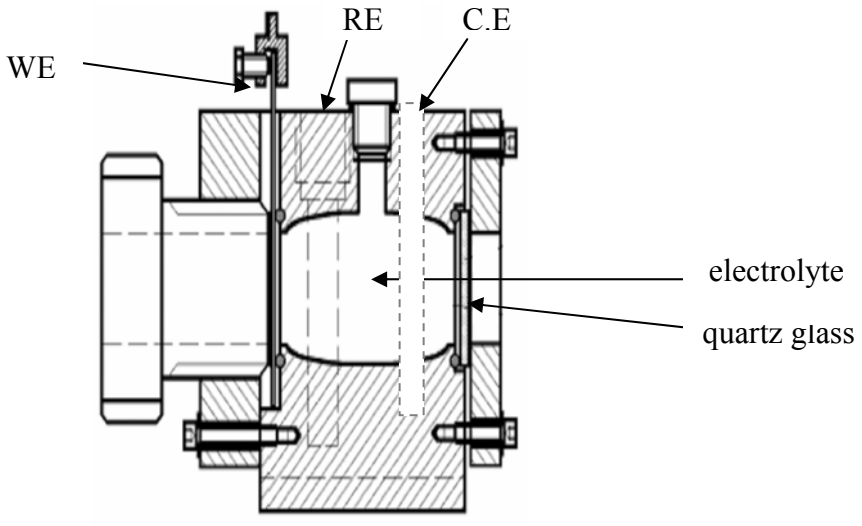

Fig. 4.1: Schematic representation of the three electrode cell used in electrochemical characterization of the electrochromic layers.

4.7.1 Cyclic Voltammetry (CV)

In this technique the potential of the working electrode against the reference is swept periodically and linearly between two fixed values at a certain scan rate and the current flow between the working electrode and the counter electrode is recorded. This has the advantage that the product of the ion and electron transfer reaction that occurred in the forward scan can be probed again in the reverse scan. In addition, it is a powerful tool for the determination of formal redox potentials, detection of chemical reactions that proceed, to follow the electrochemical reaction and evaluation of ion and electron transfer kinetics. The potential limits were –0.6 V/ +1 V vs. SCE for NiO-TiO_2 layer, –1.2 V/0.6 V vs SCE for CeO_2-TiO_2 layer and –1.5 V/ +1 V vs. SCE for Nb_2O_5:Mo layer. Higher voltages are not recommended, as the liquid electrolyte may decompose and gas bubbles develop and isolate the electrochemically active layer from the liquid electrolyte.

4.7.2 Chronoamperometry CA/Chronocoulometry CC

Chronoamperometry (CA) and Chronocoulomety (CC) have the potential step waveform. As shown in fig. 4.2, the potential is changed instantaneously from the *Initial Potential* to the *First Step Potential*, and it is held at this value for the *First Step Time*. This is a single

potential step experiment. In a double potential step experiment, the potential is changed to the *Second Step Potential* after the *First Step Time*, and it is then held at this value for the *Second Step Time*. In **CA**, the current is monitored as a function of time, whereas in **CC**, the charge is monitored as a function of time with the potentiostat and software used in this work, the *current* was recorded as a function of time during the experiment while the data displayed as charge vs. time have been calculated later.

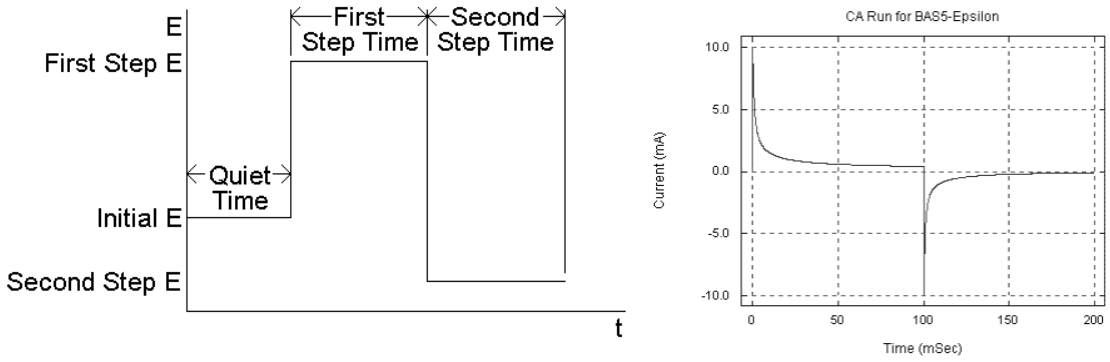

Fig. 4.2: Right side: schematic representation of double potential step chronoamperometry (CA), left side: current-time response during the experiment

Since the current is directly proportional to the rate of electrolysis, the current response to a potential step is a current 'spike' (due to initial electrolysis of species at the electrode surface) followed by a time-dependent decay due to the diffusion of ions into the electrode surface (see fig. 4.2). For a diffusion-controlled current, the current-time (i-t) curve is described by the Cottrell equation:

$$i = nFAD^{1/2}C_b/\pi^{1/2}t^{1/2} \quad (4.1)$$

where n is the number of transferred electrons, F Faraday constant 96,500 C mol^{-1}, A the electrode area (cm^2), D the diffusion coefficient ($cm^2\ s^{-1}$), C is the concentration (mol cm^{-3}) and t is the time.

The time duration for coloring and bleaching of the layers and devices was 60 s while E_1, E_2 were (–1, 0.6 V vs. SCE) for NiO-TiO_2 and (–1.2, 0.7 V vs. SCE) for CeO_2-TiO_2 and (-1.5, 1V) for Nb_2O_5: Mo

4.7.3 Chronopotentiometry (CP)

In this measurement a small constant current density is applied for a certain time t, and the potential change of the layer is monitored. The plot of the potential against time is usually

a sigmoid curve with various plateaus. Each plateau corresponds to a redox potential of a certain electrochemical reaction. The total inserted charge density can be calculated by multiplying the total time of experiment by the applied current density $Q = i * t$

Current density of $\pm 5 \mu A/cm^2$ was applied for different time periods in this work.

4.8 Optical properties

In-situ transmittance measurement was carried out during the electrochemical measurements at the wavelength 550 nm using a Cary 5E UV-VIS-NIR spectrophotometer from Varian. Spectral transmittance of the layers have been also measured in the spectral range 200-1200 nm using the same instrument. The measurement were carried out for the layers in the three electrode cell at normal incident angle against a reference cell that have a float glass substrate in the place of the working electrode. The transmittance of the devices is measured in the spectral range 300 to 3000 nm against air as a reference.

The change in optical density (ΔOD) was calculated using the measured transmittance of the layer or device in the colored (T_c) and bleached (T_b) state by applying the equation

$\Delta OD = Log_{10} T_b/T_c$

4.9 Electrochemical quartz crystal microbalance

Quartz crystal microbalance (QCM) uses a piezoelectric crystal oscillating at a very sharp defined frequency. Small mass changes of the crystal surface shift this frequency. Both sides of the crystal are coated with a gold electrode. The system is placed in an electrochemical cell that allows recording simultaneously the electrochemical parameters and the mass changes.

The EQCM measurements were made using a Maxtek, Inc microbalance connected to VMP2 multi channel potentiostat, in order to control the potential applied to the crystal, and to a computer. The frequency changes and calculating the corresponding mass changes were obtained using the RQCM data logging software. The electrochemical cell used was a double wall glass flask connected to a thermostated cycling water to control the temperature. The NiO-TiO_2 coated quartz crystal (quartz crystal 5 MHz AT-cut from maxtek, Inc) was used as working electrode, a platinum mesh as counter electrode and SCE as a reference electrode. 1 M KOH was used as electrolyte. The electrodes were fixed in three special holes in the rubber cap of the electrochemical cell. Changes in the quartz crystal resonant frequency were converted to mass changes using the Sauerbrey equation [201].

$$\Delta f = -\left(\frac{2 f_0^2}{A\sqrt{\mu\rho}} \right) \Delta m \tag{4.2}$$

where Δf is the change in frequency (Hz), Δm the mass change (μg), f_0 is the resonant frequency of the used quartz crystal (5 MHz AT-cut), ρ is the density of the quartz (2.648 g/cm^3), A is the area of the electrode (1.37 cm^3) and μ is the quartz shear modulus (2.947×10^{11} g.s^{-2}cm^{-1}). The minus sign means that the resonant frequency shifts to lower values by increasing the mass of the quartz crystal. The value between parentheses was calculated and the above equation can be written in the simple form

$$\Delta f = -C_f \Delta m \tag{4.3}$$

where C_f is the sensitivity factor of the crystal In our case C_f = 56.6 Hzμg^{-1}cm^2.

Chapter 5

Results and Discussion

5.1 Thermal properties of NiO-TiO_2 xerogel (DTA/TG/MS/IR)

The DTA/TG/DTG/GS spectra obtained for a NiO-TiO_2 xerogel (Ni concentration 75 mol %) are shown in fig .5.1.

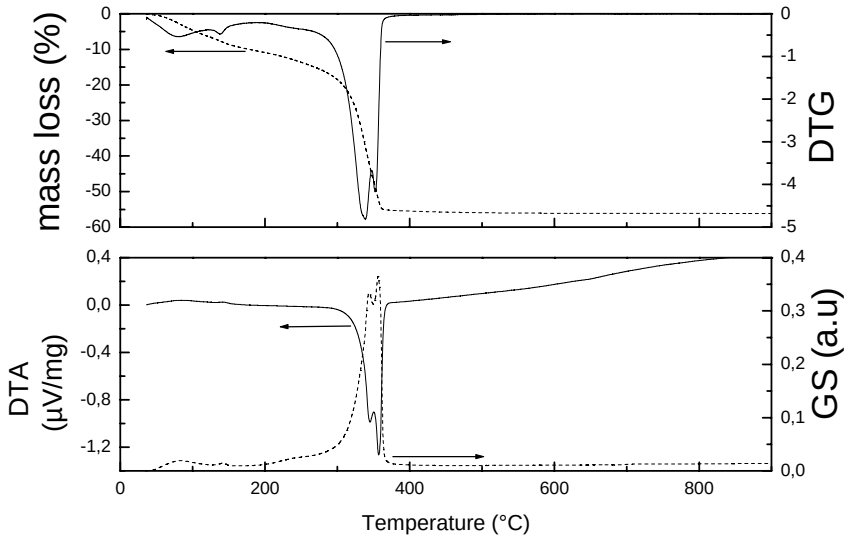

Fig. 5.1: DTA/GS/TG/DTG thermal analysis of a xerogel (Ni content 75 mol %), heating rate 2K/min in synthetic air. Top TG/DTG, bottom DTA/GS.

The Gram Schmidt curve has an overall behavior similar to the DTA/ DTG curves and indicates that most of the species evolved in the temperature range are IR active.

A first broad and small endothermic peak is observed at temperature below 200 °C accompanied by a broad mass loss of about 10wt % with a maximum slope (DTG) located at 90 °C. This corresponds to the final drying of the xerogel as simultaneous MS (fig. 5.2) and IR spectroscopy (fig. 5.3), measured at 90 °C show essentially the evolution of H_2O (M/Z= 18, IR bands manifold around 1600 and 3700 cm^{-1}) with a small evolution of CO_2 (peaks at 650 and 2300 cm^{-1}) and alcohol (peaks at 1050 and 2900 cm^{-1}).

Then a small exothermic DTA shoulder accompanied by a mass loss of 10 wt % occurs at about 240 °C.

The main fragments evolved observed by MS are CO^+ (CO, CO_2), $C_2H_4^+$(C_2H_4) (M/Z= 28) and O_2^+ (O) (M/Z= 32) and by IR spectroscopy CO_2, alcohol and acetic acid (peaks at 600, 1000, 1200, 1400, 1800, 3000 and 3600 cm^{-1}). The main feature of the DTA curve is a

strong exothermic double peak between 300 and 360 °C with maximum at 344 and 357 °C. These features are accompanied by a large two peaks mass loss of about 35wt % with maximum at 340 and 352 °C i.e. at about the same position as the DTA peaks (fig. 5.1). A careful analysis of the infrared spectra of the gases evolved at these temperature (fig. 5.3) shows that the organic compounds, acetic acid (or fragments) are essentially found during the first DTA peak (maximum at 344 °C) but not during the sharp second DTA peak (max at 357 °C). This is a strong indication that the formation of inorganic nickel compounds involving primarily NiO_x and possibly $NiCO_3$ only occurs up to about 350 °C. The formation of $Ni(OH)_2$ is discarded as according to [202], this compound is already transformed into NiO_x at 250 °C. The last DTA peak, where mainly CO_2 and small amount of H_2O are evolved, may possibly be related to the transformation of $NiCO_3$ into NiO according to $NiCO_3 \rightarrow NiO + CO_2$ as suggested in [203].

The most intense mass spectra peaks (see fig. 5.2) i. e. those with M/Z = 28 ($C_2H_4^+$ (C_xH_y), CO^+ (CO, CO_2)), M/Z = 32 (O_2^+ (O_2), M/Z = 14 (CH_2^+ (C_xH_y), CO^{2+} (CO), CH_3^+ (C_xH_y)) and M/Z = 16 (O^+ (O_2, H_2O), CH_4^+ (CH_4), CH_3^+ (C_xH_y)), M/Z = 43 ($C_3H_7^+$ (C_xH_y)) show a similar behavior and each appears as a broad single peak with maximum at 344 °C but the evolution extends to higher temperature. Smaller but sharp double peaks are observed with M/Z = 44 (CO_2^+ (CO_2), $C_2H_5OH^+$ (C_2H_5OH), M/Z = 18 (H_2O^+ (H_2O) and M/Z = 12 (C^+ (CO, CO_2, C_xH_y) resembling the shape of the DTA and GS spectra.

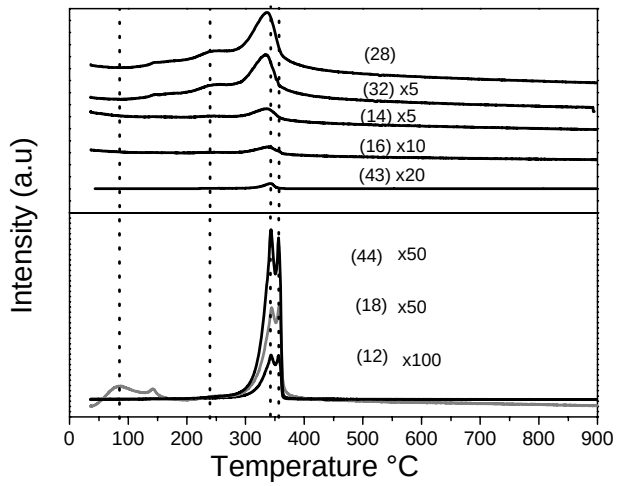

Fig. 5.2: Selected mass spectra measured simultaneously during the DTA/TG measurements of a NiO-TiO_2 xerogel (Ni content 75 mol %). Heating rate 2K/min in synthetic air. The numbers in parenthesis referred to the M/Z values. The dotted lines indicate the temperature at which the IR data shown in fig. 5.3 have been measured.

These results are in agreement with the evolution of the IR peaks (see fig. 5.3) and confirm that the last DTA peak is mainly related to the formation of oxides.

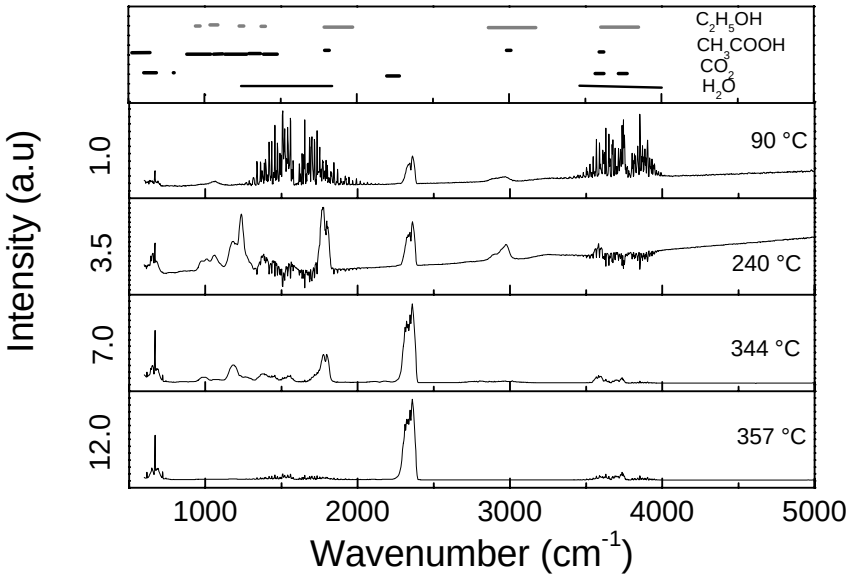

Fig. 5.3: Infrared spectra (IR) measured at 90, 240, 344 and 357 °C simultaneously with the DTA/TG measurements of a NiO-TiO_2 (Ni content 75 mol %) xerogel, heating rate 2K/min in synthetic air. The numbers written on the ordinates represent the height of each block. The position of IR reference peaks of the main components evolved are shown in the top figure [http://webbook.nist.gov/chemistry/].

TG analysis of NiO based sol-gel materials has been only reported with xerogels produced using nickel acetate as precursor where weight losses without indication of the evolved gases were found at about 80 °C and between 260 and 300 °C [80] and with xerogels made from $NiSO_4$ peptized in acetic acid which showed that the mass loss occurred mostly at about 350 °C with the release of H_2O, CO_2 and organic fragments such as CH_3^+, CH_3CO^+[81]. Recently Jesus et al. [203] have studied in detail the thermal decomposition of pure nickel acetate tetra hydrate. The weight loss measured in air at a rate of 30 °C/min using TG and MS was found to occur in two steps: a first peak at 120 °C, which the authors identified as the evolution of H_2O and acetic acid (CH_3COOH), followed by a second single broad peak at 350 °C with evolution of CO_2, acetone (CH_3COCH_3), acetic acid (CH_3COOH), ketone (CH_2CO) and formic acid (HCOOH) for which the authors suggested a decomposition of the acetate group of a basic compound having the

composition $0.56Ni(CH_3COO)_2 \cdot 0.14Ni(OH)_2$ produced during the dehydration of the salt at 120 °C and leading to the formation of NiO and Ni. Ti(Si) xerogel produced from $NiSO_4.7H_2O$ peptized by acetic acid also showed a mass loss between 300 and 380 °C with evolution of CO_2 and H_2O. However the whole process was somewhat blurred out due to the cross linking effect of the added silane [93].

5.2 Structural properties

a) Thickness and coating appearance

The thickness of single layers made by dip coating process was adjusted by varying the dip-coating withdrawal speed. For layers made with a Ni concentration of 75 mol % and sintered at 300°C, a range of thickness between 20 to 100 nm was achieved by varying the withdrawal speed between 0.5 and 4 mm/s respectively. Thicker coating up to 240 nm have been achieved by processing multilayers.

SEM pictures of the coatings made with different Ni molar concentration indicate that all layers are homogeneous without pits or cracks (figure 5.4). All coatings showed a slight greenish color.

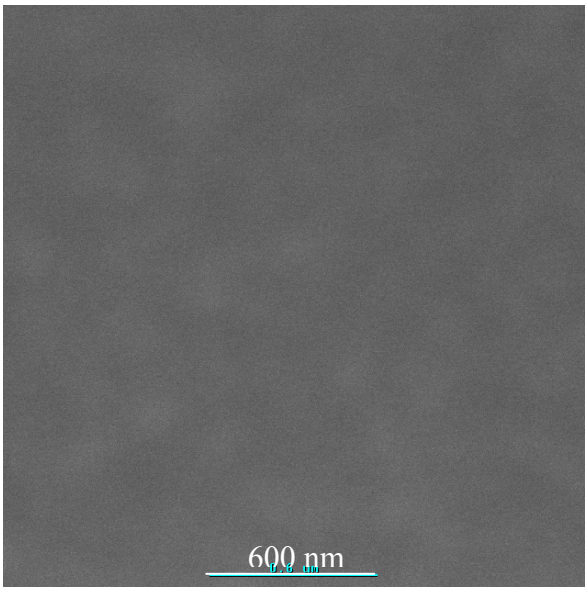

Fig. 5.4: SEM picture for NiO-TiO_2 layers (Ni concentration of 75 mol %) deposited on K-glass and sintered at 300 °C. The accelerating potential was 10 keV, resolution of 1024x1024.

b) X-ray diffraction and TEM of fresh (uncycled) layers

X-ray diffraction spectra of NiO-TiO_2 layers (Ni concentration of 75 mol %) sintered in air at 250, 300, 400 and 500 °C for 30 min are shown in fig.5.5. The layers sintered at 250 °C are amorphous and those heat treated at higher temperature exhibit the five peaks of the Bunsenite cubic nickel oxide structure. The crystallinity of the layers increases with the sintering temperature and the crystallite size calculated with the (200) peak are 2.5, 4.7 and 8 nm respectively. A slight (200) preferential orientation is observed. No evidence of a $Ni(OH)_2$, NiOOH and TiO_2 crystalline phase is found so that if these compounds exist they are X-ray amorphous.

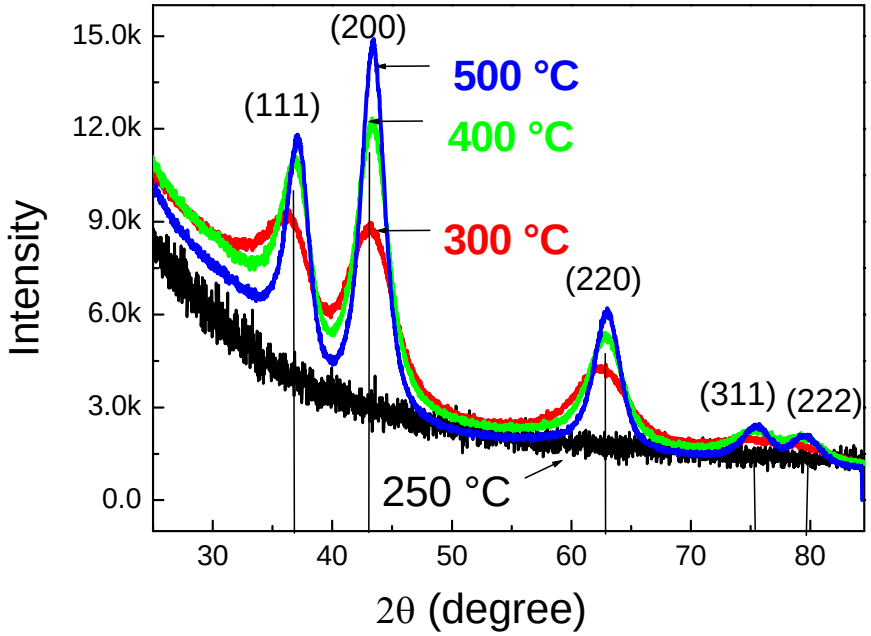

Fig. 5.5: XRD patterns for NiO-TiO_2 layers (Ni concentration of 75 mol %) deposited on float glass and annealed in air at different temperatures. The vertical lines refer to the Bunsenite nickel oxide phase (PDF-No. 71-1179).

The TEM picture (Fig. 5.6a) of a fresh (uncycled) rasped thin layer shows the presence of many very small round crystalline grains with size of about 8 nm, i.e. about 3 times that of the crystallites, impeded in an amorphous structure.

a

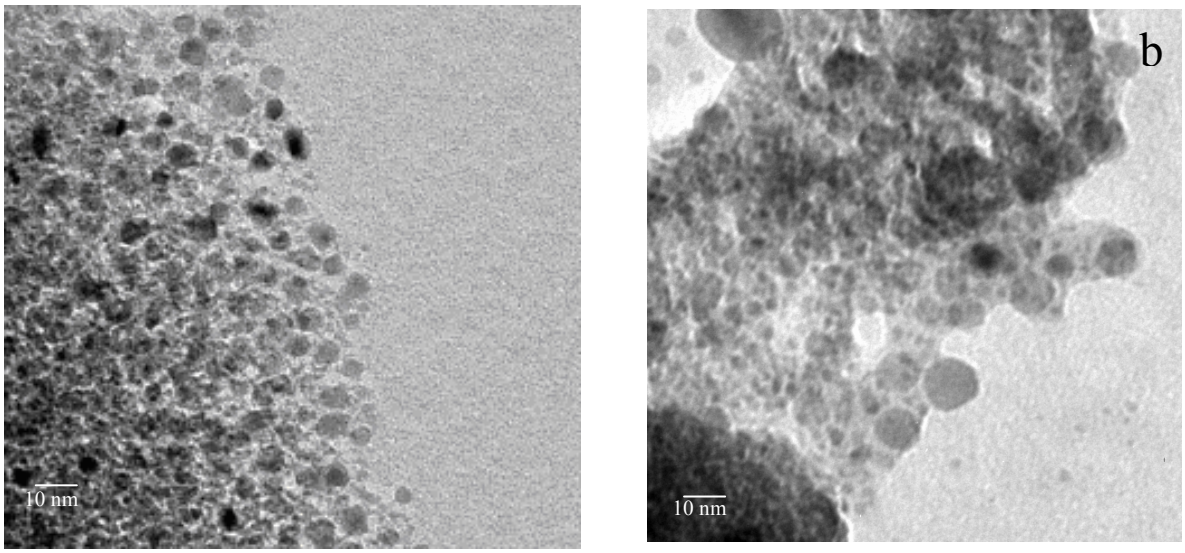

Fig. 5.6: TEM pictures of NiO-TiO_2 rasped layers (Ni concentration of 75 mol %) deposited on K-glass and sintered at 300 °C (a) fresh uncolored layer (b) colored layers after 250 cycles

XRD measurements of layers with Ni concentration between 33 and 90 % and sintered at 400 °C are shown in fig. 5.7. The degree of crystallization increases with the nickel content and the crystallite size calculated with the (111) peak are 3.6, 4.5, 5 and 6 nm for Ni concentration of 33, 66, 87 and 90 mol % respectively. The presence of TiO_2 decreases the growth of the NiO crystallites. The crystallite size is smaller than that published for pure NiO films prepared by sputtering, 20 to 300 nm [110] and sol-gel, 8 to 150 nm [82, 88]. The width of the peaks is too large to ascertain the formation of a solid solution of Ti^{4+} ions into NiO as claimed recently by Wu et al. [204].

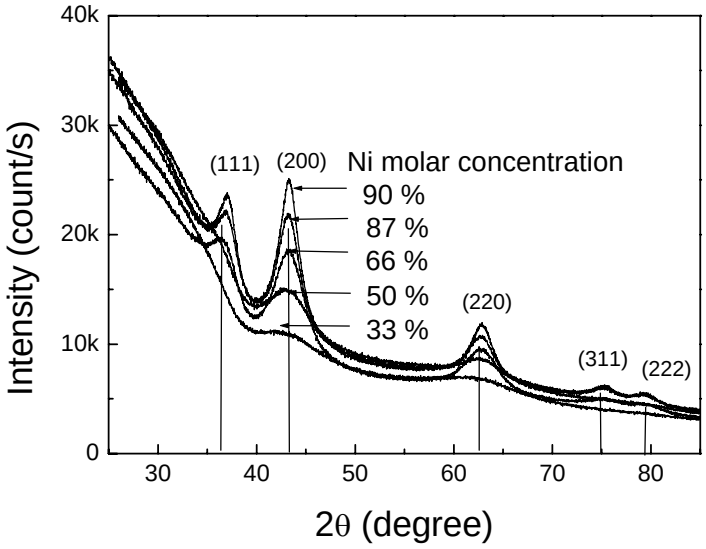

Fig. 5.7: XRD pattern for NiO-TiO_2 layers of different Ni molar concentration deposited on float glass and sintered at 400 ^{0}C. The vertical lines refer to the Bunsenite nickel oxide phase (PDF-No. 71-1179).

c) X-ray diffraction and TEM of cycled layers

As shown later in section 5.3, NiO-TiO_2 layers can be deeply brown colored electrochemically. Near grazing incidence (0.3 °) of triple layers (240 nm thick) sintered at 300 °C and cycled in KOH during 270 cycles exhibited the same Bunsenite NiO cubic structure (fig. 5.8). The presence of new peaks containing hydrogen (e.g. $Ni(OH)_2$, NiOOH) was not found in any film. The only differences that are observed is a reduction of the intensity of the Bunsenite peaks, an indication of a process of progressive amorphization during cycling, and two broad bands in the bleached layer at around 12 ° and 22.5 ° that cannot be attributed to any compounds. The results appear at first sight rather surprising but do not preclude that $Ni(OH)_2$ or NiOOH are present in the cycled layers as these compounds can be located on the outermost part of the very small NiO grains (see fig. 5.6a) and too thin to be detected.

Fig. 5.6b shows a TEM picture of a thin rasped layer in the colored state after 270 CV cycles and rather large morphology changes are observed. Although some larger grains (size 10 to 13 nm) are observed, the layer now consists of many smaller particles with size of about 3 nm i.e. the size of the NiO crystallites (2.5 nm), several of them aggregated in a filament shape. This clearly shows that the fresh NiO grains have been disaggregated into their primary crystallites during cycling. This confirms that the colored layers have a more

amorphous structure consisting essentially of very small NiO crystallites (see fig. 5.8) linked probably with hydrogenated compounds that cannot be measured by XRD.

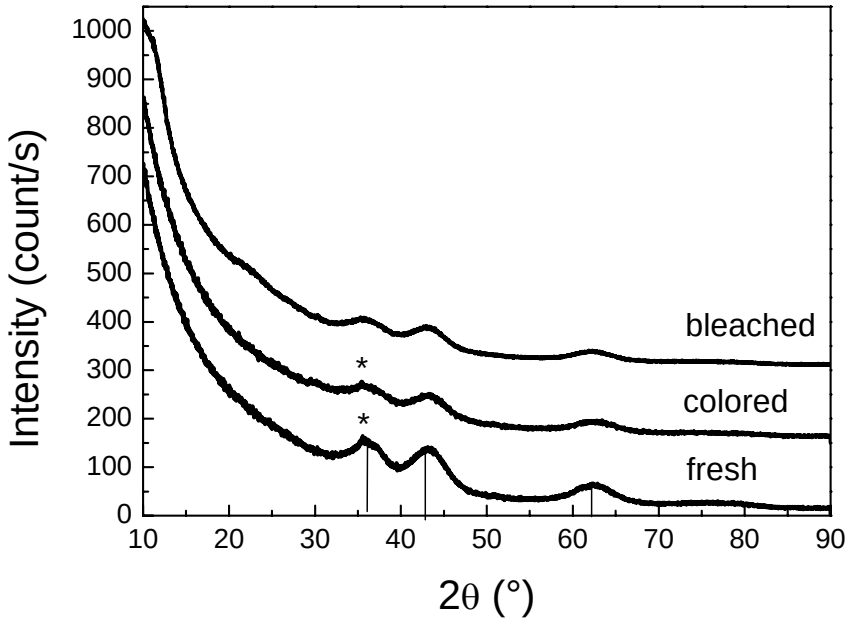

Fig. 5.8 Typical XRD pattern of triple NiO-TiO_2 layers (Ni molar concentration 75 mol % sintered at 300 °C) in the as deposited (not cycled), colored and bleached (after 270 CV cycles) states deposited on ITO coated glass. The solid lines refer to the Bunsenite peaks and the * to the main ITO peak (PDF-No.71-1179). The spectra have been displaced vertically for better visualization.

5.3 Optoelectrochemical characterization

5.3.1.Potential range –0.6 to +0.6V vs. SCE

Fig. 5.9 presents typical cyclic voltammograms measured in 1 M KOH during the 2^{nd}, 100^{th}, 400^{th}, and 1000^{th} cycles for a NiO-TiO_2 double layer (Ni content of 75 mol %) sintered at 300 °C. The potential was cycled between –0.6 and +0.6 V vs. SCE at a scan rate of 10 mV/s. These potentials were chosen to avoid any side reactions such as oxygen or hydrogen evolutions (see also 5.3.2). The change of the transmittance measured at 550 nm during the 100^{th} cycle is also shown.

No electrochemical or optical activity are observed in the anodic potential range –0.6 to -0.1 V. Two distinct peaks associated with the coloration of the layer are observed: the first is weak and occurs around 0.25 V while the other peak at about 0.55 V is strong. They shift to higher potential with the number of cycles up to 300 cycles and then remain stable. A single intense cathodic peak associated with the layer bleaching is observed at about

0.15V. It shifts slightly to lower potential value with the number of cycles but remains also stable after 300 cycles. No electrochemical or optical activity is observed at potential smaller than –0.2 V. The observed shifts of the anodic and cathodic peaks are a clear evidence that the composition of the layer evolved continuously during cycling. The same effect was reported for layers prepared electrochemically [97] and was related to freshly precipitated electronic insulating $Ni(OH)_2$ material during each cycle.

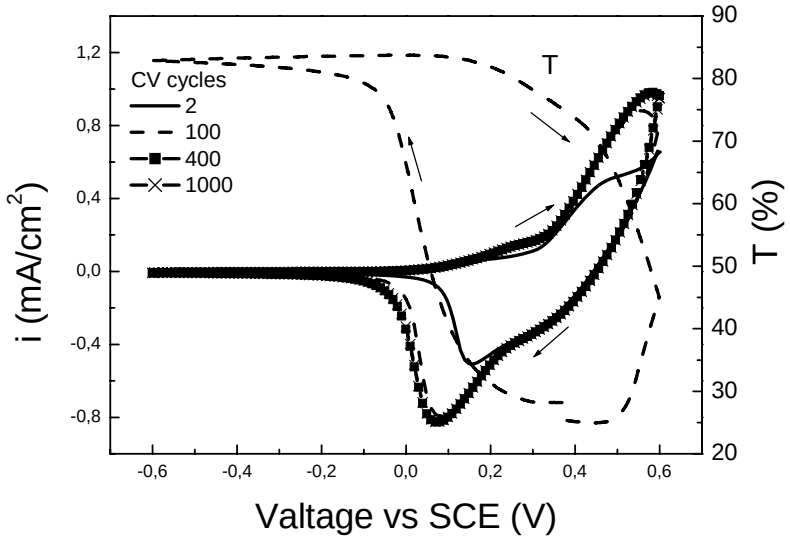

Fig. 5.9: Typical CV cycles up to 1000 cycles for a 160 nm thick double NiO-TiO_2 layer (Ni concentration of 75 mol %) heated at 300 °C, potential range -0.6 to 0.6 V vs. SCE, scan rate 10 mV/s in 1 M KOH. The dotted line is the variation of the transmittance (T) measured during the 100^{th} cycle at λ= 550 nm.

The fact that the coloration process occurs only in the anodic range and the bleaching in the cathodic range only and that both processes are linked to electrochemical processes (fig. 5.10) is particularly important. The change in the optical density (coloring state) that varies linearly with the anodic charge is therefore due to an exchange of negatively charged molecule(s) as discussed later in more detail in section 5.4.

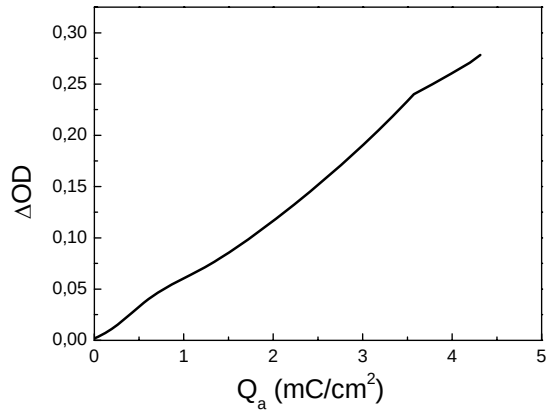

Fig. 5.10: Change in optical density with the anodic charge capacity during the anodic scan of the 100th CV cycle (-0.6, 0.6 V/ 10 mV/s) for layer in fig. 5.9.

The intensity of the cathodic and anodic peaks increases up to about 300 cycles indicating that the amount of coloring sites available for the redox reaction increases, then remains practically constant up to 1100 cycles and finally starts to decrease (not shown). Such a decrease was also observed for pure sputtered NiO by Avendano [21]. who attributed this behavior to the transformation of NiO into $Ni(OH)_2$ while Serebrennikova et al. [79] attributed it to an increased accessibility of Ni(II) sites due to an increased wetting of the layer by the electrolyte. However contrary to our observation (stable current density up to 1100 cycles), pure NiO coatings showed a faster decrease of the electrochemical waves attributed to a degradation of the layer [97].

The charge capacity Q_c has been calculated by integrating the cathodic waves in order to avoid any charge contribution of the oxygen evolution at positive potential. The value, the number of cycles needed for charge stabilization and the stability of the layer are affected by the parameters of the layer processing (sintering temperature, number of layers, humidity, the scan rate) but especially by the thickness of the coating. An example is shown in fig. 5.11 for a single layer 80 nm thick and a double layer 160 nm thick both sintered at 300 °C. In both cases the cycling life is based essentially on two step processes consisting of an *activation period* and a complex *degradation period*.
In the first domain the charge density is rather low after the first cycle (5 to 8 mC/cm^2) and increases rapidly to reach a broad maximum after 350 cycles for the thin layer and 1000 cycles for the thick layer. The maximum value is higher for the thick layer (20.5 mC/cm^2) than that of the thin layer (13.6 mC/cm^2) but does not scale with the thickness. Some tested double layers however presented even a rather large plateau between the two periods.

In the degradation period the charge density decreases continuously at a slow rate in a complex way. For the double layers system even an abrupt decrease occurs around the 4500th cycles and the charge becomes then very small. Such a behavior was not observed for any of the tested single layers.

The fact that both layers show an increase of the charge density during the activation period is compatible with the idea that the EC process occurs initially only in a very thin layer at the interface electrolyte/coating which grows during the activation period to reach eventually the full thickness of the layer when the maximum of Q_c is reached. It is therefore understandable that the maximum and the decrease of Q_c appear earlier for the thin layers than for the thick ones. The ratio of the maximum charge density, 1.5, is smaller than the ratio of the thickness, 2. This is an indication that the degradation period probably initiates already in the last stage of the activation period.

The behavior of the optical properties, as also discussed in detail later, is rather complex. The change in optical density vs. cycle number follows more or less the same behavior, i.e. an increase during the activation period and a decrease during the degradation period

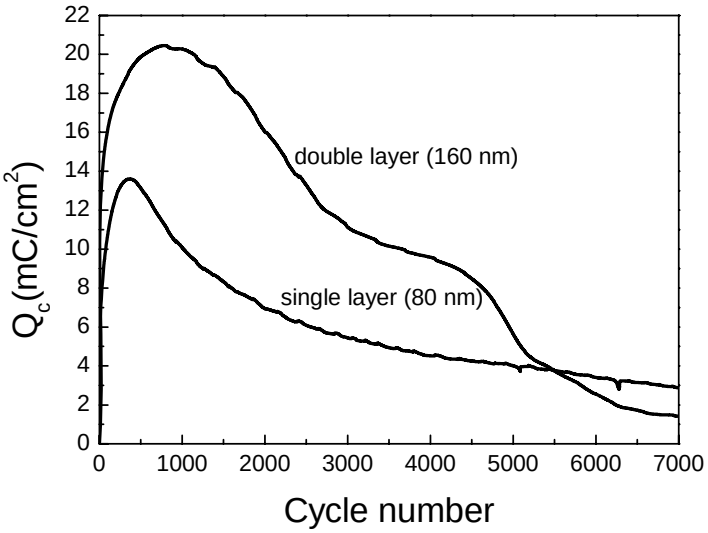

Fig. 5.11: Cathodic charge density vs. cycle number for a single (80 nm) and a double (160 nm) NiO-TiO_2 layer (Ni concentration of 75 mol %) heated at 300 °C calculated from the CVs cycles (-0.6, 0.6 V vs. SCE), scan rate 10 mV/s in 1 M KOH.

Pure NiO layers prepared by sol-gel [79], electrochemically [97] and PLD [124] showed a similar behavior with however a more rapid decrease of the charge capacity within 400 cycles only that has been attributed to a degradation of the film during cycling in the electrolyte involving the transformation of electrochemically active sites into inactive ones

with a simultaneous dissolution of the film. However stable charge capacity up to $2x10^4$ cycles has been reported for rf [102] and dc magnetron sputtered hydrated $Ni(OH)_2$ layers [190].

5.3.2 Potential range –0.6 to +1 V vs. SCE

The potentiodynamic range of CV cycles is also a very important factor affecting the charge capacity and hence the electrochromic properties of the layers. Its role was investigated for a 160 nm thick double NiO-TiO_2 layer (Ni content of 75 mol %) sintered at 300 °C by increasing step by step the positive potential from +0.6 to +1 V leaving the lowest cathodic potential constant at -0.6 V. Fig. 5.12 shows that ΔOD measured at 550 nm and the charge capacity Q_c are practically linearly related and that both values increase with the positive potential. For +1 V, ΔOD reaches a value as high as 0.8 and the coating shows a very dark brown color.

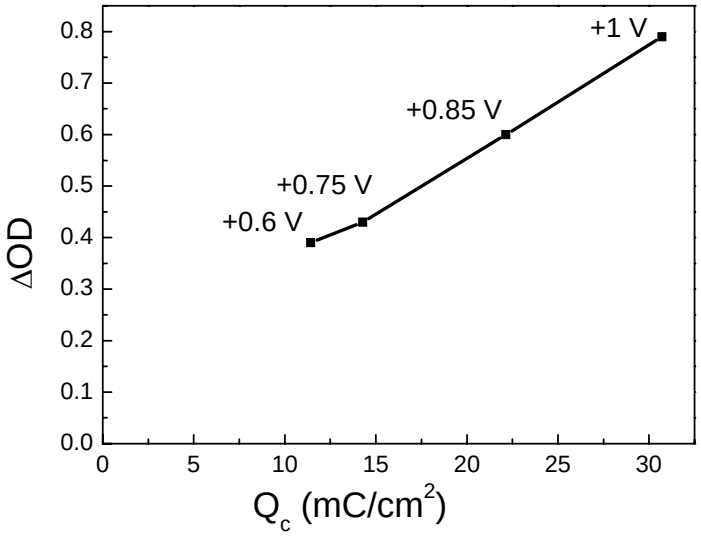

Fig. 5.12: Change of the optical density, ΔOD at 550 nm versus cathodic charge density for a 160 nm thick NiO-TiO_2 double layer heated at 300 °C obtained around the 50^{th} CV cycle in KOH. The potential scans have been done between –0.6 V and anodic potentials ranging from +0.6 to +1 V at a rate of 10 mV/s.

The main change of the transmittance spectrum takes place in the UV and visible range with a rather weak coloration in the IR range (fig. 5.13). The shape of the absorbance spectrum (ΔOD) is rather smooth without pronounced peaks. It is interesting to note that the coloration efficiency (CE) corresponding to this coloration change and calculated as

$\Delta OD/Q_c$ with $Q_c = 20.5$ mC/cm^2 is rather high. This is certainly related to the smallness of the NiO grains that have a quite high surface area where the redox reactions and consequently the coloration are occurring. This is an important result for applications.

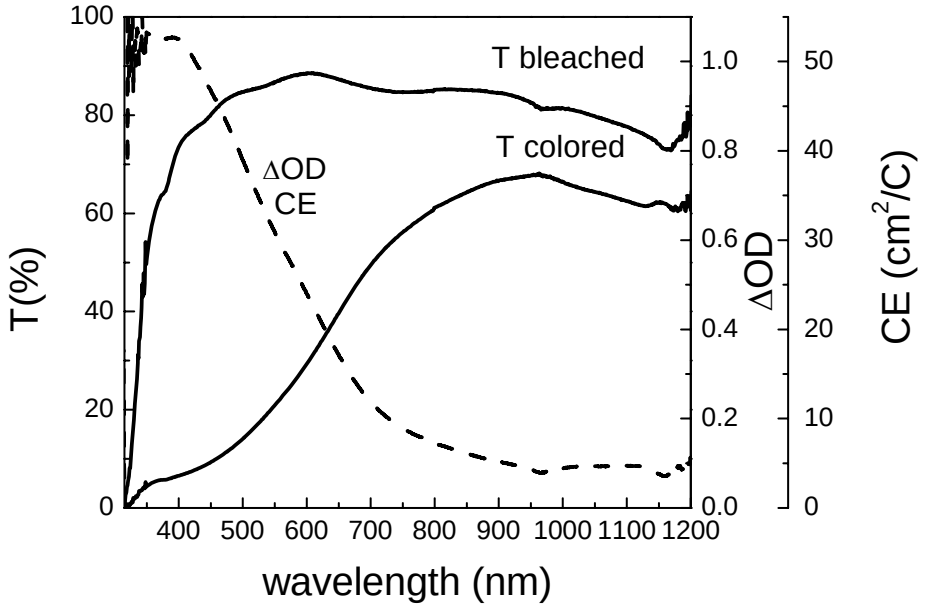

Fig. 5.13: Optical transmittance spectra of a 160 nm thick NiO_2-TiO_2 double layer heated at 300 °C measured in the colored and bleached states after the 50th CV cycle. The layer was bleached and colored by polarizing it for 20 s at –0.6 V and +1 V respectively. ΔOD and the coloration efficiency are also shown.

A typical transmittance variation of an 80 nm thick layer measured at 550 nm during the 20th CV cycle i.e. during the early part of the activation period (-0.6, +1V vs. SCE, scan rate 10 mV/s), and the corresponding CV voltammogram are shown in fig. 5.14a. The anodic and cathodic peaks are similar to those shown in fig. 5.9 except that a strong increase in the current density is observed for V > 0.6 V. As shown in fig. 5.14b, a simultaneous mass spectrum recording of the atmospheres in the EC cell indicates that this behavior is due to an oxygen evolution (also visually observed as small bubbles) originating from the decomposition of the electrolyte according to the reaction:
$4OH^- \rightarrow 2H_2O + O_2$ (g) + $4e^-$. No other gases have been detected. As before no electrochemical or optical activities are observed for potential smaller than -0.1 V. The decrease in the transmittance starts in the anodic range at +0.1V i.e. exactly at the end of the increase of the anodic current, reaching a minimum at +1 V with a maximum slope

between 0.45 and 0.7 V. The small decrease of the transmittance observed in the high potential range (V> 0.6 V) is not related to the oxygen evolution but is due to the continuation of the electrochemical peak started at V = 0.1 V.

Bleaching starts in the cathodic scan at V= 0.4 V reaching again the initial transparent state at –0.4 V with a maximum slope between +0.2 and 0 V. It is also linked to a variation of the current involving the exchange of negatively charged molecule(s).

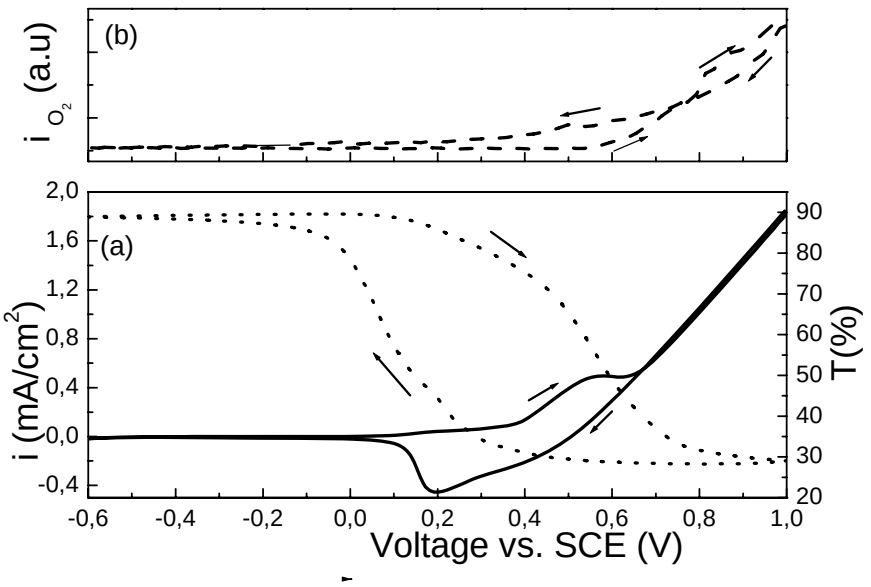

Fig. 5.14: 20th CV cycle (-0.6, +1 V vs. SCE) of a 160 nm thick double NiO-TiO_2 layer (Ni content 75 mol %), scan rate 10 mV/s in 1M KOH (—) and transmittance change measured at λ= 550 nm (….) (b) mass intensity of the gas (O_2) evolved inside the EC cell during the CV cycle.

The overall behavior of the cathodic charge Q_c versus cycle number is similar to that shown in fig. 5.11 except that the values of Q_c are higher, the position of the maxima occurs after a smaller number of cycles and the rate of the degradation period is faster.

The response time of the layer (charge and optical transmittance) is fast and in the range of a few seconds. Fig. 5.15 shows the typical evolution of the charge and transmittance change of an 80 nm thick layer with Ni content of 75 mol % sintered at 300 °C during the 5th chronoamperometry (CA) cycle (-0.6, +0.6 V vs. SCE /20 s).

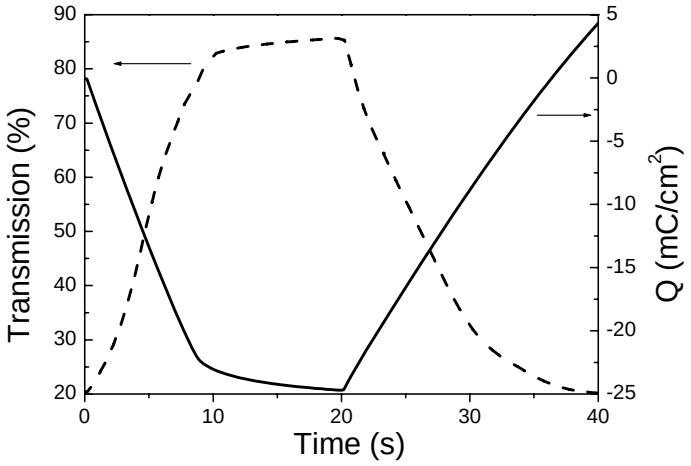

Fig. 5.15: Charge density and transmittance change measured at 550 nm for a 80 nm thick single NiO-TiO_2 layer (Ni content of 75 mol %) in KOH during the 50th CA cycle (-0.6,0.6 V vs. SCE/ 20s).

5.3.3 Effect of Ni molar concentration

The electrochromic activity of sol-gel layers sintered at 300 °C made with Ni molar concentration varying between 33 % to 100 % has been tested in 1 M KOH. Fig. 5.16a shows the voltammograms of NiO-TiO_2 layers with different Ni molar concentration. The voltammograms have basically the same shape but the maximum of the current density decreases with the increase of Ti content and its position shifts to lower potential while that of the maximum of the cathodic current densities also decrease but shifts to higher positive potentials. The cathodic charge capacity decreases by increasing the Ti content (fig. 5.16b).

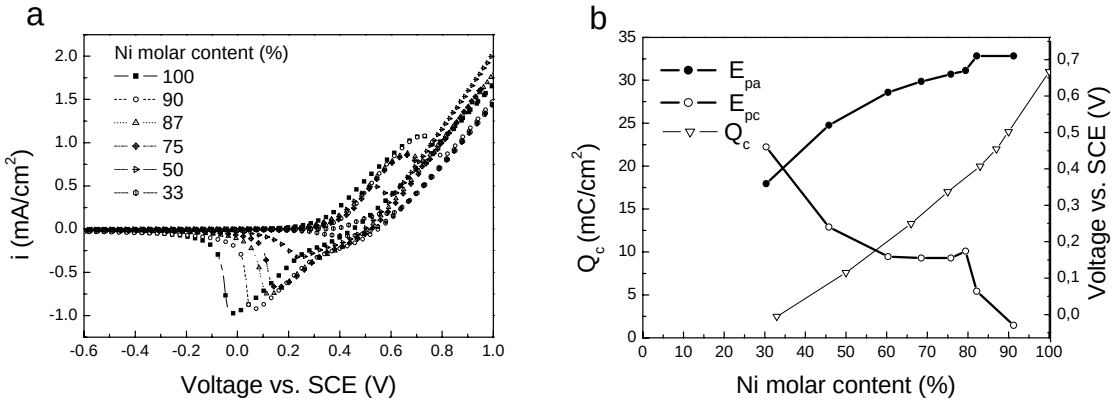

Fig. 5.16: (a) 50th CV Voltammogram (-0.6 to +0.6Vvs. SCE, scan rate 10 mV/s) in 1M KOH of 80 nm thick NiO-TiO_2 single layers with different Ni molar concentration and heat treated at 300 °C, (b) corresponding cathodic charge density, anodic and cathodic peak positions.

The transmittance change up to 700 CV cycles measured at 550 nm for two typical compositions is shown in fig. 5.17, a pure NiO and a NiO-TiO_2 with Ni content of 75 mol % both sintered at 300 °C and cycled between -0.6 and +0.75 V vs. SCE. For pure NiO the transmittance of the colored state decreases from 50 % to a minimum of 10 % in about 50 CV cycles and remains then constant while the transmittance of the bleached state remains practically constant (T = 85 %) during the first 50 cycles and then decreases sharply but continuously. The pure layer therefore starts to become permanently colored already after 50 cycles. On the contrary, for the NiO-TiO_2 layer, the transmittance in the bleached state decreases only slightly but continuously and that of the colored state decreases from 43 % down to a minimum of 14 %. The decrease of the transmittance in the colored state is compatible with the results shown in fig. 5.11 and corresponds to the increase of the charge density observed during the activation period.

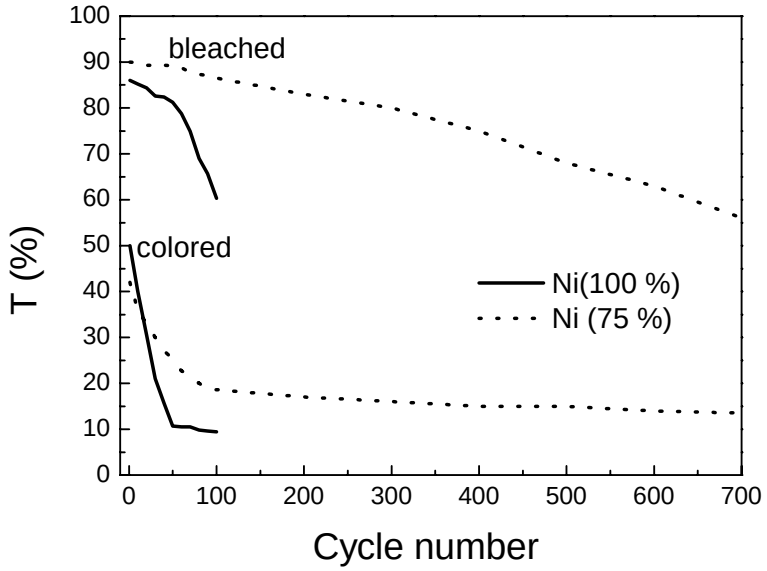

Fig. 5.17: Transmittance of the bleached and colored states measured at 550 nm during CV cycles (-0.6, +1V vs. SCE/ 10mV/s) in 1 M KOH of a 75 nm thick pure single NiO layer heat treated at 300 °C for 30 min(—) and a 80 nm thick NiO-TiO_2 layer (Ni content of 75 mol %) sintered at 300 °C (---).

Finally a summary of the results for NiO-TiO_2 layer with Ni molar concentrations varying between 33 to 100 % is shown in fig. 5.18. The permanent coloration in the bleached state is clearly depending on the Ni concentration and becomes quite high for values higher than 80 mol %. The transmittance of the colored state and consequently the values of ΔOD after 100 cycles are also strongly dependent on the NiO content.

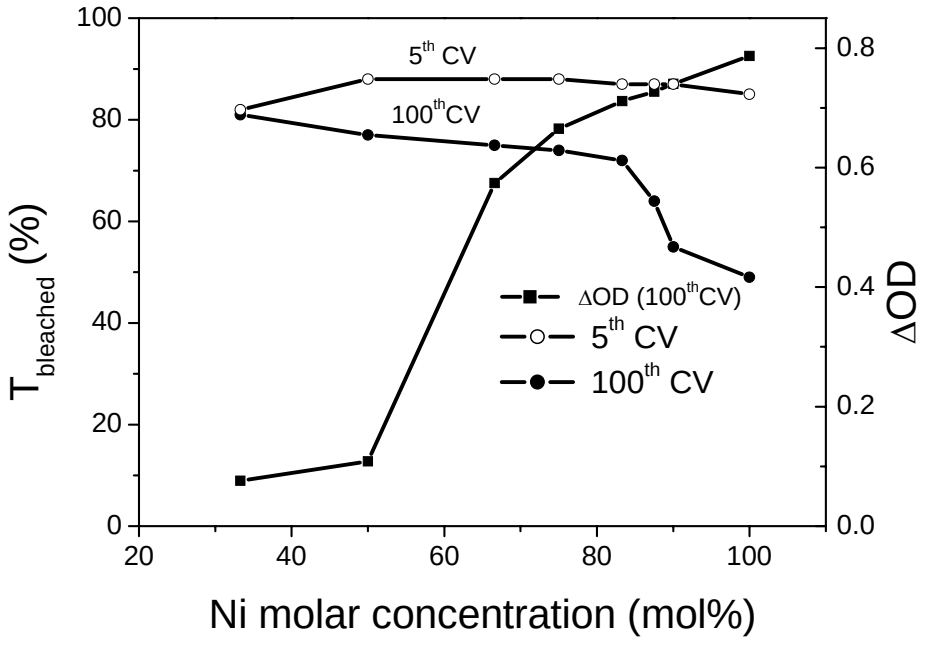

Fig. 5.18: Change of the transmittance of the bleached state and optical density measured at 550 nm for single NiO-TiO_2 layers with different Ni molar concentration and sintered at 300 ^{0}C for 30 min.

Comparing the values of $T_{bleached}$, $T_{colored}$ and ΔOD after 100 CV cycles, pure NiO layers are therefore not suitable for EC devices. Although they show the highest change in optical density (fig. 5.18) they lose very fast their transparency in the bleached state after cycling. They are also easily removed by rubbing with a finger and have therefore a poor adhesion to the substrate. Those with high Ti content are also not adequate as the electrochromic effect is poor. They are also very sensitive to humidity and tend to form a white $Ti(OH)_2$ layer on their surface. The layers with the best compromise are those having a Ni content around 75 to 80 mol %. In the activation period they remain practically transparent in the bleached state and present a rather high variation of the optical density, typically 0.65, i.e. 80 % of that of the pure NiO layer. Moreover, for this composition, a better adhesion to the substrate and a better stability are observed.

Martini et al. [188] also found that the change in optical density decreases by increasing the Ti content up to a ratio of Ni molar concentration of 54 % followed by an unexpected increase for higher Ti content. Such a behavior is not found here and the optical density always decreases by increasing the Ti content (fig. 5. 18).

5.3.4 Effect of heat treatment

Dip-coated layers (75 mol % Ni content) were heated for 30 min at different temperatures ranging from 250 to 500 °C and then cycled in 1M KOH electrolyte. Fig. 5.19a shows typical CV curves measured during the 50th CV (-0.6, +0.6 V vs. SCE, scan rate 10 mV/s). The overall behavior of the current density is similar but the large decrease of the maximum value and a shift of its position is observed especially for sintering temperatures T ≥ 350 °C. The change in optical density of the layers measured during the 1st and the 100th cycles (activation period) is shown in fig. 5.19b. The ΔOD values increase during the activation period for all sintering temperatures but reach a constant high value only for layers sintered up to 300 °C. The lower value obtained for the layers sintered at T ≥ 350 °C may possibly be due to the better dehydration of the layers and indicates that the water content and the hydration of the surface is an important factor to get a high electrochromic activity [84].

Although the layers heated at T< 300 °C showed a large change of the optical density, they gain a slight permanent coloration by cycling. On the contrary the layer sintered at 350 °C shows the same change in optical density but its transmittance change in the bleached state remains unaltered by cycling (T= 89 %) and is therefore the best compromise.

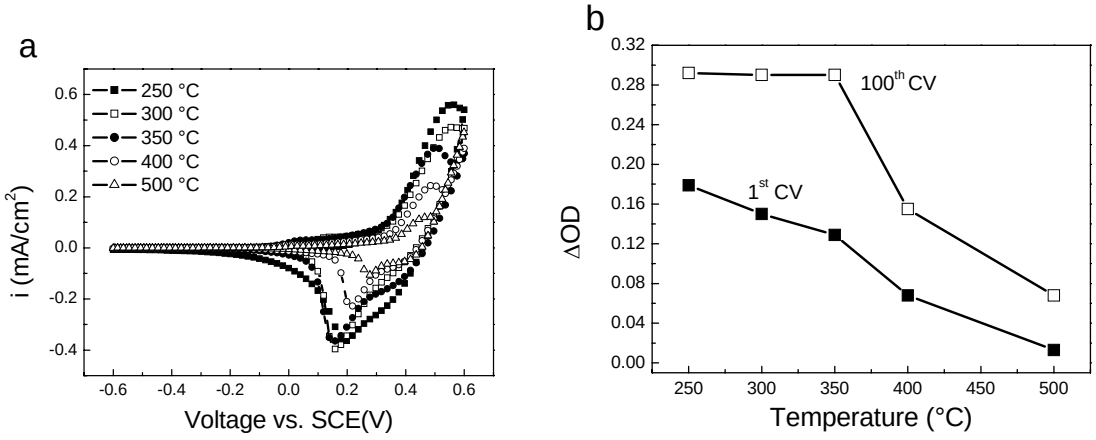

Fig. 5.19: 50th voltammogram (-0.6 to +0.6 V, scan rate 10mV/s) in 1M KOH of 80 nm thick NiO-TiO_2 single layers (Ni content 75 %) heat treated at different temperatures, (b) corresponding change of the optical density measured at the wavelength of 550 nm during the 1st and 100th CV cycles.

5.3.5 Effect of thickness

Single NiO-TiO_2 layers have been deposited on K-glass by dip coating at different withdrawal speeds ranging from 0.5 to 4 mm/s to get different thickness values. They have been sintered at 300 °C and tested in KOH as described before. Fig. 5.20a shows that the shape of the first CV cycle changes with the thickness of the layer. The current and consequently the charge increase up to about 55 nm and then remain constant. The transmittance change ΔT follows a similar behavior (fig. 5.20b). When measured during the 50th CV cycle i.e within the activation period the same overall behavior is observed but with higher values of the current, inserted charge and transmittance change (see also fig. 5.11) and a saturation effect is also observed for thickness values higher than 60 nm. This result is also a clear evidence that in the activation period the coloration of the layer is initially limited to a thin surface layer only that grows with cycling.

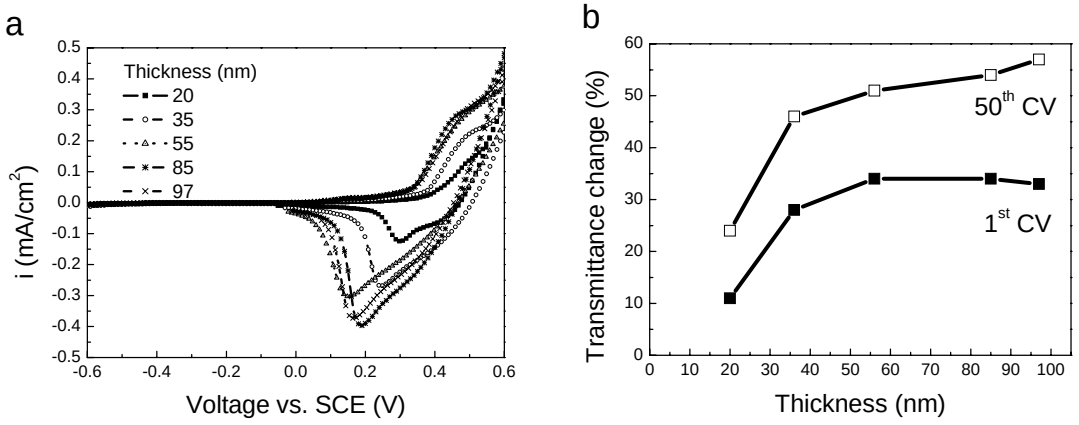

Fig. 5.20: 1st CV cycle (-0.6 to +1V vs. SCE/10 mV/s) in 1 M KOH for single NiO-TiO_2 layers sintered at 300 ^{0}C (b) transmittance change during the 1st and 50th CV cycles.

Another confirmation of this observation was obtained by performing the following experiment: an 80 nm thick single NiO-TiO_2 layer was colored during 50 cycles. The colored material was found to be easily removed with a cotton stick, leaving behind an intact transparent layer and the step left measured with a profilometer was 56 nm. Tests made during further cycling showed that the rest of the layer could be colored again. Similar tests made with layers cycled till reaching the end of the activation period (and of course also during the degradation period) show that now the whole thickness of the layer was easily removed by rubbing indicating that the coloring region had grown through the full thickness of the layer.

It is therefore proved that during the initial cycles of the activation period there is a thin layer where the EC process takes place. As shown in section 5.4 where Quartz Crystal Microbalance experiments performed during the two periods are reported, a gradual change of the composition of the surface layer occurs due to the incorporation of OH^- species with the transformation of NiO into $Ni(OH)_2$ as well as the reversible transformation of $Ni(OH)_2$ to NiOOH with dramatic evolution of the morphology of the layer (fig. 5.6) and the appearance of considerable tensile stress (already reported for rf sputtered NiO layer [38] that eventually leads to a gradual dissolution of this surface layer into the electrolyte.

5.3.6 Tests made in other OH^- based electrolytes (pH= 14)

Double NiO-TiO_2 layers, 160 nm thick, sintered at 300 °C have been tested in different electrolytes, namely 1 M KOH, 1 M $C_{16}H_{36}NOH$, 1 M LiOH and 1 M NaOH. The pH of all of them was 14. As shown in Fig. 5.21 the CV voltammograms have basically the same features. A strong anodic peak occurs near 0.7 V and a single cathodic peak near -0.05 V responsible for the layer coloration and bleaching respectively. A strong oxygen evolution peak is seen at potential higher than 0.8 V.

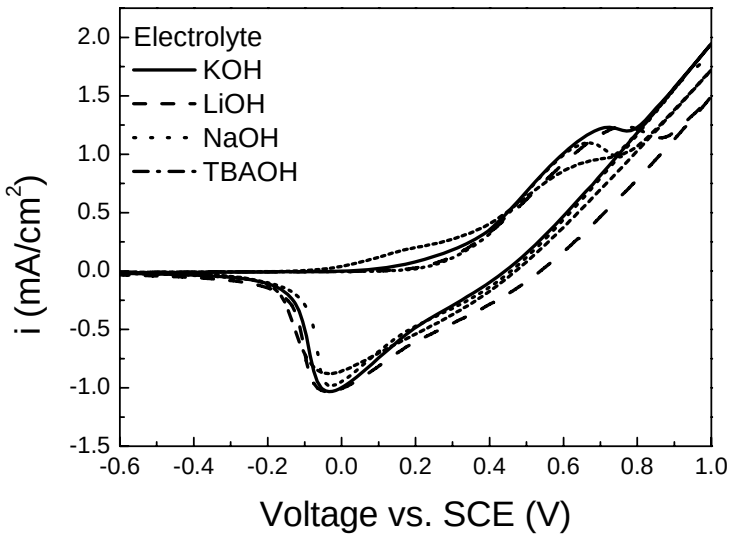

Fig. 5.21: 50th CV (-0.6 to +1 V vs. SCE) scan rate 10 mV/s for double NiO-TiO_2 layer (Ni concentration of 75 mol %, sintered at 300 °C), cycled in different electrolytes with pH of 14.

No shift in the peak positions is noticed and the current densities are almost the same in all electrolytes. The change in optical density for all the layers calculated at the 50th CV is also the same ΔOD= 0.65

As no changes are observed by changing the cations in the electrolytes (Li^+, K^+, Na^+ and $C_{16}H_{36}N^+$) it is concluded that these cations do not play an important role in the redox reaction of the NiO-TiO_2 layers and the process involves basically OH^-.

5.3.7 Effect of the pH value of the electrolyte

In order to check the effect of the pH value of the electrolyte on the electrochromism and oxidation-reduction potential of the NiO-TiO_2 layers, triple layers with Ni concentration of 75 %, sintered at 300 °C were tested in the three electrode cell filled with electrolyte with different pH values. 1 M aqueous KCl (pH=7) was used as a starting electrolyte. Then the pH value was adjusted to the studied acidic values (pH = 1 and 3) by adding very small amounts of concentrating HCl (37 wt %) so the K and Cl ions concentrations in the electrolyte are not affected. The basic pH values were adjusted to the values 9, 11 and 13 by adding small amounts of KOH crystals to 1M KCl electrolyte. The CVs were performed under the same condition for all the layers in the range –0.6 to 1 V vs. SCE at a scan rate of 10 mV/s. Kinetic transmittance measurements were performed simultaneously with CV cycling.

For pH values lower than 7, the stability of the layers is very poor (dissolution). Therefore in order to obtain the same results for the different pH values, only 2 CVs were recorded. The CV voltamogramm in the electrolyte with pH =1 shows one small anodic peak at 0.88 V. An increase in the current density is seen at the end of the anodic scan. Another very small anodic peak is seen near -0.4 V (see inset of fig. 5.22a) accompanied by a decrease in transmittance of the layer. A single cathodic peak appears around 0.96 V while another very small one is seen in the range of 0 V (see inset of fig. 5.22a). Strong tail appears at the end of the cathodic scan at the negative potential due to the hydrogen evolution. The CV profile in electrolyte with pH= 3 has almost the same features indicating that the electrochromic reaction of NiO-TiO_2 layer maybe the same in that range. The anodic and cathodic current peaks shift to higher and lower positive potential respectively. The current density is about three time higher for pH= 3.

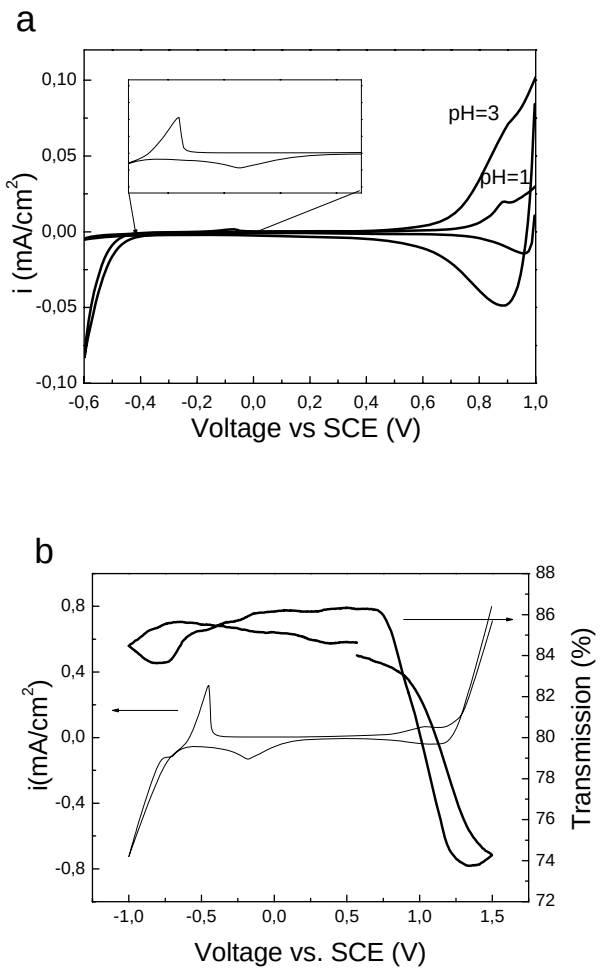

Fig. 5.22: 2nd CV voltammogram (-0.6, 1 V vs. SCE) for triple NiO-TiO_2 layer (Ni concentration of 75 mol %, sintered at 300 °C). (a) Cycled in electrolytes with PH values of 1 and 3 (inset magnification of the current density in the potential range from -.4 to 0 V vs. SC. in pH= 1). (b)**:** CV(-1,1.5V vs. SCE) scan rate 10 mV/s in electrolytes with pH of 1, together with the change in transmittance.

To check if the current density increase seen at the end of the anodic scan (fig 5.22a) when cycled in the electrolyte at pH= 1 corresponds to an electrochomic activity or not, the potential range of the CV cycle was extended to +1.5 V vs. SCE. It is observed during the successive cycles that the intensity of the peak observed at 0.88 V (fig. 5.22a) decreases and shifts to 1.2 V. It is followed by a strong increase of the current due to oxygen evolution that is not accompanied by a change in transmittance. The other two small anodic and cathodic peaks observed before (fig. 5.22a) become stronger in this potential range (fig. 5.22b).

In acidic electrolyte, the anodic peak is unstable and the colored layer loses spontaneously 83 % of its coloration at 0.6 V indicating that the oxidation product of Ni oxide layer (NiOOH) is not stable in that medium. The anodic and cathodic activities (electrochemical and optical) in electrolytes with pH ≤ 3 observed at potential higher than 0.5 V disappeared in few cycles and are replaced by process occurring at potential <0 V that does not involve OH^- species.

By increasing the pH value the CVs profile becomes different (fig. 5.23). A small anodic peak appears at V= 0.48 V for pH of 7 and shifts to lower potential values by increasing the pH value. A new peak appears in the range of V= 0.77 V in the CV of the layer cycled in electrolyte with pH =11 and becomes better defined at pH value of 14. By increasing the pH values the anodic current density peaks are shifted to lower positive potential values indicating that the reaction becomes thermodynamically favoured.

A sharp increase in the current density is seen at the end of the anodic scan for pH= 14 due to oxygen evolution. A single broad cathodic peak is seen for all pH and it becomes better defined and shifts to lower potential values by increasing the pH value.

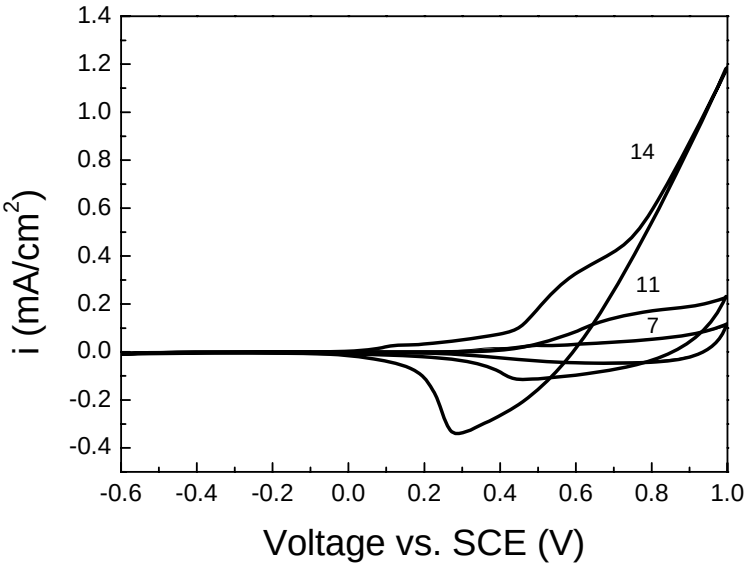

Fig. 5.23: 2nd CV voltammogram (-0.6 to +1 V vs. SCE) for triple NiO-TiO_2 layer (Ni concentration of 75 mol %, sintered at 300 °C), cycled in electrolytes with different pH values pH= 7, 11 and 14.

A summary of the anodic and cathodic peak positions is seen in table 1.

Table 1: Position of the anodic and cathodic peaks during CV (-0.6 to 1 V vs SCE) scan rate 10 mV/s for triple NiO-TiO_2 layer (Ni concentration of 75 mol %, sintered at 300 °C) cycled in electrolytes with different pH values.

pH	1	3	7	9	11	14
Vi_{pc}/ V (vs SCE	0.96	0.88	0.726	0.69	0.45	0.28
Vi_{pa}/ V(vs SCE)	0.87	0.82	0.488	0.355	0.2, 0.77	0.12, 0.59

The change in transmittance and consequently the change in optical density drastically increased by increasing the pH values of the electrolyte as seen in fig. 5.24. ΔOD changes slowly up to pH value of 9 and then increases faster.

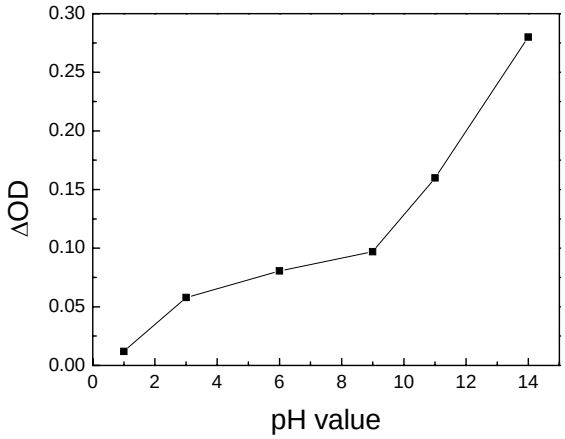

Fig. 24: Change in optical density during 2nd CV cycles for triple NiO-TiO_2 layer (Ni concentration of 75 mol %, sintered at 300 °) cycled in electrolytes with different pH values ranging from 1 to 14.

As the number of electrons involved in the electrochromic reaction is fixed (1 electron) then the increase in the anodic peak by increasing the pH value can be due to

1- an increase in the diffusion coefficient of the ions sharing in the reaction
2- an increase in the concentration of the ions

In preparing the electrolytes the K^+ and Cl^- ion concentration was kept almost constant (1 M KCl) so only the concentration of OH^-, H^+ ions was changed by changing the pH value. As the electrochromic reactions become more efficient in electrolytes with higher pH values then it is concluded that the OH^- ions are responsible for the reaction.

5.4 Coloration mechanism studied by EQCM

5.5.1 Introduction

The phenomenon of electrochromism in oxide electrodes is usually interpreted as an electron transfer reaction that accompanies the insertion of electroactive species, such as H^+, OH^- or Li^+, into the amorphous or crystalline structure of host materials, resulting in new absorption bands and an altered material coloration [205]. Understanding the mechanism of ion insertion in metal oxides during an electrochromic reaction is therefore central to clarify the optical performance but also the electrode failure. It is well known that the detailed insertion mechanisms are usually highly complex and may consist of several processes involving the diffusion of electrons and ions.

Electrochromic NiO-based coatings are among the least understood material and the electrochemical mechanisms that lead to electrochromism are still controversial. In general it is accepted that the coloration is due to the oxidation of Ni(II) into Ni(III) involving the transformation of β-$Ni(OH)_2$ into NiOOH. It is also well known that there is more than one $Ni(OH)_2$ phase. The most popular one is called β-$Ni(OH)_2$ and can intercalate water to form what is known as the α-$Ni(OH)_2$ phase. The corresponding oxidized forms are β-NiOOH and γ-NiOOH respectively. From the extended arguments found in the literature for explaining the electrochromism of nickel-based oxides (see chapter 3) it can be concluded that the mechanisms of coloration are strongly dependent on two main factors

(i) the composition and the phase of the starting nickel oxide layer, which in turn is strongly dependent on the layer deposition technique and experimental conditions

(ii) the kind of involved species during cycling. When a layer is tested in aqueous basic solution for instance the most probable ones are H^+, OH^- or both. As will be discussed in section 5.5 when an aprotic Li^+ electrolyte is used, then Li^+ will be the most probable species.

Attempts have already been made to clarify the EC mechanisms using a combination of different electrochemical and optical techniques [116, 190]. Among them, the electrochemical quartz crystal microbalance (EQCM) technique has been used to address the behavior of nickel-based oxides in alkaline solution in the field of battery [206, 207]. However, very few works have been reported aiming to understand the electrochromism of this material [78, 201]. This technique is based on a quartz crystal microbalance (QCM) that uses a piezoelectric crystal oscillating at a defined frequency and where small mass changes on the crystal surface are detected by the shift of this frequency.

Bernard et al.[206] studied the electrochemical kinetics of the ionic exchange process of *cathodically precipitated* $Ni(OH)_2$ in 5 M alkaline solution under a sinusoidal modulation and concluded that the electrochemical reaction involves both the incorporation of hydrated cations and a deprotonation according to the reaction

$$Ni(OH)_2 + y\ M(H_2O)_{x/y} \leftrightarrow M_y\ H_z\ (NiO_2)(H_2O)_x + (2\text{-}z)\ H^+ + (2\text{-}z\text{-}y)\ e^- \qquad (5.1)$$

The cations M can be Li^+, Na^+, K^+, Rb^+ or Cs^+.

Based on this reaction, Cordoba-Torresi et al. [201] found that the coloration reaction of *electrochemically deposited* $Ni(OH)_2$ in a lower concentration alkaline electrolyte (1 M KOH or LiOH) involves the incorporation of hydrated cations and that the number of coordinated H_2O molecules was depending on the kind of cations according to the reaction

$$Ni(OH)_2 + y\ M(H_2O)_{x/y} + (2\text{-}z)OH^- \leftrightarrow M_y\ H_z\ (NiO_2)(H_2O)_x + (2\text{-}z)\ H_2O + (2\text{-}z\text{-}y)\ e^- \qquad (5.2)$$

Bange et al. [78] studied the coloration mechanism of *e-beam evaporated* $Ni(OH)_x$ films in 1 M NaOH and 1 M NaOD in the potential range –0.5 to +0.6 V vs. SCE. They divided the coloration process (anodic range) into two main steps summarized by the following equations

$$E< 0.32\ V: \qquad Ni(OH)_2 - H^+ \leftrightarrow NiOOH + e^- \qquad (5.3)$$

$$E> 0.32\ V: \qquad Ni(OH)_2 + 1/3OH^- - 2/3H^+ \leftrightarrow NiOOH\cdot 1/3H_2O + e^- \qquad (5.4)$$

For E< 0.32 V only a hydrogen ejection occurs producing an electrochromic change in the optical properties and a very small decrease in mass. For potential E> 0.32 V this process is superimposed to an OH^- injection.

The goal of the present work, therefore, was to investigate the mass change of NiO-TiO_2 *sol-gel layers*, during cycling in KOH electrolyte using the EQCM technique in order to get a better understanding of the mechanism of coloration of such nickel oxide-based electrodes and hopefully to understand the role of the transformation of the different phases on the stability and the degradation of these electrodes.

For this purpose double NiO-TiO_2 layers were deposited on gold coated quartz crystal substrate by the dip coating technique. The substrate was withdrawn from the precursor solution at a rate of 3 mm/s in ambient atmosphere (RH<60 %). One side was covered to

avoid the deposition of the layer on both sides. The system was then sintered at 300°C for 30 min. in air.

All electrochemical parameters (i, Q) could be of course determined using this configuration. However the quartz crystal electrode being opaque, no determination of the transmittance change could be measured and one has to rely on the results described in fig. 5.9.

5.5.2 Envelope of the mass and charge change during 700 CV cycles

To estimate the mass of the layer, the frequency of gold coated quartz crystal was recorded before and after the layer deposition. From the frequency shift due to the layer deposition the mass of the deposited NiO-TiO_2 with Ni:Ti molar ratio of 3:1 was ***5.8 10^{-9}g/cm^2***.

Assuming a density of NiO of 6.67 g/cm^3 and that of TiO_2= 4.25 g/cm^3 the theoretical value of the mass of the layer will be m= {0.75(6.67) + 0.25(4.25)}160x10^{-7} i.e. m= ***9.66 10^{-9}g/cm^2***. This indicates that the layer has *a porosity* of 40 %.

According to the recommendation of the balance manufacturer, the coated crystals were left in the 1 M KOH electrolyte for four hours before starting the measurements. Then the mass changes were first recorded at the open circuit potential (-0.11 V) for 47min. The system was afterwards cycled by applying a potential in the range -0.4 to +0.57 V vs. SCE at a scan rate of 10 mV/s.

Fig. 5.25 shows the results of the mass change at the open circuit potential and during the first 5 CV cycles. The mass initially slightly increases linearly at a rate of about 7 ng/cm^2/min, a value much smaller than the variation observed during the cycles. This is thought to originate from a slow change in the composition of the layer due to a wetting process occurring at the interface. However electronic artifact cannot be excluded.

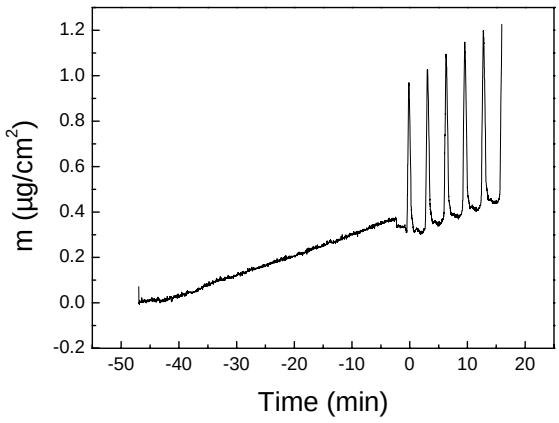

Fig. 5.25: Mass change at the open circuit potential (-0.11 V vs. SCE) during 47 min and then during the first 5 CV cycles.

Fig. 5.26 shows the recorded evolution, during 650 CV cycles, of the mass, of the instant charge and of the cathodic charge, integrated from the cathodic current. The values of the mass m and the instant charge Q have been reset to zero at the beginning of the cycling.

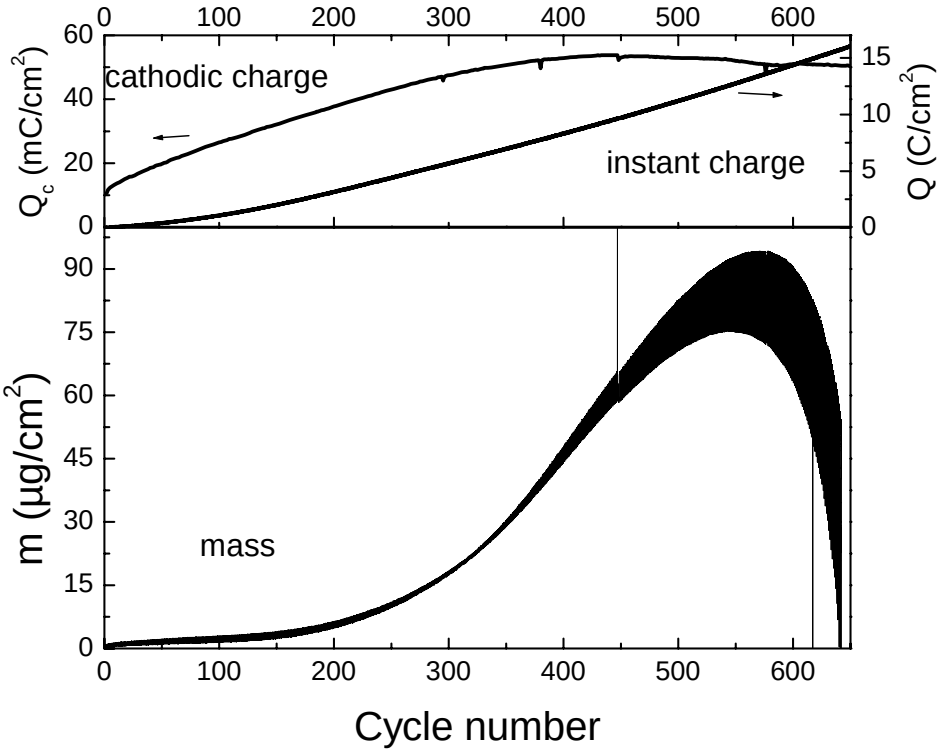

Fig. 5.26: Lower figure: Mass change during 650 CV cycles (-0.4 to +0.57 V vs. SCE, scan rate of 10 mV/s) for a NiO-TiO_2 double layer deposited on a quartz crystal, sintered at 300 °C, and tested in 1 M KOH. The value of the mass was set initially to zero at the beginning of the 1st cycle. Upper figure: cathodic and instant charge.

The variation of the cathodic charge (top figure) has to be compared with that of fig. 5.11 (double layer). The overall behavior is similar and certainly the results refer to what was called the *activation period*. It starts around the same value (9.2 m C/cm^2) then increases to a maximum value of 50 mC/cm^2 around the 450th cycle and finally decreases. The EC process of the layer deposited on gold coated quartz substrate, as discussed earlier, should also initiate in a small thin layer at the interface electrolyte/layer which grows during further cycling. However the maximum value of the cathodic charge is higher than that of fig. 5.11 and occurs after a smaller number of cycles. This is thought to be due to a more porous morphology of the layer ($P\approx$ 40 %) that has been sintered on a metallic electrode

instead of an FTO conducting oxide layer. The lower resistivity of the metallic electrode may also be responsible as the shape of the CV voltammogram is slightly different (fig. 5.27). In particular the O_2 evolution is clearly seen at a lower potential (+0.5 V instead of +0.57 V).

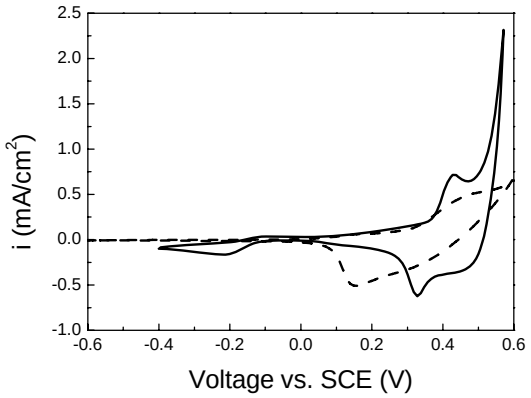

Fig. 5.27: CV voltammograms in 1 M KOH of NiO-TiO_2 double layer deposited on FTO (---) and gold coated quartz (—) with a withdrawal speed of 3 mm/s and sintered at 300 °C.

The spectrum of the recorded instant charge (fig. 5. 26) shows a continuous increase with cycling. If the system was only involving fully reversible intercalation/deintercalation processes the records should have been a straight horizontal line close to Q= 0. It is not the case and as discussed earlier (section 5.3.2 and above) part of the recorded charge is used for side reactions that do not involve a mass exchange and coloring/bleaching effect. This is the case e.g. of O_2 and H_2 evolution that occurs in the electrolyte. This also explains the change observed in the values of the current density.

The shape of the mass spectrum (fig. 5.26) is rather complex and changes continuously by cycling. The mass of the layer increases after each cycle rather slowly up to 1/3 of the *activation period* (i.e. up to about 150 cycles) and then starts to increase particularly strongly after the 250th cycle. It passes through a high maximum near the 570th cycle with high amplitude variation within each cycle to finally decreases fast even though the values of the cathodic charge decrease only slightly. Finally a complete breakdown occurs around the 650th CV cycle from which it was not possible to record any mass variation. This behavior was observed with all tested layers and seems to be due to an unknown technical problem.

Two features are particularly interesting:

The first one is clearly seen on the figure: the amplitude variation of the mass during each cycle (reflected by the width of the curve) is strongly dependent on the cycle number. It

slowly increases from the 1st cycle up to about the 150th cycle, remains almost stable up to 200th cycle and then decreases to practically zero around the 330th cycle. Then it strongly increases to reach values as high as 40 to 50 μg/cycle around the 600th cycle.

The second feature is observed by a closer look at these variations which shows that the kinetics of the mass change during each cycle is also continuously changing. As reported below the study was divided in several typical regions.

5.5.3 From the 1st to the 150th CV cycle

This period corresponds to about one third of the so-called *activation period*. Fig. 5.28a shows the mass and charge changes during the first 5 CV cycles. Although the measurements have been initiated at the open circuit potential (-0.11 V), for an easier discussion, the results are presented initiating at the most negative potential (-0.4 V) corresponding to the bleached state of the layer. The scan is performed in the direction of positive potential (+0.57 V), and then it is scanned back to the negative potential. The initial ordinate values for m and Q have been reset to zero. The lower figure shows the results recorded between the 145th and 150th CV cycle.

The overall behavior of the mass and the charge in each cycle is similar. They increase in the anodic range and decrease in the cathodic one so that the physical processes are basically the same up to 150 cycles. However one observes that:

a- the change of the mass is 0.65 μg/cm^2 during the first cycle and increases to a value of 1.6 μg/cm^2 during the 150th cycle (value then stable up to the 200th cycle)

b- the mass exchange is not fully reversible within each cycle so that the mass of the layer increases continuously and linearly during cycling at a rate of about 30.4 ng/cm^2/cycle. Taking into account the time required to perform the measurement (194 s/cycle) this value corresponds to 9.4 ng/cm^2/min i.e. a value quite close to that observed at the open circuit (7.0 ng/cm^2/min).

c- the peak height of the charge is 17 mC/cm^2 during the 1st cycle and increases to 2.042 C/cm^2 during the 150th cycle.

d- The charge is also not reversible and increases continuously but not linearly, initially at a rate of 6.7 mC/cm^2/cycle to reach a value of 20 mC/cm^2/cycle during the 150th cycle.

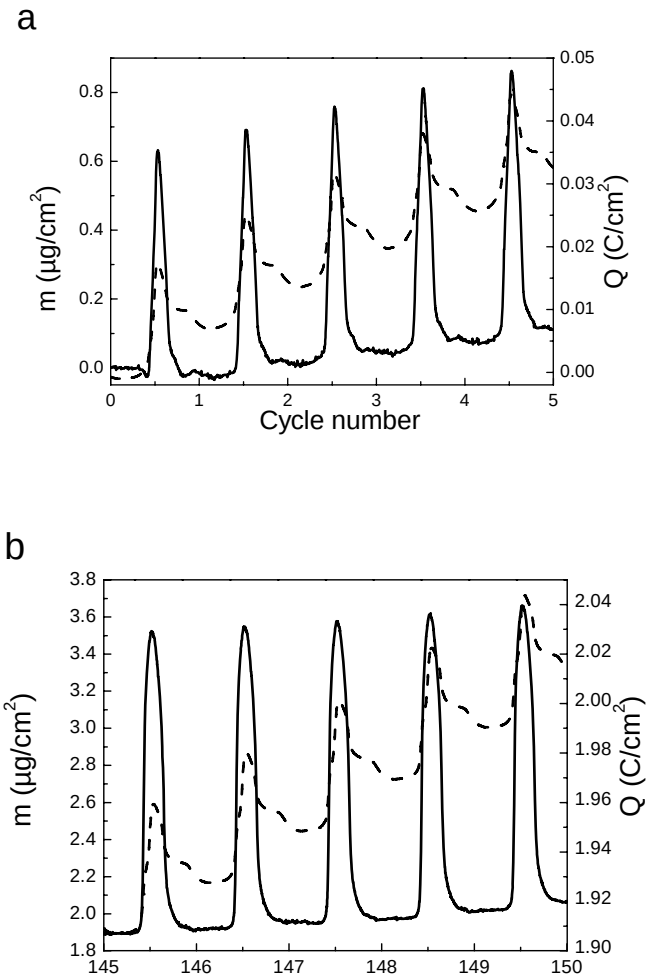

Fig. 5.28: Top: Mass (—) and charge (---) changes during the first 5 CV cycles (-0.4, +0.57 V, scan rate 10 mV/s) for a NiO-TiO_2 double layer deposited on quartz crystal substrate and tested in 1 M KOH. Lower: same for the 145th to 150th cycles. The origin of each abscissa corresponds to a potential value of –0.4 V vs. SCE

In order to better understand these observations the voltamassogram and voltammogram of the 2nd and 150th cycle are shown on an enlarged scale in fig. 5.29 and fig. 5.31 respectively.

a) 2nd cycle

The mass increases in the anodic scan and decreases in the cathodic one and the mass of the layer slightly increases at the end of the cycle by about 0.03 µg/cm^2. In the anodic scan no mass change and very little charge increase are observed in the potential range –0.4 to +0.35 V vs. SCE. The mass and charge start to increase at 0.35 V together with the current. A well defined anodic peak then occurs with a maximum at +0.43 V. It is correlated with

the layer coloration and at the peak maximum the transmittance has decreased by about 50 % (see fig. 5.9). The mass passes by a maximum before the end of the anodic range but the charge, as it should be, passes by a maximum at the end of the anodic scan when I= 0. A large current density peak related to the O_2 evolution is superimposed at the end of the anodic scan.

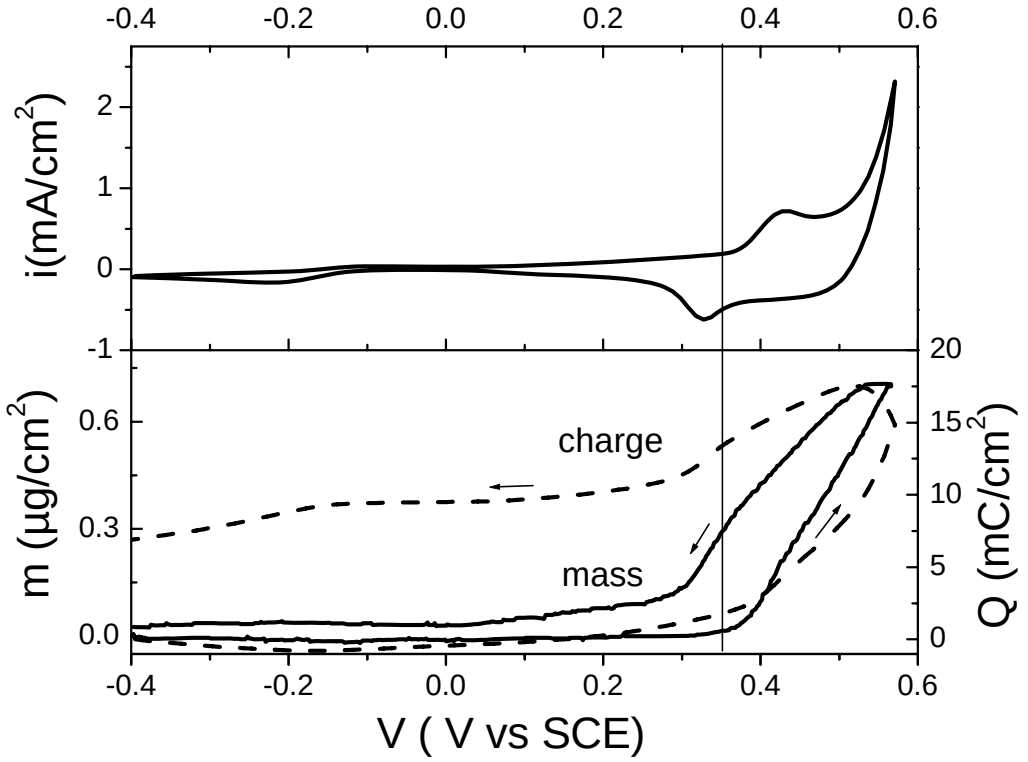

Fig. 5.29: Voltammogram and voltmassogram of NiO-TiO_2 double layer deposited on gold coated quartz crystal recorded during the second CV cycle (-0.4 to +0.57 V, scan rate 10 mV/s).

In the cathodic region, a minimum of the current density is observed at around 0.32 V corresponding to the layer bleaching as well as a very low intensity broad cathodic peak around –0.22 V. The first peak is accompanied by a decrease of the mass and the charge and the second one by a decrease of the charge and a very slight increase of the mass. The total charge does not return to the initial value ($Q-Q_0$= 6.7 mC/cm^2) and this value corresponds probably to the charge used during the oxygen evolution. The mass almost returns to its initial value so that the total mass of the layer only increases by about 0.03 µg/cm^2. It is worth to mention at this point that this second CV voltammogram,

except for the features observed around –0.22 V, presents the same features of that measured for a similar layer deposited on a K-glass substrate (see fig. 5.27).

Another representation is helpful for the discussion of the results. Fig. 5.30 shows a plot of the mass against the charge for the first three cycles. Considering again the second cycle, one clearly sees, starting at –0.4 V vs. SCE, a small slight decrease then an increase of the charge without any meaningful change in the mass. Then the mass increases first linearly with the charge with a slope of 80 µg/C and then the slope decreases to zero when the mass reaches a maximum value. When the charge decreases, the mass decreases proportionally with the same slope (80 µg/C) down to a point where there is no mass variation but still a decrease of the charge.

The change of the slope (to almost zero value) is rather easy to understand as it occurs during the O_2 evolution so that part of the recorded charge is used for a reaction that does not involve a mass change. It is therefore expected that the mass continues to increase linearly up to a plateau as shown by the dotted line in fig. 5.30.

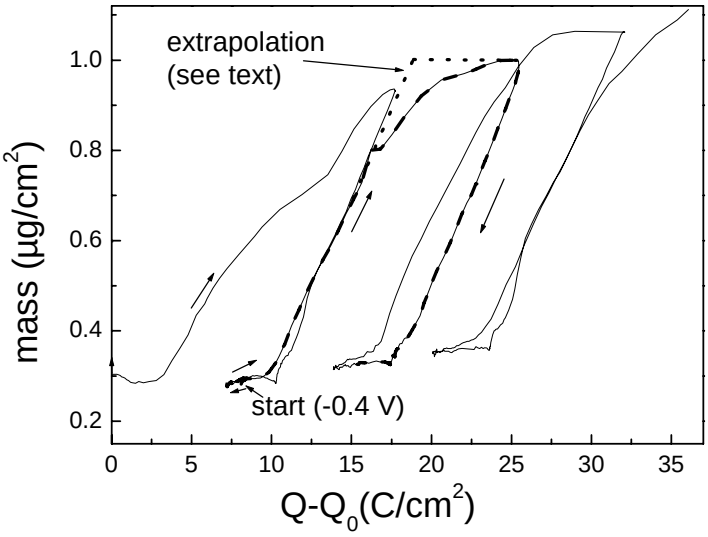

Fig. 5.30: Mass change against charge change of a NiO-TiO_2 double layer deposited on gold coated quartz crystal during the first three CV cycles (-0.4 to + 0.57 V, scan rate 10 mV/s). The second cycle is highlighted.

Before discussing a model it is worthwhile to show the results obtained during the 145th cycle.

b) 145th cycle

Fig. 5.31 shows the voltammogram, voltamassogram and the variation of the charge measured during the 145th cycle.

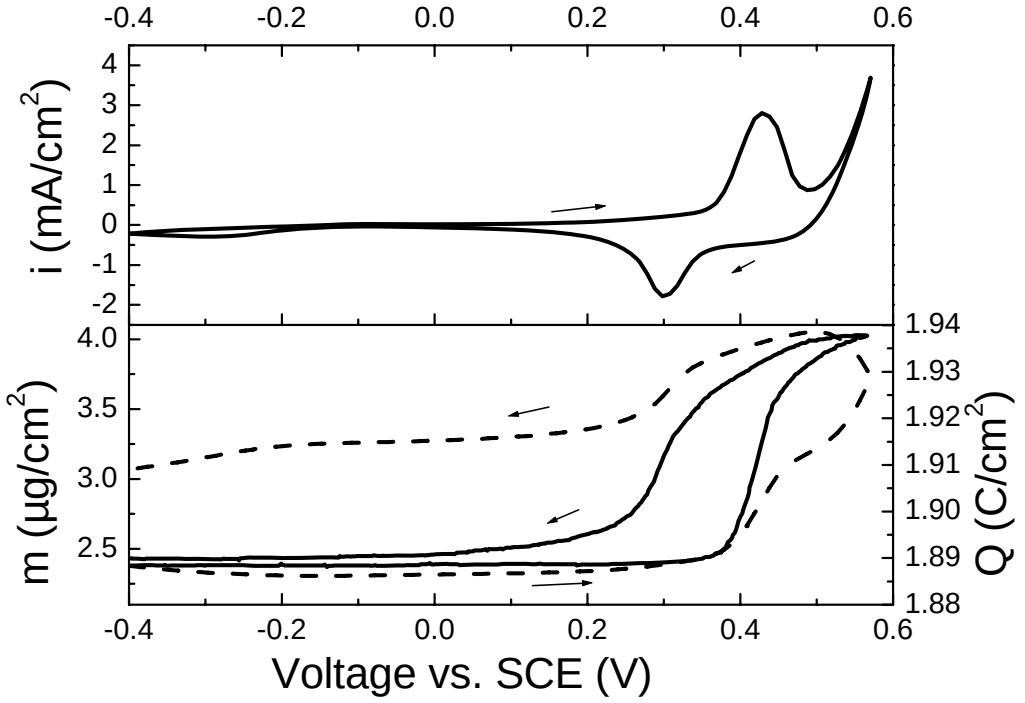

Fig. 5.31: Voltammogram and voltmassogram of a NiO-TiO_2 double layer deposited on gold coated quartz crystal during the 145th CV cycle (-0.4 to +0.57 V, scan rate 10 mV/s).

The overall behavior is similar to that shown for the 2nd cycle (fig. 5.29). However several important differences can be observed:

a) the height of the current peak related to the electrochromism in both the anodic range (at V= 0.43 V) and in the cathodic range (at V= 0.32 V) are much higher. The current peak is also better separated from the current related to the O_2 evolution.

b) as before, the change of the mass is strictly zero up to +0.35 V but the peak value is much higher (1.6 µg/cm^2 vs. 0.65 µg/cm^2) and also occurs before the end of the anodic cycle. The potential at which the mass increases is slightly shifted to more positive potential.

c) the charge exchange in the anodic range is also much higher (53 mC/cm^2 vs. 17 mC/cm^2). The net charge is also higher (2.04 C/cm^2 vs. 17 mC/cm^2) and as before is not reversible.

d) the small cathodic peak around –0.22 V also increases.

Finally fig. 5.32 shows the plot of the mass versus charge for the 145th cycle. The shape and the behavior are quite similar to those shown for the 2nd cycle and both linear variations have exactly the same slope as before, 80 µg/cm^2, but the maximum before the end of the anodic cycle is higher (1.6 µg/cm^2 vs. 0.65 µg/cm^2). At the end of the anodic range the slope decreases to zero for the same reason given above to explain the behavior of the 2nd cycle (O_2 evolution).

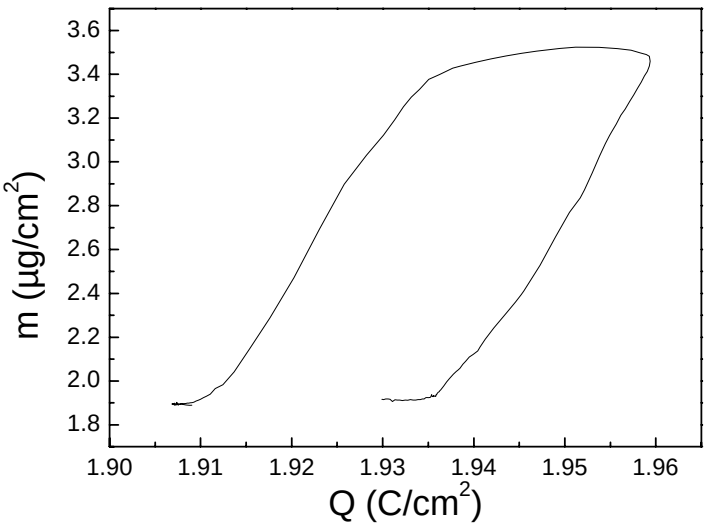

Fig. 5.32: Mass change against charge change of a NiO-TiO_2 double layer deposited on gold coated quartz crystal during the 145th CV cycle (-0.4 to +0.57 V scan rate 10 mV/s).

Model:

During the activation period up to 150th cycle two main features are observed:

a) A variation of the charge without variation of the mass in the anodic range from -0.4 V to 0.35 V and in the cathodic range from 0 to –0.4 V vs. SCE.

b) A linear increase of the mass in the anodic range and a linear decrease of the mass in the cathodic range with the same slope (80 µg/C).

The first feature is different from that observed by Bange et al.[78] for NiO layers produced by *e-beam evaporation* where a small decrease of the mass was observed during the first part of the anodic cycle explained as an evidence for a hydrogen ejection. For the sol-gel layers there is no mass evolution in this range. Therefore the process observed only as a small cathodic wave around –0.22 V should only involve reaction(s) with electrons. The wave is however not seen in the voltammograms of layers deposited on FTO (see e.g. fig.5.9) whatever is the potential range. Moreover, as it will be seen later, this wave will become much more pronounced as cycling proceeds. The discussion of its origin will be presented therefore later.

The second feature, the linear increase and decrease of the mass with the charge, is without any doubt related to an almost fully reversible exchange of OH^- groups that involves a change of the oxidation state of Ni from 2^+ to 3^+ and vice versa (coloration and bleaching respectively) at a lattice site.

The increase of the current density, charge and mass with cycling are compatible with the ideas proposed earlier that, in this activation period, only a thin layer located at the interface electrolyte/layer is active and that the thickness of this layer increases by cycling. Without knowing with precision the complex surroundings of the NiO nanparticles, where the presence of $Ni(OH)_2$ (not observed by X-ray) and H_2O too is expected because of the low sintering temperature and/or by the wetting of the layer in the electrolyte, a precise model can not be proposed. One possible equation to describe the results for E> 0.35 V is

$$xNi(OH)_2 + xOH^- \leftrightarrow (xNiOOH)\cdot yH_2O + (x-y)\,H_2O + xe^- \qquad (5.5)$$

and dividing by x

$$Ni(OH)_2 + OH^- \leftrightarrow (NiOOH)\cdot(y/x)H_2O + (1-(y/x))H_2O + e^- \qquad (5.6)$$

bleached colored

with $0 \leq y \leq x$

The x value is an arbitrary number greater than zero that describes the bonding of x hydroxyl ion per $Ni(OH)_2$ during the coloration of the film and the equation suggests the formation of NiOOH and y/x lattice water bonded to NiOOH due to the incorporation of OH^- and the transfer of (1-y/x) water into the electrolyte.

According to this equation the change in mass of the sol-gel layer during the second cycle will be

$$M_w = (y/x)M_{H2O} - M_H \qquad .(5.7)$$

$$M_w = (y/x)\ (18)\text{-}1 \qquad (5.8)$$

Using the equation relating mass and charge changes

$$\Delta m = (\Delta Q/F)\ M_w \qquad (5.9)$$

where Δm is the change of the mass ($\mu g/cm^2$), ΔQ is the variation of the charge (C/cm^2), F is the faraday constant (96485 C/cm^2) and M_w is an apparent molar mass of the involved species, and using the obtained value of $\Delta m/\Delta Q = 80\ \mu g/C$ it is found that $M_w = 7.7$ g/mol. Using this value in equation 5.8, the value of y/x is $y/x = 8.7/18 \approx 0.5$.

Another possible but slightly different reaction that gives the same $y/x \approx 0.5$ value is:

$$xNi(OH)_2 + yOH^- \leftrightarrow (xNiOOH)\cdot yH_2O + (x\text{-}y)\ H+ ye^- \qquad (5.10)$$

with $0 \leq y \leq x$

and dividing by x

$$Ni(OH)_2 + (y/x)\ OH^- \leftrightarrow (NiOOH)\cdot(y/x)H_2O + (1\text{-}(y/x))H+ (y/x)e^- \qquad (5.11)$$

bleached colored

This equation is similar to that proposed by Bange et al. [78] except that in our case about 0.5 hydrogen per $Ni(OH)_2$ will be evolved only during the coloration process and not during the earlier part of the anodic cycle i.e. for V> 0.35 V.

Both proposed reactions 5.6 and 5.11 may not be 100 % reversible so that the layer becomes richer in hydrated NiOOH leading to the slight but continuous increase of the permanent coloration (see section 5.3).

These two proposals involve only reactions between $Ni(OH)_2$ and OH^-. However it was observed during the first 150 cycles that the total mass of the layer increases after each cycle by 0.034 $\mu g/cm^2$, and that the mass exchange during each cycle was initially 0.65 $\mu g/cm^2$ but reached a value of 1.6 $\mu g/cm^2$ after 150 cycles. Also the charge exchange during each cycle increases from 17 mC/cm^2 at the second cycle to 53 mC/cm^2 after 150 cycles leading to an increase of the coloration of the layer. Therefore the amount of $Ni(OH)_2$ available for these reactions has also to increase. This may be related to the following irreversible reaction

$$NiO + zH_2O \rightarrow Ni(OH)_2 + (1\text{-}z)NiO \qquad (5.12)$$

nonactive EC active

If the continuous increase of the mass after each cycle ($0.034 \mu g/cm^2$) is due to this reaction, this will involve a value of $z = (3.4\ 10^{-8}\ g/cm^2)/(18\ g/mol) = 1.8\ 10^{-9}\ mol/cm^2$ of water, taken either from the electrolyte or from the layer. The NiO particles being rather

dense, the reaction should occur on the surface of the particles. This leads to a continuous decrease of the amount of the NiO in the layer as observed by XRD (see section 5.2).

Without a better knowledge of the composition of the layer it is not possible to give better explanations.

This model nevertheless allows explaining why the mass of the layer increases, why the layer becomes fragile (higher hydration) and also why a higher sintering temperature was not suitable for the electrochromic properties (less hydration).

Although the proposed equation is somewhat different from that of Bange et al. [78], the latter conclusions are in agreement with it. One can therefore propose the following compositions for the bleached and colored layers

bleached state $NiO + x(NiOH)_2 + TiO_2$ (5.13)

colored state $NiO + (xNiOOH)\cdot yH_2O + TiO_2$ (5.14)

where the values of x and y change continuously during cycling.

5.5.4 From the 150th cycle

The voltammograms and voltamassograms of the 200th, 300th, 330th, and 400th cycles are shown in fig. 5.33. The value of the mass at V= -0.4 V vs. SCE has been reset to zero for all records for better comparison. They were 4.76, 17.64, 24.42 and 47.4 μg/cm^2 respectively. Also the same scale of the ordinates of each cycle has been used.

The electrochromic anodic peak in the range of 0.43 V vs. SCE grows continuously so that the ratio of the intensity of this peak to that of the oxygen evolution increases. The anodic peak position is also slightly shifted to higher positive potential values by cycling. The first cathodic peak around +0.3 V vs. SCE increases also but practically does not shift by cycling. The second one at the end of the cathodic scan at –0.3V vs. SCE drastically increases by cycling and shifts to more negative potential values.

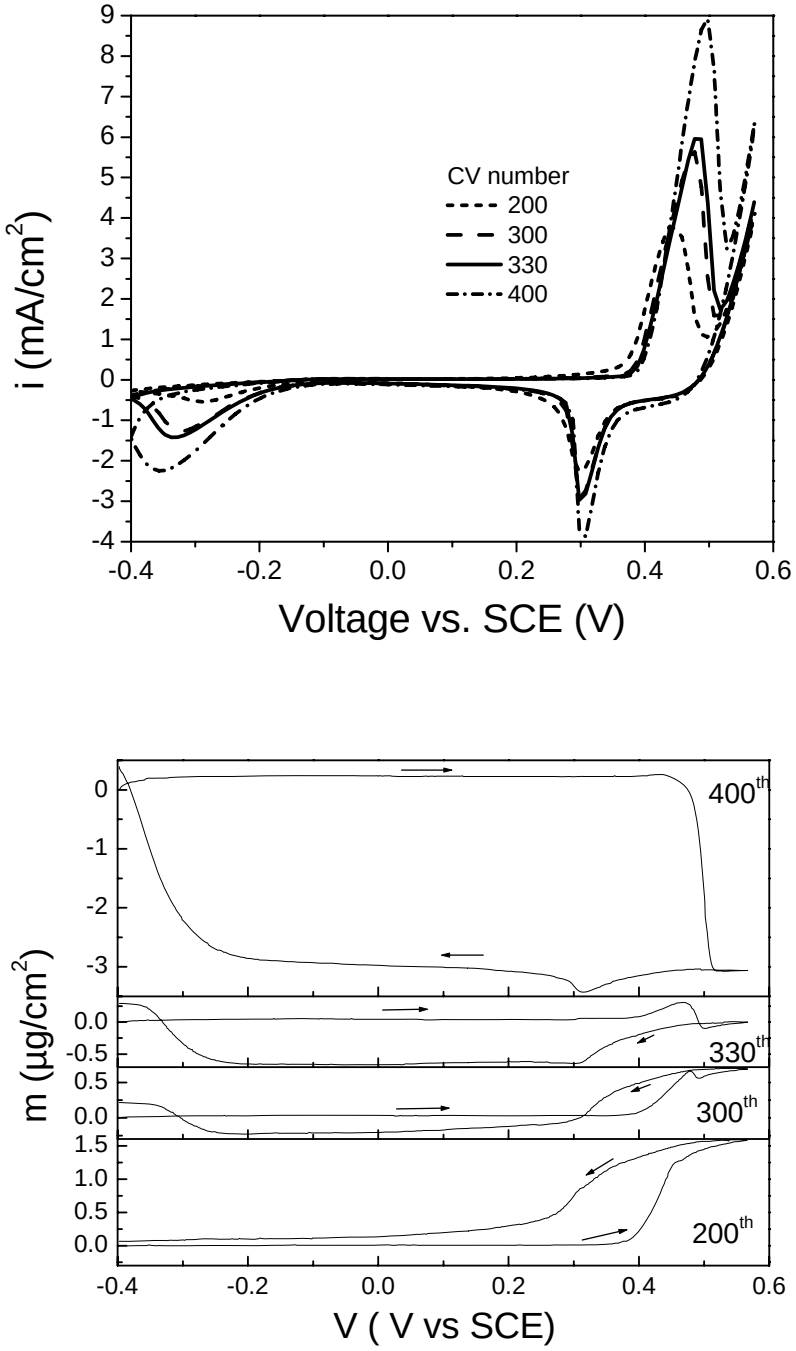

Fig. 5.33: CV voltammograms and voltamassograms of the 200, 300, 330 and 400th CV cycles of NiO-TiO_2 double layer deposited on gold coated quartz crystal, sintered at 300 °C and tested in 1 M KOH in the potential range –0.4 to 0.57 V scan rate 10 mV/s. The ordinate scales of the mass are the same in all graphs.

The shape of the voltamassogram during the 200th CV cycle (lower part of fig. 5.33) is similar to that of the 150th cycle (see fig.5.31) and the mass increase occurs during the anodic scan at a voltage corresponding to the anodic current peak. There are then however

drastic changes between the 200th cycle and the 400th cycle. As before no mass change is observed in the first part of the anodic cycle but the potential range slightly increases to more positive values (from +0.4 V at the 200th cycle to +0.47 V at the 400th cycle).

The behavior at the end of the anodic cycle becomes rather complicated. The mass increase is continuously reduced but it can still be observed up to about the 377th cycle. It is substituted by a mass decrease around 0.48 V vs. SCE that can be observed already at the 300th cycle and that occurs in a very small potential range (0.48 to 0.52 V vs. SCE). At this stage the absolute value of the mass change passes by a minimum (0.9 $\mu g/cm^2$). Its value then drastically increases with cycling to reach a value of 4 $\mu g/cm^2$ at the 400th cycle. This can be clearly observed by the width of the mass records in fig. 5.26.

At the end of the cathodic cycle a mass increase is now observed initiating at around -0.22 V vs. SCE linked clearly to the increase of the height of the second cathodic current peak. Its value grows with cycling to reach about 4 $\mu g/cm^2$ at the 400th cycle. It should be remembered that this cathodic peak was not observed by studying NiO-TiO_2 layers deposited on FTO conducting layer (see fig. 5.9).

The 330th cycle is found a good example for studying this transition period (fig. 5.34).

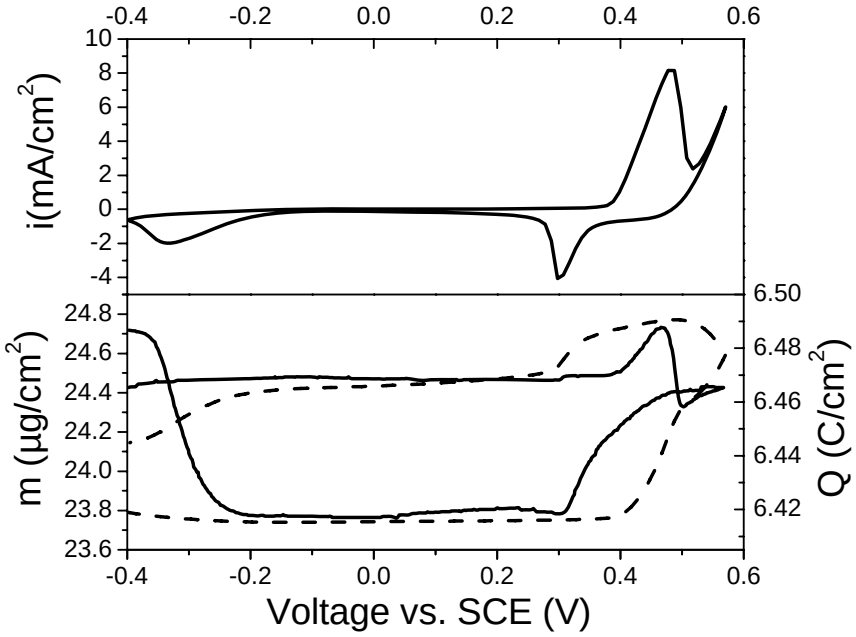

Fig. 5.34: Voltammogram and voltmassogram for a NiO-TiO_2 double layer deposited on gold coated quartz crystal during the 330th CV cycle (-0.4, 0.57 V, scan rate 10 mV/s).

In the anodic range, both the charge and the mass of the layer remain constant up to +0.4V where a sharp increase in the charge and mass are noticed corresponding to the anodic electrochromic peak. The mass starts to decrease sharply at 0.45 V before increasing again.

By reversing the potential scan, a clear decrease of the charge and the mass occurs around +0.3 V corresponding to the first cathodic peak. A slight decrease of both the mass and charge is seen down to –0.25 V where a sharp decrease of the charge starts with a large mass increase corresponding to the cathodic peak centred at –0.3 V.

It is difficult at this stage to know exactly what is occurring during this transition period. Nevertheless fig. 5.35, 5.36 show a plot of the mass change vs. charge change for the 330th and 400th cycle respectively. In the latter graph the decrease and increase of the mass have a similar behavior with a high slope of about 182 µg/C.

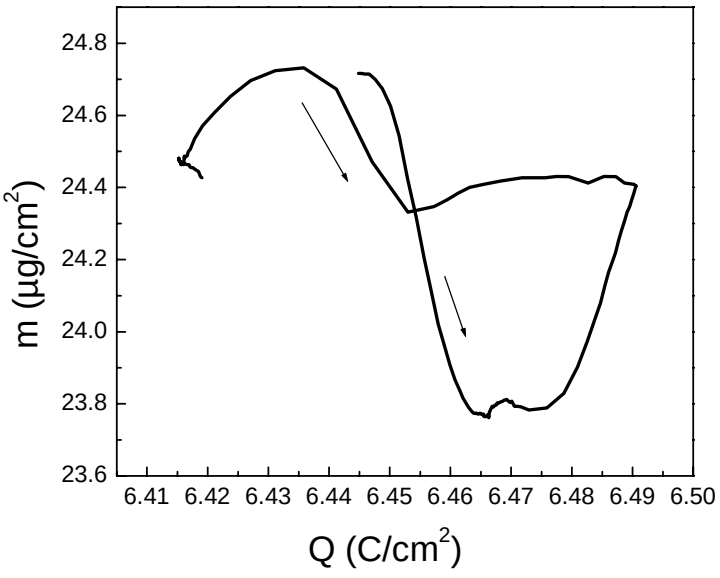

Fig. 5.35: Mass change against charge change of a NiO-TiO_2 double layer deposited on gold coated quartz crystal during the 330th CV cycle (-0.4 to +0.57 V, scan rate 10 mV/s).

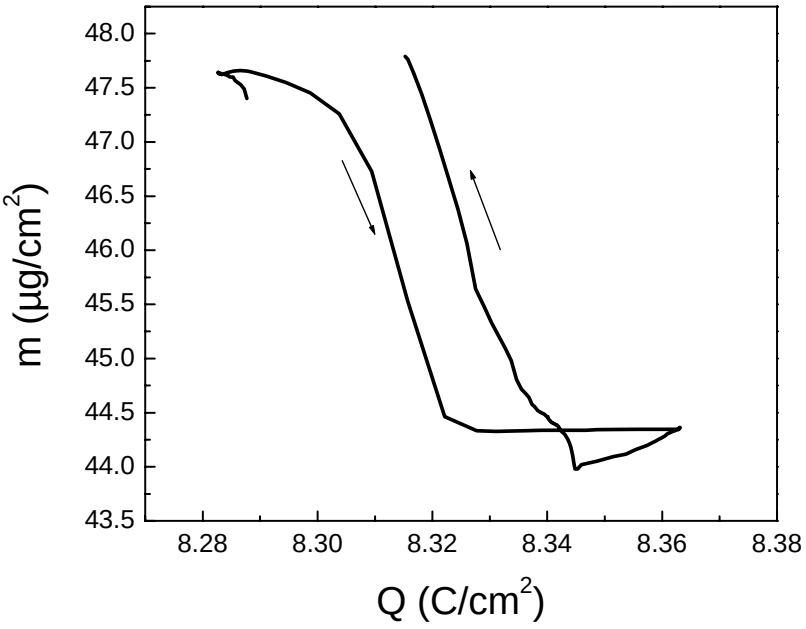

Fig. 5.36: Mass change against charge change of a NiO-TiO_2 double layer deposited on gold coated quartz crystal during the 400th CV cycle (-0.4 to +0.57 V scan rate 10 mV/s).

Finally, fig. 5.37 shows the voltammogram and voltamassogram for some of the last cycles (450th, 500th, 590th, 650th cycles). As before the mass values have been set to 0 at –0.4 V.

The shape of the CV voltammograms remains essentially constant. Compared to the 400th cycle the intensity of the anodic current peak around 0.5 V has slightly decreased from 9 mA/cm^2 to 6.5 mA/cm^2 and has slightly shifted to higher positive potentials. The first cathodic peak around 0.3 V vs. SCE and the one at the end of the cathodic scan at –0.35 V vs. SCE have both also decreased.

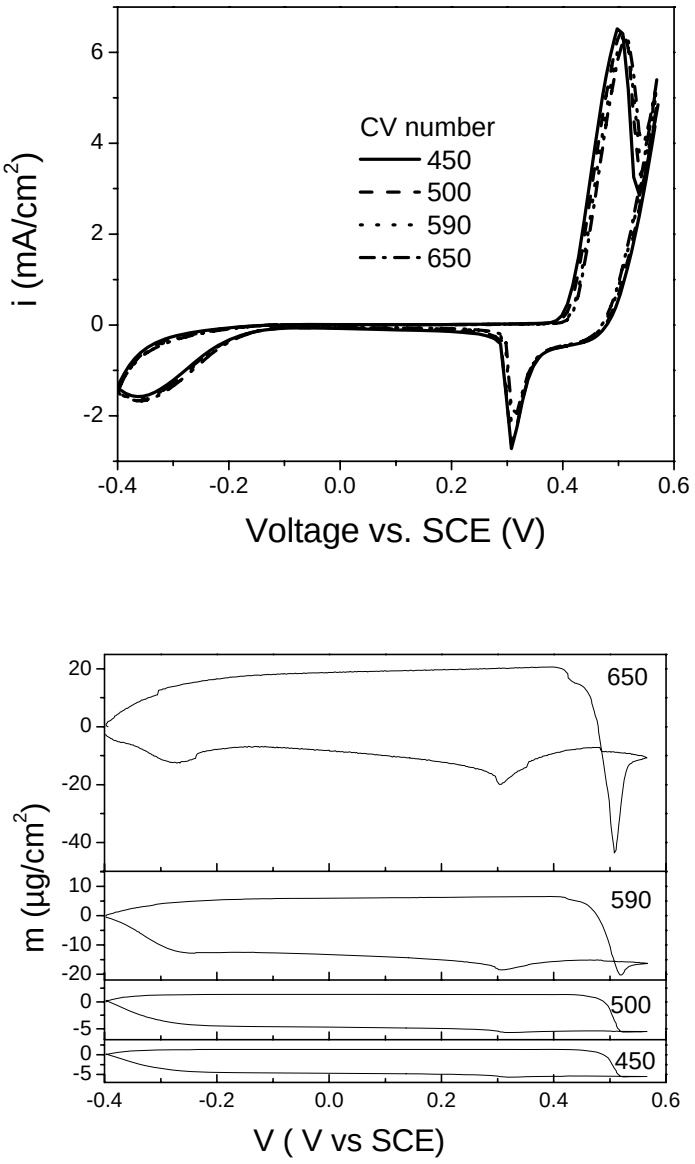

Fig. 5.37: CV voltammograms and voltamassograms of the 450, 500, 590 and 650th CV cycles of NiO-TiO_2 double layer deposited on gold coated quartz crystal, sintered at 300 °C and tested in KOH in the potential range –0.4 to 0.57 V scan rate 10 mV/s. The mass values have been set reset to zero at –0.4 V and the scales are the same in all 4 graphs.

The corresponding mass changes are shown in the lower part of fig. 5.37. They are compatible with the voltammograms. The shape of the spectra up to the 550th cycle are similar to that of the 400th cycle (fig. 5.33).

One observes however a very large increase of the mass change from 4 µg/cm^2 at the 400th cycle up to 63 µg/cm^2 at 650th cycle. Also, during the last cycles a mass increase becomes again superimposed at the end of the anodic cycle.

As the cathodic peak at the end of the cathodic scan shift to more negative potentials, the corresponding mass increase shifts in the same direction so that is only completed in the anodic scan.

The results obtained till the 150th cycle have been correlated to the exchange of OH^- during the CV cycles that reacts with $Ni(OH)_2$ to produce hydrated NiOOH (responsible for the coloration of the layer), as well as intercalated water that reacts with NiO to increase the amount of $Ni(OH)_2$ in the layer to explain the increase of ΔOD and the decrease of the size of the NiO nanoparticles by cycling. These changes in the layer composition associated by an increase of the porosity and fragility. From 330th cycle one observes a drastic change of the mass spectra that can only be explained by a partly irreversible exchange of positives ions, these can only be K^+ or hydrated $K(H_2O)_n^+$ ions. The primary hydration umber of K is 4 [208]. A similar behavior has been recently observed by Sun [144] for $(CeO_2)_{0.81}(TiO_2)_1$ sol-gel counter electrode layer in wet $LiClO_4$-PC electrolyte. The high weight of the ions explains why the ratio of mass/charge obtained (e.g. from fig. 5.36 for the 400th cycle) becomes higher (181 μg/C vs. 80 μg/C), why the total mass increases after each cycle drastically up to 570 cycles. The layer morphology and structure become therefore very loose up to a point (650th cycle) it breaks down and is dissolved in the electrolyte.

5.5 NiO-TiO_2 layer characterization in $LiClO_4$-PC electrolyte

Scrosati et al. [143, 191, 192, 209] have studied the electrochromic behavior of dc magnetron *sputtered* NiO_x layer in aprotic $LiClO_4$-PC electrolyte. It was shown that Li^+ could be intercalated via two different steps leading to interesting coloring/bleaching behavior especially useful for the development of WO_3/electrolyte/NiO EC cells.

This section describes the results obtained with *sol-gel* NiO-TiO_2 layers tested in the three electrode cell filled with $LiClO_4$-PC using Ag/$AgClO_4$-PC as reference electrode. The results are rather complex as they were found to be strongly dependent on the kinetics of the process. Therefore the presentation is not exhaustive. For sake of clarity, the section has been divided in 3 parts according to the potential range. Except for the spectrum, the transmittance has been normalized considering the value in the bleached state as 100%.

a) potential range –1 to +1 V vs. Ag/$AgClO_4$-PC

Studies for NiO based layers in a Li^+ aprotic electrolyte in the potential range –0.5 to +1 V vs. Ag/$AgClO_4$-PC have not been reported.

Fig. 5.38 shows a galvanostatic coloration of a fresh uncolored NiO-TiO_2 layer, 80 nm thick sintered at 300 °C performed by applying a small *positive* current density of +5µA/cm^2. The potential increases continuously from 0 to +1.05 V and a small decrease of the layer transmittance is observed (T/T_b decreases from 100 % to about 87 %) after having incorporating a charge of 7 mC/cm^2.

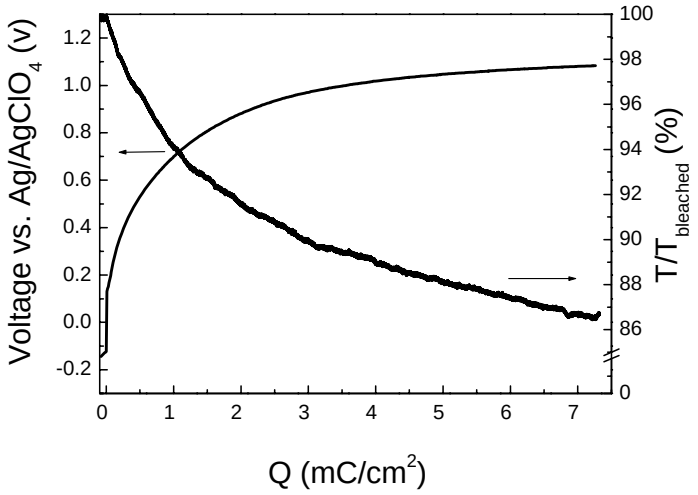

Fig. 5.38. Potential and transmittance (550 nm) evolution of an 80 nm thick single NiO-TiO_2 layer (Ni content of 75 mol %) in $LiClO_4$-PC during galvanostatic measurement using a positive current density of +5µA/cm^2.

The observed spectra of the colored layer (fig. 5.39) is slightly different from that obtained in OH^- based electrolyte (see fig. 5.13).

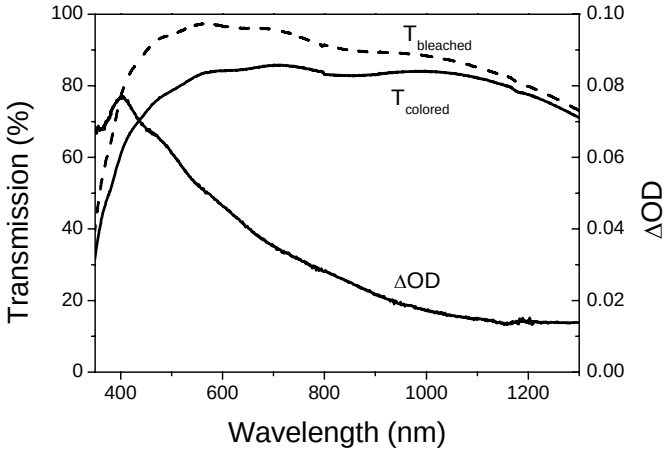

Fig. 5.39 : Transmittance spectra of $NiO\text{-}TiO_2$ layer in the colored and uncolored states and change of the optical density after a galvanostatic coloration with +5 $\mu A/cm^2$.

This behavior was confirmed by performing cyclic voltammetry at a rate of 20 mV/s between -1 and 1 V vs. $Ag/AgClO_4$-PC on single fresh layer. The first voltammogram is shown in fig. 5.40. The shape of the curve is very similar to that observed in KOH electrolyte (see e.g. fig. 20) but the maximum current density is extremely small (<0.03 mA/cm^2) i.e. typically a factor 20 smaller, the anodic charge Q_a= 0.88 mC/cm^2 and the cathodic charge Q_c= 1.6 mC/cm^2. The layer colors anodically and bleaches cathodically.

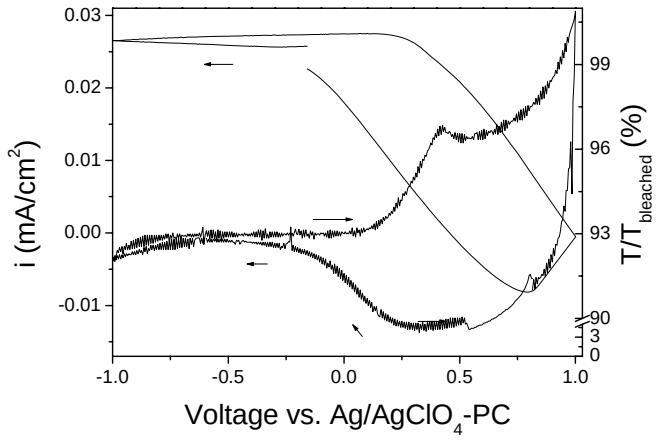

Fig. 5.40: 1St CV voltammogram and transmittance change (550 nm) for an 80 nm thick single $NiO\text{-}TiO_2$ layer (Ni concentration of 75 mol %) heated at 300 °C, potential range -1 to +1 V, scan rate 20 mV/s in 1 $LiClO_4$-PC electrolyte.

For CV cycle performed with a scan rate of 1.5 mV/s (same scan time as for galvanostatic measurement) the current density was nearly zero (7 $\mu A/cm^2$).

Taking into account the pH value of the electrolyte, the potential range where the coloration/bleaching processes occur is very similar to that obtained in KOH and LiOH electrolytes.

The sol-gel coated layers sintered at low temperature (300 °C in our case) are porous and still contain OH^- and H_2O molecules so that, when cycled in an aprotic electrolyte small amounts of OH^- will be quickly incorporated. Moreover it was shown that it is extremely difficult to prepare and keep $LiClO_4$-PC electrolyte free of water [144]. Therefore it is believed that the low intensity electrochromic process observed in this potential range follows the basic idea discussed in section 5.3 i.e. a coloration due to the transformation of NiO or $Ni(OH)_2$ into NiOOH occurring with reversible exchange of OH^- ions. The low concentration of OH^- in the electrolyte and the fact that only a layer close to the interface is involved initially (see section 5.3) explain why current density and the transmittance change are small.

b) Potential range 0 to –3 V vs. Ag/$AgClO_4$-PC

Fig. 5.41 shows a typical galvanostatic measurement obtained by applying a small *negative* current density of –5 $\mu A/cm^2$ and the change in transmittance measured at 550 nm using a fresh uncoloured 80 nm thick layer sintered at 300 °C.

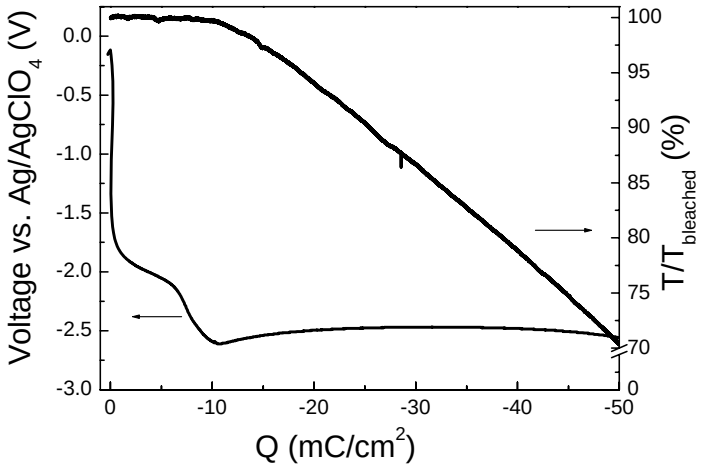

Fig. 5.41. Potential and transmittance (550 nm) evolution for a fresh 80 nm thick single NiO-TiO_2 layer (Ni content of 75 mol %) in $LiClO_4$-PC during galvanostatic measurement applying a negative current density of $-5\mu A/cm^2$.

The potential decreases first steeply and fast to reach a first plateau at about –2 V up to an inserted charge of about –6 mC/cm^2. Then the potential decreases again steeply and fast to reach a minimum of –2.6 V after having inserted a charge of about –10 mC/cm^2. Up to this value the transmittance does not change (no coloration, T/T_b= 100 %). Then the potential increases very slightly and stabilizes at a value of –2.5 V and the transmittance starts to decrease slowly but continuously. A very high value of charge could be inserted (> 600 mC/cm^2/μm) which is particularly promising for the layer use as counter electrode in EC cells. However, the layer becomes mechanically extremely fragile and the coloration is not homogeneous through the thickness, the brown color being darker near the interface. The X-ray diffraction of the layer in this stage is shown in fig. 5.42. All the rather broad peaks of NiO observed in the fresh layer have disappeared (see fig. 5.7 for comparison) and several new sharp peaks are now present. It was not possible to identify them with certainty. Some of them may correspond to a $Li_xNi_yO_z$ and Ni_2O_3 compositions.

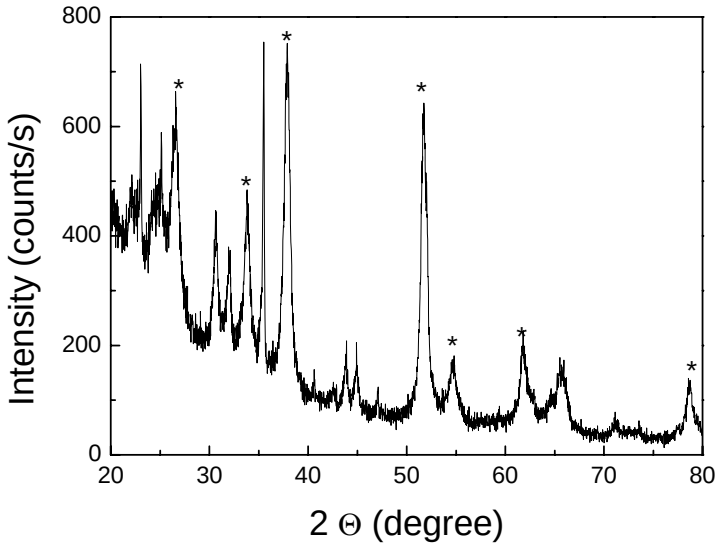

Fig. 5.42: X-ray spectra of an 80 nm thick NiO-TiO_2 layer sintered at 300 °C after applying a current density of –5 μA/cm^2 for 10000 s i.e. (-50 mC/cm^2). The peaks marked with * are from the substrate (Sn_2:F).

Although the colored layers are brown, their transmittance and absorption spectrum are different from those obtained by coloring in aqueous KOH electrolyte as well as those colored in Li^+ electrolyte in the potential range –1 to +1 V. The transmittance spectra are shown in fig. 5.43a and a comparison of the change in absorption in KOH and $LiClO_4$-PC

is shown in fig. 5.43b. The coloration efficiency (CE_{550}) is 2.7 cm^2/C i.e. much smaller than that obtained in KOH (CE_{550}= 30 cm^2/C), another indication that the coloring process is different.

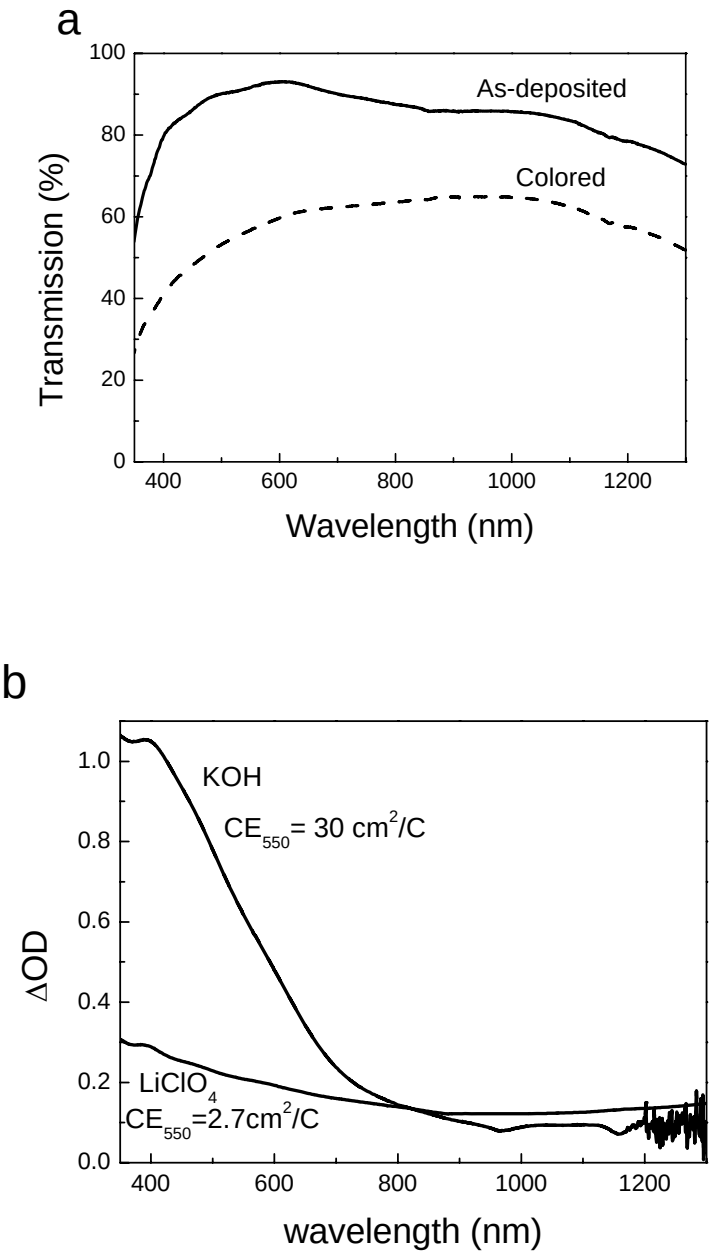

Fig. 5.43: (a) Transmittance spectra of NiO-TiO_2 layer in the colored and uncolored states. The layer was colored galvanostaically at –5 μA/cm^2 with total inserted charge of -100 mC/cm^2. (b) Change in optical density of NiO-TiO_2 layers colored by cycling in KOH (from fig. 5.13) and $LiClO_4$-PC electrolyte.

By reversing the current, i.e. by applying +5 μA/cm^2 and limiting the potential to 0 V, the behavior of the potential and the transmittance have been found to depend on the amount of charge that has been previously incorporated (fig. 5.44).

After having inserted –9 mC/cm^2 only (*initial period*) the voltage jumps quickly to +0.25 V and the value of the transmittance T/Tb= 100 % is not altered. Then the voltage increases slightly but steadily to +0.6 V. The layer slightly colors in a way similar to that observed in fig. 5.38.

When a higher amount of charge has been incorporated (-50 mC/cm^2) the potential increases slowly from –2.4 V and the previously colored layer starts to bleach slowly but only partly. These results indicate that the EC processes are totally different from those discussed using aqueous KOH based electrolyte.

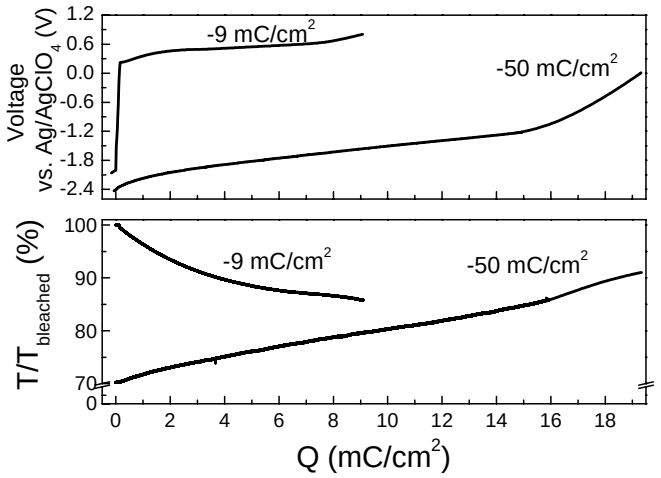

Fig. 5.44: Potential and transmittance changes vs. the de-inserted charge during galvanostatic measurement at +5μA/cm^2 for two single NiO-TiO_2 layers after being polarized at a negative current of –5 μA/cm^2 up to an inserted charge of –9 mC/cm^2 and -50 mC/cm^2.

The sol gel layers follow essentially the same behavior observed by the group of Scrosati et al. [192, 193, 195] with sputtered layers except that, in their case, the fresh layer was initially colored and it bleached during the initial period i.e. till the potential reached the minimum value i.e. after a charge injection of –212 mC/cm^2/μm (in our case -125 mC/cm^2/μm).

Our findings are also confirmed by performing CV cycles in the same potential range 0 to –3 V vs. Ag/$AgClO_4$-PC using fresh uncolored layers. The results shown in fig. 5.45 has been obtained using a very slow rate of 1 mV/s in order to meet the slow kinetics of the galvanostatic measurement in fig. 5.41.

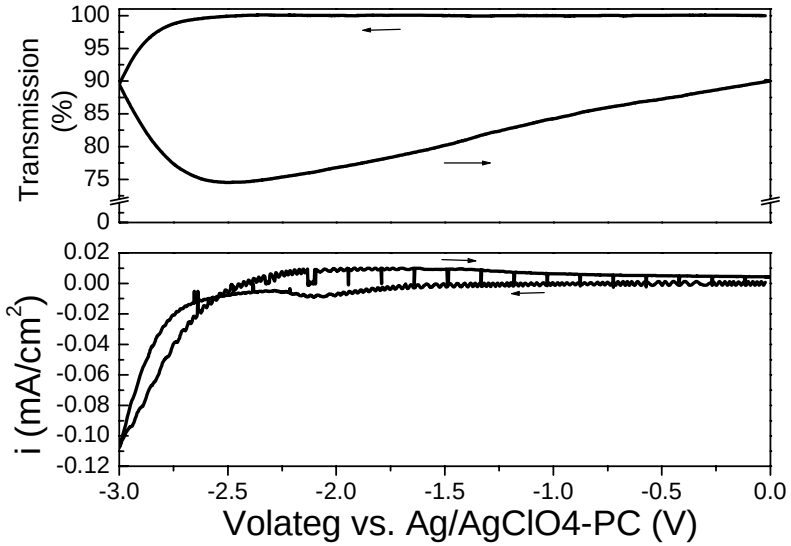

Fig. 5.45: 1st CV cycle obtained with a 80 nm thick single NiO-TiO_2 layer (Ni concentration of 75 mol %) heated at 300 °C, potential range 0 to -3 V, scan rate 1 mV/s in 1 M $LiClO_4$-PC electrolyte. The upper figure is the transmittance change at 550 nm.

First a small cathodic wave (i.e. i< 10µA/cm^2, Q_c≈5.3 mC/cm^2) is observed at –2.15 V (value of the first plateau of fig. 5.41) and no coloration occurs till reaching about –2.6 V (value of the minimum of fig. 5.41). Then the coloration is initiated as also observed in the galvanostatic measurement.

By reversing the potential the coloration continues in the cathodic range down to a value of T/T_b= 74.5 % till the current reaches the zero value. During this initial half cycle, 45 mC/cm^2 has been inserted. Then a partial bleaching follows in the anodic range (up to T/T_b= 89 %). It should be remarked also that the charge involved in the half cycle is Q_a= +7 mC/cm^2 i.e. much smaller than Q_c (-45 mC/cm^2).

The shape of the absorption spectrum of the layer is identical to that shown in fig. 5.43.

The results observed during the second CV cycle are different (fig. 5.46). The small cathodic wave observed in the 1st CV cycle at –2.15 V is not observed and the current density is strictly zero. Also contrary to the observation of Scrosati [192], no bleaching of the rest coloration is observed during the initial scan down to a potential of –2.4 V. Although the shape of the CV voltammogram is essentially the same as that observed in the 1st CV cycle, the inserted charge is smaller (Q_c= -21 mC/cm^2, instead of –45 mC/cm^2) but the deinserted charge is higher (Q_a= 12 mC/cm^2 mC/cm^2 instead of 7).

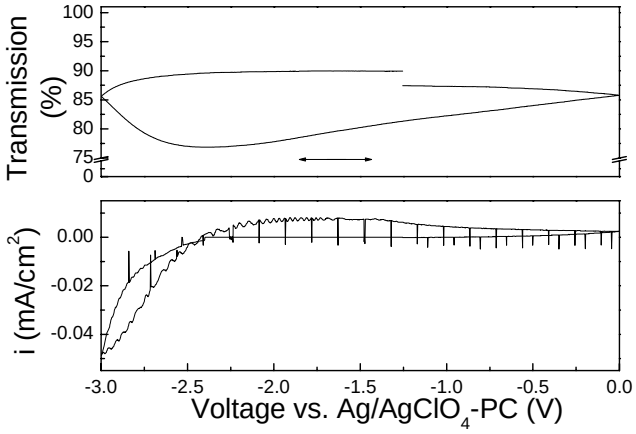

Fig. 5.46: 2nd CV cycle obtained with a 80 nm thick single NiO-TiO_2 layer (Ni concentration of 75 mol %) heated at 300 °C, potential range 0 to -3 V, scan rate 1 mV/s in 1 M $LiClO_4$-PC electrolyte. The upper figure is the transmittance change at 550 nm.

The final coloration of the layer during the cathodic range is not improved (76.5 %) and it bleaches to a slightly lower value than that obtained after the 1st cycle (T/T_b= 87.5 %). As the charge involved in the bleaching process is smaller than that involved in the coloring process, the CV behavior is therefore not fully reversible.

A further interesting observation confirming the above results is shown in fig. 5.47. A fresh layer has been first submitted to a cyclic voltammetry in the potential range 0 to -2.15 V, then a galvanostatic measurement has been made using –5µA/cm².

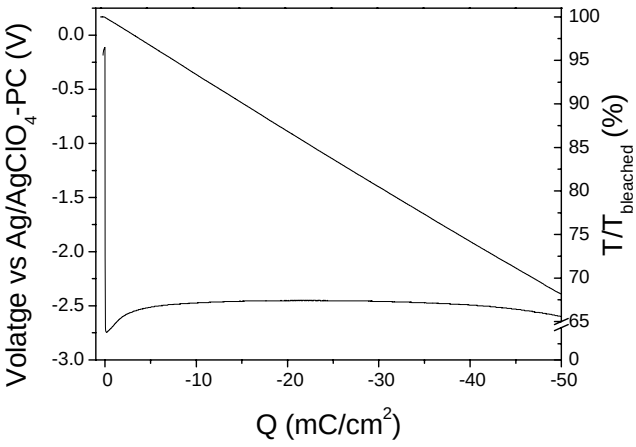

Fig. 5.47: Potential and transmittance (550 nm) evolution for 80 nm thick single NiO-TiO_2 layer (Ni content of 75 mol %) in $LiClO_4$-PC during a galvanostatic measurement applying a negative current density of –5µA/cm². The layer was previously cycled in the potential range 0 to –2.15 V for 2 CVs.

Contrary to the result shown in fig. 5.41, the potential drops instantly down to –2.75 V and remains then at a constant value of –2.5 V. This is accompanied by a continuous coloration of the layer reaching the same value of the transmittance, T/T_b= 68 %, after intercalating -50 mC/cm^2. The initial activation period is therefore not observed so that one can conclude that this period is linked to the small cathodic wave observed only in the 1st CV cycle around –2.15 V.

The group of Scrosati has explained the behavior of sputtered NiO_x layer cycled in the same Li^+ electrolyte and in the same potential range according to polaron models assuming that their electrodes consist of amorphous, nonstoichiometric nickel oxide (NiO_x), the deviation from the stoichiometry being ascribable to nickel vacancies. In the as deposited state, the sputtered electrodes are initially colored due to the presence of Ni^{3+} necessary to balance the Ni vacancies. The electrochromic process was therefore divided into two steps.

During the initial period of a galvanostatic process i.e. during the period in which the potential decreases to a minimum value (see e.g. fig. 5.41), Li^+ and e^- are injected irreversibly into the layer according to

$$NiO_x + yLi^+ + ye^- \rightarrow Li_yNiO_x \qquad (5.15)$$

While the Li^+ influences the *electrochemical* behavior of the NiO_x electrode, the injection of electrons influences the *electrochromic* behavior where they interact with the Ni^{3+} ions according to

$$Ni^{3+} + e^- \leftrightarrow Ni^{2+} \qquad (5.16)$$

colored bleached

This process leads to the progressive elimination of the vacancies and thus to the elimination of the associated Ni^{3+} polaron producing transparent Li_yNiO_x electrode. It describes in fact a type of activation of the NiO_x thin film i.e. an irreversible uptake of Li^+ ions in the NiO_x host structure inducing phase modification of the original NiO_x sample.

This activation step is followed by a further forced reversible injection of Li^+ to which an electrochromic effect is associated according to

$$Li_yNiO_x + zLi^+ + ze^- \leftrightarrow Li_{y+z}NiO_x \qquad (5.17)$$

A convincing evidence for these assumptions was obtained by following the expansion of the host oxide matrix during this activation process.

When the intercalated charge exceeds a limit (i.e. the value needed for the activation), the injected electrons may be localized (by interacting with Li^+ ions or Ni^{2+}) or delocalized giving again rise to the formation of polarons. In the later case the mechanism becomes

similar to that of a cathodic electrochromic material and the layer colors at a negative potential.

Our findings however are slightly different because an as deposited sol-gel NiO-TiO_2 layer is initially transparent so that no colored Ni^{3+} polarons exist. When the layer is polarized at a negative current, no change in transmittance is observed during the initial period of the CV cycle until the layer potential reaches –2.6 V vs Ag/$AgClO_4$-PC (see fig. 5.41, 5.45 and 5.46). This value should nevertheless correspond to the Li^+ insertion potential. The layer becomes colored and as observed by the XRD the composition of the electrode changes. As it was not possible to identify the phases one just label them as Li_zNiO-TiO_2. This process is not fully reversible neither by reversing the current nor by closing the CV cycle and part of the injected Li^+ ions stay in the electrode so that the layer remains slightly colored. Our proposal therefore is to divide the reactions of NiO-TiO_2 layer in $LiClO_4$-PC in the potential range 0 to –3 V into three main processes:

i- when applying a negative current galvanostatically (first region) down to a potential of -2.15 V (-9 mC/cm^2) or during the first cathodic CV scan between 0 and –2.15 V.

Here as the electrochemical reaction occurs only once and is irreversible and no coloration or bleaching of the layer is observed, the proposal of Passerini et al. [192, 193, 195] cannot be applied. It is proposed instead that the EC process occurring in this potential range is linked to an irreversible composition change involving either two uncolored compounds as e.g. NiO and small amounts of $Ni(OH)_2$, or more simply water that are expected to exist in the layer due to the low sintering temperature (300 °C) and the processing in normal air (RH= 40 %),.

The first process may involve the following reaction

$$2Ni(OH)_2 + 2e^- \rightarrow 2NiO + 2OH^- + H_2\ (gas) \qquad (5.18)$$

uncolored uncolored

The second process, as it is known from literature, will involve the decomposition of H_2O according to

$$2H_2O + 2e^- \rightarrow 2OH^- + H_2\ (gas) \qquad (5.19)$$

This reaction occurs at –0.827 V vs. NHE i.e. within the voltage range –1.7 to –2.2 V vs. Ag/$AgClO_4$-PC.

This explains why no coloration of the layer is observed, why only a current is flowing, and since all OH^- groups contained in the layer will react (corresponding to 5.3 mC/cm^2) why the process is irreversible and occurs only once.

ii- when applying a negative current galvanostatically during the constant potential of -2..6 V (long plateau of fig. 5.41) or during the cathodic range of CV cycle down to –3 V.
The proposal of Scrosati is quite possible. Li^+ together with e^- may effectively be incorporated cathodically into the layer according to

$$\underset{\text{bleached}}{NiO\text{-}TiO_2} + zLi^+ + ze^- \rightarrow \underset{\text{colored}}{Li_zNiO\text{-}TiO_2} \qquad (5.20)$$

As shown in fig 5.42 the composition of the layer has changed drastically and unfortunately it was not yet possible to identify the components Therefore one can only assume that the coloration is due to electrons localized by interacting with Ni^{2+} or most likely with defects involving Li^+ ions or delocalized giving rise to the formation of polarons. In any case a mechanism similar to that of cathodic electrochromic material like WO_3, Nb_2O_5 is observed and the layer becomes colored with an absorption spectrum different from that observed in KOH electrolyte (due to NiOOH).
The fact that the coloration efficiency during this process is rather small (about 2 mC/cm^2) may indicate that not all inserted Li^+ ions lead to the formation of active (colored) centers and mostly participate to the modification of the phases of the layer contributing to its fragility, (expansion of the host oxide matrix). If that reaction is reversible is not yet known.

iii- when reversing the galvanostatic current and limiting the potential to about 0 V or during an anodic CV scan up to 0 V.
As the layer does not bleach completely it is probable that Li^+ ions are deinserted slowly out of the layer according to

$$\underset{\text{colored}}{Li_zNiO\text{-}TiO_2} \rightarrow \underset{\text{less colored}}{Li_{z-y}NiO\text{-}TiO_2} + y\,Li^+ + y\,e^- \qquad (5.21)$$

Therefore by further cycling the composition of the layer will oscillate between $Li_aNiO\text{-}TiO_2$ and $Li_bNiO\text{-}TiO_2$ according to

$$\underset{\text{higher T (\%)}}{Li_aNiO\text{-}TiO_2} \leftrightarrow \underset{\text{lower T (\%)}}{Li_bNiO\text{-}TiO_2} \qquad (5.22)$$

where b> a.

c) Potential range +1V to –3V vs. Ag/AgClO$_4$-PC

It was shown in section a) and b) that the sol-gel NiO-TiO$_2$ layers can be colored either cathodically (potential range < 0V) or anodically (potential range > 0V) in LiClO$_4$-PC electrolyte. This is an interesting for the development of EC devices. It is however necessary to find out if the mechanisms outlined above interfere or not. A Fresh 80 nm thick layer sintered at 300 °C have been therefore switched in the whole potential range –3 to +1 V vs. Ag/AgClO$_4$-PC

Fig. 5.48 shows three galvanostatic measurements made in sequence with a total charge of 50 mC/cm^2 by applying

a) –5 µA/cm^2 then
b) +5 µA/cm^{2}again
c) –5 µA/cm^2 (as in a)

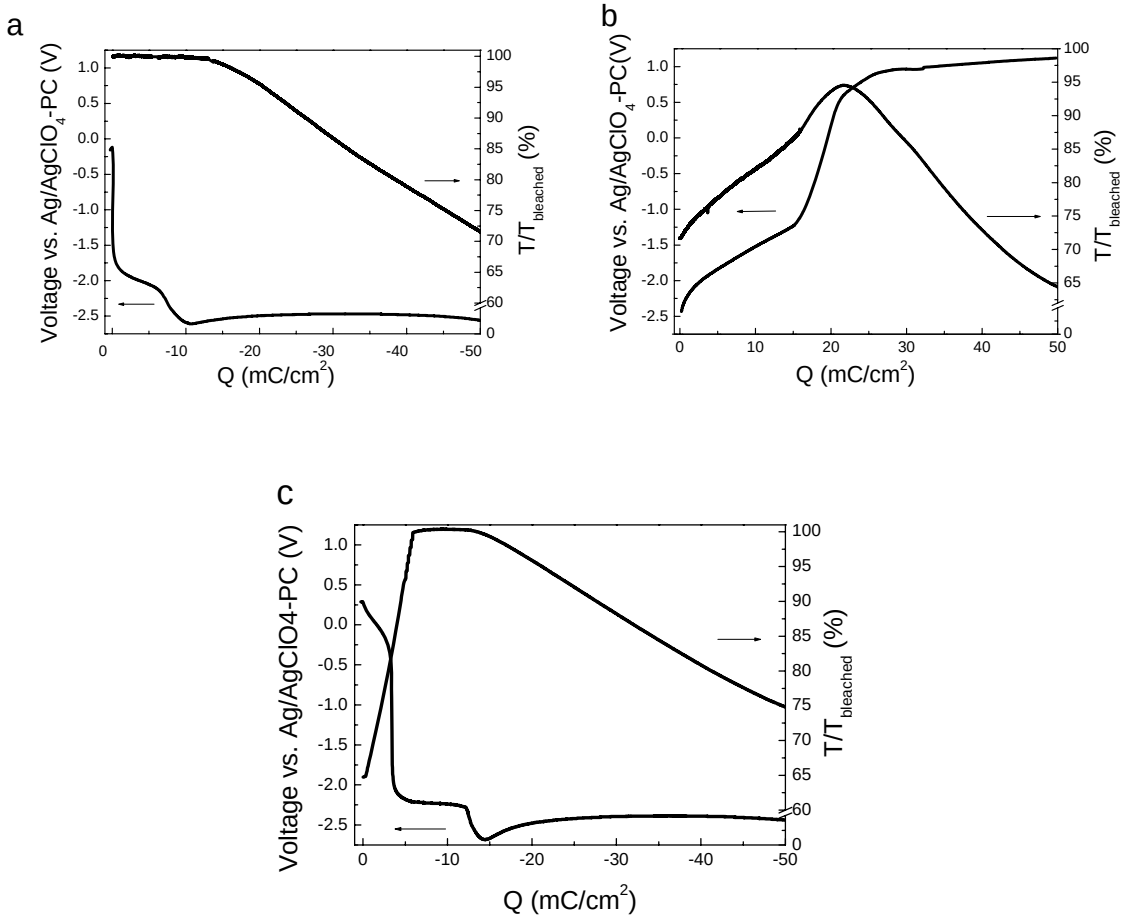

Fig. 5.48: Potential and transmittance (550 nm) evolution for 80 nm thick single NiO-TiO$_2$ layer (Ni content of 75 mol %) in LiClO$_4$-PC during a galvanostatic measurement applying (a) a negative current density of –5µA/cm^2, then (b) positive current of + 5µA/cm^2, then (c) again negative current of –5µA/cm^2

Fig. 5.48a is similar to that shown in fig. 5.41 and the results have been discussed already in section b). The coloration obtained after incorporating –50 mC/cm^2 was assumed to be due to simultaneous insertion of Li^+ and e^- and the composition of the layer was drastically altered.

The initial part of fig. 5.48b is also similar to fig. 5.44. However it is observed that the potential drastically increases after a charge insertion of about +15 mC/cm^2 to level up around + 1V. The transmittance starts also to increase later, passing by a maximum at potential of +0.5 V and then continuously decreases down to about T/T_b= 65 %.

In section a) it was shown that fresh NiO-TiO_2 layers could be slightly colored ($\Delta T/T_b$=9- 13 %) in this potential range (V> 0V vs. Ag/$AgClO_4$-PC) and this was explained by the incorporation of traces of OH^-. After a first Li^+ ion insertion however, the composition of the layer have been drastically altered so that the above mechanism is certainly not valid.

Therefore, without performing more detailed and certainly high complex investigations, it is not possible at the present time to propose a mechanism for this coloration.

Fig. 48c shows the results obtained by applying again a negative small current density of - 5 μA/cm^2. Since the layer is colored (see fig. 5.48b) the behavior recorded is different from that shown during the first galvanostatic test (fig. 5.48a). The potential drop to the last plateau at –2.5V occurs now in two steps and is accompanied by a very fast increase of the transmittance from $\Delta T/T_b$= 65 % up to 100 % (the complete bleaching of the layer) after using a charge of 5 mC/cm^2 only then as before the layer remains uncolored till the end of the first plateau and as before starts to color during the second plateau with exactly the same kinetics. The initial behavior is now identical to that found by Scrosati group [194] with fresh colored sputtered NiO layers. As the bleaching of the layer is fast and needs only about 5 mC/cm^2, the process may only involve electrons that recombine with the colored species. However such phenomenon is not observed with the defects that give rise to the coloration due to the insertion of Li^+ and e^- (fig. 5.46a), but only with those colored during the very slow coloration obtained after that deinsertion (fig. 5.48b).

5.6 Characterization of CeO_2-TiO_2 layer in KOH

A CeO_2-TiO_2 layer is used in this work as counter electrode together with a NiO-TiO_2 layer as working electrode to build electrochromic devices. So it is important to test it in KOH electrolyte.

Cyclic voltammetric recordings were performed in order to obtain electrochemical fingerprints of the studied CeO_2-TiO_2 layers in aqueous basic solution of 1 M KOH (fig. 5.49a). The potential in each measurement was swept from –1.2 to +0.7 V vs. SCE. A well defined anodic peak occurs at –0.238 V while the cathodic peak occurs at –0.63 V. The stability of the layers was checked by cycling up to 2000 cycles. A stable response was achieved after 50 cycles where no change in peak current density was noticed. The cathodic and anodic charges are almost the same indicating that the insertion process is highly reversible and no faradic process occurs in parallel to the electrochromic charging process (fig. 5.49b).

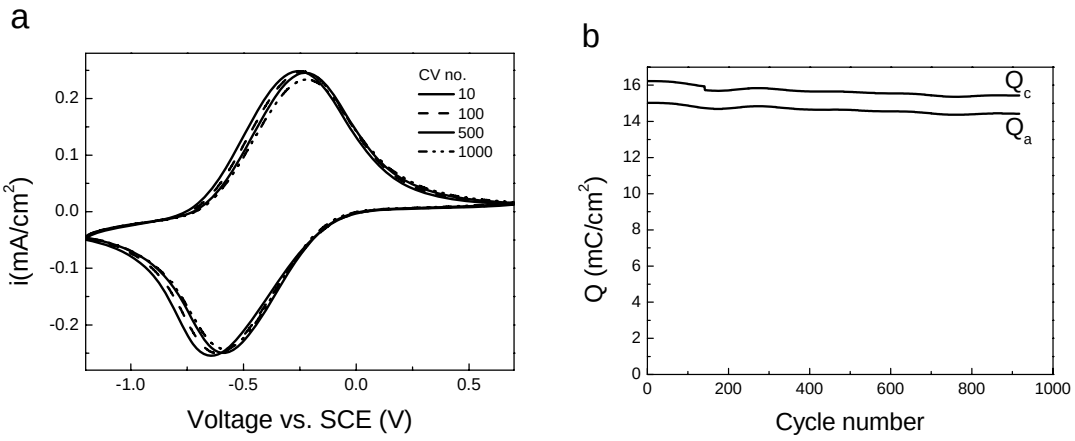

Fig. 5.49: Typical CV voltamogramms up to 1000 cycles for a 200 nm thick single CeO_2-TiO_2 layer heated at 550 °C, potential range -1.2 to 0.7V, scan rate 10 mV/s in 1 M KOH. (b) Calculated charge density in the anodic (Q_a) and cathodic (Q_c) range.

a) Layer thickness

The dependence of the CV response on the film thickness is depicted in fig. 5.50. The current density increases by increasing the thickness up to 240 nm. Increasing the layer thickness also shifts the anodic peak slightly to more positive potential values while the cathodic peak shifts to more negative potentials.

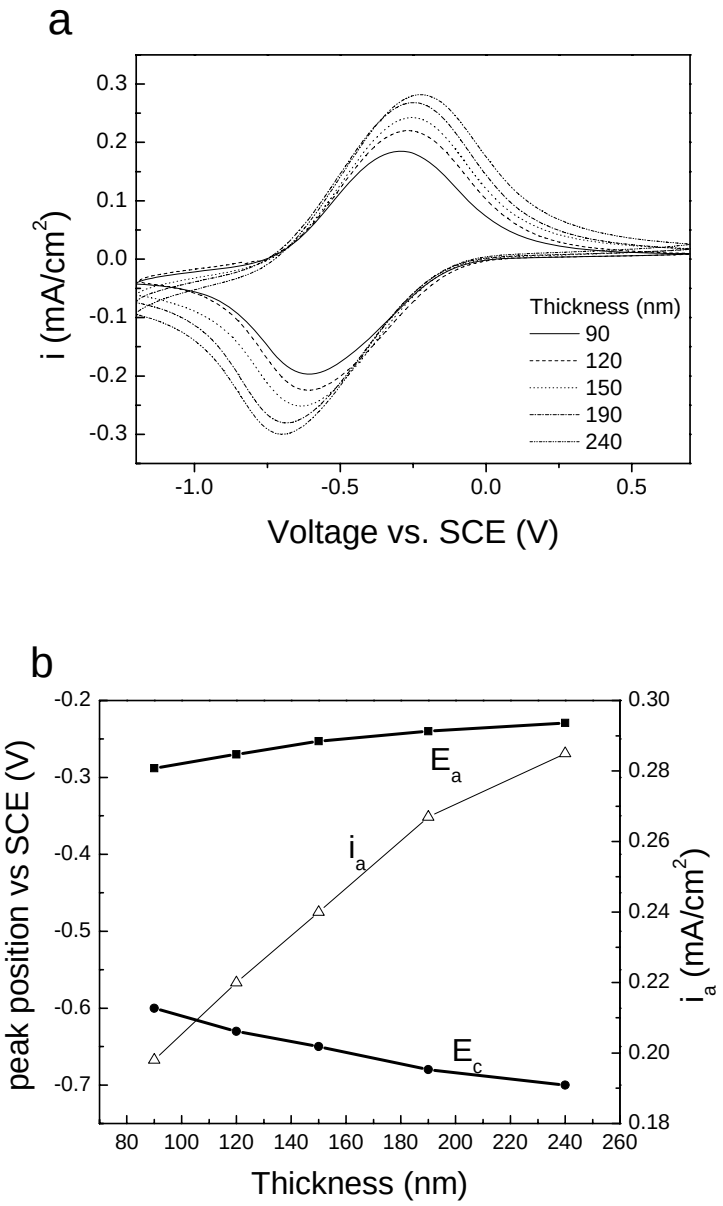

Fig. 5.50: 100th CV voltammogram (-1.2, +0.7 V vs. SCE, scan rate 10 mV/s) in 1M KOH of single CeO_2-TiO_2 layer of different thickness heated at 550 °C (b) corresponding anodic and cathodic peak positions and value of the peak current density.

For thick layers it is noticed that the value of the charge capacity slightly decreases during the first cycles compared to that of the thin layers (fig. 5.51).

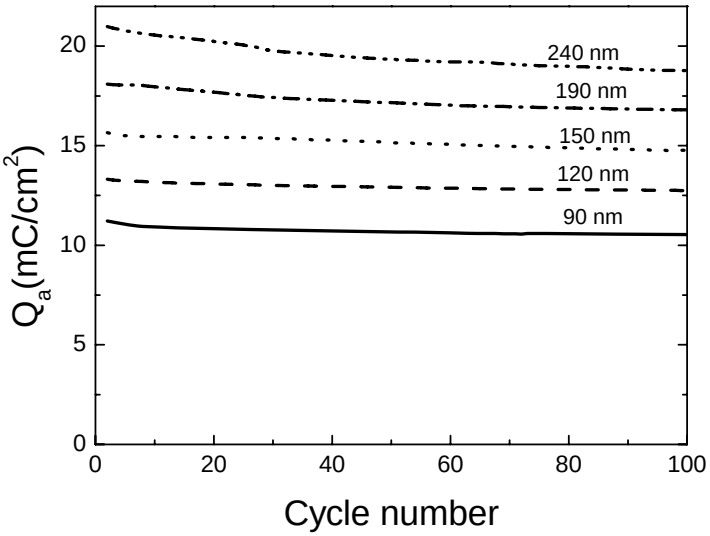

Fig. 5.51: Anodic charge density during 100 CV cycles (-1.2, +0.7 V, scan rate 10 mV/s) in 1 M KOH of single CeO_2-TiO_2 layers of different thickness heated at 550 °C.

b) Scan rate

CV voltammograms at different scan rates in the range between 1 to 7 mV/s and 10 to 500 mV/s are shown in fig. 5.52a and b respectively for single layer 200 nm thick. In both cases the value of the anodic and cathodic current density raises and at high scan rates the cathodic peaks are not completed.

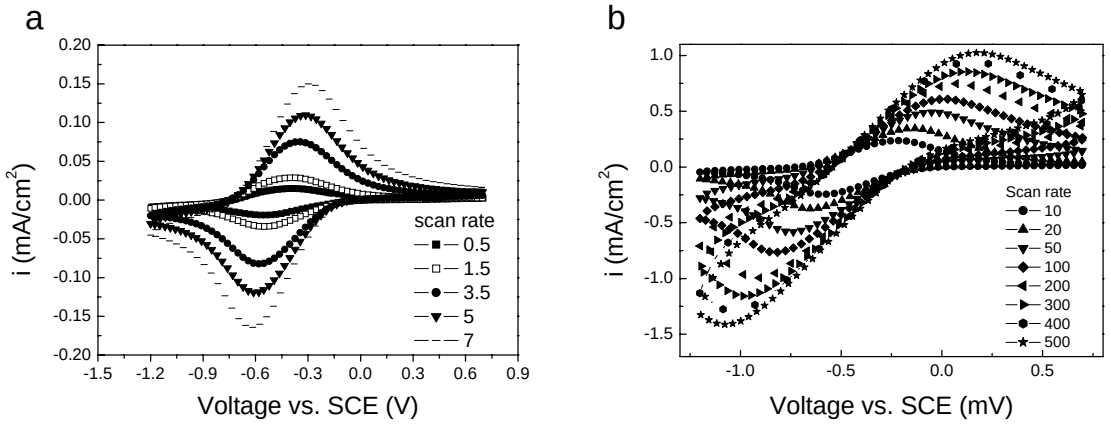

Fig. 5.52: CV voltammograms (-1.2, +0.7 V) of a 200 nm thick single CeO_2-TiO_2 tested in 1 M KOH at different scan rates (a) up to 10 mV/s (b) higher than 10 mV/s

In general, for a redox reaction to be reversible, the concentrations of the oxidized and reduced species at the electrode surface must be maintained at the values defined by the Nernst equation. In practical terms, a redox reaction is reversible if the rate of electrons

transfer is fast relative to the scan rate and if the oxidized and reduced species are stable on the experimental time scale (i.e., they do not undergo any significant chemical reactions). One advantage of cyclic voltammetry is that it is relatively easy to see from a cyclic voltammogram whether a system is reversible. The peak potential difference for a reversible system is about 60 -70 mV (depending on the temperature and the switching potential), and the peak currents are equal. In addition, the peak potential difference does not change with scan rate. If the electron transfer kinetics are slow, the peak potential separation is larger, and increases with increasing scan rate.

In our case, by increasing the scan rate up to 10 mV/s, the anodic and cathodic peaks positions and separations are almost constant (fig. 5.52a) indicating reversible redox reaction but by increasing the scan rate the systems deviates from the reversible one.

The anodic current densities are plotted as a function of the square root of the potential scan rate, $\nu^{1/2}$ (fig. 5.53). It is know that the current density is directly proportional to the rate of electrolysis at the electrode surface. Electrolysis occurs at the electrode surface in response to a change in potential in order to try to maintain the surface concentrations of the oxidized and reduced species at the values required by the Nernst equation. Therefore, the faster the rate of change of potential (i.e. the scan rate), the faster the rate of electrolysis, and hence the larger the current. For reversible systems the current peak density is directly proportional to the square root of the scan rate. Fig. 5.53 shows that the anodic current density is proportional to $\nu^{1/2}$ for scan rate $\leq$ 10 mV/s (see inset of fig. 5.53), indicating a reversible transfer of ions in the thin film. The slope increases by increasing the scan rate due to the change of the kinetics or reactions.

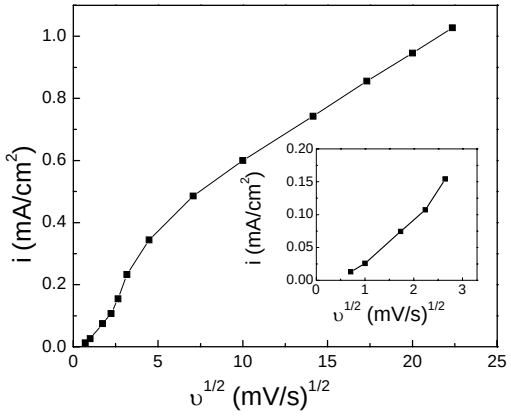

Fig. 5.53: Anodic peak current density of a 170 nm thick single CeO_2-TiO_2 tested in 1 M KOH measured during CV (-1.2, +0.7 V) at different scan rates versus the corresponding scan rate. Inset is magnification of the graph in the scan rate up to 10 mV/s.

c) Different electrolytes comparison (pH= 14)

Single CeO_2-TiO_2 layers, 200 nm thick, sintered at 550 °C have been then tested in different aqueous electrolytes, namely 1 M KOH, $C_{16}H_{36}NOH$ and LiOH. The pH of each electrolyte was 14. The layers show basically the same voltammogram characteristics in the three different electrolytes (fig. 5.54a). Slightly higher current densities are noticed with LiOH but the values decreases after 200 cycles in a similar way to that measured in KOH (fig. 5.54b). The layers tested in TBAOH could not be tested for more than 200 cycles due to the precipitation of the electrolyte.

As the CV voltamograms and the charge capacities of CeO_2-TiO_2 layer in the three different electrolytes are almost the same, it could be concluded that OH^- is the species which is responsible for the observed electrochemical activity of the layer in aqueous solutions in the potential range –1.2 to +0.7 V vs. SCE.

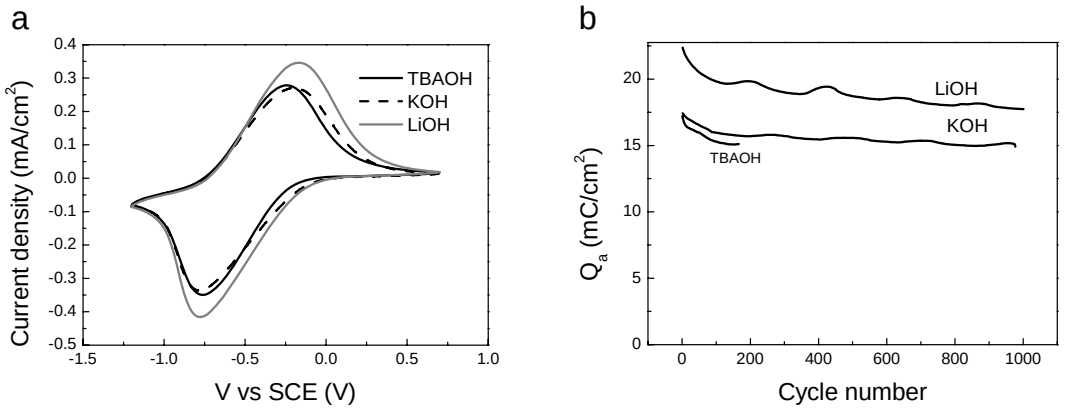

Fig. 5.54: (a) 2nd CV voltammograms (-1.2, +0.7 V vs. SCE) scan rates of 10 mV/s of 170 nm thick single CeO_2-TiO_2 tested in three different electrolytes (b) corresponding anodic charge densities versus cycle number.

5.7. Characterization of Nb_2O_5:Mo layer in KOH

EC devices have been also laminated using Nb_2O_5:Mo layers so it was also necessary to test their behavior in KOH electrolyte.

Fig. 5.55a presents typical cyclic voltammograms measured during the 2nd, 100th, 600th and 1000th cycles in KOH of a Nb_2O_5:Mo double layer sintered at 500 °C. The potential was cycled between –1.5 and +1.0V vs. SCE at a scan rate of 10 mV/s. These potentials were chosen to get the maximum transmittance change avoiding any side reactions such as oxygen evolution at the positive potential or hydrogen evolution at the negative potential.

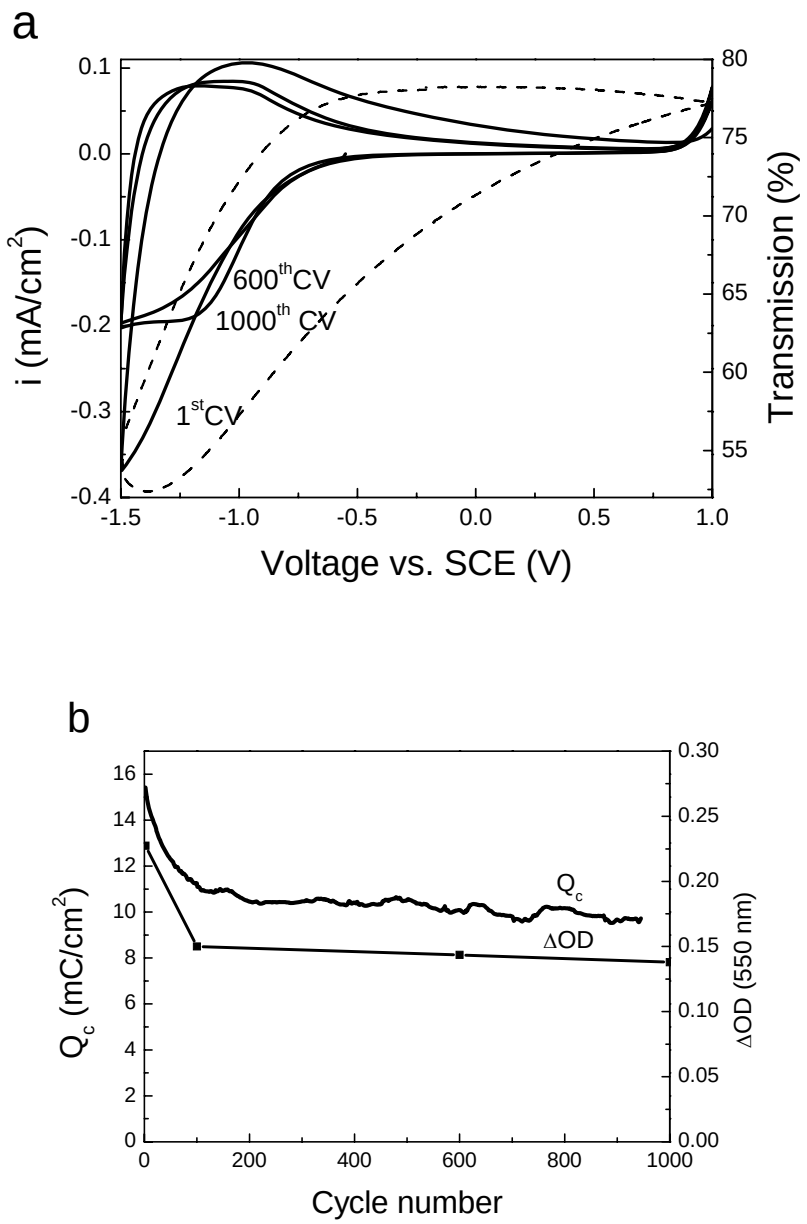

Fig. 5.55: Typical CV voltammograms up to 1000 cycles of a 160 nm thick double Nb_2O_5:Mo layer heated at 500 °C, potential range -1.5 to 1.0 V, scan rate 10 mV/s in 1 M KOH. The dotted line is the transmittance (T) measured during the 100th cycle at λ= 550 nm. (b) Corresponding charge capacity Q_c and change in optical density ΔOD.

A broad cathodic peak associated with the layer coloration is seen around –1.2 V. In the initial cycling, only one side of the peak is reached and it interferes with the hydrogen evolution peak at the end of the cathodic scan. By cycling, the peak becomes better defined and separated from the hydrogen evolution peak. A broad anodic peak accompanied by the

layer bleaching occurs in the range of –1.1 V. No electrochemical activity is seen in the positive potential range but it is found important to sweep the potential to + 1 V during the anodic scan to get a better bleaching of the layer. The current density and consequently the corresponding charge capacity (fig. 5.55b) decrease sharply up to 100 cycles (from 16 down to 10.7 mC/cm^2) then the values remain practically stable. The stable value of the charge capacity of double Nb_2O_5:Mo is about 10.3 mC/cm^2, a value lower than that of single CeO_2-TiO_2 (14.5 mC/cm^2)

The change in optical density also decreases by cycling, intensively up to 100 cycle and then slowly. A rather small value of 0.15 is then reached.

The transmittance spectra of the layer in the colored and bleached states are shown in fig. 5.56 with the corresponding ΔOD. The layer was colored and bleached by polarizing it for 1 min at –1.5 V and +1 V respectively. The transmittance change occurs mainly in the visible range but the absorption peak is broader than that of NiO-TiO_2 layer.

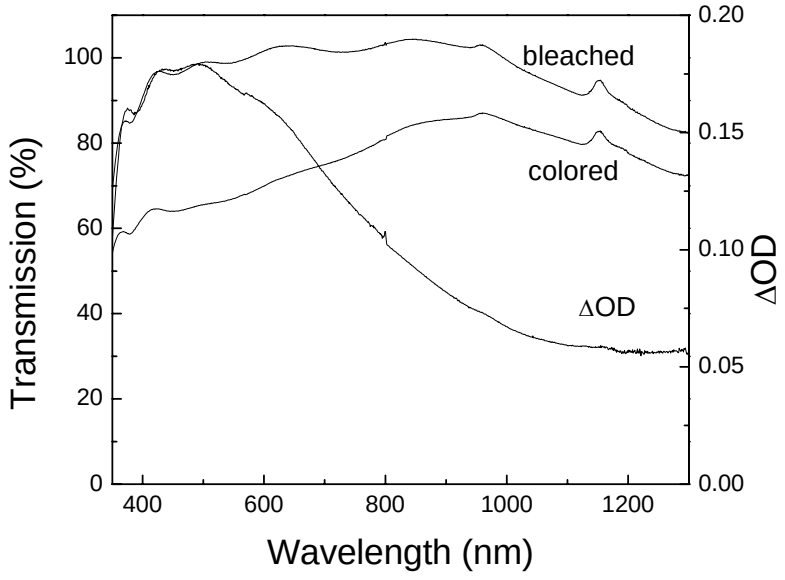

Fig. 5.56: Transmittance spectra of a 160 nm thick double Nb_2O_5:Mo layer heated at 500 °C in colored and bleached states. The layer was colored and bleached by polarizing it for 1 min at –1.5 V and +1 V respectively.

5.8 Electrochromic Windows

NiO-TiO_2 layers were used to make electrochromic windows. The devices have been laminated using different configurations, where the layer was used as working electrode in couple with either a CeO_2-TiO_2 or a Nb_2O_5 :Mo layer both acting as counter electrode and using either a liquid KOH or a gel KOH electrolyte. Windows with the configuration

where the NiO-TiO_2 layer was sued as counter electrode in couple with a sol-gel WO_3 layer as working electrode and the INM organic-inorganic composite electrolyte were also tested.

5.8.1 EC-devices made with a liquid KOH electrolyte

a) ***Windows with single NiO-TiO_2 layer***

5x10 cm^2 windows with the configuration glass/ FTO/ NiO-TiO_2/ 1 M liquid KOH/ CeO_2-TiO_2/ FTO/ glass were laminated. A single 80 nm thick NiO-TiO_2 layer sintered at 300 °C was used. The CeO_2-TiO_2 layer was sintered at 550 °C for one hour and had a thickness of 200 nm. The device was filled with 1 M KOH and tested in the potential range –1 to +1.2 V.

Typical CV voltammograms of the EC devices are shown in fig. 5.57. The shape remains practically the same. A small anodic peak which disappears by cycling occurs in the range of 0.5 mV. Only the raising side of a strong second anodic peak is reached within the used potential range. A single well defined cathodic peak occurs around +0.43 V. The current density of the EC device increases during the early cycles then starts to decrease slightly from the 1000th CV cycle, whereas the positions of the anodic and cathodic peaks do not change significantly.

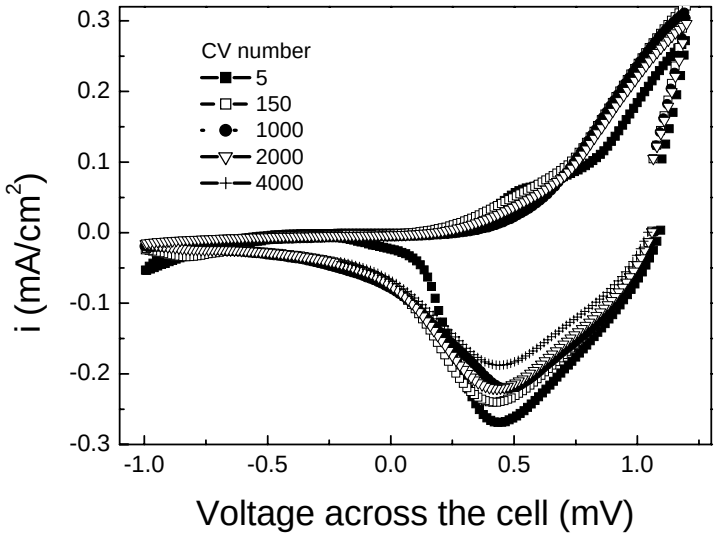

Fig. 5.57: CV voltamogramms of a window with the configuration glass/ FTO/ NiO-TiO_2/ 1 M liquid KOH/ CeO_2-TiO_2 /FTO/glass tested in the potential range –1 to 1.2 V, scan rate 10 mV/s. An 80 nm thick single NiO-TiO_2 layer sintered at 300 °C was used with a 200 nm thick single CeO_2-TiO_2 layer sintered at 550 °C for one hour.

The transmittance spectra of the window in the bleached and colored states are shown in the right side of fig. 5.58 with the corresponding ΔOD. The main transmittance change occurs in the visible and infrared region with a maximum of ΔOD at 432 nm and the color of the window is brown (same ΔOD as in fig. 5.13). Left side shows a picture of the window in the bleached and colored states.

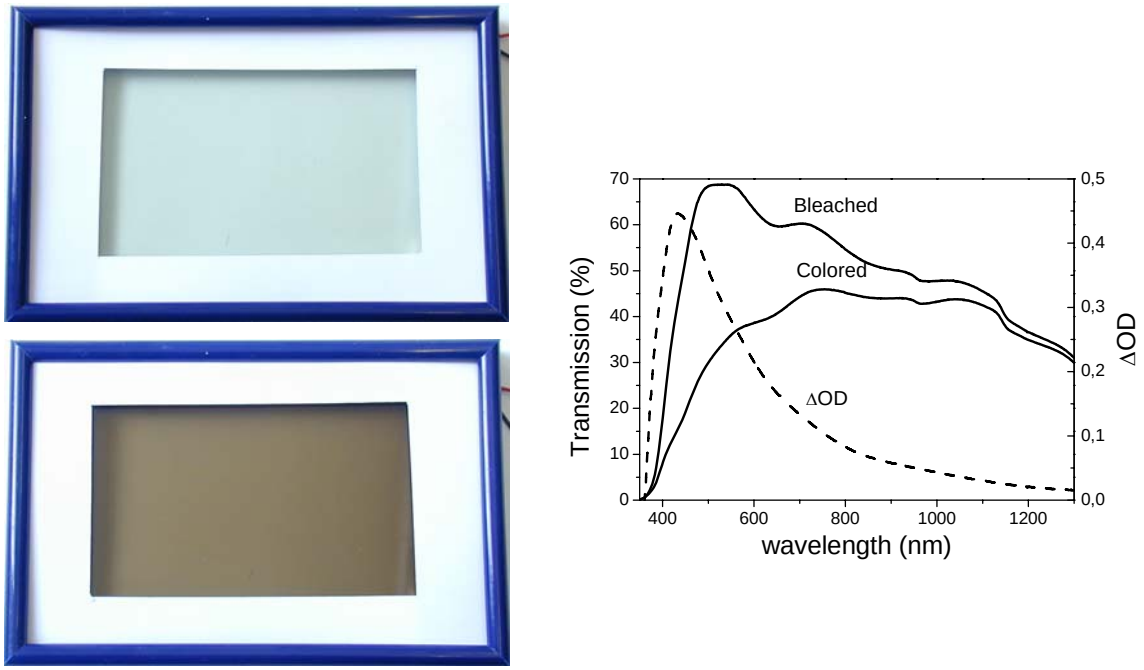

Fig. 5.58: Left pictures in the bleached and colored states of a window with the configuration glass/ FTO/ NiO-TiO_2/1 M liquid KOH/ CeO_2-TiO_2 / FTO/ glass obtained by polarization for 1 min at +1.2 and –1 V respectively. Right corresponding transmittance spectra and ΔOD.

Fig. 5.59 shows the evolution of the transmittance and optical density (at λ= 550 nm) as a function of the CA cycle number. Drastic variations are observed by cycling. The transmittance of the bleached state of the window is initially rather high, about 65 % but decreases continuously so that the window becomes permanently colored. The transmittance of the colored state is initially rather low, 38 % and decreases down to 20 %. As a consequence, ΔOD is initially about 0.23, increased up to 0.30 after 150 cycles, remains practically stable up to about 1000 cycles and then decreases drastically to 0.16.

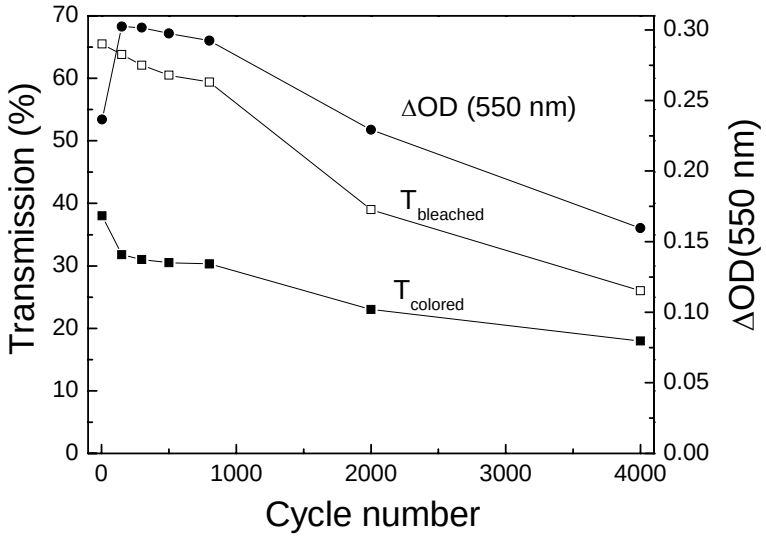

Fig. 5.59: Transmittance and ΔOD of a window with the configuration glass/ FTO/ NiO-TiO_2/ 1 M liquid KOH/ CeO_2-TiO_2 / FTO/ glass in the bleached and colored states at λ = 550 nm as a function of the number of CA cycle (-1 V, +1.2 V, 1min).

The time evolution of the transmittance of the EC devices measured at 550 nm during different CA cycles (-1 V, 1 min/ +1.2 V, 1 min) is shown in fig. 5.60. The kinetics of coloration of the devices is rather fast (< 30s) and does not change by cycling. That of the bleaching is even faster in the early cycles but becomes rather slow. As also shown in fig. 5.59 by further cycling the window gained a permanent brown color. This permanent coloration was also encountered when NiO-TiO_2 layer cycled in KOH (section 5.3).

The corresponding inserted and deinserted charges are shown in fig. 5.60b. The charge insertion kinetics follow the same behavior as the change in transmittance. The cathodic charge capacity increases in the activation period (up to 1000 cycles) then decreases by cycling. The inserted charge value is 8 mC/cm^2.

The current density measured during the 1000 cycle is shown inset fig. 5.60b. The value of the anodic current density does not reach the zero value after 1 min indicating that a side electrochemical reaction beside the electrochromic reaction continues to happen at the positive potential and this results in higher measured anodic charge density.

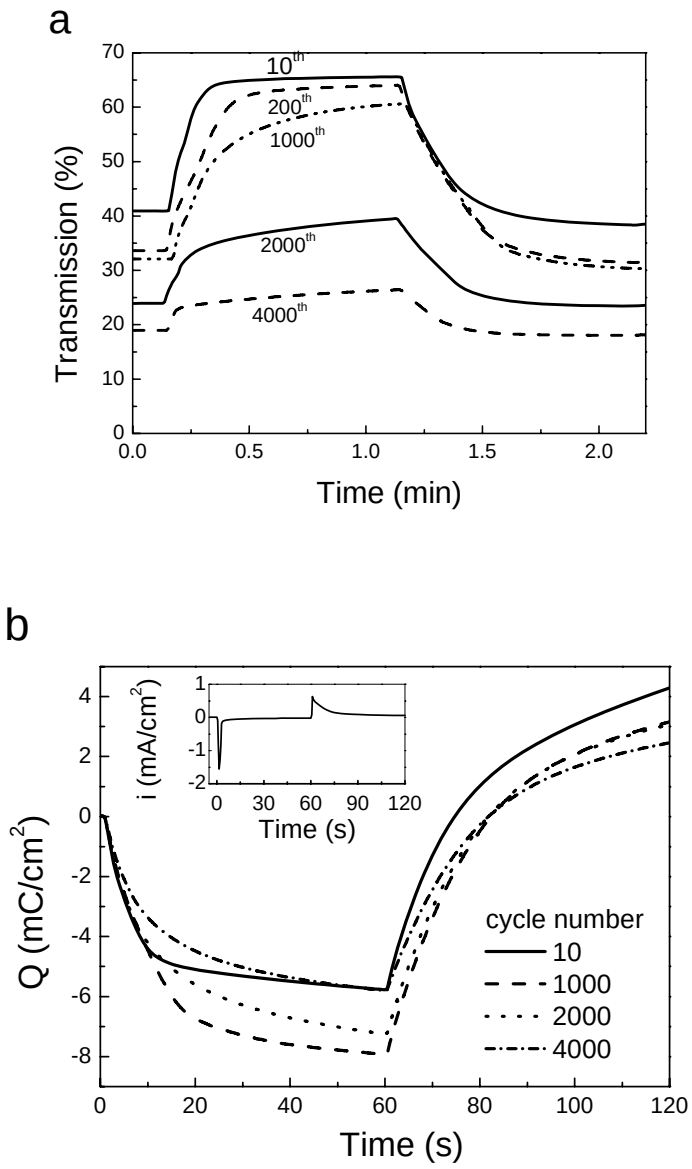

Fig. 5.60: Time evolution at λ = 550 nm of EC-device glass / FTO/ NiO-TiO_2/ 1 M liquid KOH / CeO_2-TiO_2 /FTO/glass during different CA cycles (-1 V, +1.2 V, 1min) (b). Corresponding inserted and de-inserted charges, inset: the current density during the 1000th CA cycle.

b) Comparison of windows made with single and double NiO-TiO_2 layers

A double NiO-TiO_2 layer has a higher thickness and its use should improve the charge capacity as well as the stability of the device at long time cycling (see section 5.3). In order to test these parameters, windows with the configuration K-glass/NiO-TiO_2/KOH/CeO_2-TiO_2/K-glass with double NiO-TiO_2 layer were mounted and tested in the same potential range and conditions as the windows mounted with a single layer (see a) above). The first layer was deposited on K-glass at a withdrawal speed of 3 mm/s and sintered at 300 °C.

The second layer was deposited on the top of the first one and sintered at the same temperature. The thickness of the single layer was 80 nm, so that 160 nm is expected for the double layer.

Fig. 5.61 shows the voltammograms of windows made with single and double NiO-TiO_2 layers. They have practically the same shape except a small shift in the anodic and cathodic peak positions of the window with double NiO-TiO_2. No difference is noticed in the current density of the two windows.

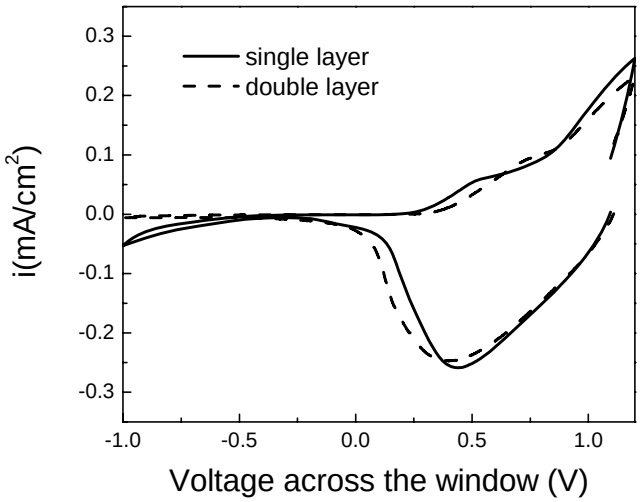

Fig. 5.61: CV voltammograms of windows with the configuration K glass/ NiO-TiO_2/ KOH/ CeO_2-TiO_2/ K-glass with single (—) and double (…) NiO-TiO_2 layers.

However the use of a double layer improves especially the cycling stability of the transmittance of the window in the bleached state that decreases only slightly by cycling from 70 % (initial cycles) down to 60 % after 7000 CA cycles so that the transmittance of the device in the bleached state remains largely unaltered contrary to the behavior observed with a single layer (fig.5.62a). However the transmittance of the colored state is somewhat higher (30 % after 7000 cycles). The change of the optical density at 550 nm is therefore somewhat different and the device still works very well after 7000 cycles. By further cycling a corrosion starts to occur at the edge of the devices.

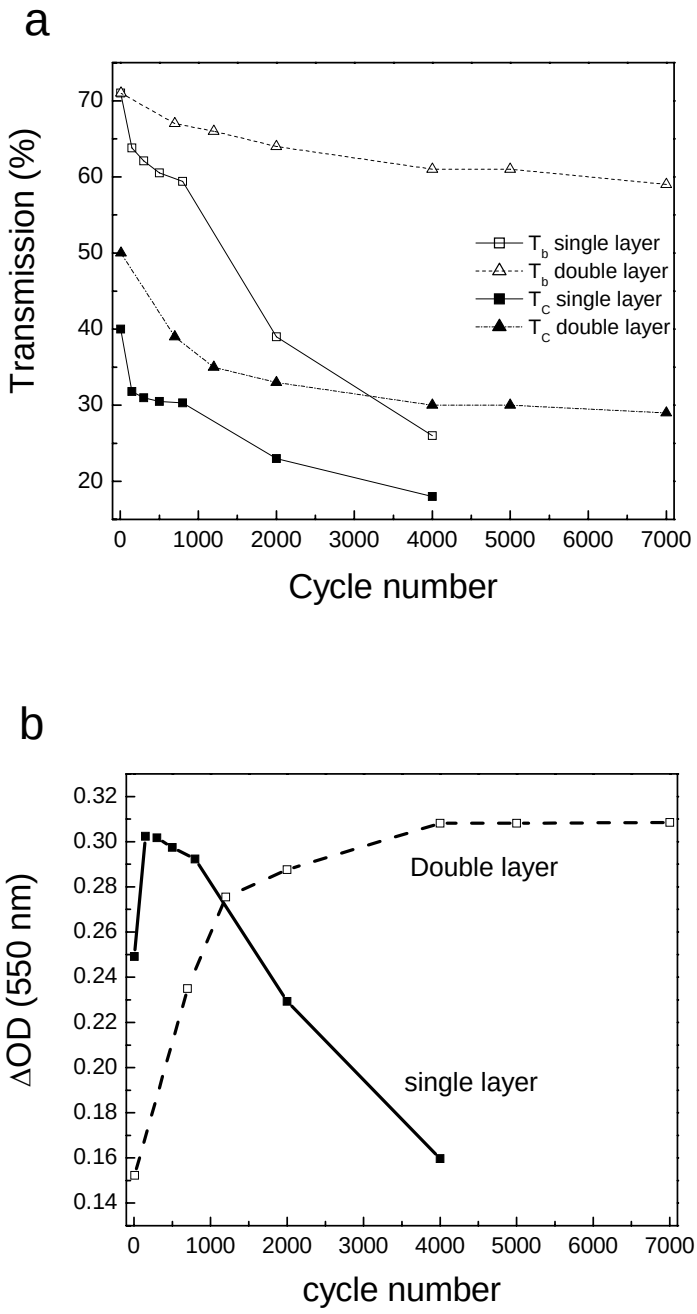

Fig. 5.62: (a) Transmittance of the bleached and colored states at $\lambda = 550$ nm of an EC-device glass/ FTO/ NiO-TiO_2/1 M liquid KOH/ CeO_2-TiO_2/ FTO/glass mounted with a single and a double NiO-TiO_2 layer, during CA cycles (-1 V, +1.2 V, 1min).(b) corresponding change in optical density.

c) Slow kinetics

As seen above, the devices gain permanent brown color by cycling, due to NiO-TiO_2 layer. This permanent coloration is accompanied to a slow bleaching kinetics and low cathodic charge capacity of the device when polarized at negative potential of -1.2 V. In order to

check whether it is possible to bleach the device to the initial transmittance value by inserting the same amount of charge involved in coloration, the device was polarized galvanostaically at small negative current of –5 μA/cm^2 for a long time to obtain total inserted charge of 9 mC/cm^2.

The transmittance and the potential change were measured during galvanostatic measurement for cells built with single and double NiO-TiO_2 layers (fig. 5.63). The lower potential limit was set to –2 V. It is noticed that –9 mC/cm^2 was enough to increase the transmittance of the window with double layer from 30 to 63 % while the potential across the window drop to –1.2 V only. For a window with single NiO-TiO_2 layer, -9 mC/cm^2 increased the transmittance of the window from 31 to 57 % only while the potential across the window dropped down to 1.85 V. This measurement carried out after cycling the cell for 2000 CA (-1,1.2V/60s).

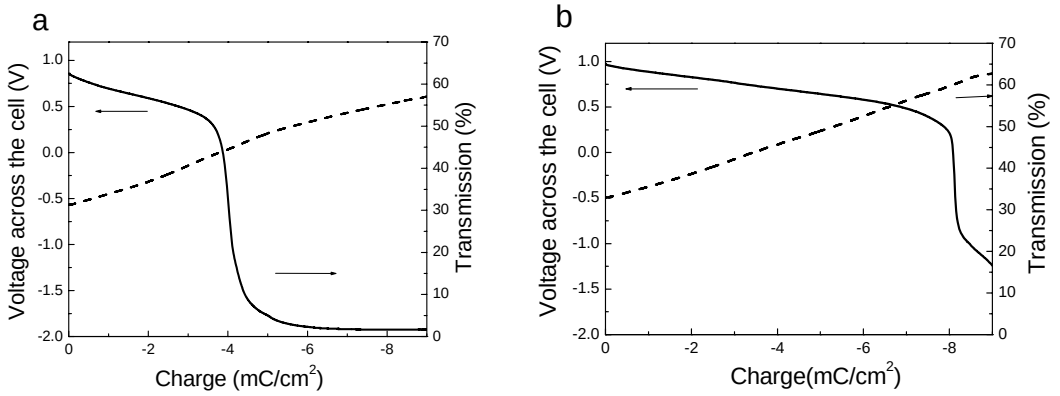

Fig. 5.63: Potential and transmittance evolution measured at 550 nm EC-device glass/ FTO/ NiO-TiO_2/ 1M liquid KOH/ CeO_2-TiO_2/ FTO/ glass with single (a) and double NiO-TiO_2 layer (b) during chronopotentiometric measurement at small negative current density of -5μA/cm^2.

Another measurements have been done to bleach the window by polarizing it in the colored state at the negative potential (-1 V) for different time periods (see fig. 5.64). This measurement was carried out after cycling the window for 7000 cycles. It was found that the device could be effectively bleached practically to the same initial value (T= 68 %) after applying the potential for 90 minutes. However when the window is cycled again between –1 V and 1.2 V (1 min) it could only be bleached to the level it reached before (59 %). This means that there are at least two different coloring sites (with two different kinetics) one needed much more energy to be bleached. It may be possible that the initial sites in bleached states β-$Ni(OH)_2$ are slowly transformed by cycling into α-$Ni(OH)_2$ ones.

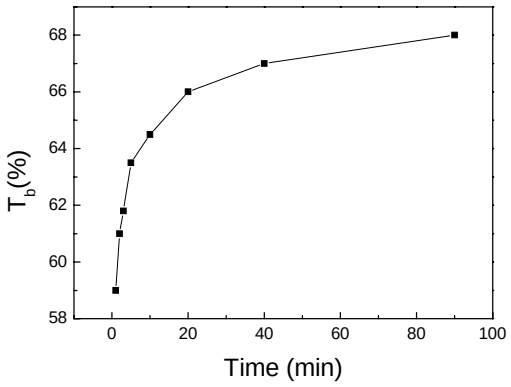

Fig. 5.64: Transmittance value of the bleached state reached by polarizing the window at the negative potential (-1 V) for different period.

d) Potential range

Two windows with the same configuration K-glass/NiO-TiO_2/KOH/CeO_2-TiO_2/K-glass have been tested by cycling between two different potential ranges, namely (–1 to +1.2V) and (–1 to +1.9 V). Double NiO-TiO_2 layer sintered at 300 °C after each coating run and single CeO_2-TiO_2 layer 200 nm thick, sintered at 550 °C for one hour were used. Fig. 5.65 represents the voltammograms of the two windows.

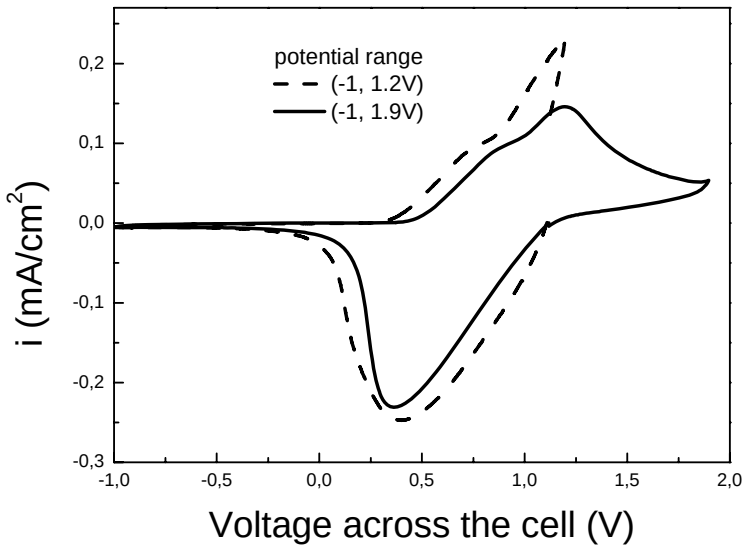

Fig. 5.65: CV voltammograms of windows with the configuration K glass/NiO-TiO_2/KOH/CeO_2-TiO_2/K-glass with double NiO-TiO_2 layers cycled in two different potential ranges (-1 to +1.9 V)(—) and (-1 to +1.2 V) (---) scan rate 10 mV/s.

Two full anodic peaks appear within the potential range –1 to +1.9 V, the first occurring around 0.8 V, the second around 1.2 V. One well defined peak appears in the cathodic scan

in the range of 0.3 V. The voltammogram of the window cycled between –1 and 1.2 V has the same feature but the second anodic peak is not complete and only the raising edge of the peak is reached. Beside the electrochromic reaction another reaction is expected to occur at the positive potential. The current density does not go to zero in the falling edge of the second anodic peak, but, on the contrary, it starts to increase again probably because of the oxygen evolution.

Although the second anodic peak is complete for –1 to +1.9 V scan range, the transmittance change, ΔOD and the long time stability of the devices are comparatively worse (see fig. 5.66). This confirms that the use of a higher positive potential leads to a faster degradation of $NiO\text{-}TiO_2$ layer as discussed before in section 5.3b.

Therefore increasing the positive voltage range to get the full second anodic peak did not improve the coloration contrast of the window and on the other hand caused a faster degradation of the device.

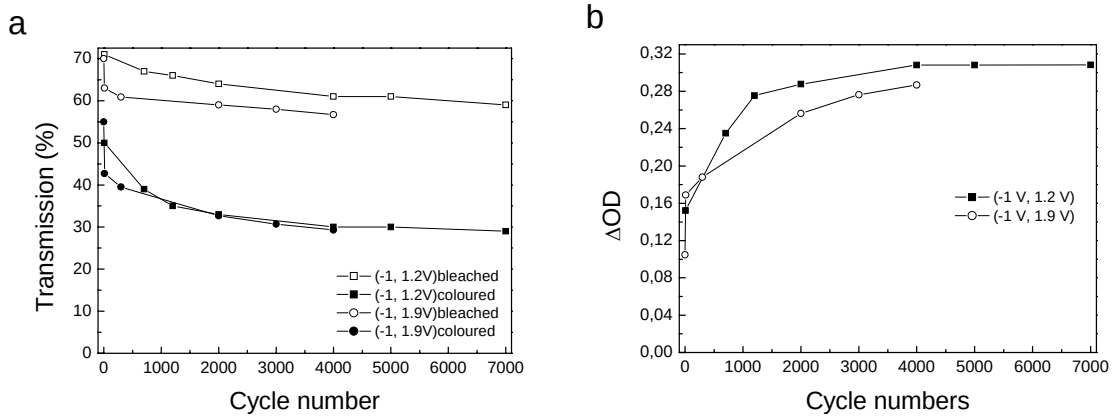

Fig. 5.66: (a) Transmittance of the bleached and colored states measured at 550 nm of EC-device glass/FTO/$NiO\text{-}TiO_2$/1 M liquid KOH/$CeO_2\text{-}TiO_2$ /FTO/glass with double $NiO\text{-}TiO_2$ layer, during CA cycles in two different potential ranges. (b) corresponding change of the optical density.

A macroscopic pictures of EC devices with double $NiO\text{-}TiO_2$ layer before and after degradation are shown in fig. 5.67.

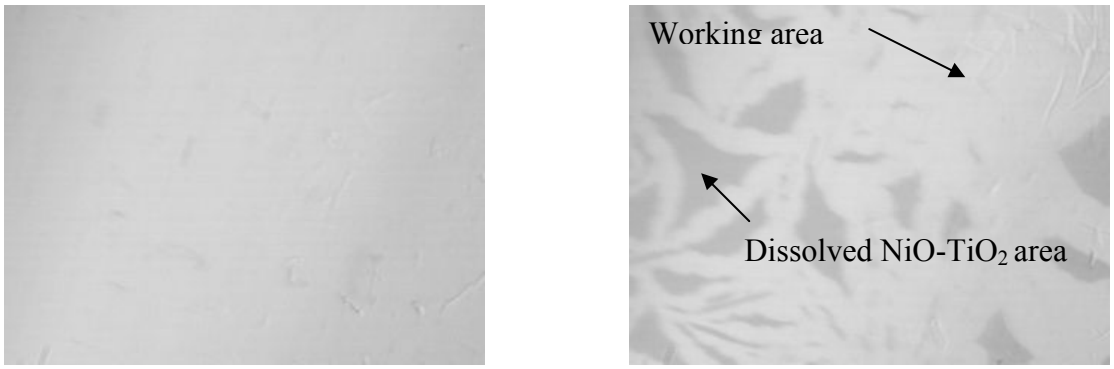

Fig. 5.67: Macroscopic pictures of EC devices with the configuration device glass/ FTO/ NiO-TiO_2/1 M liquid KOH/CeO_2-TiO_2 / FTO/ glass with double NiO-TiO_2 layer before (left) and after degradation (right).

5.8.2 EC-devices built with NiO-TiO_2 layers protected against corrosion

The long time stability of the devices based on NiO-TiO_2 layers is not high (almost 7000 cycles) as layers degrade when cycled in KOH electrolyte. It is known from the literature that thin layers of dielectric oxides may be used as anticorrosion layers. Following these ideas thin layers of ZrO_2, TiO_2, Al_2O_3 and CeO_2-TiO_2 (all 20 to 25 nm thick) have been deposited on top of the NiO-TiO_2 layer to improve the corrosion resistance in KOH electrolyte and therefore the cycling stability. After depositing single NiO-TiO_2 layer and sintering at 300 °C, a thin protective layer was deposited by dip coating at a very small drawing speed (0.5 mm/s) and then sintered at 300 °C. It was not possible to use higher temperature (>500 °C) in order to get crystallized dielectric thin films as recommended for anti corrosion coatings since the high temperature results in poor electrochromic response of NiO-TiO_2. Fig. 5.68 shows the CV voltammograms of devices assembled using such NiO-TiO_2 protected layers.

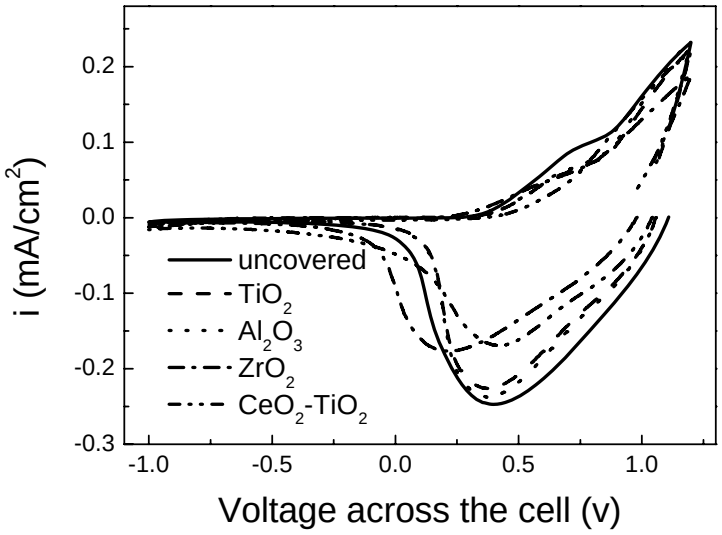

Fig. 5.68: 1000th CV voltammogram (-1 to +1.2 V), scan rate of 10 mV/s of windows with the configuration K glass/ protected NiO-TiO_2 /KOH/CeO_2-TiO_2/K-glass.

The voltammograms keep the same shape with comparable anodic and cathodic current peak densities. Only when ZrO_2 was used as protecting layer a shift to lower positive potential is noticed with a clear decrease in the current density.

The changes in optical density of devices built using unprotected and protected NiO-TiO_2 have almost the same behavior. It increases in the beginning (i.e. during activation period) then starts to decrease. The use of protected layers improves the long time stability of the devices (e.g. 18000 cycles with ZrO_2) but the value of ΔOD is smaller (fig. 5.69).

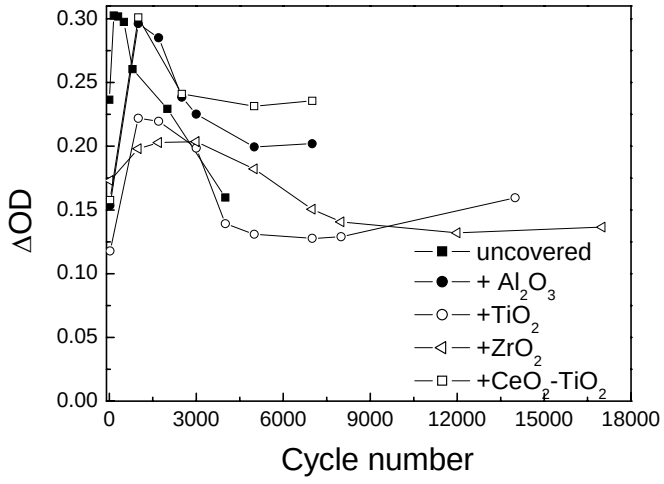

Fig. 5.69: Change in optical density with the CA cycle number (-1, +1.2 V/1 min) of windows with the configuration K glass/protected NiO-TiO_2/KOH/CeO_2-TiO_2/K-glass.

5.8.3 EC-devices with new KOH based organic electrolyte

Windows made with liquid electrolytes are not recommended especially when large size devices are used. Moreover aqueous KOH may burn the skin if a window is broken. A new electrolyte containing KOH has been therefore developed in order to assemble almost all solid state devices. A description of the preparation method is given in the experimental section. Windows with the configuration K-glass/ NiO-TiO_2/ starch (KOH)/CeO_2-TiO_2/ K-glass have been assembled and tested in the voltage range –0.7 V to 1.9 V. Double180 nm thick NiO-TiO_2 layers, has been used with single 200 nm thick CeO_2-TiO_2 layers.

Fig. 5.70 represents typical CV voltammograms (scan rate 10 mV/s). The first CV shows two anodic peaks, the first one is weak and occurs around 0.8 V while the other is strong and occurs in the range of 1.4 V. One well defined cathodic peak occurs around 0.7 V. The shape is very similar to those already presented (see fig. 5.65) and typical of NiO-TiO_2 layer. By cycling the strong anodic peak disappears and the anodic current density becomes very small. On the other hand the cathodic peak persists with the same shape and becomes even more intense with a slight shift to lower positive values (see e.g. 50th cycle) but, then starts to decrease and shift back to higher positive values.

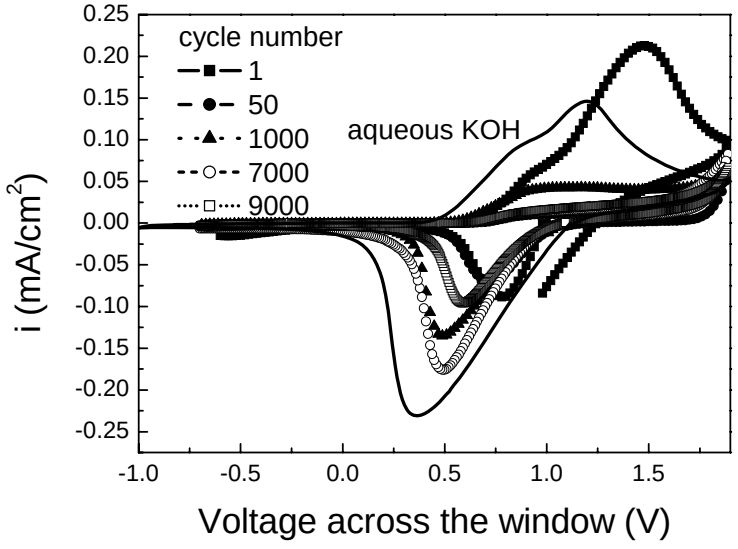

Fig.5.70: CV voltamogramms up to 9000 cycles of a window with the configuration glass/ FTO/ NiO-TiO_2/ gel KOH/ CeO_2-TiO_2 / FTO/ glass tested in the voltage range –0.7 to +1.9 V scan rate 10 mV/s. Solid curve is 1000th CV of window with same configuration but with aqueous KOH electrolyte (for comparison).

All voltammograms present the same general characteristic but a small shift of the second anodic peak to higher positive potentials for the window filled with starch (KOH) when compared with voltammogram of window with the same configuration but filled with aqueous KOH electrolyte. The cathodic peak is shifted to higher positive potential also and occurs in the range of 0.7 V while that of windows filled with KOH is broader and occurs in the range of 0.25 V.

The transmittance spectra of the window in the bleached and colored states are shown in fig. 5.71 with the corresponding ΔOD. The main transmittance change occurs in the visible and infrared region with a maximum of ΔOD at 432 nm and the color of the window is brown (same ΔOD as in fig. 5.13)

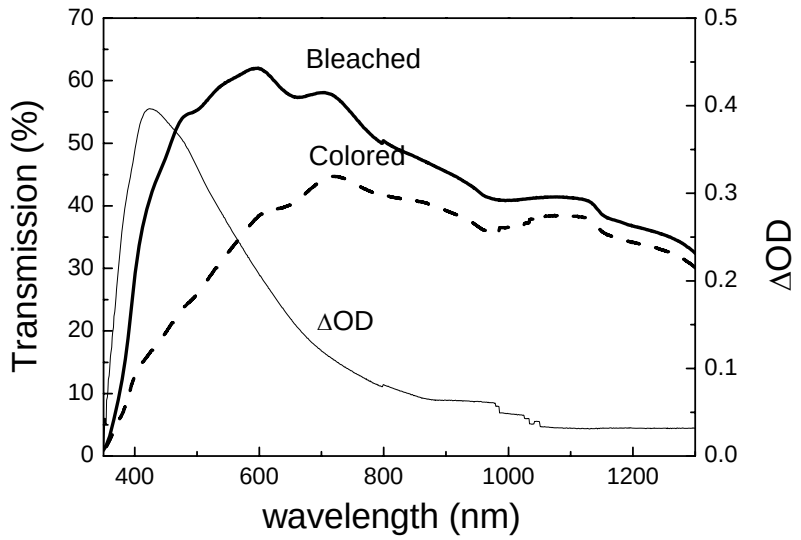

Fig. 5.71: Spectra in the bleached and colored states and ΔOD of a window with the configuration glass/ FTO/ NiO-TiO_2/ 1 M STARCH(KOH)/CeO_2-TiO_2/ FTO/ glass obtained by polarization for 1 min at +1.9 and –0.7 V respectively.

Fig. 5.72 represents the corresponding transmittance of the bleached and colored states and the change in optical density (ΔOD) with cycle number. During the first cycle the window exhibits a high transmittance change (70 % down to 26 %) without any activation period and ΔOD is rather high (0.42). In the next few cycles $T_{bleached}$ decreases from 69 to 61 % and $T_{colored}$ reverse from 26 to 48 % and ΔOD decreases from 0.42 to 0.1. These variations reflect the strong variation observed in the voltammograms in fig. 5.70. The efficiency of

the window improves again by cycling where ΔOD increases up to 0.27 after 2000 cycles then starts to decrease again gradually.

Comparing the change in optical density. It is found that of the window filled with KOH starts with a low ΔOD value (0.1) and increases gradually up to 0.29 after 4000 cycles when corrosion of the layer starts. On the other hand ΔOD of windows filled with starch (KOH) electrolyte is high initially (0.42), decrease in the initial cycles, but follow the same behavior as that of the referee cell (filled with KOH) till 2000 cycles and then decreases.

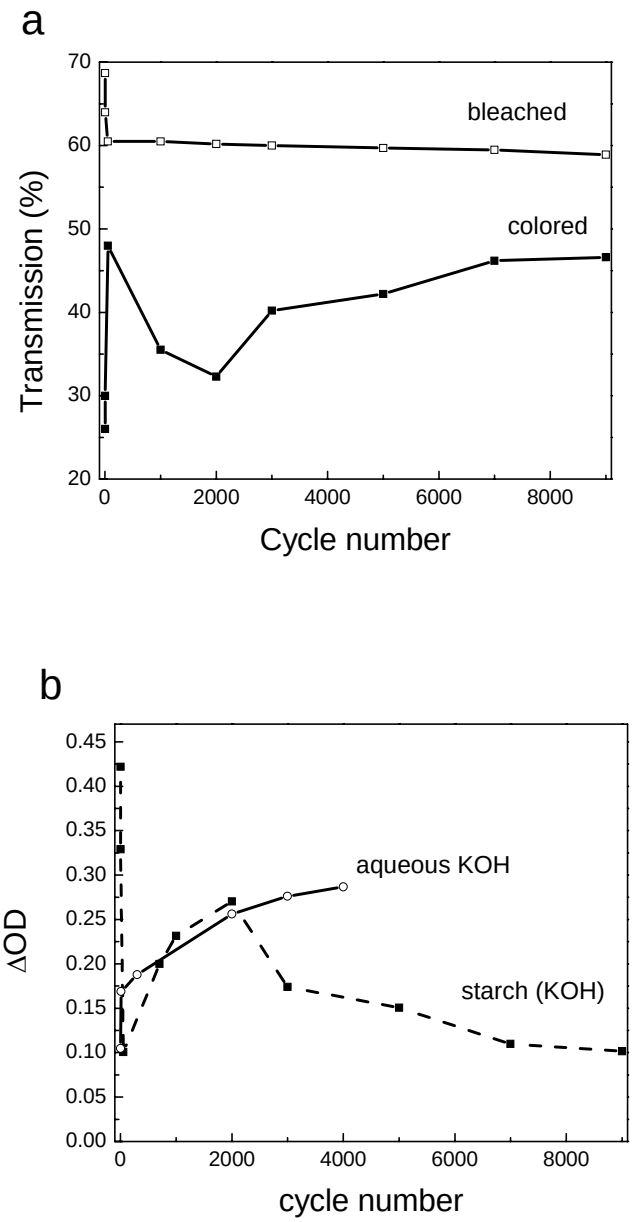

Fig. 5.72: (a) Transmittance of the bleached and colored states versus CA cycle number (-0.7, 1.9V/ 1min) of a window with the configuration K-glass/ NiO-TiO_2/ Starch (KOH)/ CeO_2-TiO_2/ K-glass. (b) Corresponding ΔOD of window, the dotted line is ΔOD of a window with same configuration but filled with aqueous KOH electrolyte (for comparision).

a) Kinetics

The kinetics of the coloration of the window is rather slow. In order to check if it is possible to get deeper coloration, galvanostatic tests using different small currents (5, 10, 15 and 20 μA/cm^2) have been made for different time periods keeping the total involved charge of 13m C/cm^2 and limiting the potential to maximum of +2 V.

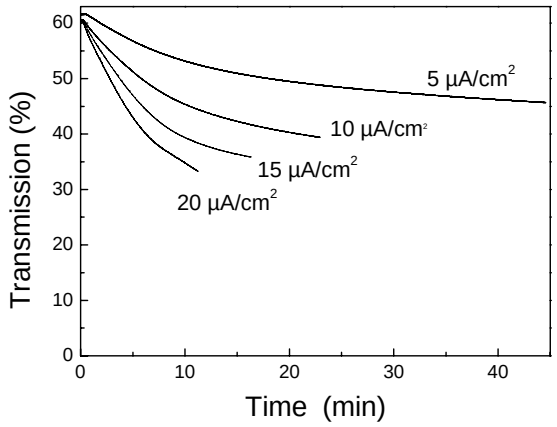

Fig. 5.73: Evolution of the transmittance of windows with the configuration K-glass/ NiO-TiO_2/ Starch (KOH)/ CeO_2-TiO_2/ K-glass during galvanostatic measurements performed using different current densities.

The coloration kinetics get faster by increasing the current density applied to the window, and the potential across the window did not exceed the secure level (2V) in all cases. The fastest coloration was obtained by applying a current density of +20μA/cm^2 and it took 11 min to reach a transmittance change from 60 % down to 33 % (ΔOD= 0.3).

b) Memory test

Window has been colored by polarizing it at the positive potential (+1.9V) for 1 min. The transmittance was then measured in open circuit to check the memory of the window i.e. to get the evolution of the transmittance of the colored window. The result is shown in fig. 5.74. The window transmittance increases from 39 % to 49 % after 1 hour.

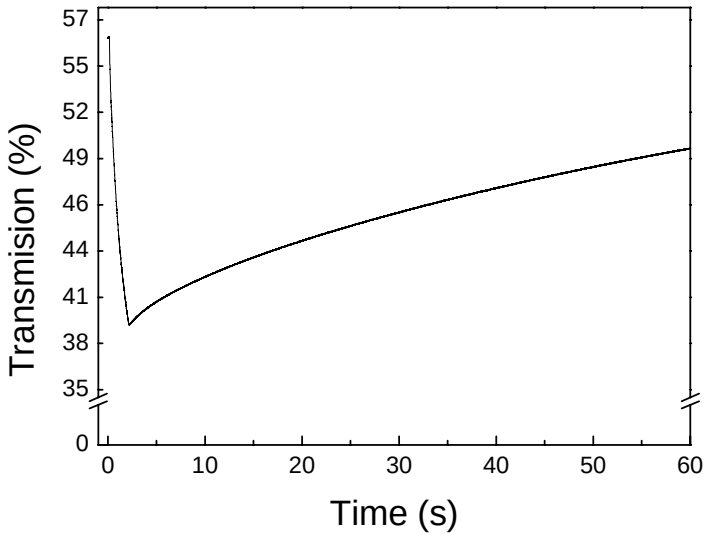

Fig. 5.74: Evolution of the transmittance of a window with the configuration K-glass/ NiO-TiO_2/ Starch (KOH)/ CeO_2_TiO_2/ K-glass in open circuit configuration after being colored at +1.9 V for 1 min.

5.8.4 Electrochromic devices with Nb_2O_5:Mo layer as counter electrode

Double, 200 nm thick Nb_2O_5:Mo double layers, sintered at 500 °C 30 min have been used as counter electrodes to laminate windows with the configuration glass/FTO/NiO-TiO_2/1 M aqueous KOH/Nb_2O_5:Mo/FTO/glass. Double, 160 nm thick NiO-TiO_2 layers sintered at 300 °C were used. The devices were filled with 1 M KOH and tested in the potential range –1 to +1.9 V.

The 1000^{th} CV voltammogram of the EC devices is shown in fig.5.75. No electrochemical activity is seen in the anodic scan in the potential range –1 V to 0.38 V but one side of a single intense anodic peak is seen at potential >1.3 V. It is accompanied by brown grey coloration of the device. Two well defined peaks occurs in the cathodic range. The first is broad and seen around +1.4 V while the second one at –0.74 V is narrower and better defined.

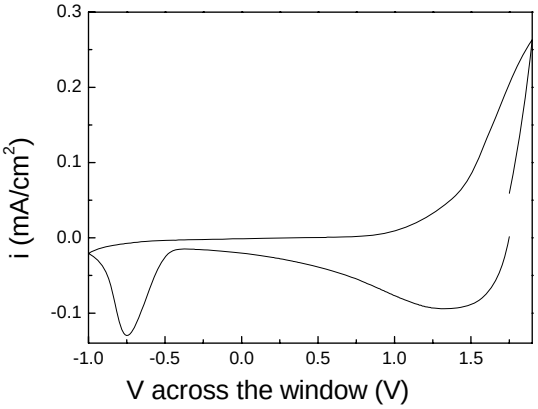

Fig. 5.75: 1000th CV voltammograms (-1 to +1.9 V) scan rate of 10mV/s of a window with the configuration K glass/ NiO-TiO_2/ 1 M KOH/Nb_2O_5:Mo/ K-glass with double NiO-TiO_2 and Nb_2O_5:Mo layers.

The transmittance spectra of the device in the bleached and colored states and the corresponding ΔOD are shown in fig. 5.76. The main transmittance change occurs in the visible range with a broad maximum of ΔOD between 390 and 440 nm The spectra look very similar to that of devices with the same configuration but using CeO_2-TiO_2 counter electrode (see fig. 5.58) but the transmittance of the bleached state is a little smaller in the visible range and the maximum of ΔOD is broader.

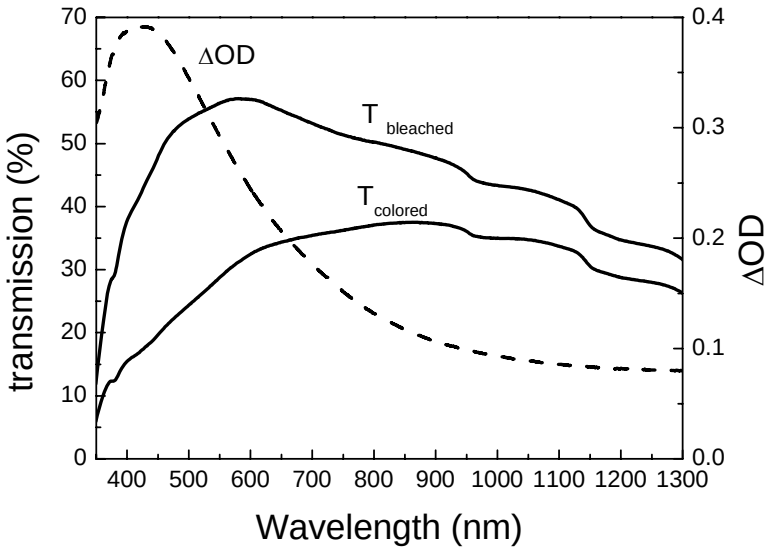

Fig. 5.76: Transmittance in the bleached and colored states of a windows with the configuration glass/ FTO/NiO-TiO_2/ 1 M liquid KOH/ Nb_2O_5:Mo/ FTO/ glass. It was colored and bleached by polarizing for 1 min at +1.9 V and –1 V respectively. The dotted curve is the corresponding ΔOD.

Fig. 5.77 shows the evolution of $T_{bleached}$, $T_{colored}$ and ΔOD as a function of the CA cycle number. Initially ΔOD has a value of 0.3, increases to 0.36 after 700 cycles and remains almost constant up to 2000 cycles and then begin to decrease gradually to 0.25. The transmittance of the window in the bleached state decreases however by cycling from 65% down to 35% after 5000 cycles. As observed the window becomes permanently colored and this coloration comes mainly from NiO-TiO_2 layer as discussed earlier in section 5.3. The transmittance of the coloured state decreases only in the first 700 cycles and then it remains practically constant at a low value of 20 % indicating that both EC layers Nb_2O_5:Mo and NiO-TiO_2 color simultaneously

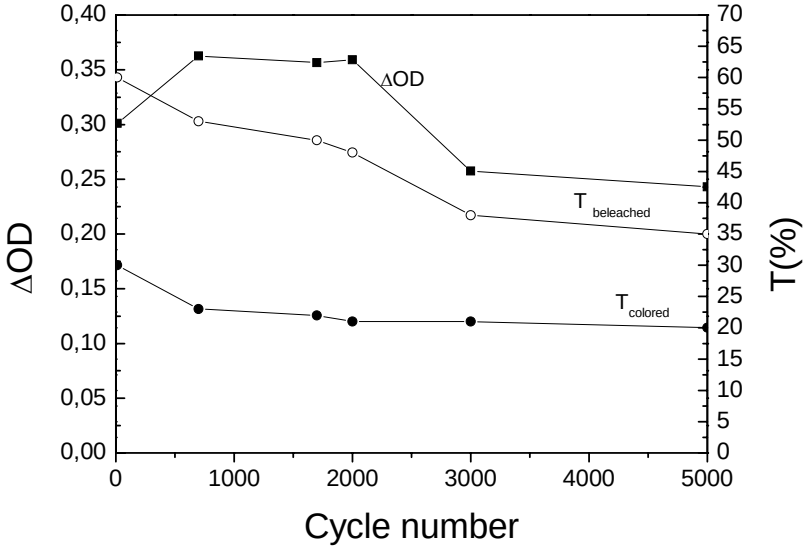

Fig. 5.77: Change of the optical density ΔOD at λ = 550 nm of EC-device K glass/ NiO-TiO_2/ KOH/ Nb_2O_5(Mo)/ K-glass as a function of the number of CA cycle (-1 V, +2 V, 1min) with the corresponding transmittance of the window in the bleached and colored states.

The use of a Nb_2O_5:Mo layer as cathodic coloring layer improves the optical density of the device compared with that assembled with a passive CeO_2-TiO_2 layer but the stability of the EC devices is worse.

5.8.5 EC-devices made with Li based (ORMOLYTE) electrolyte

a) Water content in the electrolyte

EC devices with the configuration K-glass/NiO-TiO_2 (80 nm)/inorganic-organic composite electrolyte/ (WO_3 (200 nm)/ K-glass were mounted with water content from 0 to 5 wt.% in the composite electrolyte. The WO_3 layer was considered here as the working electrode.

The time evolution of the transmittance of the EC device with different wt % water measured at 550 nm during the 50th CA cycle (-2 V, 2 min/+2 V, 2 min) is shown in fig 5.78a. Although the overall behavior of the kinetics is not changed, an EC device made with wet electrolyte colors deeper than the one built with a dry electrolyte. The coloration and bleaching kinetics are also faster with water in the electrolyte.

The charge intercalated during CA cycles (fig. 5.78b) follows the same tendency. Without water the value was –1.5 mC/cm^2 in the 50th CA cycle and it increases with the amount of water to –4 mC/cm^2 for 5wt % water. This explains the behavior of the transmittance change.

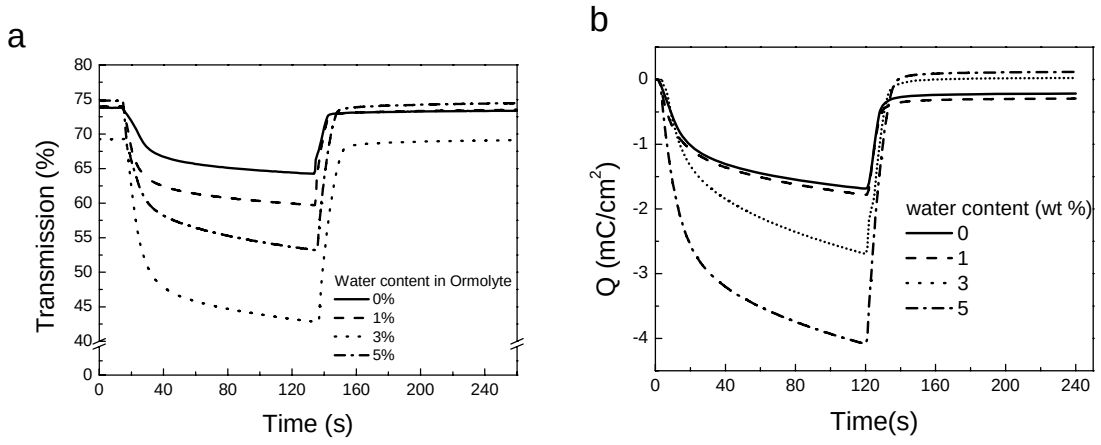

Fig. 5.78: (a) Transmittance change measured during CA (-2, 2 V/ 2min) of a window with the configuration K-glass/ NiO-TiO_2/ ORMOLYTE/ WO_3/ K-glass with different water content in the electrolyte, b) the corresponding inserted and de-inserted charge.

This behavior is also reflected in the optical density of the devices (fig. 5.79) which increases with the water content.

The long time stability of the devices is poor and affected by the water content of the electrolyte. EC-devices built with wet electrolyte have initially a higher value of ΔOD (about 0.20 as in fig. 5.79) but break down after about 50 cycles. Windows made with a dry electrolyte have a strong decrease of ΔOD (0.06) but remain stable up to higher number of cycles (about 500 cycles).

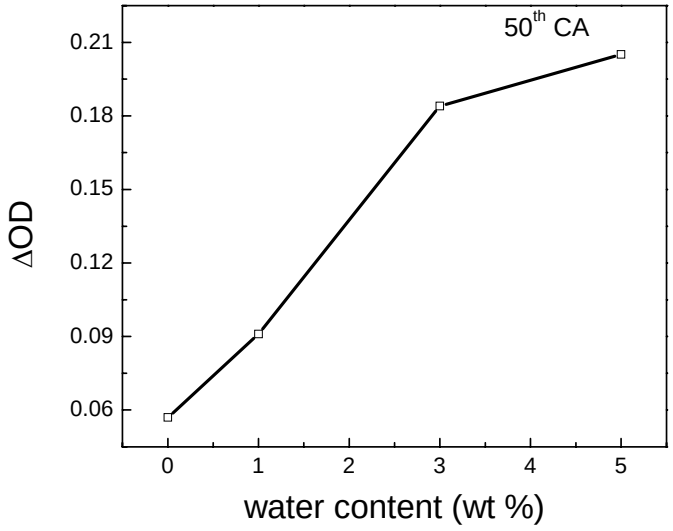

Fig. 5.79: Change in the optical density during the 50th CA (-2, +2 V/2min) of windows with the configuration K-glass/ NiO-TiO_2/ ORMOLYTE/ WO_3/ K-glass as as function of the water content in the electrolyte

b) Windows with NiO-TiO_2 layers with different Ni molar concentration

The electrochromic activity of devices with the configuration K-glass/WO_3/ormolyte (2 wt %) H_2O/NiO-TiO_2/K-glass made with NiO-TiO_2 layers with Ni molar concentration varies between 50 and 100 % and sintered at 300 °C has also been tested.

Fig. 5.80 shows the transmittance measured at 550 nm during the 2nd CA cycle (-2, 2 V/2 min). The transmittance of the colored state increases by increasing the Ni molar concentration in the NiO-TiO_2 layer. The bleaching kinetics was found somehow slower for pure NiO layer. ΔOD increases by increasing Ni content in the layer from 0.12 for layers with nickel content of 50 mol % to 0.21 for pure NiO layers. The long time stability deceases drastically by increasing the Ni content (fig. 5.80b).

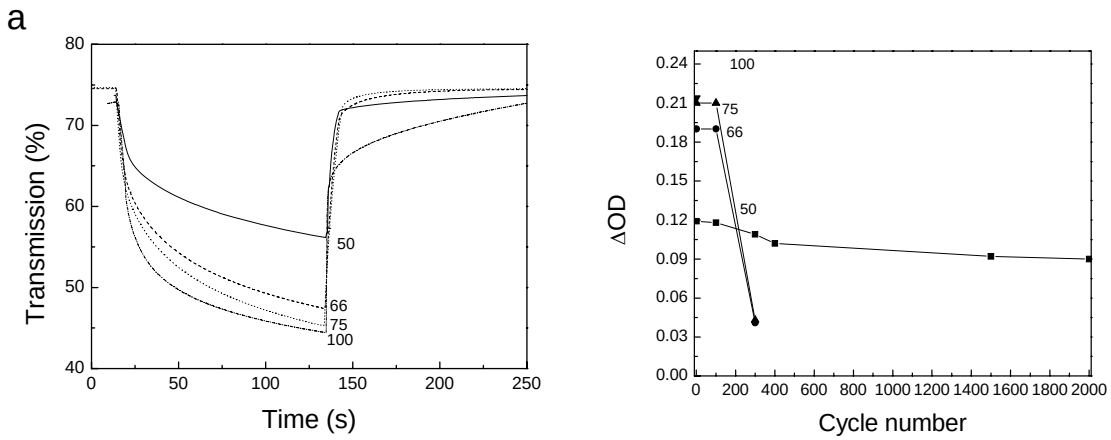

Fig. 5.80: (a) Transmittance measured at 550 nm during 2nd CA (-2, +2 V/2min) of windows with the configuration K-glass/ NiO-TiO_2/ ORMOLYTE (2wt % H_2O)/ WO_3/ K-glass. NiO-TiO_2 layers have ben prepared with different Ni molar concentration. (b) Change in optical density as a function of cycle number.

Chapter 6

Summary and Conclusion

$NiO-TiO_2$ xerogels and layers have been prepared by the sol-gel route with several Ni molar concentrations. Transparent single and multiple layers with total thickness up to 240 nm have been deposited on FTO coated glass by dip-coating and sintered up to 500 °C.

Thermal analysis of xerogels has been performed using simultaneous DTA-TG coupled to mass and infrared spectroscopy. A mass loss of about 10 wt% accompanied by an H_2O evolution was detected by MS and FTIR spectroscopy below 200 °C, corresponding to a final drying of the layer. The main feature of the DTA curve was a strong exothermic double peak between 300 and 360 °C with maximum at 344 and 357 °C. These features were accompanied by a large two peaks mass loss of about 35 wt %. A careful analysis of the infrared spectra of the gases evolved at these temperature values shows that the formation of inorganic nickel compounds, involving primarily NiO_x and possibly $NiCO_3$, only occurs up to about 350 °C. The last peak at 357 °C corresponds to the transformation of $NiCO_3$ into NiO.

SEM pictures of the coatings made with different Ni molar concentration indicated that all layers were homogeneous without pits or cracks. All coatings showed a slight greenish color.

Sol-gel $NiO-TiO_2$ layers sintered at different temperatures up to 500 °C had the Bunsenite cubic NiO structure regardless of the Ni concentration. The crystallinity of the layers increased with the sintering temperature and the crystallite size calculated with the (200) peak were 2.5, 4.7 and 8 nm after sintering at 300, 400, 500 °C respectively.

The electrochromic properties of the layers have been tested using cyclic voltammetry and chronoamperometry in 1 M aqueous solution of KOH as a function of the potential range, of the Ni content, of the heat treatment and of the thickness. Pure NiO layers showed a poor adhesion to the substrate, a permanent brown coloration after already 50 CV cycles and were easily degraded in the electrolyte. The adhesion was clearly improved by increasing the Ti content. For example the transmittance in the bleached state remained high and constant (> 75 %) up to 400 cycles when the Ni molar concentration was

<85 mol %. However both the optical density and the charge capacity decreased continuously by increasing the Ti content. The layers that presented the best properties were 160 nm thick double layers having a Ni molar concentration of 75 mol % and sintered between 300 and 350 °C. When cycled between –0.6 and +1 V vs. SCE, they showed a deep reversible brown coloration with change of transmittance at 550 nm between 90 and 25 %, an extended stability of about 2000 cycles and a fast switching time <10 s. The coloration of NiO-TiO_2 initiates in a thin interface layer (about 40-50 nm) that grows with cycling till reaching the full depth of the layer at the end of a so-called *activation period* that lasts up to about 1000 cycles depending on the potential range, the thickness of the layer and the sintering temperature. Simultaneously a slow degradation period takes place in which a passive, irreversible colored and very fragile layer is formed. This period is clearly observed after about 1000 cycles in which both the exchanged charge and the transmittance in the bleached state and correspondingly the change in optical density decrease. Due to the extreme fragility of this passive layer, the NiO-TiO_2 is also gradually disaggregated into the electrolyte till the layer is completely removed from the substrate after about 7000 to 10000 cycles.

The coloration mechanism of NiO-TiO_2 layers in KOH electrolyte was studied using a quartz crystal microbalance (QCM) in the potential range –0.4 to +0.57 V vs. SCE. Models have been suggested and discussed. The increase of the current density, charge and mass with cycling are compatible with the ideas proposed earlier that, in this activation period, only a thin layer located at the interface electrolyte/layer is active and that the thickness of this layer increases by cycling. Without knowing with precision the complex surroundings of the NiO nanoparticles, where the presence of $Ni(OH)_2$ (not observed by X-ray) and H_2O too is expected because of the low sintering temperature and/or by the wetting of the layer in the electrolyte, it is not possible to precisely assign a model. One possible equation to describe the results for E> 0.35 V is

$$Ni(OH)_2 + OH^- \leftrightarrow (NiOOH).(y/x)H_2O + (1-(y/x))\,H_2O + e^-$$

with $0 \leq y \leq x+1$

This formula describes the bonding of hydroxyls ions to $Ni(OH)_2$ with formation of hydrated NiOOH giving rise to the coloration of the film, the equation suggesting also the formation of lattice water.

The irreversible increase of both the mass and charge exchanged during each cycle was interpreted to be due to an increase of the amount of $Ni(OH)_2$ according to

$$NiO+z\ H_2O \rightarrow\ Ni(OH)_2 + (1-z)NiO$$

This allowed to understand the increase of the coloration behavior of the layer and the change of its morphology as observed by the TEM measurement.

This gradual change of the morphology lead also to a more open and mechanically fragile structure so that unusual large increase of the mass of the layer during each cycle has been observed eventually after the 330 cycles. This was interpreted as due to the incorporation of K^+ ions and water that led to the degradation period.

The electrochromic properties of the layers have been also tested in the three electrode cell filled with a $LiClO_4$-PC using $Ag/AgClO_4$-PC as reference electrode. It was proposed that the EC process involving a cathodic charge of up to 9 mC/cm^2 (for 80 nm thick film) was linked to an irreversible compositional changes of $Ni(OH)_2$ with the decomposition of small amount of water remaining in the layer. At more negative potentials Li^+ together with e^- can be effectively incorporated cathodically into the layer and the composition of the layer continuously changed to Li_zNiO-TiO_2. The electron may be localized by interacting with Ni^{2+} or most likely with the defects containing Li^+ or delocalized giving rise to the formation of polarons. In this case a mechanism similar to that of cathodic electrochromic materials like WO_3 and Nb_2O_5 is observed and the layer became colored. By reversing the galvanostatic current but limiting the potential to 0 V or during an anodic scan between–2.4 to 0 V, Li^+ ions are deinserted slowly out of the layer. Depending on the current and involved charge the layer may not be bleached completely, so that by further cycling, the composition of the layer oscillates between a partially transparent Li_aNiO-TiO_2 and a colored Li_bNiO-TiO_2 where b> a.

Brown coloring electrochromic devices have been built using NiO-TiO_2 layers with the configuration glass/FTO/NiO-TiO_2 (160 nm)/1 M liquid KOH/CeO_2-TiO_2 /FTO/ glass. The change in optical density of the device was in the range of 0.3 with coloration efficiency of about 41 cm^2/C. The window gained a permanent brown color by cycling due to the permanent coloration of NiO-TiO_2 layer. The long term stability of the devices was improved to 7000 cycles by using double NiO-TiO_2 layers instead of single layers (4000 cycles).

By depositing thin layers of dielectric oxides such as ZrO_2, TiO_2, Al_2O_3 and CeO_2-TiO_2 (all 20 to 25 nm thick) on top of the NiO-TiO_2 layer, the corrosion resistance in KOH electrolyte was improved so that long time stability up to 17000 cycles could be obtained.

Electrochromic devices using Nb_2O_5:Mo as cathodic counter electrode instead of the passive CeO_2-TiO_2 with the configuration glass/ FTO/ NiO-TiO_2 (160 nm)/ 1 M aqueous KOH/ Nb_2O_5:Mo (200 nm)/ FTO/ glass have been also tested in the potential range –1 to 1.9 V. the colored state of these devices were grey-brown. The use of a Nb_2O_5:Mo layer improved the change in optical density of the device (0.36) but their stability was worsened (5000 cycles only).

A new gel electrolyte containing KOH has been also developed to assemble almost all solid state devices. Windows with the configuration K-glass/ NiO-TiO_2/ starch (KOH)/ CeO_2-TiO_2/ K-glass have been assembled and tested in the voltage range –0.7 V to +1.9 V. During the first cycles the window exhibits a high transmittance change (70 % down to 26 %) without any activation period and ΔOD was rather high (0.42). In the next few cycles $T_{bleached}$ decreased from 69 to 61 % and $T_{colored}$ reversed from 26 to 48 % so that ΔOD decreased from 0.42 to 0.1. The efficiency of the window was improved again by cycling and ΔOD value up to 0.27 have been obtained after 2000 cycles.

Appendices

A.1 Optimisation of dip-coating soaking time

The effect of the time period during which the substrate remains in the sol during the dip coating process was tested by varying it between 15 and 240 s. The thickness of the layers was not affected.

However for period of time longer than 60 s, the layer was found hazy and not homogeneous. The change in optical density and in the charge capacity for layers soaked for different period of times are shown in fig.A.1

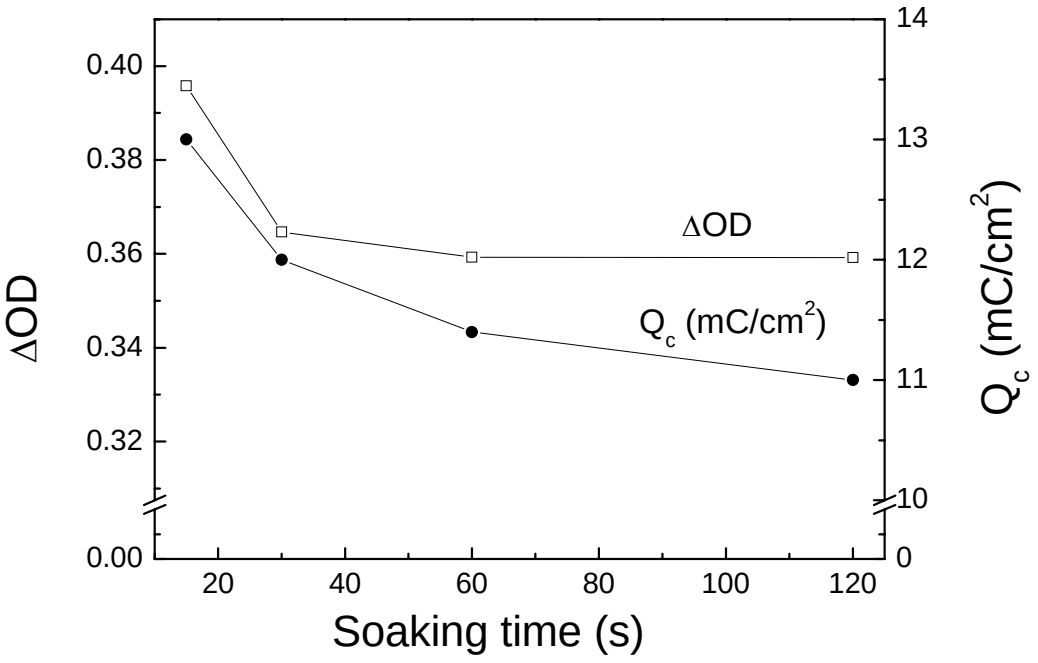

Fig. A.1: Charge capacity and change in optical density calculated from CV recording (-0.6 to +1 V) in KOH for NiO-TiO_2 layers (Ni molar concentration of 75 m %) deposited by dip coating technique with different soaking time and then sintered at 300 °C.

The change in optical density and the charge capacity decrease slightly by increasing the soaking time. 15 s was found an optimum

A.2 XPS spectrum

Studies realized with NiO based systems have always given very complex XPS spectra where the O 1s peaks bounded to Ni^{2+} and Ni^{3+} also Ni $2p_{3/2}$ peaks coming from Ni^{2+} and Ni^{3+} are overlapped [210].

The composition of NiO-TiO_2 layer in the colored and uncolored states was tested by XPS spectroscopy. An M-Probe (SSI surface science) spectrometer with Al-Kα 1486.6 eV monochromatic radiation was used. For sputter depth profiling, an Ar^+ beam of 2.5 KV was used to bombard an area of 2x2 mm^2 during 60s in $15x10^{-8}$ mbar vacuum.

The XPS spectra were recorded in the range 5 to 1000 eV for fresh and colored layer. The O 1s and Ni $2p_{3/2}$ results are shown in fig. A.2 and A.3 respectively. The energy scale was corrected with respect to the position of C 1s peak at 284.8 eV.

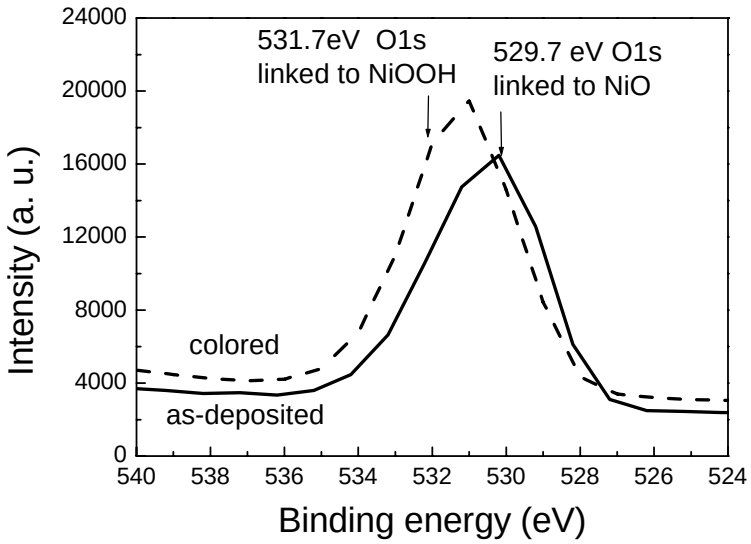

Fig. A.2 : O 1s spectrum at the surface of as-deposited and colored NiO-TiO_2 layers (Ni molar concentration of 75 mol. %) sintered at 300 °C. The layer was colored by cycling in a three electrode cell in KOH electrolyte for 50 CV cycles (-0.6 to +1 V) and disconnected in the colored state at +1 V. The values in the graphs are from literature [21].

O 1s states in nickel oxide compounds give one single peak centred at 529.7 for stoichiometric NiO (Ni^{2+}) and at 531.3, 531.7 eV in hydrogen containing phases $Ni(OH)_2$ (Ni^{2+}) and NiOOH ($Ni3^+$) respectively [21].

The overall width of the intensity vs. binding energy is much larger than that published in the literature (usually FWHM =1-1.5 eV). This may come from an instrument artifact but

more probable indicates that O 1s is linked to different oxides (e.g NiO, $Ni(OH)_2$, TiO_2, etc) so that the observed peak is the average of at least 3 peaks that can not be separated.

In the colored state, the maximum of the peak is shifted to higher binding energy but the width remains large. It shows nevertheless that part of the O is now bounded to Ni^{3+} but that a large part still linked to other oxides with 2+ value.

It is interesting to notice that the intensity of O1s spectra is lower for as deposited layer than colored one while Ni $2P_{3/2}$ spectra had opposite behavior indicating higher oxygen content in the colored phase.

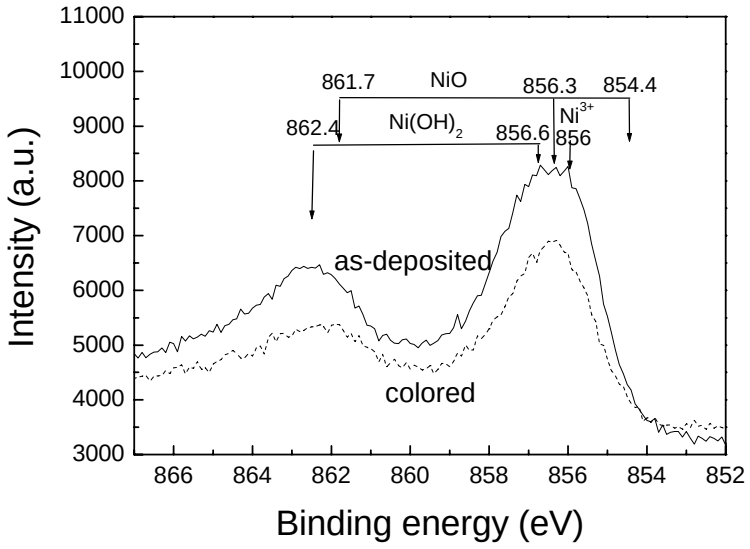

Fig. A.3: Ni $2p_{3/2}$ spectra at the surface of as-deposited and colored NiO-TiO_2 layers (Ni molar concentration of 75 mol. %) sintered at 300 °C. The layer was colored by cycling in a three electrode cell in KOH electrolyte for 50 CV cycles (-0.6 to +1 V) and disconnected in the colored state at +1 V. The values in the graphs are from literature [210].

Comparing the Ni2p spectrum in fig. A.3, the overall behavior is similar to that reported in the literature and the width of the peaks is also somewhat larger.

Previous research has supported assignment of BEs of (854.5, 856.3 and 861.7eV), and (856.6 and 862.4 eV) to Ni $2p_{3/2}$ XPS spectra for NiO and $Ni(OH)_2$ [210]. The main Ni^{3+}feature is seen around 856 eV [211].

The position of the peaks for the as deposited layer is therefore in rather good agreement and they reflect overlap of Ni $2p_{3/2}$ peaks due to NiO and $Ni(OH)_2$. It is nevertheless not possible to separate them.

The spectrum of the colored layer also reflects large width but their height is smaller than that of the as deposited layer. This is compatible with the fact that the amount of Ni in NiO and $Ni(OH)_2$ form has decreased but unfortunately no increase of Ni^{3+} peak (NiOOH) is observed.

The spectrum of the colored layer after sputter depth profiling is shown in fig. A.4 where nickel oxide reduction takes place and metallic Ni is formed reflected in the peak centred at 852.9 eV.

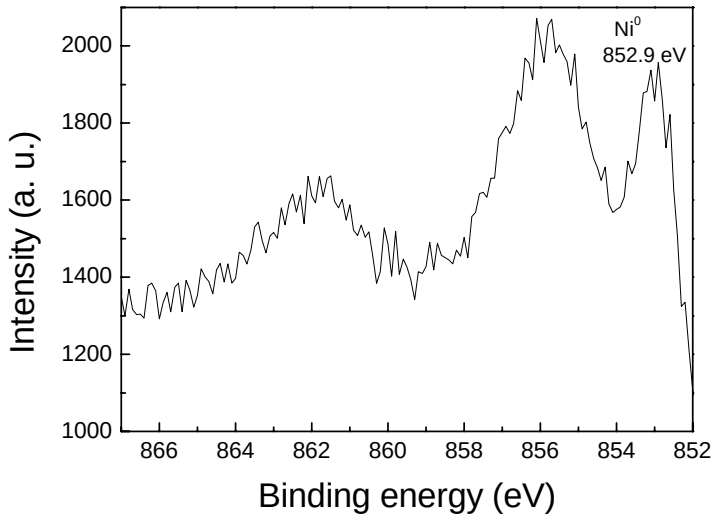

Fig. A.4: Ni $2p_{3/2}$ spectra of colored NiO-TiO_2 layers (Ni molar concentration of 75 mol. %) sintered at 300 °C after sputter depth profiling.. The layer was colored by cycling in a three electrode cell in KOH electrolyte for 50 CV cycles (-0.6 to +1 V) and disconnected in the colored state at +1 V.

The presence of Ni^0 is certainly due to the decomposition of NiO during the ion depth profiling. This is therefore an artifact of the measurement and of course no Ni^0 is present during our EC test.

The XPS analysis is rather difficult because of a complicated peak structure. Such measurement however are interesting and are underway with layers deposited on FTO and Au electrodes before and after some well defined EC procedures using higher resolution (search for O, Ni and K).

A.3 Devices made with FTO as ion storage layer

To check the possibility of using FTO as ion storage layer instead of CeO_2-TiO_2, devices with the configuration glass /FTO/NiO-TiO_2/KOH/FTO/glass have been built and tested in the potential range from –1 to 2 V.

Such a system works also and could be tested up to about 8000 cycles. The results are rather similar to those presented in section 5.8.1 except that the change in transmittance during cycling is smaller, the permanent coloration in the bleached state occurs faster, the transmittance at 550 nm decreasing from 70 % down to 20 % after 8000 cycles and that the CV profile of device is different. As an example the 1200th voltammogram of this device is shown in fig. A.5. It has two overlapping anodic peaks centred at 1.4 and 1.7 V that are accompanied with the device coloration also a well defined cathodic peak appears at -0.93 V associated with the bleaching. The anodic and cathodic current peak positions and the accompanied coloring and bleaching are however displaced to higher and lower values respectively when compared to that of devices with the same configuration but with CeO_2-TiO_2 layer as counter electrode represented by dotted line in fig. A.5. The reason for this shift is not yet known but indicates that the bleaching process may involve reaction that are different from those proposed in section 5.4.

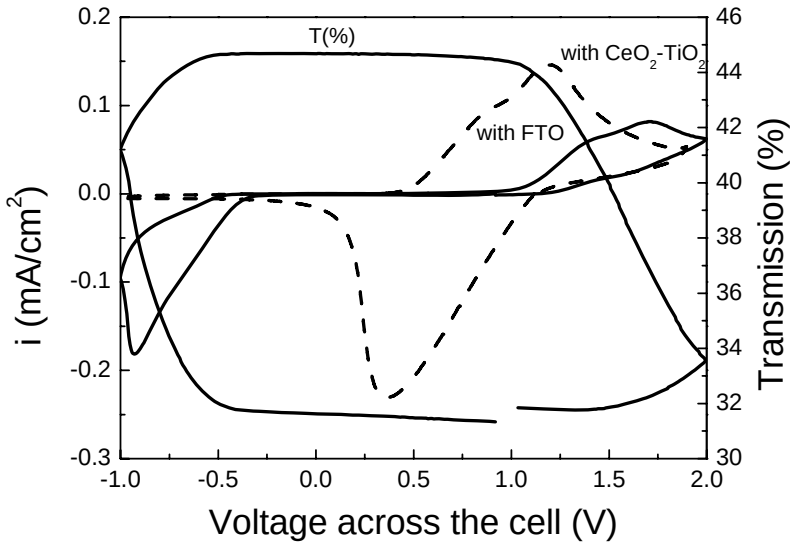

Fig. A.5: The 1200th CV voltammogram (-1, 2V) of EC devices with the configuration glass /FTO/NiO-TiO_2/KOH/FTO/glass. Scan rate 10 mV/s and the transmittance measured at 550nm.

Dotted curve represents the CV voltammogram of window with same configuration but with CeO_2-TiO_2 layer as counter electrode for comparison.

The reason of the strong permanent coloration of the device with cycling is similar to that discussed in section 5.8.1. The device can be in fact fully bleached by applying a negative potential during a longer time. Fig. A.6 shows the results for a window after being cycled for 1200 CA cycles (-1, +2 V/1 min). The transmittance effectively increases by increasing the polarizing period however as in the case of devices made with CeO_2-TiO_2 as a counter electrode, the device returns to the previous low transmittance value of the bleached state by performing 1 new cycle.

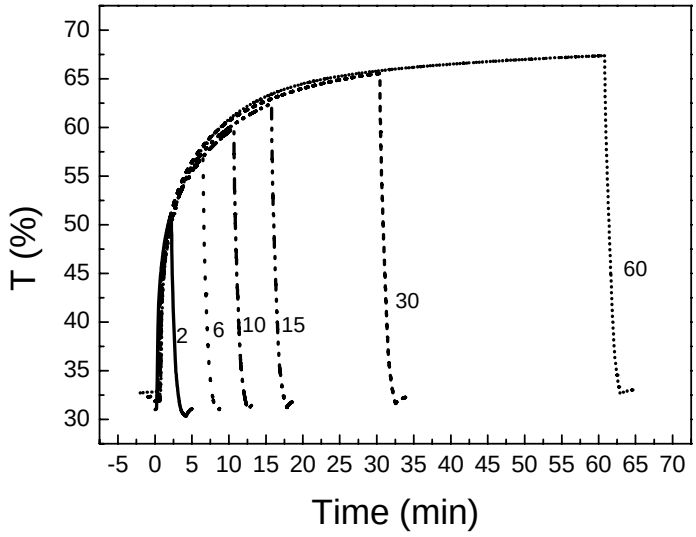

Fig.A.6: Optical transmittance of a device with the configuration glass/FTO/NiO-TiO_2/KOH/FTO/glass during CA measurements coloring:1 min at +2 V and bleaching: different time periods at the negative potential –1 V. The measurements have been taken after 1200 CA cycles (-1, 2 V/1 min).

B) List of chemicals used in this work:

Chemicals	Symbol	Supplier	Purity (%)
Nickel acetate tetrahydrate	$Ni(CH_3COO)_2.4H_2O$	Fluka	99+
Titanium n-propoxide	$Ti(C_3H_7O)_4$	Heraeus	≥90
Cerium (III)nitrate hexahydrate	$Ce(NO_3)_3 \cdot 6H_2O$	Chempur	99.9
Phosphomolybdic acid hydrate	$H_3[P(Mo_3O_{10})_4]$ ·	Kluka	≥98.5
Niobium(V) chloride	$NbCl_5$	Chempur	99+
glycidoxypropyltrimethoxysilane (GPTS),	$C_9H_{20}O_5Si$	ABCR	≥98
Lithium perchlorate	$LiClO_4$	Fluka	≥98
zirconium (IV) n-propoxide	$Zr(OC_3H_7)_4$	Chempur	70 % solution
tetraethylene glycol (TEG)	$HO(CH_2CH_2O)_3CH_2CH_2OH$	Acros Organics	≥99.5
propylene carbonate	C4H6O3	Fluka	Puriss: ≥99
Silver perchlorate	$AgClO_4$	RdH	≥98.5
Aluminium tri-sec butylate	$C_{12}H_{27}AlO_3$	MERCK-Schuchard	Al >97
Starch from maize	$(C_6H_{10}O_5)_n$	Fluka	
Glycerol	$C_3H_8O_3$	Fluka	Assay >99.5
Formaldehyde	CH2O	Fluka	Assay >36.5 in water
Potassium hdroxide	KOH	Fluka	Assay >98.5
Sodium hydroxide	NaOH	Fluka	Assay >97
Lithium hydroxide	LiOH	Fluka	Assay >97
Tetrabutylammonium hdroxide	C16H36NOH	Sigma-Aldrich	1 M in water

C) List of equipments used in this work

Measurement	Equipment	Supplier
Substrates cleaning	Wash machine, Professional IR 6001	Miele
Dip coating	Iselautomation CNC Kontroller C142-1	Rosenberg Electronik Messtechnik &Datenierabteitung
Heat treatment (<300 °C)	Furnace	Heraeus
Heat treatment (>300 °C)	Furnace	Carbolite
Film thickness	Profilometer, P10 surface Profiler	TENCOR
Transmittance	CARY 5E UV-VIS-NIR Spectrophotometer	Varian
Electrochemical measurements	VMP2 Multichannel Potentiostat and Potentiostat/Galvanostat Model 273 A	Princeton Applied Reasearch
Microbalance measurements	Research Quartz Crystal Microbalanc	MAXTEK
Thermal analysis (DTA/TG) combined with MS and FTIR Spectroscopy	STA 449C/3G Jupiter QMS403C Aeolos TENSOR27-FTIR	Netzsch Netzsch Brucker
X-ray diffraction (XRD)	X'Pert Philips- MPD, $CuK\alpha_{1,2}$	Philips
Transmittance Electron Microscopy	JEOL JEM-2010 Gatan MSC	JEOL
Scanning Electron Microscopy	JEOL JSM-6400F	JEOL
X ray Photoelectron Microscopy	M-Probe with Al-K_α 1486.6 eV monochromatic radiation	SSI Surface Science Instrument

References

1. C.M. Lampert, *Materials Today*, **7** (2004) 28.

2. J.P. Cronin, T.J. Gudgel, S.R. Kennedy, A. Agrawal, D.R. Uhlmann, *Material Research*., **2** (1999) 1.

3. N.A. O'brien, J.Gordon, H. Mathew, B.P. Hichwa, *Thin solid films*, **345** (1999) 312.

4. A. Azens, E. Avendaño, J. Backholm, L. Berggren, G. Gustavsson, R. Karmhag, G.A. Niklasson, A. Roos, C.G. Granqvist, *Materials Science and Engineering* B, **119** (2005) 214.

5. C.G. Granqvist, *Journal of the European Ceramic Society*, **25** (2005) 2907.

6. H. Dislich, *Noyes Publications*, (1988) 51.

7. H. Schmidt, In sol-gel optics: proceeding and applications ed by L.Klein, Dordrecht: kluwer (1994) 451.

8. K.A. Mauritz, R.M. Warren, *Macromolecules*, **22** (1989) 1730.

9. L.L. Hench, J.K. West, *Chem. Rev*., **90** (1990) 33.

10. H. Schmidt, *Sol-Gel Scienece and Technology*, **14-19** (1989) 61.

11. C.J. Brinker, G.W. Scherer, chapter 2, Academic Press, Inc. (1990).

12. S.V. Davis, K.A. Mauritz, *Am. Chem. Soc. Polym. Preperation*, **34** (1993) 608.

13. J. Puetz, M.A. Aegerter, Dip Coating techniques in M.A. Aegerter and M. Menig (eds) Handbook on sol-gel techniques for glass users and producers, Veröffentlichung (2004).

14. H.K Schmidt., *Macromolecular Symposium*, **101** (1996) 333.

15. N. Al-Dahoudi, *PhD Thesis*, Leibnitz Institute for New Materials (INM) and University of Saarland, Saarbruecken, Germany (2003) 13.

16. Http://Homepage.Ntlworld.Com/Colin.Pratt/Chromism.Pdf,

17. P.M.S. Monk, S.P. Akhtar, J. Boutevin, J.R. Duffield, *Electrochimica Acta*, **46** (2001) 2091.

18. G.A. Niklassona, L. Berggrena, A. Jonssona, R. Ahujab N.V. Skorodumovab, J. Backholma, M. Strømmea, *Solar Energy Materials & Solar Cells*, **90** (2006) 385.

19. P.M.S. Monk, R.J. Mortimer, D.R. Rosseinsky, *Electrochromism: Fundamentals and Applications*. (1995) Weinheim, VCH.

20. C.G. Granqvist, *Handbook of Inorganic Electrochromic Materials*. (1995) Amsterdam, Elsevier.

21. E. Avendano, *Uppsala Dissertation* from the faculty of science and technology (56), (2004).

22. Http://Library.Kcc.Hawaii.Edu/External/Chemistry/Everyday_Electro.Html,

23. P.R. Somani, S. Radhakrishnan, *Materials Chemistry and Physics*, **77** (2002) 117.

24. J. Livage, D. Ganguli, *Solar Energy Materials & Solar Cells*, **84** (2004) 315.

25. S. Radhakrisnan, S. Unde, A.B. Mandale, *Materials Chemistry and Physics*, **48** (1997) 268.

26. M. Ohyama, H. Kozuka, T. Yoko*, J. Am. Ceram. Soc*., **81** (1998) 1622.

27. S.F. Corgan, T.D. Plante, M.A. Parker, R.D. Rauh, *Solar Energy Materials*, **14** (1986) 185.

28. J.S.E.M. Svensson, C.G. Granqvist, *Thin Solid Films*, **126** (1985) 31.

29. C.G. Granqvist, *J Solar Energy Materials and Solar Cells*, **60** (2000) 201.

30. J.P. Cronin, D.J. Tarico, J.C.L. Tonazzi, A. Agrawal, S.R. Kennedy, *Solar Energy Materials & Solar Cells*, **29** (1993) 371.

31. J. Nagai, T. Kamimori, M. Mizuhashi, *Proc. SPIE*, **502** (1984) 59.

32. A. Deneuvillea, P. Gérarda, R. Billata, *Thin Solid Films*, **70** (1980) 203.

33. P. Judeinstein, J. Livage, A. Zarudiansky, R. Rose, *Solid State Ionics*, **28-30** (1988) 1722.

34. O. Bohnke, C. Bohnke, G. Robert, B. Carquille, *Solid State Ionics*, **6** (1982) 121.

35. M. Green, W.C. Smith, J.A. Weiner, *Thin Solid Films*, **38** (1976) 89.

36. D.K. Benson, C.E. Tracy, J.S.E.M. Svensson, B.E. Liebert, *SPIE Proceedings - The International Society for Optical Engineering*, **823** (1987) 72.

37. R. Hurdich, *Electron. Lett*, **11** (1975) 142.

38. A. Chemseddien, M. Henry, J. Livage, *Rev. Chim. Miner*, **21** (1984) 487.

39. J.-G. Zhang; C.E. Tracy, D.K. Benson; S.K. Deb, *Journal of Materials Research*, **8** (1993) 2649.

40. S. Badilescu, P.V. Ashrit, N. Minh-Ha, G. Bader, F.E. Girouard, V.-V. Truong, *Thin Solid Films*, **250** (1994) 47.

41. I. Shiyanovskaya, M. Hepel, *Journal of the Electrochemical Society*, **145** (1998) 1023.

42. J.D. Klein, A. Yen, *Materials Research Society Symposium Proceedings*, **293** (1993) 389.

43. C. Cantalinia, H. T. Suna, M. Facciob, M. Pelinoa, S. Santuccic, L. Lozzic, M. Passacantandoc, *Sensors and Actuators B: Chemical,* **31** (1996) 81.

44. L.S. Wang, B.P. Hichwa, S.P. Sapers, J.G.H. Mathew, N.A. O'brien, *The Electrochemical Society, Pennington*, **95-22** (1995) 63.

45. A. Georg, W. Graf, V. Wittwer, *Solar Energy Materials & Solar Cells,* **51** (1998) 353.

46. J.S. Hale, M. Devries, B.Dworak, J.A. Woollam, *Thin Solid Films*, **313-314** (1998) 205.

47. J. Wang, J. M. Bell, *Solar Energy Materials & Solar Cells*, **43** (1996) 377.

48. T.A. Taylor, H.H. Patterson, *Applied Spectroscopy*, **48** (1994) 674.

49. T. Nanbaa, T. Takahashia, J. Takadaa, A. Osakaa, Y. Miuraa, I. Yasuib, A. Kishimotob, T. Kudob, *Journal of Non-Crystalline Solids*, **178** (1994) 233.

50. J. Göttsche, A. Hinsch, V. Wittwer, *Solar Energy Materials & Solar Cells*, **31** (1993) 415.

51. U. Riaz, *Thin Solid Films*, **235** (1993) 15.

52. H. Unuma, K. Tonooka, Y. Suzuki, T. Furusaki, K. Kodaira, T. Matsushita, *Journal of Materials Science Letters*, **5** (1986) 1248.

53. K. Yamanaka, H. Oakamoto, H. Kidou, T. Kudo, *Japanese Journal of Applied Physics, Part 1: Regular Papers & Short Notes*, **25** (1986) 1420.

54. F.H. Moser, N.R. Lynam, *United States Patent* **4855161**.

55. M. Deepa, T.K. Saxena, D.P. Singh, K.N. Sood, S.A. Agnihotry, *Electrochimica Acta*, **51** (2006) 1974.

56. M. I. Yanovskayaa, I. E. Obvintsevaa, V. G. Kesslerb, B. Sh. Galyamova, S. I. Kucheikob, R. R. Shifrinaa, N. Ya. Turovab, *Journal of Non-Crystalline Solids*, **124** (1990) 155.

57. E.O. Zayim, N.D. Baydogan, *Solar Energy Materials & Solar Cells*, **90** (2006) 402.

58. E. O. Zayim, *Solar Energy Materials & Solar Cells*, **87** (2005) 695.

59. A. Cremonesia, D. Bersania, P.P. Lotticia, Y. Djaouedb, P.V. Ashritc, *Journal of Non-Crystalline Solids*, **345-346** (2004) 500.

60. C.O. Avellaneda, L.O.S. Bulhões, *Solar Energy Materials & Solar Cells*, **90** (2006) 395.

61. R. Ramachandran, A.P. Nidhi, S.A. Agnihotry, *Indian Journal of Pure and Applied Physics*, **37** (1999) 353.

62. M. Deepa, R. Sharma, A. Basu, S.A. Agnihotry, *Electrochimica Acta*, **50** (2005) 3545.

63. S.A. Agnihotry, R. Sharma, M. Kar, T.K. Saxena, *Solar Energy Materials & Solar Cells*, **90** (2006) 15.

64. S.A. Agnihotry, N. Sharma, M. Deepa, R. Kishorek.N. Sood, S.K. Sharma, *SPIE Proceedings - The International Society for Optical Engineering*, **3788** (1999) 111.

65. C.O. Avellaneda, P.R. Bueno, R.C. Faria, L.O.S. Bulhões, *Electrochimica Acta*, **46** (2001) 1977.

66. A. Pennisi, F. Simone, *Solar Energy Materials & Solar Cells*, **28** (1992) 233.

67. T. Nishide, F. Mizukami, *Journal of Materials Science Letters*, **15** (1996) 1149.

68. Y. Huang, Y. Zhang, X. Hu, *Solar Energy Materials & Solar Cells,* **77** (2003) 155.

69. K. Yoshimura, T. Miki, S. Tanemura, S. Iwama, *Thin Solid Films*, **281-282** (1996) 235.

70. T. Maruyama, T. Kanagawa, *J. Electrochem. Soc*., **141** (1994) 2868.

71. R.C. Faria, LO.S. Bulhoes, *Journal of the Electrochemical Society*, **141** (1994) L29.

72. D.A.B. Filho, P.P.A. Filho, U. Werner, M.A. Aegerter, *J. Sol-Gel Science and. Technology*, **8** (1997) 735.

73. M. Macek, B. Orel, U.O. Krasovec, *J. Electrochem. Soc*., **144** (1997) 3002.

74. M. Schmitt, M. A. Aegerter, *Electrochimica Acta*, **46** (2001) 2105.

75. A.V. Rosario, E.C. Pereira, *Electrochimica Acta*, **46** (2001) 1905.

76. A. Donnadieu, D. Davazoglou, A. Abdellaoui, *Proc. SPIE*, **1016** (1988) 124.

77. O. Zelaya-Angel, C. Menezes, F. Sanchez-Sinencio, G.F.L. Ferreira., *Journal of Applied Physics*, **51** (1980) 6022.

78. A. Nemetz, A. Temmink, K. Bange, S.C. De Torresi, C. Gabrielli, R. Torresi, A. Hugot-Le Goff, *Solar Energy Mterials & Solar Cells*, **25** (1992) 93.

79. I. Serebrennikova, V.I. Birss, *J. Electrochem. Soc*., **144** (1997) 566.

80. R. Cerc Korosec, P. Bukovec, *Thermochemica ACT*, **410** (2004) 65.

81. R.C. Korosec, P. Bukovec, B. Pihlar, A. Surca Vuk, B. Orel, G. Drazic, S*olid State Ionics*, **165** (2003) 191.

82. A. Surca, B. Orel, B. Pihlar, P.Bukovec, *Journal of Electroanalytical Chemistry*, **408** (1996) 83.

83. A. Surca, B.Orel, *Journal of Sol-Gel Science and Technology*, **8** (1997) 743.

84. Fantini, M.C.A., *SPIE Proceedings,* **1536** (1991) 81.

85. A.E. Jiménez-González, J.G. Combray, *Surface Engineering*, **16** (2000) 73.

86. J.L. Garcia-Miquel, Q. Zhang, S.J. Allen, A. Rougier, A. Blyr, H.O. Davies, A.C. Jones, T.J. Leedham, P.A. Williams, S.A. Impey, *Thin Solid Films*, **424** (2003) 165.

87. P.A. Williams, A.C. Jones, J. F. Bickley, A. Steiner, H. O. Davis, T. J. Leedham, S. A. Impey, J. Garcia, S. Allen, A. Rougier, A. Blyr, *Journal of Materials Chemistry*, **11** (2001) 2329.

88. P.K. Sharma, M.C.A. Fantini, A. Gorenstein, *Solid State Ionics*, **113-115** (1998) 457.

89. D. Santos Lopez, *Diplom Thesis*, Leibnitz Institute for New Materials, Saarbruecken, (2003).

90. T. Miki, K. Yoshimura, Y. Tai, M. Tazawa, P. Jin, S. Tanemura, *SPIE Proceedings*, **2531** (1995) 135.

91. J.-Y. Park, K.-S. Ahn, Y.-C Nah, H.-S. Shim, *Journal of Sol-Gel Science and Technology*, **31** (2004) 323.

92. Z. Jiao, M. Wu, Z. Qin H. Xu, *Nanotechnology*, **14** (2003) 458.

93. A. Surca, B. Orel, R.C. Korosec, P.Bukovec, B.Philer, *Journal of Electroanalytical Chemistry*, **443** (1997) 57.

94. F. Svegl, B. Orel, V. kaucic, *Solar Energy*, **68** (2000) 523.

95. F.H. Moser, N.R.Lynam, *United States Patent*, **4959247** (1987) Appl. No 132196.

96. Z. He, Z. Ji, S. Zhao, C. Wang, K. Liu, Z.Ye, *Solar Energy*, **80** (2006) 226.

97. M. Fantini, A. Gorenstein, *Solar Energy Materials*, **16** (1987) 487.

98. Terresi, S.I. Cordoba De, *Electrochimica Acta*, **40** (1995) 1101.

99. A.E. Jimenez-Gonzalez, J.G. Cambray, A.A. Ruiz Gutierrez, *Surface Engineering*, **16** (2000) 77.

100. D.D. Ragan, P. Svedlindh, C.G. Granqvist, *Solar Energy Mterials & Solar Cells*, **54** (1998) 247.

101. T.J. Richardson, M.D. Rubin, *Electrochimica Acta*, **46** (2001) 2119.

102. J.S.E.M. Svensson, C.G. Granqvist, *Applied Physics Letters*, **49** (1986) 1566.

103. L. Ottaviano, A. Pennis, F. Simone, *Surface and Interface Analysis*, **36** (2004) 1335.

104. S.R. Jiang, P.X. Yan, B.X. Feng, X.M. Cai, J. Wang, *Materials Chemistry and Physics*, **77** (2002) 384.

105. A. Azens, C.G. Granqvist, *Journal of Applied Physics*, **84** (1998) 6454.

106. A. Azens, J.Isidorsoon, R. Karmhag, C.G. Granqvist, *Thin Solid Films*, **422** (2002) 1.

107. E. Avendano, A. Azens, G. A. Niklasson, C.G. Ganqvist, *J. Solid State Electrochem*., **8** (2003) 37.

108. I.C. Faria, M. Kleinke, A. Gorenstein, M.C.A. Fantini, M.H. Tabacniks, *J. Electrochem. Soc*., **145** (1998) 235.

109. K. Yoshimura, T. Miki, S. Tanemura, *SPIE Proceedings*, **2531** (1995) 127.

110. F.F. Ferreira, M.H. Tabacniks, M. C. A. Fantini, I. C. Faria, A. Gorenstein, *Solid State Ionics*, **86-88** (1996) 971.

111. X.Y. Song, Y.X. He, C.M. Lampert, X.F. Hu, X.F. Chen, *Solar Energy Mterials & Solar Cells*, **63** (2000) 227.

112. E. Avendaño, A. Azens, J. Isidorsson, R. Karmhag, G. A. Niklasson,C. G. Granqvist, *Solid State Ionics*, **165** (2003) 169.

113. M. Kitao, K. Izawa and K. Urabe, T. Komatsu, S. Kuwano, S. Yamada, *Japanese Journal of Applied Physics, Part 1: Regular Papers & Short Notes*, **33** (1994) 6656.

114. M. Kitao, K. Izawa and S. Yamada, *Solar Energy Materials & Solar Cells*, **39** (1995) 115.

115. J.S.E.M. Svensson, C.G. Granqvist, *Solar Energy Materials,* **16** (1987) 19.

116. A. Azens, L. Kullman, G. Vaivars, H. Nordborg and C.G. Granqvist, *Solid State Ionics*, **113-115** (1998) 449.

117. F. Michalak, K. Von Rottkay, T. Richardson, J. Slack, M. Rubin, *Electrochimica Acta*, **44** (1999) 3085.

118. Kwang-Soon Ahn, Yoon-Chae Nah, Yung-Eun Sung, *Solid State Ionics*, **156** (2003) 433.

119. Y.G. Wu, G.M. Wu, X.Y. Ni, X. Wu, *Solar Energy Materials & Solar Cells,* **63** (2000) 217.

120. K.D. Lee, W.C. Jung, *Journal of Corean Physical Society*, **45** (2004) 447.

121. J. Nagai, *Solar Energy Mterials & Solar Cells*, **31** (1993) 291.

122. A. Agrawal, H.R. Habibi, R.K. Agrawal, J.P. Cronin, D.M. Roberts, R. Caron-Popowich, C.M. Lampert, *Thin Solid Films*, **221** (1992) 239.

123. T. Seike, J. Nagai, *Solar Energy Materials*, **22** (1991) 107.

124. I Bouessay, A. Rougier, P. Poizot, J. Moscovici, A. Michalowicz, J.-M.Tarascon, *Electrochimica Acta*, **50** (2005) 3737.

125. I. Bouessay, A. Rougier, J-M. Tarascon, *Journal of the Electrochemical Society*, **151** (2004) H145.

126. I. Bouessay, A. Rougier, B. Beaudoin, J. B. Leriche, *Applied Surface Science*, **186** (2002) 490.

127. S-J. Wen, J.Kerr, M. Rubin, J. Slack, K. Von Rottkay, *Solar Energy Mterials & Solar Cells*, **56** (1999) 299.

128. Y. Makimura, A.RougierJ.-M. Tarascon, *Applied Surface Science*, **I199** (2002) 259.

129. N. Penin, A. Rougier, L. Laffont, P. Poizot and J.-M. Tarascon, *Solar Energy Materials & Solar Cells*, **90** (2006) 422.

130. S. Taunier, C. Guery, J.-M. Tarascon, *Electrochimica Acta*, **44** (1999) 3219.

131. R. D. Rauh, S. F. Cogan, *Solid State Ionics*, **28-30** (1988) 1707.

132. S. F. Cogan, T. D. Plante, R. S. Mcfadden, R. D. Rauh, *Solar Energy Materials*, **16** (1987) 371.

133. Y. Sato, *Vaccum*, **41** (1990) 1198.

134. A. Osaka, T. Takatsuna, Y. Miura, *Journal of Non-Crystalline Solids*, **178** (1994) 313.

135. G. Lodi, A. De Battisti, G. Bordin, C. De Asmundis, A. Benedetti, *Journal of Electroanalytical Chemistry*, **277** (1990) 139.

136. C. Chen, S. Trasatti, *J. Appl. Electrochem*, **23** 559.

137. A. Donnadieu, *Materials Science and Engineering*, **B3** (1989) 185-195.

138. S.F. Cogan, T.D. Plante, R.S. Mcfadden,R.D. Rauh, *SPIE Proceedings - The International Society for Optical Engineering*, **823** (1987) 106.

139. S.F. Cogan, N.M. Nguyen, S.J. Perrotti, R.D. Rauh, *J. Electrochem. Soc*., **57** (1988) 1016.

140. S.F. Cogan, R.D. Rauh, N.M. Nguyen and T.D. Plante and J.D. Westwood, *J. Electrochem. Soc.*, **140** (1993) 112.

141. P. Baudry, A. C. M. Rodrigues, M. A. Aegerter, *Journal of Non-Crystalline Solids*, **121** (1990) 319.

142. Y. Katsuta, A.E. Hill, A. M. Phahle, J. H. Calderwood, *Thin Solid Films,* **18** (1973) 53.

143. M. Ottaviani, S. Panero, S. Morzilli, B. Scrosati, M. Lazzari, *Solid State Ionics*, **20** (1986) 197.

144. D. Sun, *PhD thesis*, Leibnitz Institute for New Materials (INM) and saarland University, Saarbreucken (2005) .

145. C. O. Avellaneda, A. Pawlickab, *Thin Solid Films,* **335** (1998) 245.

146. F.E. Ghodsi, F.Z. Tepehan, G.G. Tepehan, *Electrochimica Acta*, **44** (1999) 3127.

147. M. Rubin, K. Von Rottkay, S.-J. Wen, N. Özer, J. Slack, *Solar Energy Materials & Solar Cells*, **54** (1998) 49.

148. A. Makishima, M.i Asami, K. Wada, *Journal of Non-Crystalline Solids*, **100** (1988) 321.

149. A. Makishimaa, M. Asami, K. Wada, *Journal of Non-Crystalline Solids*, **121** (1990) 310.

150. U. L. Stangar , B. Orel, I. Grabec, B. Ogorevc, K. Kalcher, *Solar Energy Materials & Solar Cells*, **31** (1993) 171.

151. J.C.L. Tonazzi, B. Valla, M.A. Macedo, P. Baudry, M.A. Aegerter, A.C.M. Rodrigez, L.O. Bulhöes, *Proc*. *SPIE*, **1328** (1990) 375.

152. D. Kéomany, J.-P. Petit, D. Deroo, *Solar Energy Mterials & Solar Cells*, **36** (1995) 397.

153. D. Kéomany, C. Poinsignon and D. Deroo, *Solar Energy Mterials & Solar Cells*, **33** (1994) 429.

154. A. Verma, S. B. Samanta, A. K. Bakhshi, S. A. Agnihotry, *Solid State Ionics*, **71** (2004) 81.

155. N. Ozer, F. Tepehan, N. Bozkurt, *Thin Solid Films*, **219** (1992) 193.

156. V.M.M. Mercier, P.V.Der Sluis, *Solid State Ionics*, **145** (2001) 17.

157. Y. Charbouillot, D. Ravaine, M. Armand, C. Poinsignon, *Journal of Non-Crystalline Solids*, **103** (1988) 325.

158. C.M. Lampert, *Solar Energy Materials & Solar Cells*, **52** (1998) 207.

159. A.W. Czanderna, D.K. Benson, G.J. Jorgensen, J.-G. Zhang, C.E. Tracy, S.K. Deb, *Solar Energy Materials & Solar Cells*, **56** (1999) 419.

160. J. Gordon H. Mathew, S.P. Sapers, M.J. Cumbo, N.A. O'brien, R.B. Sargent, V.P. Raksha, R.B. Lahaderne, B.P. Hichwa, *Journal of Non-Crystalline Solids*, **218** (1997) 342.

161. R.J. Warren, P. Christopher, *Journal of Electroanalytical Chemistry,* **460** (1999) 263.

162. D.R.R. Monk, L. Jacaranda, *Journal of Electroanalytical Chemistry*, **270** (1989) 473.

163. F.G.K. Baucke, K Bange, T Gambke, *DISPLAYS*, (1988) 179.

164. F.G.K. Baucke, *Solar Energy Materials & Solar Cells*, **19** (1987) 67.

165. R. Lechner, L. K. Thomas., *Solar Energy Materials & Solar Cells*, **54** (1998) 139.

166. J. Nagai, G.D. Mcmeeking, Y. Saitoh, *Solar Energy Materials & Solar Cells*, **56** (1999) 309.

167. C. Trimble, M. Devries, J.S. Hale, D. W. Thompson, T.E. Tiwald, J. A. Woollam, *Thin Solid Films*, **355-356** (1999) 26.

168. J. Nagai, *SPIE Proceedings - The International Society for Optical Engineering*, **1728** (1992) 194.

169. A. Azens, G. Vaivars, M. Veszelei, L. Kullman, C.G. Granqvist, *Journal of Applied Physics*, **89** (2001) 7885.

170. O. Karlsson, A. Roos, *Solar Energy*, **68** (2000) 493.

171. A. Pennisi, F. Simone, G. Barlettac, G.Di Marcod, M. Lanzad, *Electrochimica Acta*, **44** (1999) 3237.

172. Ahn, Kwang-Soon; Nah, Yoon-Chae; Park, Jin-Young; Sung, Yung-Eun; Cho, Ki-Yun; Shin, Seung-Shik; Park, Jung-Ki, *Applied Physics Letters*, **82** (2003) 3379.

173. Antinucci, Marcello; Ferriolo, Antonio, *Proceedings of SPIE - The International Society for Optical Engineering*, **2255** (1994) 395.

174. A. Azens, G. Gustavsson, R. Karmhag, C. G. Granqvist, *Solid State Ionics*, 165 (2003) 1.

175. K.-S. Lee, H.-J. Koo, K.-H. Ham, W.-S. Ahn, *Bull.Korean.Chem.Soc*., **16** (1995) 164

176. S. Hüfner, T.riserer, *Physical Review B*, **33** (1986) 7267 .

177. Http://Www.Webelements.Com/Webelements/Compounds/Text/Ni/Ni1o1-1313991.Html, .

178. A.R. Williams, J. Kübler, K. Terakura, *Phys. Rev. Lett*, **54** (1985) 2728.

179. R. Merlin, *Phys Rev. Lett*, **54** (1985) 2727.

180. N. Sac-Epe, M.R. Palacin, A. Delahaye-Vidal, Y.Chabre, J-M. Tarascon, *J. Electrochem. Soc*., **145** (1998).

181. P. Oliva, J. Lenoardi, J.F.Laurent, C.Delmas, J.J. Braconnier, M. Figlarz, F. Fievet, A. De Guibert, *Journal of Power Sources*, **8** (1982) 229.

182. S. Deabate, F. Henn, *Electrochimica Acta*, **50** (2005) 2823.

183. H.Bode, K. Dehmelt and J. Witte, *Electrochimica Acta*, **11** (1966) 1079.

184. S. Le, M. Figlarz, *Electrochimica Acta*, **18** (1973) 123.

185. R.S. Mcewen*, J. Phys. Chem*., **75** (1971) 1782.

186. N. Sac-Epee, M.R. Palacin, A. Delahaye-Vidal, T.Jamin, Y.Chabre, J-M. Tarascon, *J. Electrochem. Soc.,* **144** (1997) 3896.

187. D. Toumi, *J. Electrochem. Soc*., **112** (1965) 1.

188. M. Martini, *Electrochimica Acta*, **46** (2001) 2275.

189. M.K. Carpenter, R.S. Conell, D.A. Corrigan, *Solar Energy Materials,* **16** (1987) 333.

190. J. Scarminio, W. Estrada, A. Andersson, A. Gorenstein, F. Decker, J. *Electrochem. Soc*., **139** (1992) 1236.

191. S. Passerini, B. Scrosati, A. Gorenstein, A.M. Andersson, C.G. Granqvist, *J. Electrochem. Soc*, **136** (1989) 3395.

192. S. Passerini, B. Scrosati, A. Gorenstein, *Journal of the Electrochemical Society*, **137** (1990) 3297.

193. S. Passerini, *Solid State Ionics*, **53-56** (1992) 520.

194. F. Decker, S. Passerini, R. Pileggi, B. Scorosati, *Electrochimica Acta*, **37** (1992) 1033.

195. S. Passerini, *Journal of the Electrochemical Society*, **141** (1994) 889.

196. D.L. Sun; S. Heusing; J. Puetz ; M.A. Aegerter, *Solid State Ionics*, **165** (2003) 181.

197. M. Schmitt, M.A. Aegerter*, SPIE Proceeding*, **3788** (1999) 75.

198. H. Schmidt, H. Krug, N. Merl, A. Moses, P Judeinstein, A. Berni, *Electrochromic thin film systems and components thereof, Patent WO 95***28663**, (1994) .

199. B. Munro, P. Conrad, S. KraMer, H. Schmidt, P. Zapp, *Solar Energy Materials & Solar Cells*, **54** (1998) 131.

200. R. Bhargava, I.W. Leven, *Applied Spectroscopy*, **58** (2004) 995.

201. S. I. Cordoba-Torresi, C. Gabrielli, A. Hugot-Le Goff, and R. Torresi, *Journal of Electroanalytical Chemistry*, **138** (1991)

202. Kim, Kyung-Wang Nam and Kwang-Bum, *Journal of the Electrochemical Society*, **149** (2002) A346.

203. J.C. De Jesus, I. Gonzalez, A. Quevedo, T. Puerta, *Journal of Molecular catalysis A: Chemical*, **228** (2005) 283.

204. Y. Wu, Y. He, T. Chen, W. Weng and H. Wanf, *Materials Letters*, **59** (2005) 3106.

205. P.R. Buenoa, T, R.C. Fariab, L.O.S. Bulho˜Esb, *Solid State Ionics,* **176** (2005) 1175.

206. P. Bernard, C. Gabrielli, M. Keddam and H. Takenouti, *Electrochemica Acta*, **36** (1991) 743.

207. T. Ohligschläger, G. Schwitzgebel, *Phys. Chem. Chem. Phys*, **3** (2001) 5290.

208. F.A. Cotton, G. Wilkinson, *chapter 4*: The group IA (1) elements Li, Na, Rb, Cs, Fr, Wiley (1988).

209. J.A. Scarminio A. Gorenstein, F. Decker, S. Passerini, R. Pileggi, B. Scrosati, *SPIE Proceedings - The International Society for Optical Engineering,* **1536** (1991) 70.

210. S. Oswald, W Breuckner, *Surface and Interface Analysis*, **36** (2004) 17.

211. A.P. Grosvenor, M.C. Biesinger, R.C. Smart, N. S. McIntyre, *Surface Science* in Press (2006)